Flagellar proteins regulating motility, assembly and photobehavior in *Chlamydomonas reinhardtii*

A DISSERTATION
SUBMITTED TO THE FACULTY OF THE GRADUATE SCHOOL
OF THE UNIVERSITY OF MINNESOTA
BY

Kristyn E. VanderWaal Mills

IN PARTIAL FULFILLMENT OF THE REQUIREMENTS
FOR THE DEGREE OF
DOCTOR OF PHILOSOPHY

Advisor: Dr. Mary Porter

July 2011

Acknowledgements

I first wish to thank the many people who have helped me with specific experiments during my thesis research. Thanks to undergraduate students Claire Palmer (Wesleyan University) and Jaimee Reck (University of Minnesota) for assistance with the analysis of swimming velocities, photo-accumulation, and photoshock. Special thanks to Jaimee Reck for help on the IFT related Western blots while I was focusing on writing. I also acknowledge Shota Mochiji (University of Tokyo) for assistance with the phototaxis assays, Kimberly VanderWaal (University of California at Davis) for assistance with statistical analysis of quantitative waveform data, and members of the Dutcher lab (Washington University) for providing the equipment, instruction, and guidance for the recording and analysis of flagellar waveforms. Thanks also to Stuart Goldstein (University of Minnesota) for helpful discussions on waveform parameters. We acknowledge the College of Biological Sciences' Imaging Center at The University of Minnesota, including assistance from Mark Sanders with fluorescence microscopy. Thank you to Lai-wa Tam for providing the MBO2 and OEE3 antibody.

In addition to help with many specific experiments, all the past and current members of the Porter lab have been invaluable to me. Specifically, Cathy Perrone taught me many of the microscopic imaging techniques and gave me the tools to develop new microscopic assays; Kelly Bower continues to be the best resource in our lab for all protein biochemistry questions and experiments; and Doug Tritschler assisted me with many of the molecular biology techniques and cloning. Members of the Sale lab (Emory University), particularly Laura Fox and Win Sale, have also helped with microtubule sliding assays and discussion of the I1 dynein data. Eileen O'Toole, at University of Colorado at Boulder, did the EM analysis. All of these scientists have contributed specifically to figures throughout my thesis, which I have noted in the figure legends. In Appendix 1, I worked on writing up methods for analysis of IFT in *Chlamydomonas* flagella with Dr. Dentler, where I wrote up the portions on analysis using fluorescence microscopy while he wrote up the DIC microscopy methods.

I am also very fortunate to have a fantastic advisor in Mary Porter. Not only has she been the driving force behind my thesis research and ideas, but she has supported me through my struggles with experiments and helped me shift focus to new, but related projects. She encouraged me to pursue my research, my career goals, and my personal happiness, and that balance of encouragement was a large part of my success in graduate school.

I have had several sources of funding for my graduate thesis, including a 3M Science and Engineering Fellowship, a pre-doctoral fellowship from the American Heart Association Fellowship (0715799Z), a Doctoral Dissertation Fellowship from the University of Minnesota and a Grant-in-Aid (20828) from the University of Minnesota Graduate School to MEP. Special thanks also to my committee of Ann Rougvie, Carolyn Silflow, David Odde, and Stu Goldstein for their support and advice during my time in graduate school.

Finally, I must deeply thank my family and friends for their emotional (and sometimes, experimental) help these last six years. My parents encouraged me to be persistent when I was struggling the most. My younger sister, who is also getting her Ph.D. in biology, was an immense help and comfort to me. Not only could she actually be a sounding board for my ideas and assist me with statistical analysis, but she also was one of my greatest supporters. I sincerely thank my friends both in and out of graduate school, Calhoun Isles community band, and Tempo Rosa Brass Quintet for their love, support and understanding when graduate school sometimes was first priority. Last, my husband has been exceedingly understanding through this entire process. Because he received his Ph.D. in chemistry from the University of Minnesota, he could speak first hand to the struggles of actually writing a thesis. He has also been a steadfast pillar for me to lean on during all of the emotional struggles and highs. Our marriage survived two Ph.D. theses, and we're now ready to move on to our next adventure!

Abstract

Cilia and flagella are microtubule-based organelles that perform critical functions in human health and development. The I1 inner arm dynein and the IC138 subunit play a key role in the regulation of flagellar motility. To understand how the IC138 protein and its associated subunits modulate I1 activity, we characterized the molecular lesions and motility phenotypes of several *bop5* alleles in *Chlamydomonas reinhardtii*. We first characterize a mutation (*bop5-2*) that disrupts an IC138 protein sub-complex located at the base of the I1 inner arm dynein. We found the *bop5-2* deletion also affects the *Tubby-1 (TBY1)* gene. To characterize *TBY1's* activity, tagged versions of *TBY1* were transformed into *bop5-2*. TBY1 protein localizes to a unique ring shaped structure found between the two contractile vacuoles and within the nucleo-flagellar apparatus. The *bop5-3, bop5-4* and *bop5-5* strains, like other I1 mutants, swim forwards with reduced swimming velocities and display an impaired reversal response during photoshock. However, unlike mutants lacking the entire I1 complex, *bop5* strains exhibit normal phototaxis. Analysis of the *bop5-3* flagellar waveform reveals that loss of the IC138 sub-complex reduces shear amplitude, sliding velocities, and the speed of bend propagation. The results indicate that the IC138 sub-complex is necessary to generate an efficient waveform for optimal forwards and backwards motility, but it is not essential for phototaxis. Assembly and maintenance of eukaryotic cilia and flagella requires the conserved, bidirectional movement of protein complexes along the length of the axoneme known as intraflagellar transport (IFT). We characterize the function of various components of the IFT complex responsible for the retrograde transport of particles towards the cell body. We quantify the defects in retrograde IFT and flagella assembly observed in a series of mutants of the retrograde complex subunit *LIC*. We also analyze the expression and distribution of retrograde IFT components in a family of flagellar assembly mutants known as *fla*, and attempt to correlate these patterns with defects in IFT parameters and other behavioral phenotypes. We provide new evidence that defects in IFT motors can alter photoshock and phototaxis behaviors.

Table of Contents

List of Tables

Chapter 2:

Chapter 3:

Chapter 4:

List of Figures

Chapter 1:

Chapter 2:

Chapter 3:

Chapter 4:

Appendix 1:

CHAPTER 1

Introduction

1.1 Cilia and Flagella in Human Physiology and Development

Cilia and flagella are microtubule-based structures that are conserved throughout eukaryotes, are found on most cells in the human body, and have emerged as important organelles in physiology and development. Typically, we think of cilia as motile structures; indeed, many of their functions involve their motility. Motile cilia are important for the directed transport of particles, cells, fluids, and/or signaling molecules in the respiratory tract, reproductive system and the embryonic node (reviewed in Fliegauf *et al.,* 2007). These include the cilia lining the airways and female reproductive tract, as well as the flagella that drive sperm cell motility (Fliegauf *et al.,* 2007). Primary cilia do not have specific roles in motility, but instead act as sensory organelles and transduce signals from the extracellular environment to the cell body and control gene expression, cell function, and behavior (reviewed in Pazour & Witman, 2003). Many human cells have this type of cilia, but notably, the cilia on kidney cells sense fluid flow, the photoreceptor connecting cilia link the two parts of the photoreceptor cell, and cilia in the olfactory neurons detect odorant molecules (Fliegauf *et al.,* 2007). In addition, cilia play a key part in both Hedgehog and Wnt signaling during development (reviewed in Berbari *et al.,* 2009).

Because of the variety of functions that cilia and flagella have, mutations in genes required for the assembly, motility, and function of cilia or flagella result in a wide variety of defects. Defects in ciliary motility can lead to chronic respiratory disease, infertility and disruptions to the movement of nodal fluid in the embryonic node (reviewed in Ishikawa and Marshall, 2011, Berbari *et al.,* 2009, Fliegauf *et al.,* 2007). Because the asymmetric movement of fluid in the embryonic node by nodal cilia ultimately establishes the left/right body axis and the looping of the heart, defects in the

assembly and/or motility of nodal cilia cause severe defects in cardiovascular development and a 50% occurrence of *situs inversus*, a condition in which the visceral organs are placed on the opposite side of the body (Nonaka *et al.,* 1998; Supp *et al.,* 2000). Common symptoms resulting from primary cilia signaling or assembly defects include kidney and liver cysts, retinal dystrophy and degeneration, anosmia (lack of smell), obesity and polydactyly (from improper Hedgehog signaling) (reviewed in Badano *et al.,* 2006).

Diseases caused by ciliary defects are characterized by several of the above symptoms and are known as ciliopathies. For instance, Bardet-Biedl syndrome (BBS) is a complex ciliopathy characterized by obesity, diabetes, hypertension, *situs inversus* and other cardiac malformations, mental retardation, and retinal dystrophy (Deffert *et al.,* 2007). These pleiotrophic defects are caused by mutations in at least twelve different proteins of the BBS complex that have all been localized to cilia and/or centrosome/basal bodies (Li *et al.,* 2004; Badano *et al.,* 2006). This complex is thought to be involved in trafficking of cilia-specific membrane proteins (Nachury *et al.,* 2007; Loktev *et al.,* 2008; Berbari *et al.,* 2008; Lechtreck *et al.,* 2009; reviewed in Ishikawa *et al.,* 2011). The BBS phenotypes exemplify the global role that cilia play in human health.

1.2 Architecture of Cilia and Flagella

Cilia and flagella are composed of a microtubule-based core, called the axoneme, surrounded by a specialized ciliary membrane (Figure 1.1). The axoneme has a highly ordered structure, with most eukaryotic flagella consisting of nine microtubule doublet pairs called outer doublets extending from the cell body. This doublet structure is distinctive, as each doublet has one complete A tubule connected to a second, incomplete B tubule (Figure 1.1). The outer doublets may or may not surround a central pair of microtubules (9+2 or 9+0 arrangements, respectively). Most 9+2 flagella have outer doublets connected by dynein arms and are motile, while most 9+0 flagella lack dynein arms and are immotile and known as primary cilia (Figure 1.1). Motility is achieved when the dynein arms translocate along the adjacent microtubule generating a sliding force that bends the axoneme. Radial spokes extend from the central pair towards the outer doublets and are involved in regulation of the dyneins to coordinate the flagellar beat. Two types of dyneins are attached to the outer doublets: outer arm dyneins, which are located further from the central pair and generate the force for axonemal bending and control beat frequency while inner arm dyneins, located closer to the central pair, play a role in modulating the flagella beat to produce the variety of beat patterns (reviewed in Harris, 1989; Porter and Sale, 2000; Wirschell *et al.,* 2007; Chapter 3).

The microtubules in the axoneme extend from the basal body, which is derived from the centriole (Figure 1.1). The basal body contains nine sets of triplet microtubules that act as a microtubule organizing center and make up the base of the nine doublet microtubules in the axoneme. It is anchored to the plasma membrane with a series of fibers that create a "transition zone" between the cytoplasm and the ciliary compartment. This transition zone is also thought to play a role in regulating the proteins that enter or exit the flagella (Figure 1.1; reviewed in Beisson and Wright, 2003; Chapter 2).

Formation and maintenance of flagella is facilitated by intraflagellar transport (IFT), a microtubule motor-based transport system (Kozminksi *et al.,* 1993). IFT related proteins are organized into several complexes. Because axonemal microtubules are always oriented with their plus-ends at the tip of the flagella, a plus-end directed kinesin

complex is necessary for anterograde transport (away from the cell body), while a minus-end directed dynein complex provides retrograde transport (towards the cell body). Anterograde transport is facilitated by heterotrimeric kinesin-2 and associated proteins (Figure 1.1; Kozminski *et al.,* 1995) while retrograde transport is accomplished by cytoplasmic dynein 1B and associated proteins (Figure 1.1; Pazour *et al.,* 1998; Signor *et al.,* 1999; Porter *et al.,* 1999; Table 4.2). There are also two IFT sub-complexes that hold the IFT particles together and assist with binding to cargoes: complex A with about 6 polypeptides and complex B with about 17 polypeptides (Figure 1.1; Cole *et al.,* 1998; Piperno *et al.,* 1998; reviewed in Ishikawa and Marshall, 2011; Table 4.2). The IFT machinery not only transports axonemal components needed for building and maintaining a flagella, but it also moves cilia-specific membrane proteins and signaling molecules (Qin *et al.,* 2005; Wang *et al.,* 2006; Chapter 4).

Along with the structural proteins of the axoneme and basal body, the IFT machinery proteins are highly conserved across ciliated species (Li *et al.,* 2004; reviewed in Ishikawa and Marshall, 2011; Table 4.2). The high degree of similarity makes it relatively straightforward to study cilia and flagella in model organisms and then apply the knowledge more directly to humans. Hence, much of our knowledge about cilia and flagella has been learned from studying ciliated model organisms such as the nemotode, *C. elegans,* and the alga, *Chlamydomonas* (reviewed in Silflow and Lefebvre, 2001).

1.3. Chlamydomonas as a model organism to study flagella

Chlamydomonas reinhardtii is a haploid cell that swims in liquid media using its two flagella. These two flagella are located at the anterior end of the cell, are 10-15 μm in length and are important for responding to environmental stimuli and mating. As both a motile and a photosynthetic organism, *Chlamydomonas* cells react to light levels in their environment. They detect light using specialized rhodopsin-like photoreceptors located at the eyespot near the anterior of the cell (reviewed in Witman, 1993). Normally, cells swim towards optimal light conditions for photosynthesis in a process called phototaxis. During this type of swimming, cells move forwards using a ciliary-type waveform that looks something like a human breaststroke. If the light intensity suddenly becomes too bright, the cells will pause, briefly swim backwards with a flagellar-type waveform, before recovering and moving towards better light conditions. These behaviors are easily observed using both macroscopic and microscopic assays (Harris, 1989; Silflow and Lefebvre, 2001; Chapter 3, 4).

Chlamydomonas is ideal for studying flagellar components because of its amenability to combined genetic, molecular and biochemical analyses. Following mutagenesis, mutations in flagellar genes are detected by screening for cells that cannot swim normally, lack flagella, or behave inappropriately to varying light conditions (Harris, 1989). Such screens have been used to identify over 90 loci that affect flagellar assembly or motility (Dutcher, 1995; Mitchell, 2000). Further characterization of mutants is facilitated using genetic and molecular markers such as single-nucleotide polymorphisms (SNP) or restriction fragment length (RLFP) polymorphisms (Ranum *et al.,* 1988; Harris, 1989, 2001; Silflow *et al.,* 1995; Vysotskaia *et al.,* 2001; Kathir *et al.,* 2003; Bowers *et al.,* 2003). to identify over 90 loci that affect the flagella (Dutcher, 1995; Mitchell, 2000).

To generate new motility mutants that are tagged with a molecular marker, several labs that study *Chlamydomonas* have used a general insertional mutagenesis strategy to create new collections of mutant strains (Figure 1.2). For example, a wild-type copy of the nitrate reductase gene (*NIT1)* is transformed into a strain with wild-type

motility and a *nit1* mutation in the genetic background (Kindle *et al.,* 1989, 1990; Tam and Lefebvre, 1993; Myster *et al.,* 1997). The *nit1* mutation prevents cells from growing on media lacking ammonium. The *NIT1* gene integrates randomly into the *Chlamydomonas* genome, and the insertion event frequently disrupts the expression of other genes by DNA rearrangements and deletions at the site of insertion (Kindle *et al.,* 1989, 1990; Tam and Lefebvre, 1993; Myster *et al.,* 1997). Colonies that grow on media containing only nitrate can then be screened for aberrant motility phenotypes and kept for future analysis (Tam and Lefebvre, 1993).

Colonies with motility phenotypes can be screened for *NIT1* insertion events into previously cloned genes by probing Southern blots of wild-type and mutant DNA with gene specific probes and checking for the presence of RFLPs (Myster *et al.,* 1997). The Porter laboratory has used this strategy to isolate and identify new alleles of several dynein genes (Figure 1.2). Specifically, we isolated a new allele of *PF9/DHC1,* the gene encoding the I1 dynein alpha heavy chain (Myster *et al.,* 1997, 1999) and a new allele of *IDA2/DHC10,* the gene encoding the I1 dynein beta heavy chain (Perrone *et al.,* 2000). The Porter laboratory has also used this approach to identify mutations in *IDA7/IC140,* which encodes the I1 dynein intermediate chain IC140 (Perrone *et al.,* 1998), and *STF1/cDHC1b,* which encodes the heavy chain of the IFT dynein (Porter *et al.,* 1999). Insertional mutant libraries have also been used to identify new genes affecting motility by using the *NIT1* plasmid to identify genomic DNA in the region flanking the plasmid insertion site (Figure 1.2) (Tam and Lefebvre, 1993; Rupp and Porter, 2003).

Molecular analysis in *Chlamydomonas* is facilitated by the relatively small genome size (~120 Mb) and the availability of the genome sequence (Merchant *et al.,* 2007; http://genome.jgi-psf.org/chlamy/chlamy.home.html). In addition to the genomic sequence, we have the ability to experimentally stimulate the expression of genes coding for flagellar components by severing the flagella and isolating RNA samples over the time course (~90 min) of flagellar regeneration (Lefebvre and Rosenbaum, 1986; Stolc *et al.,* 2005). Comparative genomics between the *Arabidopsis,* human and *Chlamydomonas* genomes has defined a flagellar and basal body proteome (FABB) useful for identifying genes needed exclusively for basal body and flagellar function (Li *et al.,* 2004).

Proteomic analysis using mass spectroscopy of isolated flagella has identified a subset of ~680 flagellar associated proteins or FAPs that constitute a flagellar proteome (Pazour *et al.,* 2005).

In addition to the molecular tools described above, nuclear transformation of *Chlamydomonas* has made it possible to rescue mutations by transformation with wild-type genes (Kindle *et al.,* 1989, 1990; Diener *et al.,* 1990) or to disrupt specific gene function by RNA interference with constructs encoding double stranded RNAs (Li *et al.,* 2004; Iomini *et al.,* 2006; Wang *et al.,* 2006). Both Rohr *et al.* (2004) and Molnar *et al.* (2009) have developed RNAi protocols using tandem repeats and artificial microRNAs for straightforward design of RNAi constructs and efficient silencing of genes. Another molecular tool for analysis of genes in *Chlamydomonas* is a large insert BAC library that allows for positional cloning (Dutcher *et al.,* 2002; Nguyen *et al.,* 2004).

Chlamydomonas cells are also highly amenable to biochemical and structural analyses. First, cells are easily grown in large quantities for biochemical analysis and isolated flagella can be purified by differential centrifugation (Lefebvre and Rosenbaum, 1986). Also, the highly ordered and repetitive structure of the axoneme make detailed structural analysis possible using electron microscopy and image averaging of isolated axonemes (Porter *et al.,* 1992; O'Toole *et al*., 1995; Nicastro *et al.,* 2006).

Chlamydomonas is a valuable experimental model for elucidating basic cellular processes that underlie human disease. For example, the process of intraflagellar transport (IFT) was first described in this organism and the majority of the proteins involved in the process were first identified and characterized in *Chlamydomonas* (Kozminski *et al.,* 1993; Kozminski *et al.,* 1995; Porter *et al.,* 1999; Pazour *et al.,* 1999; Cole *et al.,* 1998). Also, *Chlamydomonas* has been used to identify and characterize BBS4 and BBS5, two of the proteins associated with BBS in humans (Lechtreck *et al.,* 2009; Li *et al.,* 2004). Several other studies in *Chlamydomonas* have identified or characterized proteins implicated in ciliopathies, including PKD2 and IFT88 for polycystic kidney disease (Pazour *et al.,* 2000; Huang *et al.,* 2007;). In addition to genes implicated directly in ciliopathies, genes with high conservation between humans and *Chlamydomonas,* such as *BLD1,* have been shown to be necessary for flagellar assembly

in *Chlamydomonas* and hence, are also likely to have a role in assembly of human cilia (Brazelton *et al.,* 2001).

1.4. Understanding the I1 inner arm and the retrograde IFT dynein complexes

The inner dynein arms consist of more than seven different subspecies that are localized to specific regions within each 96 nm repeat (Mastronarde *et al*., 1992; Porter *et al*., 1996; Porter and Sale, 2000; Nicastro *et al*., 2006; Wirschell *et al*., 2007; Bui *et al*., 2008; Brokaw and Kamiya, 1987; Brokaw, 1994; Kamiya,. 2002; Yagi *et al*. 2009) Each inner arm dynein likely plays a unique role in the formation of the flagellar bend (Kamiya, 2002; Brokaw, 1994; 2009), but the specific function of each isoform is still unclear.

One inner arm dynein subspecies, known as I1, is the most highly conserved and widely distributed inner arm dynein (reviewed in Porter and Sale, 2000; Kamiya, 2002; Wirschell *et al*., 2007; Wickstead and Gull, 2007). The I1 complex is the only two-headed inner arm dynein, and contains two motor domains from the two dynein heavy chains (DHCs), 1α and 1β, and a base that consists of the DHC tail domains, intermediate chains (IC97, IC138, and IC140), light chains (LC7a, LC7b, LC8, TcTex1, and Tctex2b) and FAP120. (Figure 3.1; Goodenough and Heuser, 1985a,b; Piperno *et al*., 1990; Smith and Sale, 1991, 1992; Porter *et al*., 1992; Myster *et al*., 1997, 1999; Harrison *et al*., 1998; Perrone *et al*., 1998, 2000; Yang and Sale, 1998; DiBella *et al*., 2004a,b; Hendrickson *et al*., 2004; Wirschell *et al*., 2009, Bower *et al.,* 2009; Ikeda *et al.,* 2009). A collection of mutations in the genes encoding different I1 subunits has been useful in determining the locations of, interactions between, and functions of different subunits of the complex (Chapter 2, Chapter 3).

Diverse evidence indicates the IC138 subunit of the I1 dynein is a regulatory phosphoprotein important for control of motility (reviewed in Porter and Sale, 2000; Smith and Yang, 2004; Wirschell et al., 2007). This evidence is based on biochemical and genetic analysis revealing that IC138 is the key phosphorylated protein in I1 and that the kinases and phosphatases that control I1 are physically located in the axoneme near the I1 complex (Habermacher and Sale, 1997; King and Dutcher, 1997; Yang and Sale, 2000; Hendrickson *et al.,* 2004; Bower *et al.,* 2009). Thus, we predicted that assembly of IC138 and closely associated proteins are required for regulation of microtubule sliding.

Based on earlier studies of I1 dynein mutants, we also postulated that assembly of IC138 would be required to control swimming speed, flagellar waveform, and phototaxis (Myster *et al*., 1997, 1999; Perrone *et al*., 1998, 2000; Hendrickson *et al*., 2004; Wirschell *et al*., 2009). Here, we examine a series of IC138 mutant strains, *bop5-1* through *bop5-6,* to investigate the role of IC138 in I1 assembly, microtubule sliding, flagellar waveform, and cell behavior (Chapter 2, 3). We also use this mutant family to better understand the location of the I1 inner arm dynein within the axonemal structure (Chapter 2).

Assembly and maintenance of eukaryotic cilia and flagella requires the conserved, bidirectional movement of protein complexes along the length of the axoneme known as intraflagellar transport (IFT) (Rosenbaum and Witman, 2002; Scholey, 2003). In addition to transporting proteins important for assembly and maintenance of flagella, IFT transports specific receptors and signaling proteins into and out of the cilium (Christensen et al., 2007; Pan et al., 2005). The motor that facilitates retrograde IFT is cytoplasmic dynein 1b (Pazour et al., 1999; Porter et al., 1999; Signor et al., 1999), and like other dyneins, it is a minus-end directed microtubule motor composed of several proteins, four of which have been identified: heavy chain DHC1b, light chain LC8, light intermediate chain LIC and intermediate chain FAP133 (reviewed in King, 2002; Ishikawa and Marshall, 2011; Porter *et al.,* 1999; Pazour *et al.,* 1999; Pazour *et al.,* 1998; Perrone *et al.,* 2003; Rompolas *et al.,* 2007; Table 4.2).

In *Chlamydomonas,* null mutations in the genes encoding the DHC1b protein (*stf1-1, stf1-2)* and the LC8 (*fla14*) protein result in stumpy flagella that accumulate IFT particles (Pazour et al., 1998; Pazour *et al.,* 1999; Porter *et al.,* 1999). Also, the *Chlamydomonas* LIC subunit interacts directly with DHC1b, while FAP133 associates with DHC1b, LIC, and LC8 (Perrone *et al.,* 2003; Rompolas, *et al.,* 2007; Table 4.2; Figure 4.2). Despite these advances in understanding the retrograde IFT complex, questions remain on how specific retrograde IFT subunits influence flagellar assembly and normal IFT motility. Also, since IFT transports signaling proteins into and out of the flagellum, we postulate that defects in retrograde IFT or other IFT complexes may disrupt cell behaviors dependent on flagellar signaling such as phototaxis and photoshock.

In this study, we further characterize the function of various components of the retrograde IFT complex. We quantify the defects in retrograde IFT and flagella assembly observed in a series of *LIC* mutants. We also analyze the expression and distribution of retrograde IFT components in a family of flagellar assembly mutants known as *fla*, and attempt to correlate these patterns with defects in IFT parameters and other behavioral phenotypes. We provide new evidence that defects in IFT motors can alter photoshock and phototaxis behaviors (Chapter 4).

1.6. TABLES AND FIGURES

Figure 1.1. Illustration of a typical motile flagellum (Adapted from Hu *et al.,* 2011).

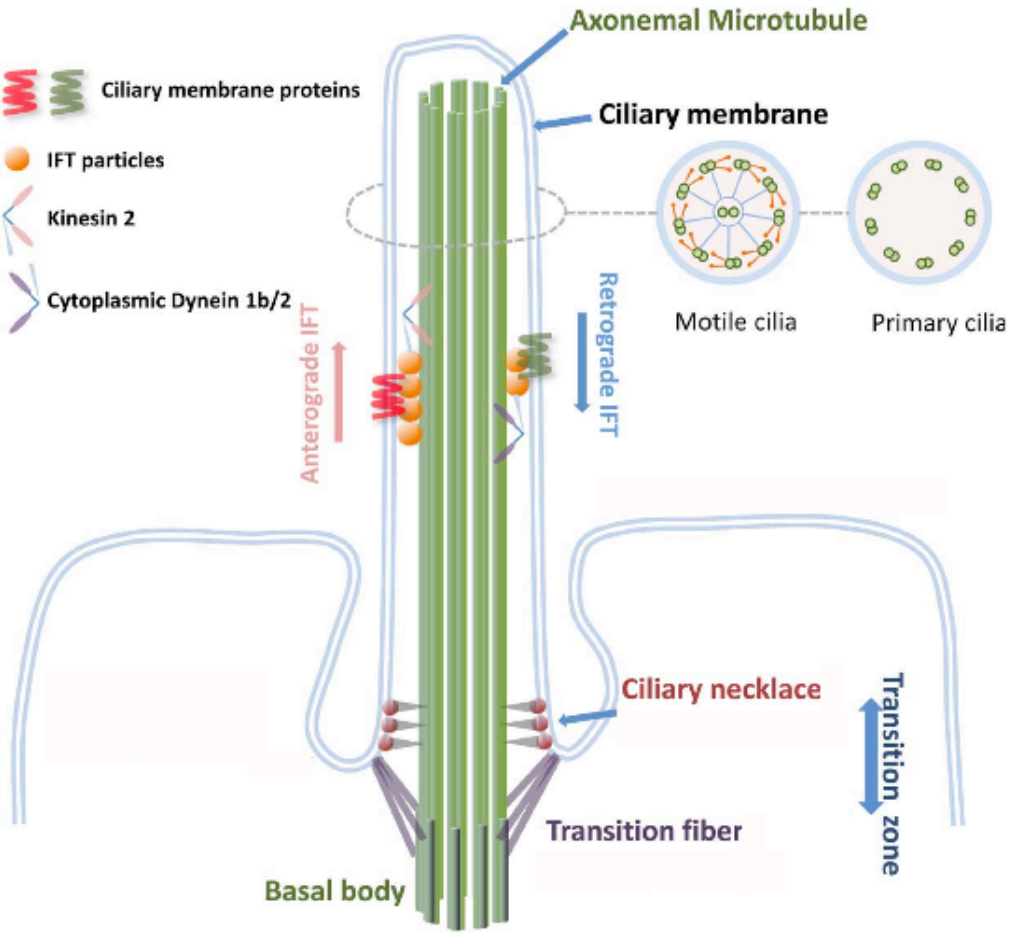

Figure 1.2. General *NIT1* insertional mutatgenesis strategy (Adapted from Tam and Lefebvre, 1993).

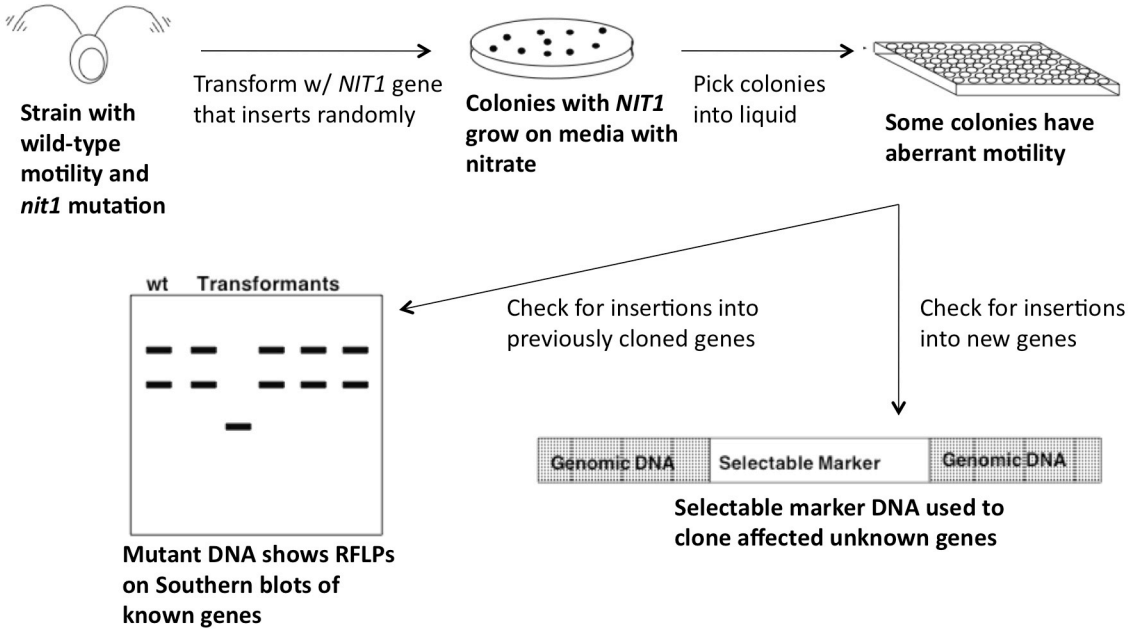

CHAPTER 2

Characterization of IC138 and TBY1 using the *bop5-2* mutant

Modified from
Bower, R., VanderWaal, K.E., O'Toole, E., Fox, L., Perrone, C.A., Mueller, J., Wirschell, M., Kamiya, R., Sale, W.S., and Porter, M.E. (2009). IC138 defines a subdomain at the base of the I1 dynein that regulates microtubule sliding and flagellar motility. *Molecular Biology of the Cell, 20,* 3055-3063.*

*Significant modifications including more introductory material, additional data on *bop5-2* isolation, complete data on TBY1 experiments, and complete data on experiments pertaining to MBO2.

Abbreviations:

IC = Intermediate Chain
LC = Light Chain
BOP = Bypass Of Paralysis
IDA = Inner Dynein Arm
FAP = Flagellar Associated Protein
BOP5 locus = *DIC4* locus = *IC138* gene (Hom *et al.,* submitted)

2.1. INTRODUCTION

The dynein motors form the inner and outer rows of arm structures attached to the doublet microtubules of cilia and flagella (Porter and Sale, 2000; Smith and Yang, 2004). Several lines of evidence have indicated that the outer and inner arm dyneins are functionally distinct, differing in their subunit composition and organizational arrangement in the axoneme. In *Chlamydomonas reinhardtii*, a model genetic organism

for cilia/flagellar studies, the inner dynein arms are composed of at least seven different dynein subspecies precisely organized in a 96-nm repeat pattern along with the outer dynein arms, radial spokes and dynein regulatory complex (DRC) (Goodenough and Heuser, 1985; Mastronarde *et al.,* 1992; Porter *et al.*, 1996; Porter and Sale, 2000; Nicastro *et al.,* 2006; Bui *et al*., 2008; Wirschell *et al*., 2007). Genetic and phenotypic analyses have shown that the inner arm dyneins are responsible for control of the size and shape of the axonemal bend (Brokaw, 1994, 2008; Brokaw and Kamiya, 1987; Kamiya, 2002). However, we do not know how each dynein isoform is localized to its unique position in the 96-nm repeat structure or how the activity of each isoform is regulated.

To address general questions of assembly and regulation of dynein, we have taken advantage of motility mutants in *Chlamydomonas* and focused on the structural and functional properties of the I1 inner arm dynein, also known as dynein *f* (reviewed in Porter and Sale, 2000; Kamiya, 2002; Wirschell *et al.,* 2007). I1 dynein is the only two-headed inner arm dynein and is located near the base of radial spoke 1, where it forms a tri-lobed structure at the proximal end of the axonemal 96-nm repeat (Figure 3.1). I1 is composed of two heavy chains (HC), 1α and 1β; three intermediate chains, IC140, IC138, and IC97; and several light chains, including LC7a, LC7b, LC8, Tctex1, and Tctex2b (Goodenough and Heuser, 1985; Piperno *et al*., 1990; Smith and Sale, 1991, 1992b; Porter *et al*., 1992; King and Patel-King, 1995; Harrison *et al*., 1998; Myster *et al*., 1997, 1999; Yang and Sale, 1998; Perrone *et al*., 1998, 2000; DiBella *et al*., 2004a, b; Hendrickson *et al.,* 2004; Wirschell *et al.,* 2009).

Mutations that disrupt specific I1 subunits, or specific domains of those subunits, often result in assembly of incomplete or partial I1 dynein complexes, useful for revealing protein interactions, structural domains, and regulatory functions. For example, the *bop5-1* mutant expresses a truncated IC138 and assembles all of the I1 dynein subunits with the exception of LC7b and FAP120, a recently identified I1-dynein associated protein, revealing an interaction between the C-terminus of IC138, LC7b, and FAP120 (Hendrickson et al., 2004; Ikeda et al., 2009; this study). Likewise, mutant strains expressing truncated dynein HCs that lack the motor domains of either the 1α or 1β HC still assemble the remaining I1 dynein subunits (Myster *et al.* 1999; Perrone *et al.*

2000). EM of isolated axonemes revealed the location of the globular motor domains within the tri-lobed structure of the I1 dynein, and thereby indirectly suggested the location of the IC/LC complex at the base of I1 dynein (Myster *et al.* 1999; Perrone *et al.* 2000). One goal is to test this model for organization of the IC/LC domain in the axoneme.

Diverse evidence indicates that I1 dynein plays a key role in regulation of microtubule sliding by a mechanism involving phosphorylation of IC138 (reviewed in Porter and Sale, 2000; Smith and Yang, 2004; Wirschell et al., 2007). Unlike other axonemal dyneins, the isolated I1 complex does not efficiently translocate microtubules in *in vitro* motility assays, possibly indicating a novel regulatory function (Smith and Sale, 1991; Kotani et al., 2007; Kikushima and Kamiya, 2008). Mutations in I1 assembly or IC138 phosphorylation result in altered axonemal bending and disrupted phototaxis, suggesting an important role in these processes (Brokaw and Kamiya, 1987; King and Dutcher, 1997; Hennessey *et al.* 2002; Okita et al., 2005, Chapter 3). Thus we predict that assembly of IC138 is required for regulation of microtubule sliding.

Here we focus on *bop5-2*, obtained by insertional mutagenesis, that lacks most of the *IC138* gene and deletes another 20 kb of genomic DNA. Most I1 dynein subunits are present in *bop5-2* axonemes, but IC138, IC97, FAP120, and presumably LC7b are missing. We propose that these proteins form a regulatory unit, referred to as the "IC138 sub-complex." Analysis of *bop5-2* axonemes by EM and computer image averaging revealed a defect at the base of the I1 dynein, thus confirming the location of the IC138 sub-complex in the 96-nm axoneme repeat. Microtubule sliding velocities are also reduced in *bop5-2* axonemes. Transformation with the wild-type *IC138* gene restores assembly of the IC138 sub-complex and rescues microtubule sliding.

The *bop5-2* mutation also affects expression of the *Tubby-1* (*TBY1)* gene. Mutations in members of the *Tubby* gene family in other species result in ciliopathic-like phenotypes. Ciliopathies are human genetic disorders involving defects in ciliary motility, assembly and signaling and have symptoms such as cardiac defects, kidney and liver cysts, retinal dystrophy and degeneration, infertility, defects in the development of the nervous system, and obesity (Badano *et al.,* 2006; Fliegauf *et al.,* 2007; Tobin *et al.,*

2009). The *Tubby* gene was originally discovered through the analysis of a mouse mutant strain that exhibited obesity, sterility and retinal degeneration (Ohlemiller *et al.,* 1995; North *et al.,* 1996; reviewed in Carroll *et al.,* 2004). Mutations in other *Tubby* related mouse genes (Tubby-like proteins, or TULPs) were subsequently identified that showed additional phenotypes that are trademarks of ciliopathies such as cochlear degeneration, neurosensory defects, insulin resistance, and embryonic lethality (Carroll *et al.,* 2004; Mukhopadhyay and Jackson, 2011).

The C-terminal portions of tubby proteins are highly conserved across phyla and form the "tubby domain" (Figure 2.6A). *In vitro* experiments suggest that the tubby domain binds $PI(3,4)P_2$, $PI(4,5)P_2$, and $PI(4,5)P_3$ phosphoinisotides and are thought to be anchored to the plasma membrane when bound to these phosphoinisotides (Santagata *et al.,* 2001). The crystal structure of the domain has been determined as a unique beta barrel surrounding a central alpha helix (Santagata *et al.,* 2001). Tubby-domain containing proteins are common, occurring in single celled organisms such as *Chlamydomonas reinhardtii,* higher plants such as rice and *Arabidopsis,* and higher animals such as mice and humans (Figure 2.6A, Table 2.2).

In humans and mice, *Tubby* genes are widely expressed in ciliated tissues including the testes, brain, eyes, and heart (North *et al.,* 1997, Nishina *et al.,* 1998). Specifically, the mouse *tubby* gene is expressed in cochlea, retina and throughout the brain and mutations in the human *tubby* gene are a risk factor for human obesity (Reviewed in Carroll *et al.,* 2004; Mukhopadhyay and Jackson 2011; Shiri-Sverdlow *et al.,* 2006). TULP1 is expressed mainly in the retina and mutations in the *TULP1* gene cause retinitis pigmentosa in humans (Reviewed in Carroll *et al.,* 2004; Mukhopadhyay and Jackson 2011; Hagstrom *et al.,* 1998; Ikeda *et al.,* 1999). This phenotype may be caused in part from lack of rhodopsin transport through the connecting cilia of photoreceptor cells in *TULP1* mutant mice (Hagstrom *et al.,* 2001). Mouse and human *TULP2* transcripts are detected in both the testes and retina but no phenotype has yet been associated with this gene (Reviewed in Carroll *et al.,* 2004; Mukhopadhyay and Jackson 2011; North *et al.,* 1997). *TULP3* is expressed almost ubiquitously during vertebrate development and is also expressed in adult tissues and *TULP3* mutant mice

have failures in neural-tube closure and die early in development (Reviewed in Carroll *et al.,* 2004; Mukhopadhyay and Jackson 2011; Nishina *et al.,* 1998; Ikeda *et al.,* 2001). More recent work indicates that TULP3 associates with intraflagellar transport proteins and regulates flagellar entry of specific ciliary GPCRs in mammalian cell lines (Mukhopadhyay *et al.*, 2010; reviewed in Mukhopadhyay and Jackson 2011). Interestingly, many cilia localized receptors are GPCRs (Stolc *et al.,* 2005).

The *C. elegans tubby* homologue, *TUB-1,* is expressed primarily in ciliated sensory neurons and the *tub-1* mutant has defects in chemosensation and fat storage (Mak *et al.,* 2006). This phenotype is similar to the Bardet-Biedl Syndrome mutant, *bbs1-1,* which also accumulates lipids abnormally (Mak *et al.,* 2006). Limited evidence suggests that tubby proteins may undergo intraflagellar transport in *C. elegans* (Mak *et al.,* 2006). Work in *C. elegans* also links tub-1 function to membrane trafficking through Rab proteins (Mukhopadhyay *et al.,* 2007). *Drosophila tubby* homologues are also expressed in the nervous system, suggesting a possible conserved role for tubby proteins in nervous tissue (Ronshaugen *et al.,* 2002). The evidence from both vertebrates and *C. elegans* suggest that some *Tubby* gene products play a role in ciliary signaling.

Plants such as *Arabidopsis,* maize and rice also contain tubby-like proteins (North *et al.,* 1997; Lai *et al.,* 2004; Yang *et al.,* 2008, Table 2.2). Because higher plants do not have cilia (Li *et al.,* 2004), this suggests that tubby proteins may also play a role in other signaling pathways. All plant tubby proteins are characterized by and additional F-box domain in addition to the tubby domain (Lai *et al.,* 2004; Yang *et al.,* 2008). Plant tubby proteins also tend to have a larger variety of different types of tubby proteins in one organism; for example, there are 11 *tubby-like* genes in *Arabidopsis* and 14 in rice (Yang *et al.,* 2008). The plant tubby proteins are expressed in all plant tissues and are likely involved in abscisic acid sensitivity in *Arabidopsis* and host-pathogen interactions in rice (Lai *et al.,* 2004; Kou *et al.,* 2009).

Chlamydomonas reinhardtii has four proteins that are predicted to contain this conserved C-terminal domain. Two of the four proteins are predicted to be about 80 amino acids long, which is only about a quarter of the length of a full tubby domain (about 250 amino acids). Therefore, these are less likely to have a conserved, tubby-

domain related function and were not analyzed further. The other two proteins, TBY1 and TBY2, have highly conserved tubby domains similar to the ones found in other organisms (Figure 2.6A). Specifically, TBY1 and TBY2 are more closely related to mammalian tubby proteins (TBY1 is most similar to mouse TULP2 by BLAST analysis, Figure 2.6A) rather than plant tubby proteins (rice TLP11 is most similar to TBY1 by BLAST analysis, Figure 2.6A) because *Chlamydomonas* TBY1 and TBY2 proteins lack the F-box domain characteristic of the plant TULPs.

Here, we use the *bop5-2* mutant strain, which is null for *TBY1*, to study the potential functions of *TBY1* in *Chlamydomonas*. We show that *TBY1* mutations do not cause a clear-cut motility defect. We also present evidence suggesting that the *TBY1* protein product is localized to a ring-shaped structure that we hypothesize may be involved in regulating signaling proteins in the basal body region and/or the flagella.

2.2. MATERIALS AND METHODS

Strains, Culture Conditions and Genetic Analyses

Strains used in this study are summarized in Table 2.I. The *bop5-2* strain (6F5, CC4284) was generated by transformation of the A54e18 strain (*nit1, ac17, mt plus*) with the plasmid pMN56 containing the nitrate reductase gene *NIT1* (Myster et al., 1997). Cells were maintained on Tris-acetate phosphate (TAP) medium (Harris, 1989). Unless indicated differently, a pea-sized amount of cells was resuspended in minimal media lacking nitrogen (Harris, 1989) and rocked overnight under constant light to encourage maximum flagellar assembly and motility.

To determine whether the motility phenotype was linked to the *NIT1* plasmid, *bop5-2 (CC4284)* was crossed to L8 (*nit1-305, apm1-19, mt minus*), and the resulting progeny of seven complete tetrads and additional random progeny were analyzed for their motility phenotypes and their ability to grow on selective media lacking ammonium. IC138 rescued strains were generated by transformation of *bop5-2* with a plasmid containing the wild-type *IC138* gene (Hendrickson et al., 2004) and the selectable marker pSI103 containing the *aphVIII* gene (Sizova et al., 2001) and plating cells on TAP medium containing 10ug/ml paromomycin. Because transformation with *IC138* did not clearly rescue the motility defects, whole cell extracts of the transformants were screened on Western blots probed with the IC138 antibody. Dominance tests were performed by mating *bop5-2* (CC4284, which also contains an *ac17* mutation) to *arg7-2*, and selecting for diploid cells on minimal medium. All diploids were mating type minus and displayed wild-type motility.

To test for possible complementation between *mbo3 (CC3670)* and *bop5-2 (CC4416)*, the two strains were mated and the mating mixture was plated on M-NO_3 plates, which lacked acetate and ammonium. *mbo3* strains have a *nit1* mutation and cannot grow without ammonium, and *bop5-2* strains have an *ac17* mutation and cannot grow without acetate (Myster et al., 1997). Both parental strains would die on M-NO_3 plates while a diploid strain would live. Colonies that grew on M-NO_3 plates were confirmed as true diploids by PCR analysis of the mating type locus. Separate reactions

were done for the presence of the mating type plus and the mating type minus genes, as described in Zamora *et al.* (2004). If the strain had bands for both mating types, then it was designated a diploid strain (Table 2.4).

Southern and Northern Blots

Isolation of genomic DNA, restriction enzyme digests, agarose gels, and Southern blots were performed as previously described (Perrone et al., 2000, 2003; Rupp et al., 2001; 2003). Expression of *Tubby* genes was analyzed on Northern blots as described in Perrone *et al.* (1998). Briefly, total RNA (20 μg per lane) was isolated both before and 45 min after deflagellation induced by pH shock (Wilkerson *et al.,* 1994), fractionated on 1.0% agarose-formaldehyde gels, and transferred to an Immobillon-NY+ membrane (Millipore). After drying, RNA was cross-linked using UV light from a Stratalinker II (Stratagene) at 20,000 J. The blots were hybridized with two different RT-PCR products obtained from the 5' (non-conserved) ends of the *TBY1* (primers: 5'-TGACCAATGTCG TTTCCACTGTG-3' and 5'-TGCTTAGACCCACGCCCAAG) and *TBY2* (5'-TCCTAC AGCACCATTAGAGCAAGAC-3' and 5'- GCCCGACATCTCGTCCATCAC-3') genes. They were also hybridized with a control probe for the *CRY1* gene encoding the ribosomal S14 protein (Nelson *et al.,* 1994). Probes were radiolabeled with ^{32}P-dCTP using the Rediprime Labeling Kit (Amersham) to similar specific activities and tested for specificity on Southern blots before use on the Northern blots as described previously (Perrone *et al.,* 1998). Both the *TBY1* and *TBY2* probes hybridized to distinct, single copy genes with the appropriate restriction patterns at the same exposure.

Isolation of Flagella, Axonemes and Whole Cells and Western Blot Analysis

To isolate flagella, cells were subjected to pH shock, and then isolated flagella were separated from the cell bodies as described previously (Witman, 1986). The resulting flagella were resuspended in HMEEN (10 mM HEPES, pH 7.4, 5 mM $MgSO_4$, 1 mM EGTA, 0.1 mM EDTA, 30 mM NaCl) with 0.1 mg / ml protease inhibitors (pepstatin, leupeptin, aprotinin) and 1 mM dithiothreitol (Bower et al., 2009). To isolate axonemes, the flagella were further treated with 0.1% NP-40 to remove the membranes

(Bower *et al.,* 2009). For whole cell blots, cells were grown in minimal media overnight, and then cell densities were determined. Samples were concentrated by centrifugation to 3–5 x 10^6 cells/lane, and then 5X SDS sample buffer was added to a concentration of 1x sample buffer, and the samples were placed in a boiling water bath for 5 minutes. Samples were run on 5-15% polyacrylamide gradient gels, transferred to Immobilon P (Millipore, Billerica, MA), and probed with primary and secondary antibodies as described previously (Bower et al., 2009). Primary antibodies for western blotting were used at several concentrations but in general antibodies were used at the following concentrations: TBY1 column affinity purified antibody at 1:5000, OEE3 antibody at 1:3000 (Mayfield *et al.* 1987), GFP antibody, 1:1000 (Covance), 1α DHC, 1:1000, (Myster et al., 1997); IC140, 1:10,000, (Yang and Sale, 1997); IC138, 1:20,000, (Hendrickson et al., 2004); IC97, 1:10,000 (Wirschell et al., 2009); IC69, 1:10:000 (Sigma Aldrich); FAP120, 1:10,000 (Ikeda et al., 2009), MBO2, 1:10,000 (Tam and Lefebvre, 2002), tctex1, 1:50 (Harrison et al., 1998), tctex2b, 1:50 (Dibella et al., 2004b). Immunoreactive bands were detected using alkaline phosphatase conjugated secondary antibodies and the Tropix chemiluminescent detection system (Bedford, MA).

Electron Microscopy and Analysis

Axonemes were fixed, stained, and embedded for electron microscopy as previously described (Porter *et al*., 1992). Thin-sectioned material was imaged at the Boulder Laboratory for 3D Fine structure and analyzed by computer image averaging as described previously (Mastronarde *et al*., 1992; O'Toole *et al*., 1995).

Analysis of microtubule sliding

Microtubule sliding velocity was measured using the method of Okagaki and Kamiya (1986), and as previously described (Howard et al., 1994; Habermacher and Sale, 1996, 1997; Hendrickson et al., 2004). Briefly, isolated flagella were resuspended in buffer without protease inhibitors, demembranated with buffer containing 0.5% Nonidet-P-40, and added to perfusion chambers. Microtubule sliding was initiated by the addition of buffer containing 1 mM ATP and 3 mg/ml subtilisin A Type VIII protease (Sigma

Aldrich, St. Louis, MO). Sliding was recorded using a Zeiss Axiovert 35 microscope equipped with dark field optics and a silicon intensified camera (VE-1000, Dage-MTI, Michigan City, IN). The video images were converted to a digital format using Labview 7.1 software (National Instruments, Austin, TX). Sliding velocity was determined manually by measuring microtubule displacement on tracings calibrated with a micrometer.

Generation of TBY1-GFP, TBY1-HA, and TBY2-GFP expressing strains

A 6.9 kb EcoRV/Kpn1 restriction fragment from BAC 23k17 containing the *Tubby1* gene was subcloned into pBluescript. The *Tubby1* stop codon was mutated to a BspE1/AccIII site using the QuickChange Mutagenesis Kit (Stratagene) and the primers 5' – ACGTGGCGTGCGAGTCCGGAAGTGGTG ATGCAG – 3' and 5' – GCTGCATCACCACTTCCGGACTCGCACGCCAGCT – 3'. The region containing the stop codon was sequenced to confirm the presence of the new restriction site. CrGFP was amplified by PCR using primers with BspE1/AccIII sites (5' – ATGTC CGGAATGGCCAAG GGCGA – 3' and 5' – CCTCCGGATTACTTGTACACG – 3'), subcloned into pGEM, digested with BspE1/AccIII, and ligated into the mutated Tubby1 subclone. An HA tag with flanking AccIII sites was isolated by PCR and swapped for the GFP tag using the BspE1/AccIII site. The final plasmids were completely sequenced to check for the presence of the mutated stop codon, the two different epitope tags, and the absence of other mutations.

To make a *TBY2-GFP* construct, the *TBY2* gene was obtained by digesting BAC 27L19 with BamH1 and Xho1 and subcloned into pBluescript (Stratagene). A smaller 0.5 kb clone (Rsr1/Sbf1 digest) containing the 3' end of the *TBY2* gene was ligated into pGEM (Promega) for mutagenesis of the stop codon to a BspE1/AccIII site. The primers used for mutagenesis were: 5'- GCTGTGCTACGCGTTGTCCGGACTGGCAGTTTGC AC - 3' and 3'- CGACACGATGCGCAACAGGCCTGACCGTCAAACGTG – 5'. The *GFP* gene was amplified using primers that contain a BspE1/AccIII restriction site, subcloned into pGEM, digested, and then ligated into the BspE1/AccIII site of the *TBY2*

gene. The orientation of the *GFP* tag was checked by sequencing, and then the 3'end containing the *TBY2-GFP* piece was swapped into the original *TBY2* gene in pBS.

Wild-type and mutant strains that express tagged *Tubby* genes were generated by co-transformation with the pSI103 plasmid containing the *aphVIII* gene (Sizova et al., 2001) and the appropriate construct (Hendrickson et al., 2004). Transformants that grew on TAP (Tris Acetate Phosphate) plus 10 mg/ml paromomycin were screened for GFP or HA expression on Western blots and by immunofluorescence.

Preparation of antibodies against the TBY1 protein

To make specific antibodies against the TBY1 protein, a peptide from the non-conserved N-terminal region (RASYDPNEGQEEVPS) was synthesized, coupled to KLH, and injected into rabbits for polyclonal antibody production (Spring Valley Laboratories, Woodbine, MD). To purify the TBY1 peptide antibody, 20 mls of antisera was diluted 1:1 and run over a Sulfo-link column (Pierce) coupled to TBY1 peptide. The column was washed with several volumes of PBS, and then the purified antibody was eluted with 0.2 M glycine HCl, neutralized with 1M Tris, dialyzed, and tested on Western blots of total cell extracts from wild-type, mutant, and rescued strains.

Analysis by Light Microscopy: immunofluorescence, live cell imaging, NFAPs, and motility

For most immunofluorescence experiments, *Chlamydomonas* cells were fixed using the cold methanol procedure of Sanders and Salisbury (1995) and then processed as described in Perrone et al., 2003. Briefly, cells were labeled with primary antibodies including GFP at 1:100 (Covance #MMS118), centrin at 1:1000 (Salisbury *et al.,* 1988), epsilon tubulin at 1:1000 (Dutcher et al., 2002), and DAPI at 0.1 mg/ml (Invitrogen); and Alexafluor-488 labeled, secondary antibodies including goat anti-mouse IgG (1:100) and goat anti-rabbit IgG (1:100) (Molecular Probes, Eugene, OR). Slides were washed in three changes of PBS and then mounted in Prolong antifade medium (Molecular Probes).

Images of fixed and live cells were obtained using 100x objectives on either a Nikon Eclipse E800 photomicroscope (Melville, NY, Figure 2.9A, 2.11A, 2.11D) or a Carl Zeiss Axioscope, (Thornwood, NY, Figure 2.9B, 2.9C, 2.10, 2.11B, 2.11C, 2.11E) equipped with DIC and fluorescence optics and a UV light source for epi-illumination. Digital images were collected using either a Roper CoolSnap HQ camera (Tuscon, AZ, Figure 2.9A, 2.11A, 2.11D), an Axiovision camera (Carl Zeiss, Thornwood, NY, Figure 2.11B, 2.11C), or a Rolera MGi camera (QImaging, Surrey, BC, Figure 2.9B, 2.9C, 2.10, 2.11E). Image processing was done with a combination of ImagePro Plus (Media Cybernetics, Bethesda, MD), Metamorph version 7.6.5.0 (Molecular Devices, Sunnyvale, CA), and/or ImageJ (NIH, Bethesda, MD).

For figure 2.11D, cells were fixed in 4% paraformaldehyde/10 mM HEPES for 30 min. on ice before permeabilization with cold methanol. These images were batch deconvolved using a Huygens Maximum Likelihood estimation algorithm before maximum intensity projections were made as described by Piasecki *et al.,* 2008.

Nucleo-flagellar apparatuses (NFAPs) were obtained by treating ~0.5ml of cells grown in TAP with 2ml autolysin and rocking in light for 30 min to digest the cell walls. The cells were then washed once, resuspended in microtubule stabilizing buffer (MTSB: 50 mM HEPES, 3 mM EGTA, 3 mM $MgSO_4$, 250 mM NaCl), and allowed to adhere to 0.1% polyethylenimine coated slides. The cells were then washed 1x with MTSB, lysed for 2 min with 1% NP-40 in MTSB, and mounted in 0.75% low melting point agarose for viewing the GFP signal that remains associated with the unfixed, unstained NFAPs..

The motility phenotypes of freely swimming cells were monitored using an Axioscope (Carl Zeiss, Thornwood, NY) equipped with phase contrast optics and a halogen light source. For quantitative data, individual cells from cultures made on several different dates were scored as swimming forwards, backwards, spinning or not moving. Spinning or not moving cells were not included in the final numbers shown in figure 2.8B. To illustrate cell motility, selected fields of cells were recorded using 0.5-1.0 second exposures on a Rolera-MGi EM-CCD camera (Q-Imaging, Tucson, AZ).

2.3. RESULTS

Identification of a null mutation in IC138 and TBY1

To identify new alleles at the *IC138/BOP5* (now called *DIC4,* Hom *et al.,* submitted*)* locus, we screened a collection of motility mutants generated by insertional mutagenesis with the nitrate reductase gene, *NIT1*. This collection has been previously used to identify mutations in other I1 dynein subunits, central pair proteins, and the DRC (Myster et al., 1997, Perrone et al., 1998, 2000; Rupp et al., 2001; Rupp and Porter, 2003). Southern blots of genomic DNA isolated from more than fifty mutant strains were hybridized with a 9 kb fragment containing the complete *IC138* gene. One strain, 6F5, was associated with a significant rearrangement of the *IC138* gene (Figure 2.1A, Bower *et al.,* 2009). PCR of wild-type and 6F5 DNA indicated that ~20 kb of genomic DNA had been deleted, including more than 90% of the *IC138* transcription unit and part of the *TBY1* transcription unit (Figure 2.1B). To confirm that the mutant motility phenotype is linked to the insertion of the *NIT1* plasmid and associated deletion, we backcrossed the 6F5 strain, now known as *bop5-2*, to a *nit1* strain with wild-type motility (L8). Analysis of tetrad progeny showed that the motility defects co-segregated with the ability to grow on ammonium free medium and the absence of IC138 (see Material and Methods).

Loss of IC138 disrupts the assembly of I1 dynein subunits

Null mutations in other I1 dynein subunits, such as the two dynein HCs and IC140, typically result in the failure to assemble the I1 dynein complex into the flagellar axoneme (Myster, et al., 1997, 1999; Perrone et al., 1998, 2000). To determine whether the loss of IC138 has a similar phenotype, we analyzed axonemes from wild-type and mutant strains on Western blots probed with antibodies to dynein subunits (Figure 2.2). Consistent with previous reports, the 1α HC, IC140, and IC138 are missing or reduced in the *IC140* mutant, *ida7-1*, and IC138 is truncated in *bop5-1* (Perrone et al., 1998; Hendrickson et al., 2004). However, although *bop5-2* axonemes lack IC138, both the 1α HC and IC140 are present at wild-type levels (Figure 2.2A, Bower *et al.,* 2009). Recent studies have identified two other I1 dynein associated proteins, IC97 (Wirschell et

al. 2009) and the axoneme polypeptide, FAP120 (Ikeda et al., 2009). Western blots probed with antibodies to IC97 and FAP120 revealed that these two proteins are missing in *bop5-2* axonemes (Figure 2.2B, Bower *et al.,* 2009). Because LC7b is a subunit of both I1 and outer arm dyneins (Dibella et al., 2004a), we did not analyze its assembly in *bop5-2*. However, previous studies of *bop5-1* have shown that the I1 dynein lacks LC7b when IC138 is truncated (Hendrickson et al., 2004). Thus it is likely that I1 dynein lacks LC7b when IC138 is missing.

We previously transformed the *bop5-1* mutation with a wild-type copy of the *IC138* gene and observed rescue of the slow swimming motility phenotype and re-assembly of the full-length IC138 polypeptide (Hendrickson et al., 2004). However, in initial efforts to rescue the *bop5-2* motility defect with *IC138*, we failed to recover transformants with wild-type motility. These observations suggested that there must be a another mutation in *bop5-2* that affects motility even though IC138 has reassembled into the axoneme (see below). We therefore analyzed whole cell extracts from 74 transformants on Western blots probed with an antibody specific for IC138 and identified three strains that expressed wild-type levels of the IC138 polypeptide in their cytoplasm. As the motility phenotypes of all three strains were very similar, the 2BA transformant was chosen for further study. Western blot analysis confirmed that re-expression of IC138 was accompanied by the reassembly of IC138, IC97 and FAP120 into the axoneme (Figure 2.2B, Bower *et al.,* 2009).

Localization of the IC138 sub-complex within the structure of the I1 dynein

Previous work has shown that the I1 dynein forms a tri-lobed structure located at the proximal end of the 96-nm axoneme repeat (Goodenough and Heuser, 1985; Piperno et al., 1991; Mastronarde et al., 1992; Nicastro et al., 2006). We also analyzed several strains in which constructs encoding the amino-terminal portions of the two I1 HCs were used to restore the assembly of I1 dyneins lacking one or the other I1 motor domain (Myster et al., 1999; Perrone et al., 2000). Analysis of isolated axonemes by thin section EM and image averaging identified the position of the two motor domains within the structure of the I1 dynein. These studies suggested that the multiple ICs and LCs are

located within the third lobe of the I1 dynein, at a strategic position between the radial spoke 1 and the outer dynein arms (See Chapter 3).

To directly determine the location of the I1 dynein IC/LC complex, we prepared isolated axonemes from wild-type, *bop5-2*, and *IC138* rescued strains for thin section EM. Longitudinal sections of axonemes with clear views of the 96 nm repeat were processed by computer image averaging (O'Toole et al., 1995). Comparison of all three strains indicated that some of the densities associated with the I1 dynein are reduced in *bop5-2* axonemes and restored in axonemes from the *IC138* rescued strain (*bop5-2::IC138*) (Figure 2.3). Difference plots demonstrated that the defect in the assembly of the IC138 sub-complex is associated with a statistically significant decrease in the density of the third lobe of I1 dynein. This third lobe corresponds to the base of the I1 dynein, which is also responsible for interaction of I1 with the A-tubule of the underlying outer doublet.

The IC138 sub-complex alters dynein-driven microtubule sliding

To test the hypothesis that the IC138 sub-complex plays a regulatory role in control of microtubule sliding, we used a microtubule sliding disintegration assay to measure sliding velocities in isolated axonemes (Okagaki and Kamiya, 1986). This assay has proven to be a reliable method to assess dynein activity, or regulation of dynein activity, in axonemes that are paralyzed or otherwise impaired for motility (Witman et al., 1978; Smith and Sale, 2001; Smith, 2002). Our prediction was that IC138 plays a fundamental role in I1 dynein function, that its assembly is required for normal microtubule sliding, and that sliding velocities would be reduced in *bop5-2* axonemes, similar to the reduced sliding velocities characteristic of I1 dynein mutants (Smith and Sale, 1991; Habermacher and Sale, 1997).

As previously described, in 1 mM MgATP, microtubule sliding is very rapid in isolated wild type axonemes (Figure 2.4) (Howard et al., 1994; Habermacher and Sale, 1997; Smith, 2002). As predicted, microtubules slide at greatly reduced velocities in *bop5-2* axonemes. Moreover, microtubule sliding is increased when *bop5-2* cells are transformed with *IC138,* but not after transformation with *TBY1-HA* (Figure 2.4).

Wild-type flagellar motility is not restored in the IC138 rescued strain

Although transformation with *IC138* restores assembly of I1 dynein, we did not observe complete rescue of the motility defects. Both the original *bop5-2* mutant and IC138 rescued cells swim poorly, with a high percentage of cells that move backwards or spin in place (Figure 2.12A). The lack of rescue suggested that another gene affecting flagellar motility is also defective in *bop5-2*, so we looked more closely at the genes in the deleted region of *bop5-2*. Other than *bop5,* there are 6 other putative transcripts affected by the *bop5-2* deletion (Figure 2.5). Three transcripts, 520850, 520800 and 520650, also have apparent homologues in *Volvox carteri* (Figure 2.5A). 520850 matches SOH1, a mediator of RNA polymerase II transcription (Figure 2.5B). 520800 matches a small portion of a possible secreted protein (Figure 2.5B). Finally, 520650, or TBY1, shows homology to Tubby domain containing proteins in many organisms. The other three transcripts (520900, 520750, and 520700) do not have a clear homologue in *Volvox*, nor do they have close matches by BLASTp to proteins in other organisms, and so these are less likely to have a conserved function (Figure 2.5B). We also looked at BLASTp scores to the closest related protein that was not algal (non-*Volvox* or *Chlamydomonas*). The *Chlamydomonas* TBY1 sequence has the highest BLASTp score to its most closely related non-algal protein, at 784; the next closest BLASTp score is 299, for SOH1 (Figure 2.5B). The TBY1 sequence also has high homology with *V. carteri* as the homology plot shows many peaks over the TBY1 transcript (Figure 2.5A). Even though only about half of the *TBY1's* transcription unit is deleted in *bop5-2,* the entire C-terminal tubby domain is affected (Figure 2.6A), making this gene a good candidate for a second gene that might influence flagellar motility in the *bop5-2* strain.

To investigate the possible roles that the *Chlamydomonas* TBY proteins might have in flagella function, we isolated RNA from wild-type cells from before and 45 minutes after pH shock induced deflagellation (Wilkerson *et al.,* 1994). Deflagellation induces the expression of >300 genes encoding proteins that the cells use to regenerate two new flagella (Lefebvre and Rosenbaum, 1986; Keller, 1995; Stolc *et al.,* 2005). Transcription of the flagellar genes is rapidly upregulated, and many flagellar mRNA

transcripts involved in motility accumulate between 15-60 minutes before gradually decreasing to pre-deflagellation levels (Lefebvre and Rosenbaum, 1986; Keller, 1995; Stolc *et al.,* 2005). We found that the *TBY2* transcripts are more abundant after deflagellation, but we could not detect any change in the *TBY1* transcripts before and after deflagellation by Northern blot analysis of total RNA (Figure 2.6B).

bop5-2 is null for TBY1

To better understand the possible role a *TBY1* mutation may have on flagella function, we generated anti-peptide antibody and fusion protein constructs to assess expression of the protein in wild-type and mutant cells. The peptide antibody was specific for the TBY1 protein, which migrates at <50 kD on SDS-PAGE gels of whole cell extracts. The endogenous TBY1 band is seen in the lanes containing the wild-type (CC-1691), *cc1691::TBY1-HA (B12)* and *cc1691::TBY1-GFP (3D4)* cell extracts (Figure 2.7). We also probed cell extracts from the *bop5-2* strain but we did not detect any cross-reactive TBY1 band, suggesting that *bop5-2* is null for TBY1 expression (Figure 2.7). Expression of TBY1 protein in *bop5-2* can be restored by transformation with either the HA-tagged or GFP-tagged *TBY1* constructs (Figure 2.7). The TBY1-GFP band is shifted and migrates at <75 kD; it is slightly less abundant than the endogenous TBY1 in wild-type (Figure 2.7). The TBY-GFP fusion protein is seen in both *bop5-2::TBY1-GFP (3F12)* rescued cells and *cc1691::TBY1-GFP (3D4)* cells, where *TBY1-GFP* was transformed into a wild-type background (Figure 2.7). The TBY1-HA fusion protein migrates at just over 50 kD in *bop5-2::TBY1-HA (E4A)* rescued cells and *cc1691::TBY1-HA (B12)* (*TBY1-HA* construct transformed into wild-type cells) cell extracts; it is significantly less abundant than other TBY1 bands (Figure 2.7).

To confirm that *BOP5* and *TBY1* are the only two genes affecting the *bop5-2* motility phenotype, we attempted to rescue *bop5-2* by co-transformation of the wild-type *IC138* gene and several different *TBY1* gene constructs. Unfortunately, we never recovered a transformant that clearly expresses both genes (see results and discussion below), although we tried several transformations with many combinations of constructs and screened over 2000 transformants for improved motility (Table 2.3). We also tried to

recover a *bop5-2* strain that expresses both genes by crossing *bop5-2::IC138 mt+* with *cc1691::TBY-HA (B12) mt-*. In this case, we mated the two strains, selected for zygotes, and dissected each zygote into four tetrad progeny. Assuming that the two genes integrated randomly in the genome and assort independently, we expected that some of the resulting progeny would have the genotype *bop5-2::IC138, TBY1-HA*. We dissected 25 tetrads and recovered 47 progeny (only some progeny survived from each tetrad), and screened each colony for HA expression by immunofluorescence, IC138 expression by Western blot, and the presence of the *bop5-2* deletion by PCR. None of the progeny analyzed showed both HA and IC138 expression along with the *bop5-2* deletion.

TBY1 protein is concentrated in the cell body and is expressed near the basal bodies

To better understand where TBY1 is expressed in the cells, we performed cell fractionation experiments using the *bop5-2::TBY1-GFP (3F12)* and *pf2::PF2-GFP* strains. PF2 is a flagellar protein that is part of the dynein regulatory complex (DRC) and acts as a control for a GFP-tagged protein that is assembled in the flagella (Rupp and Porter, 2003). The two strains were fractionated by pH shock and differential centrifugation into cell bodies and isolated flagella. The flagella were further fractionated by detergent treatment to recover whole axonemes and membrane plus matrix fractions (Figure 2.8). Each fraction was loaded stoichiometrically onto a gel, transferred to PVDF, and probed with various antibodies. The blots were first probed with an antibody to OEE3, a cell body specific protein (Mayfield *et al.,* 1987). As expected, OEE3 bands are only seen in the whole cells and cell bodies of both *TBY1-GFP* and *PF2-GFP* expressing cells, but very little signal is seen in isolated flagella and axonemes (Figure 2.8). Next, the blots were probed with an antibody to IC69, an outer arm dynein intermediate chain that should be enriched in isolated flagella and axonemes. As expected, IC69 bands are seen in both flagella and axonemes from each strain (Figure 2.8). Finally, each blot was probed with a GFP antibody. In the *PF2-GFP* strain, the GFP signal is observed in whole cells and cell bodies, but clearly enriched in flagella and axonemes (Figure 2.8). However, the GFP signal in *TBY1-GFP* is only seen in whole cells and cell bodies suggesting that TBY1 is not enriched in the flagella (Figure 2.8).

To confirm the results from the cell fractionation experiments, and to determine specifically where TBY1 is localized within the cell body, we analyzed expression of TBY1-GFP and PF2-GFP in live cells. First, note that many images taken of *Chlamydomonas* cells show a high level of background signal in the cell body. This signal is not specific and is likely auto-fluorescence from the many photosensitive pigments in the *Chlamydomonas* chloroplast. PF2-GFP localizes to the flagella and to two spots at the anterior end of the cell, which likely correspond to the two basal bodies, similar to other integral axonemal proteins (Tam and Lefebvre, 2002; Rupp and Porter, 2003). Piasecki *et al.* (2008) and Dutcher *et al.* (2002) also saw a similar two spot pattern using antibodies against basal body specific proteins (Figure 2.9A). The TBY1-GFP signal is not detected in the flagella, instead being concentrated in a large, round spot at the anterior end of the cell (Figure 2.9A). This pattern differs from the two spot pattern typical of basal body and flagellar proteins.

Because our initial observations on the location of the TBY1-GFP signal were obtained in the *bop5-2* mutant background, it is formally possible that the defects in the mutant background prevented the TBY1-GFP from localizing properly. It is also formally possible that the large GFP tag altered the normal distribution of TBY1. To exclude these possibilities, we analyzed the distribution of endogenous, HA tagged, and GFP tagged TBY1 in wild-type backgrounds (Figure 2.9B). When wild-type cells are fixed and probed with the TBY1 peptide antibody, a weak signal is observed in the anterior region of the cell (Figure 2.9B). The signal may be weak because the peptide antigen is not very abundant and/or the peptide antibody is not very high titer. To confirm the localization of TBY1-GFP seen in live cells, we also analyzed wild-type cells expressing either TBY1-HA (*cc1691::TBY1-HA (B12)*) or TBY1-GFP (*cc1691::TBY1-GFP (3D4)*). In both cases, we observed antibody labeling in a similar region of the cell as that seen with the TBY1 antibody and/or live cell TBY1-GFP (Figure 2.9B).

The concentration of TBY1 at the anterior end of the cell could potentially overlap with the basal bodies, and so we wanted to determine whether the pattern of the TBY1 signal changes during the cell cycle in a similar way as the pattern of basal body staining. During interphase, the basal bodies are located in the anterior region of the cell,

at the base of the flagella where they nucleate flagellar assembly. In dividing cells, the basal bodies serve as the centrioles and move to the poles of the mitotic spindle (Coss, 1974, reviewed in Silflow and Lefebvre, 2001; Dawe *et al.,* 2007). To analyze the localization of TBY1 during the cell cycle, we examined *bop5-2::TBY1-GFP (3F12)* cells growing asynchronously in rich media. At all stages of the cell cycle, the TBY1-GFP remains at the anterior end of the cell (Figure 2.9C). In a small number of cells that appear to be in or just completing mitosis, two TBY1-GFP spots are seen (Figure 2.9C, last panel). Similar results were observed with the *cc1691::TBY1-HA* strain when these cells were grown in a culture synchronized with a light/dark cycle (data not shown).

TBY1 is located in a ring shaped structure at the anterior region of the cell

The expression of TBY1-GFP in the anterior region of the cell did not have the typical "two-spot" pattern seen with the localization of basal body associated proteins (See Figure 2.9A, results above; Dutcher *et al.,* 2002; Piasecki *et al.,* 2009). Using light microscopy of live cells, we recognized that TBY1-GFP is located in a ring approximately 1.5 mm in diameter (Figure 2.10A). The ring shaped structure is most clearly observed in images of living TBY1-GFP cells, and appears to be compromised following fixation (Note Figure 2.9B). We presume that the endogenous TBY1 and TBY1-HA proteins are also found in a ring shaped structure, as they localize to the same region in fixed cells.

To determine more specifically where the TBY1 ring is located, we compared the location of TBY1–GFP to the position of other structures in the anterior end of the cell. A summary of these structures is shown in Figure 2.10B. First, we examined the position of the TBY1-GFP ring relative to the two contractile vacuoles, which *Chlamydomonas* uses to regulate osmotic pressure while living in a fresh water environment (Ruiz *et al.,* 2001). Depending on the orientation of the cell, the ring structure appears to located between the two contractile vacuoles. When both contractile vacuoles are observed in the same focal plane, the TBY1-GFP forms a line between the vacuoles (Figure 2.11A). When viewed in a different orientation, with the two contractile vacuoles stacked on top

of one another, a focal series through the cell demonstrates that the TBY1 ring is located in the region between the two vacuoles (Figure 2.11A).

To look at location of TBY1 relative to other subcellular organelles, we fixed and stained *bop5-2::TBY1-GFP (3F12)* cells with a series of antibodies. The fixation compromises the ring structure but allows us to compare the position of TBY1 relative to other organelles. By staining cells with antibodies against both GFP and ε-tubulin, a protein specific to the posterior end of the basal bodies (Dutcher *et al.,* 2002), we determined that TBY1-GFP is located posterior to the basal bodies (Figure 2.11B). Next, we used DAPI to label DNA. Because there is also DNA in the chloroplast, the signal is not limited to the nucleus, but the brightest, most circular signal corresponds to the nuclear region. As shown in Figure 2.11C, the nuclear staining is posterior to the TBY1-GFP signal.

We also compared the position of the TBY1-GFP signal to pattern of centrin staining. Centrin is a component of the distal striated fiber that connects the two basal bodies (Salisbury *et al.,* 1988). Centrin fibers also extend from the basal bodies to the nucleus where they wrap around the nuclear envelope (Wright *et al.,* 1985). This pattern is seen in Figure 2.11D, where the centrin signal surrounds the DAPI signal from the nucleus. The TBY1-GFP signal is also encompassed by the centrin signal, but in this case, the most anterior part of the centrin signal surrounds the TBY1 signal (Figure 2.11D).

To address a possible association between centrin and TBY1, we isolated and stained the nuclear-flagellar apparatus (NFAP). NFAPs contain the two flagella and basal bodies in close association with a remnant of the cell nucleus (Taillon and Jarvik, 1995). The NFAP isolation procedure removes the cell wall with autolysin and dissolves the cell membrane and chloroplast, which occupies most of the cell volume, with a nonionic detergent. However, the remaining NFAPs retain the proteins associated with the cell's cytoskeleton. As a control, we also prepared NFAPs from cells expressing PF2-GFP. PF2-GFP signal associates with the NFAP, as expected, and is concentrated along the length of the axoneme (Figure 2.11E). The TBY1-GFP signal also remains

associated with the isolated NFAP, but the signal is only seen at the base of the two flagella (Figure 2.11E).

Transformation of bop5-2 *with* IC138, TBY1-HA *or* TBY1-GFP *changes motility*

To understand the possible impact of the *TBY1* mutation on the motility phenotypes of *bop5-2,* we assessed the swimming patterns of mutant and transformed strains in greater depth. Unlike wild-type, where most cells swim in a forward direction, a typical population of *bop5-2* cells swims in a mixture of directions, with approximately equal numbers of cells swimming forwards, backwards, and/or spinning in place (Figure 2.12A). These motility phenotypes are similar to those described previously for the *move backwards only (mbo)* mutations (Figure 2.12A, Segal et. al., 1984). *mbo* mutants are associated with defects in the assembly of six axonemal polypeptides (Segal et al., 1984). Specifically, of the *mbo* strains, *mbo3* looks most similar to *bop5-2,* with a mixture of swimming directions (Figure 2.12A). Initially, we hypothesized that the mbo-like phenotype was caused by either the lack of IC138 or TBY1, but transformation with constructs containing either gene did not restore motility to wild-type (Figure 2.12A). Transformation with IC138 does, however, change the ratio of cells swimming in any one direction, as more cells swim backwards and fewer swim forwards (Figure 2.12A).

Transformation with *TBY1* constructs also changes motility, with slightly more cells swimming forwards than in the parental strain (Figure 2.12B, 2.12C). Because the percentage of spinning cells remains nearly constant in all *bop5-2* strains, the graph in Figure 2.12B compares the percentage of forwards and backwards swimming cells observed in strains transformed with various *TBY1* constructs. *TBY1* transformed cells appear to be slightly more motile than the original parent strain, *bop5-2 6D* (Figure 2.12C). The slight increase of forward swimming cells is statistically significant ($p < 0.05$) (Figure 2.12B, See discussion).

Mbo-like defect contributes to the bop5-2 *phenotype*

To determine whether there might be any *mbo* related deficiencies in the *bop5-2* strain that cause the backwards swimming phenotype, we probed Western blots of whole

cells and isolated axonemes with an antibody against MBO2p (Tam and Lefebvre, 1993). MBO2p is the gene product from the *mbo2* locus and encodes a conserved coiled-coil axonemal protein (Tam *et al.,* 2003). As expected, MBO2p is missing in whole cells and axonemes from *mbo2* and is reduced in whole cells and axonemes from *mbo3* (Figure 2.13). MBO2p is missing or greatly reduced in isolated axonemes from *bop5-2* and all of the "rescued" strains (Figure 13), even though MBO2p could be detected in whole cell extracts (Figure 2.13).

Given the absence of the MBO2 protein in the flagella of *bop5-2,* we also investigated whether *bop5-2* flagella have normal axonemal structure by electron microscopy or whether they have structural defects similar to those observed the *mbo* mutants. Wild-type axonemes contain beak-like projections inside the B-tubule of doublets 1, 5, and 6. The *mbo* family of mutants have defects in these beak structures: *mbo1* lacks beaks in doublets 5 and 6, *mbo2-3* mutant strains lack the beak structure in doublets 5 and sometimes 6, and *mbo3* has more variable beak defects (Segal *et al.,* 1984; Tam *et al.,* 2002). Interestingly, we observed that the beak structures are consistently missing in doublets 5 and 6 of *bop5-2* axonemes (Figure 2.14), similar to what is seen in the *mbo* mutants.

Because transformation with either *IC138* or *TBY1* did not restore flagellar assembly of MBO2, it is possible that there is another, *mbo*-like mutation that affects assembly of MBO2 and forwards motility in the *bop5-2* strain. Of the known *mbo* mutants, *bop5-2* most closely resembles *mbo3,* because both strains have a mixed population of cells that swim in different directions (Figure 2.12A). To see whether there might be a mutation in *bop5-2* that is related to the *MBO3* locus, we constructed diploid strains and tested for complementation.

Four *mbo3 bop5-2::IC138* and four *mbo3 bop5-2* diploid strains were constructed and confirmed as true diploid strains (see Materials and Methods for details; Table 2.4). Once confirmed as diploids, we analyzed their motility phenotypes. If the mutations are in different genes, usually the two mutant alleles are complemented by the wild-type alleles in the diploids, and wild-type motility will be observed. If the *mbo* mutations are in the same gene, the motility phenotype of the diploids will resemble the parent strains.

All of the diploids that we recovered swam forwards, indicating that complementation between *bop5-2* and *mbo3* did occur (Table 2.4).

As an alternative strategy to identify the mutation(s) responsible for the *bop5-2* motility defects, we tried to rescue the phenotype by transforming *bop5-2* with a BAC (23K17) that covered the entire region deleted in *bop5-2* (Figure 2.15). Unfortunately, we never recovered any rescued cells with wild-type motility, even after three rounds of transformations and screening 501 transformed colonies (Figure 2.15). Because we previously showed the *bop5-2* motility phenotype is closely linked to the *NIT1* insertion event (see Material and Methods), these observations suggest that any additional mutations that might be responsible for motility defects are located within 500 kb of the *bop5-2* deletion. We therefore attempted to rescue the *mbo-like* phenotype by transforming *bop5-2* cells with BACs located close to the deleted region. These BAC clones (9C9, 20H20, 18C10, 20K9, 34L6) also contain predicted flagellar genes, described in Figure 2.15B, and so we hypothesized that the motility defects might result from a defect in one of these genes. Unfortunately, although we screened 60-100 colonies from each BAC transformation, we did not recover any transformants with forwards motility (Figure 2.15). Note that we screened for forwards motility, not wild-type motility, because *IC138* would still be disrupted in a strain rescued with one of these BACs. The *IC138* mutation would prevent a full restoration to wild-type swimming.

2.4. DISCUSSION

IC138 is not required for assembly of the I1 dynein

To better understand the role of IC138 in the control of dynein activity, we identified a null mutation, *bop5-2*, associated with the deletion of >90% of the *IC138* gene. Surprisingly, loss of IC138 did not impact assembly of I1 dynein into the axoneme; both I1 HCs, IC140, Tctex1, and Tctex2b are still present (Figure 2.2). Mutations in either outer arm intermediate chains usually block assembly of the outer arm dynein (Mitchell and Kang, 1991; Wilkerson et al., 1995), and mutations in IC140 are associated with defects in assembly of the I1 dynein (Perrone et al., 1998). However, IC138 is part of a distinct sub-complex, which is not required for either I1 dynein assembly or targeting into the axoneme.

The IC138 sub-complex: IC138 is closely associated with LC7b, IC97 and FAP120

Previous studies of *bop5-1* have shown that the I1 dynein lacks LC7b when IC138 is truncated (see Hendrickson et al., 2004). Because LC7b is also an outer dynein subunit (Dibella et al., 2004a), we did not directly analyze its presence in *bop5-2*. However, we can reasonably infer that the I1 dynein lacks LC7b when IC138 is missing. IC97 is a novel I1 subunit that shares homology with axonemal proteins in several organisms, including the murine Las1 (lung adenoma susceptibility 1) protein. Several biochemical assays indicate that IC97 interacts directly with tubulin subunits (Wirschell et al., 2009). We show here that assembly of IC97 into the axoneme depends on the presence of IC138, as it is missing in *bop5-2* axonemes, but restored in the IC138 rescued strain (Figure 2.2B).

IC138 also influences the assembly of FAP120, a novel ankyrin related protein recently identified as an I1 associated protein (Ikeda et al., 2009). We show here that FAP120 is missing in *bop5-2* and restored in the *bop5-2::IC138* rescued strain, which confirms the close association between this polypeptide and IC138 (Figure 2.2B). However, the interaction between FAP120 and IC138 may be mediated indirectly

through LC7b, as FAP120 is also missing in *bop5-1*, which assembles a truncated version of IC138 but lacks LC7b (see Ikeda et al., 2009).

Taken together, these observations demonstrate that IC138, LC7b, IC97 and FAP120 form a distinct sub-complex within the I1 dynein complex The presence of multiple sub-complexes within the I1 dynein is consistent with the phenotype of a *tctex2b* mutation, which blocks assembly of Tctex2b, but does not prevent assembly of other I1 subunits into the axoneme (Dibella et al., 2004b).

The IC138 sub-complex is located at the base of the I1 dynein

Our previous studies of I1 dynein HC mutants identified the positions of the two motor domains, and by implication, suggested the position of the IC/LC complex (Figure 3.1). Here we show directly by EM image averaging of *bop5-2* axonemes that the IC138 sub-complex is located at the base of the I1 dynein, between radial spoke 1 and the outer dynein arms (Figure 2.3). However, the N-terminal regions of the dynein HCs, IC140, and other I1 LCs are likely still present in this region. More detailed insight into the unique position of each subunit and their respective interactions within the IC138 sub-complex will require cryo-electron tomography of I1 mutant axonemes with less severe structural defects (e.g., *bop5-1, ida7::IDA7 5a, tctex2b, fla14-3*), as well as the development of alignment and averaging procedures that can accurately determine differences in three dimensions. Even so, the analysis of *bop5-2* clearly locates IC138, which is the only known I1 phosphoprotein, in a position to be regulated by the radial spoke phosphorylation machinery (Porter and Sale, 2000; Smith and Yang, 2004; Gaillard et al., 2006; Wirschell et al., 2008). The position of the IC138 sub-complex may also facilitate interactions between the inner and outer dynein arms to coordinate their activity (reviewed in Brokaw, 1994; Kamiya, 2002).

The IC138 sub-complex is required for I1 dynein mediated microtubule sliding

Given that several defective genes affect flagellar motility in *bop5-2*, and to more directly assess the effect of the *bop5-2* mutation on I1 activity, we measured microtubule sliding velocities during sliding disintegration *in vitro,* an assay useful for assessing

dynein activity in axonemes that are otherwise paralyzed or defective in motility (Witman et al., 1978; Okagaki and Kamiya, 1986; Smith and Sale, 1991). Interestingly, loss of the IC138 sub-complex was correlated with a decrease in sliding velocity similar in magnitude to that observed with the loss of the entire I1 dynein complex (Habermacher and Sale, 1997). Re-assembly of the IC138 sub-complex restored sliding velocities to wild-type levels (Figure 2.4). Thus the IC138 sub-complex is required to couple the activity of I1 motor domains to microtubule sliding.

Bop5-2 *is null for TBY1*

Transformation of *bop5-2* with *IC138* did not restore wild-type motility; instead *bop5-2::IC138* cells had an even higher percentage of cells swimming backwards than *bop5-2* (Figure 2.12A). This enhancement of backwards swimming may be a result of the restored I1 complex. Because wild-type motility is not restored upon *IC138* transformation, we hypothesized that another gene affecting motility was defective in *bop5-2*. Initially, we hypothesized that this gene might be *TBY1,* as TBY proteins have been implicated in flagellar functions in other organisms, but transformation of *bop5-2* with either *TBY1-HA* or *TBY1-GFP* did not dramatically change motility of the rescued strains (Figure 2.12). There is a slight increase of forward swimming cells that is statistically significant ($p < 0.05$), but we are uncertain whether this change is biologically relevant given the relatively high variability of the percentage of swimming directions in different experiments. We have tried to control for variables such as culture conditions, cell density, light-dark cycles, and other factors, but we have not been able to establish conditions that clearly demonstrate *TBY1* rescue. In addition, all of the transformants express TBY1p at less than wild-type levels, and so it is possible that the failure to recover wild-type motility may be related to TBY1 protein abundance or stability. We also hypothesized that the HA or GFP tag may interfere with the ability of the *TBY1* construct to rescue the motility defects, as the tags were located at the C-terminus near the conserved Tubby domain. To test for this, we attempted to rescue *bop5-2* with an untagged *TBY1* construct (Table 2.3). Unfortunately, we were unable to isolate any strains with wild-type motility, so we are not able to rule out this possibility.

Although it is possible that the presence of the C-terminal epitope tags reduces TBY1 expression in *Chlamydomonas*, C-terminal epitope tags do not interfere with the rescue of *Tubby* related mutants in other species (Santagata *et al.,* 2001; Mukhopadhyay *et al.,* 2005). Additional studies using other constructs that increase TBY1 expression may be useful in resolving this apparent discrepancy.

Although the effect of the *TBY1* mutation on the motility phenotype of *bop5-2* is unclear, we continued to analyze mutant and rescued strains to determine whether we could discern other TBY1 functions. We developed a peptide antibody to TBY1 and probed Western blots containing whole cell extracts from wild-type, *bop5-2*, and rescued strains. These blots clearly showed that *bop5-2* is null for TBY1 protein, but also that the rescued strains do not express TBY1 at wild-levels. If there is some phenotype related to the loss of TBY1 in *bop5-2*, we still may be able to uncover it. However, given the genetic complexities of the strain, it may be more straightforward to develop a series of TBY1 mutants by RNA interference to determine TBY1 function. RNA interference has been used to decrease expression and identify the function of several candidate proteins involved in flagellar assembly, motility, and mating, including the *BBS*, *Agg* and *PKD2* genes (Li *et al.,* 2004; Iomini *et al.,* 2006; Wang *et al.,* 2006).

TBY1 is localized to a ring at the anterior of the cell

Northern blots of total RNA probed with *TBY1* showed very little signal before or after deflagellation, although a *TBY2* signal was detected after deflagellation (Figure 2.6B). Given that the *TBY* hybridization probes readily detected single copy genes on Southern blots, and that we were able to detect expression of multiple flagellar genes on parallel Northern blots (data not shown), it is likely that both transcripts are not very abundant in the pool of total RNA. Additional experiments to analyze TBY1 transcripts by qRT-PCR or RNAseq would be a more sensitive assay for TBY1 expression. Two groups have looked at *TBY1* and *TBY2* mRNA expression by RNAseq. Gonzalez-Ballester *et al.,* (2010) found that *TBY1* transcripts are present in higher numbers than *TBY2* transcripts, but did not analyze the deflagellation response. The Dutcher lab has performed a RNAseq experiment comparing transcript levels before and after

deflagellation. They found that *TBY2* transcripts are much more abundant after deflagellation while *TBY1* transcripts are only slightly increased after deflagellation (Dutcher and Kwan, personal communication). Consistent with all of these results, we have been unable to detect any signal for TBY1 protein in the flagellum by Western blot analysis or imaging of live or fixed cells (Figure 2.8). Instead, the TBY1 protein is always localized to a spot in the anterior region of the cell (Figure 2.9). We see similar localization patterns in multiple strains using a variety of reagents (*bop5-2::TBY1-GFP, cc1691::TBY1-HA, cc1691::TBY1-GFP* and wild-type cells), and so we think it is unlikely that this pattern is an artifact (Figure 2.9A, 2.9B). Also, in some cells that appear to be completing mitosis, two TBY1-GFP spots are seen (Figure 2.9C). This suggests that the TBY1 structure may replicate during cell division.

Closer examination of TBY1 localization suggests that the protein resides in a ring shaped structure (Figure 2.10). This ring is located in between the contractile vacuoles, but it does not co-localize with the vacuoles (Figure 2.11A). Also, the TBY1 localization is anterior to the nucleus and posterior to the basal bodies, but within the centrin structure (Figure 2.11B, 2.11C, 2.11D). Because TBY1-GFP remains with the NFAP (Figure 2.11E), it is more likely associated with the cytoskeletal components involved with flagella function and less likely a detergent-soluble membrane protein involved with vacuolar function. Another argument against a role in the contractile vacuole is the fact that the TBY1 ring does not contract or change shape during vacuolar pumping, and that the *bop5-2* strain does not have any obvious abnormalities in vacuole pumping or vacuolar structure by DIC microscopy (Figure 2.11A). Further study of *bop5-2* cells by transmission electron microscopy may reveal a subtler structural defect.

The pattern of TBY1 distribution has not been described previously in *Chlamydomonas* cells and is therefore somewhat difficult to interpret. One possibility is that the TBY1 protein ring regulates transport of proteins into or out of the flagella because TBY1 is located near where proteins bound for the flagella must be loaded onto or unloaded from the flagella. Several lines of evidence add support to this hypothesis.

First, proper flagellar function requires the localization and transport of membrane proteins to the ciliary membrane; this transport is likely regulated through

activation of specific Rab-GTPases including Rab8 (Nachury *et al.,* 2007; Yoshumura *et al.,* 2007; reviewed in Lim *et al.,* 2011). For example, when the Rab8 pathway is disrupted, the flagella specific calcium channel PKD2 has reduced flagellar expression (Follit *et al.,* 2006). Tubby proteins are also implicated in Rab-GTPase signaling, as *C. elegans* tub-1 helps activate the Rab-GTPase Rab7 involved in membrane trafficking (Mukhopadhyay *et al.,* 2005, 2007).

The hypothesis that TBY1 may regulate flagella protein trafficking is consistent with Mukhopadhyay *et al.* (2010), which shows that Tubby-like protein 3 (TULP3) facilitates transport of a subset of G-protein coupled receptors (GPCRs) into the primary cilia of mammalian cells. Specifically, they found that TULP3 directly associates with IFT complex A and when TULP3 expression is knocked down, some, but not all, flagella specific GPCRs do not localize to the flagella (Mukhopadhyay *et al.,* 2010). Ciliary-localized GPCRs, such as SSTR3 and MCHR1, are much reduced in flagella of TULP3. However, ciliary-localized proteins in the hedgehog pathway, such as smoothened and Gli3, are localized normally

TBY1 can also be linked to flagellar protein trafficking through its interactions with the BBS proteins, which are implicated in flagellar protein trafficking (Nachury *et al.,* 2006; Lechtreck *et al.,* 2010). Nachury *et al.* (2007) observed that lack of BBS proteins prevents cilia growth in mammalian cultured cells. Lechtreck *et al.* (2009) demonstrated that *BBS4* mutations cause defects in phototaxis and the accumulation of several, poorly characterized proteins in flagella of *Chlamydomonas*. Many flagellar signaling proteins, such as PKD2 and FMG1, did localize normally in the *Chlamydomonas bbs4* mutant strain. There are several direct links between BBS proteins and Tubby proteins. First, in *Chlamydomonas,* even though BBS4 is localized to the flagella, some BBS4 is located in the cell body in a similar pattern to TBY1 (Lechtreck *et al.,* 2009). Also, *tubby* and *bbs* mutant mice share similar phenotypes such as obesity, retinal degeneration and hearing loss (Ohlemiller *et al.,* 1995). *tub-1* and *bbs-1* are in the same genetic pathway in *C. elegans* as *bbs-1 tub-1* double mutants do not have amore severe phenotype than either single mutant (Mak *et al.,* 2006). Last, BBS5 recognizes the PI(3)P phosphoinisotide on PIP blots (Nachury *et al.,* 2007), while the tubby domain is

known to bind PI(3,4)P_2, PI(4,5)P_2, and PI(4,5)P_3 phosphoinisotides (Santagata *et al.,* 2001).

To determine whether TBY1 in *Chlamydomonas* might be part of a complex regulating flagellar signaling similar to BBS4, we could look for defects in localization of signaling proteins in flagella from *bop5-2* or *TBY1* knockdown strains. For instance, we could test isolated flagella for changes in the accumulation of known flagellar proteins such as FMG1, PKD2, CAV2, and TRP channels (Bloodgood *et al.,* 1986; Huang *et al.,* 2007; Fujiu *et al.,* 2009; Fujiu *et al.,* 2011). Perhaps we would see an accumulation of certain proteins similar to those described above by Lechtreck *et al.,* (2009) in the *bbs* mutants. In particular, we could look for accumulation of PKD2 and FMG1 by Western blot, which were not affected in the *bbs* mutants. We could also test for unknown proteins that accumulate in *tby* mutants by iTRAQ labeling and mass spectroscopy. We could also determine whether TBY1 co-localizes with BBS4 by immunofluorescence. Finally, we could use TBY1-HA or TBY1-GFP in immunoprecipitations to pull-down any associated proteins. Preliminary results suggest that TBY1-GFP protein is soluble, so this experiment is a reasonable first step to better understand the role of TBY1 in the cell.

TBY2 may also have a flagellar function

Our Northern blot results indicated that *Tubby-2* mRNA is upregulated after deflagellation (Figure 2.6), and *Tubby-2* mRNA was also found in a genome wide analysis for transcripts upregulated after deflagellation (Stolc *et al.,* 2005). These observations suggest that Tubby-2 is a relatively abundant protein that plays a role in flagellar assembly or motility. However, it is still unknown whether Tubby-2 is required for flagella assembly, motility, phototaxis, or mating. Therefore, we could use RNA interference to knockdown the expression of Tubby-2 and screen for flagellar phenotypes. To learn more about the subcellular localization of and proteins associated with TBY2, we constructed a *TBY2-GFP* transgene and attempted to express this construct in *Chlamydomonas* cells following transformation. We have screened about 300 transformants, but we have thus far only detected weak GFP signals in the flagella of three strains by immunofluorescence. Unfortunately, we have been unable to detect the

TBY2-GFP in isolated flagella by Western blots, even after prolonged exposure. Efforts are currently underway to troubleshoot why this construct might not be expressed at higher levels, and we are re-sequencing the entire transgene to make sure no unexpected mutations were introduced during the cloning steps. Future experiments surrounding the Tubby project include production of antibodies to either a TBY2 peptide or fusion protein. Once we have a functional TBY2-GFP construct and/or specific TBY2 antibody, we could perform co-immunoprecipitation and localization experiments to determine whether TBY2 is contained within a protein complex and where that complex might be located.

Bop5-2 has another mutation causing motility and MBO2p assembly defects

The phenotypes of *bop5-2* and the *IC138* and *TBY1* rescued strains indicate that there may be another, closely linked mutation that affects flagellar motility in *bop5-2*. Transformation with *IC138* restored the I1 related defects (Figures 2.2, 2.3, 2.4), and transformation with *TBY1* restored the TBY1 protein (Figure 2.7), but neither construct restored wild-type motility. Because the motility defects were similar to those seen in the *mbo* family of mutants, we investigated whether MBO2p was defective in the strains. Interestingly, although the MBO2p is expressed in whole cells of *bop5-2* strains, the MBO2 protein is not assembled into the flagella of *bop5-2* strains or *bop5-2* rescues. This observation suggests the possibility of a defect in transport of MBO2p to the flagella in *bop5-2*. We also looked at cross-sections of *bop5-2* flagella to determine whether there was an *mbo-like* defect in the assembly of beak structures. As expected, the beak structures normally observed in the B-tubule of doublets 1, 5 and 6 are missing in *bop5-2*.

These observations suggest there could be a third, *mbo-like* mutation in *bop5-2* that causes backwards swimming and lack of transport of MBO2p to the flagella. We attempted to determine where the locus of the *mbo-like* mutation is by creating diploids between *bop5-2* and *mbo3* and by transformation with other BAC clones. The *bop5-2 mbo3* diploid strains did swim exclusively in the forwards direction, which suggests that *bop5-2* does not contain a mutation in the *MBO3* locus (Table 2.4). Transformation of *bop5-2* with BACs that contain putative flagellar genes both upstream and downstream of

the *DIC4* locus also did not result in rescue of the backwards swimming phenotype (Figure 2.15). It is possible that we did not screen a sufficient number of transformants, as we only analyzed 60-100 colonies per transformation (Figure 2.15). More transformations and backcrosses to wild-type will be needed to isolate and identify the *mbo-like* mutation.

Given the genetic complexities of the *bop5-2* strain, we decided to analyze other *bop5* mutations that only affect the *BOP5* gene to better understand the specific function of IC138 in I1 dynein function and flagellar motility (See Chapter 3). We also plan to generate knockdowns of TBY1 by RNA interference to better understand the TBY1 phenotype. However, although the *bop5-2* strain is genetically complex, we were able to glean valuable information about the structure of the I1 dynein complex and the localization of TBY1 from our studies.

2.5. TABLES AND FIGURES

Table 2.1. Summary table of *bop5-2* and *tby1* related strains.

Strain Name (Genotype, CC#)	*Phenotype*	*Strain Creation*	*Original Study*
Wild-type 137c+ (mt+ nit1 nit2, CC125)	Wild-type	None	
Wild-type 137c- (mt- nit1 nit2, CC124)	Wild-type	None	
Wild-type 6145c (CC1691)	Wild-type	None	
Wild-type L8 (mt- nit1 apm1-19, CC4264)	Wild-type	Isolated by Lai-wa Tam	Tam and Lefebvre, 1993
bop5-2 (mt+ nit1 ac17, CC4284)	Missing IC138 sub-complex, MBO2p, TBY1	Transformation of A54 e18 with *NIT1*	Bower et al., 2009
bop5-2 6D (mt+, CC4416)	Missing IC138 sub-complex, MBO2p, TBY1	Crossed *bop5-2* to L8	Bower et al., 2009
bop5-2 1C (mt+)	Missing IC138 sub-complex, MBO2p, TBY1	Crossed *bop5-2* to L8	This study
bop5-2 2D (mt+)	Missing IC138 sub-complex, MBO2p, TBY1	Crossed *bop5-2* to L8	This study
bop5-2 C2 (mt-)	Missing IC138 sub-complex, MBO2p, TBY1	Crossed *bop5-2 mt+ 6D* to A54	This study
bop5-2::IC138 (2BA) (CC4285)	Missing MBO2p, TBY1	Co-TFM w/pHx (IC138) and pSI103 into CC4284	Bower et al., 2009
bop5-2 6D::TBY1-HA (E4A) (CC4417)	Missing IC138 sub-complex, MBO2p, Expresses TBY1-HA	Co-TFM w/ TBY1-HA and pSI103 into *bop5-2 mt+ 6D*	This study
bop5-2 6D::TBY1-GFP (3F12) (CC4418)	Missing IC138 sub-complex, MBO2p, Expresses TBY1-GFP	Co-TFM w/ TBY1-GFP and pSI103 into *bop5-2 mt+* 6D	This study
CC1691::TBY1-HA (B12) (CC4419)	Expresses TBY1-HA	Co-TFM w/ TBY1-HA and pSI103 into CC1691	This study
CC1691::TBY1-GFP (3D4) (CC4420)	Expresses TBY1-GFP	Co-TFM w/ TBY1-GFP and pSI103 into CC1691	This study

Figure 2.1. Identification of an IC138 and TBY1 null strain. (A) Southern blot of wild-type (A54) and *bop5-2* (6F5) genomic DNA probed with an ~9 kb genomic fragment containing the *IC138* gene. Note the absence of restriction fragments in the *bop5-2* lanes. (B) Schematic representing the deleted region in *bop5-2.* (D. Tritschler and K. VanderWaal)

A)

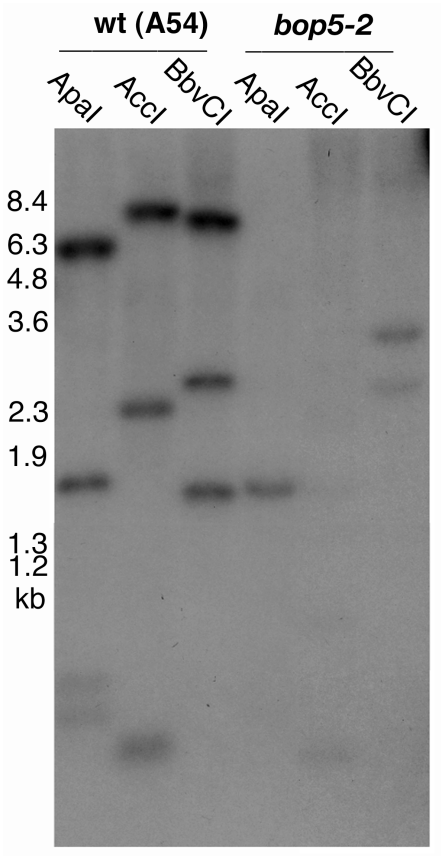

B)

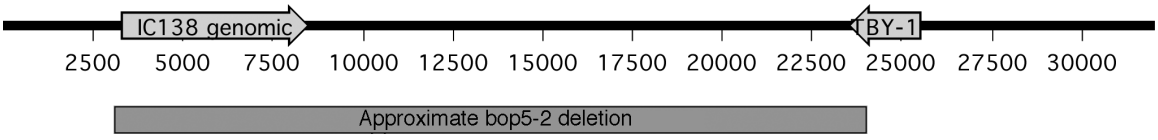

Figure 2.2. Western blots of isolated axonemes from wild-type and mutant cells probed with I1 dynein components. (A) Western blot of isolated axonemes from wild-type and mutant cells. Note the presence of IC140 and the 1α HC in the *bop5-2* axonemes, but the absence of IC138. As reported previously, IC138 is truncated in *bop5-1* and shifted by hyperphosphorylation in *mia1* and *mia2*. The outer arm subunit IC69 serves as a loading control. (B) Western blot of isolated axonemes from wild-type, *bop5-2*, and IC138 rescued cells. IC138, IC97 and FAP120 are missing in *bop5-2* axonemes, but all three polypeptides are restored in axonemes from the IC138 rescued strain. (Note that the MBO2 protein is not part of the IC138 sub-complex, as it missing in axonemes from both *bop5-2* and the IC138 rescued strain.) (R. Bower and K. VanderWaal)

A) B)

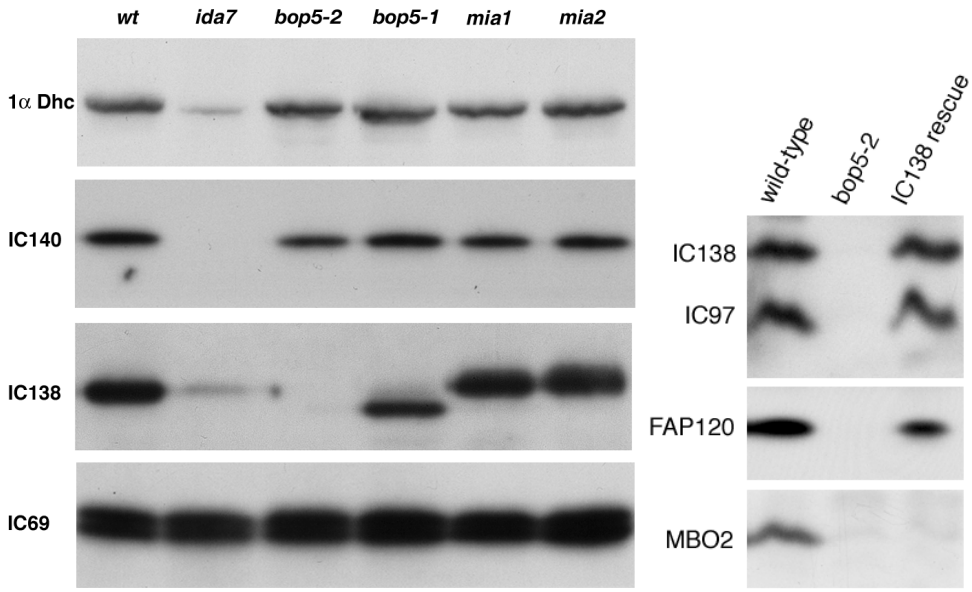

Figure 2.3. Defects in I1 structure in *bop5-2* axonemes. Top Row: Averages of the 96-nm axoneme repeat from wild-type, *bop5-2*, and IC138 rescued (*bop5-2::IC138*) cells, based on six, six, and nine individual axonemes and 61, 63, and 93 repeating units, respectively. The proximal end of the repeat is on the left, the outer arms (OA) are shown on the top, and the two radial spokes (S1 and S2) are shown on the bottom. The I1 dynein is the tri-lobed structure at the proximal end of the repeat. The density of the third lobe near the base of S1 is reduced in *bop5-2* and restored in the IC138 rescued (*bop5::IC138*) strain. Bottom Row: Diagram of densities within the 96-nm repeat and difference plots showing a statistically significant difference in the third lobe of the I1 dynein in *bop5-2* (see arrow) (E. O'Toole).

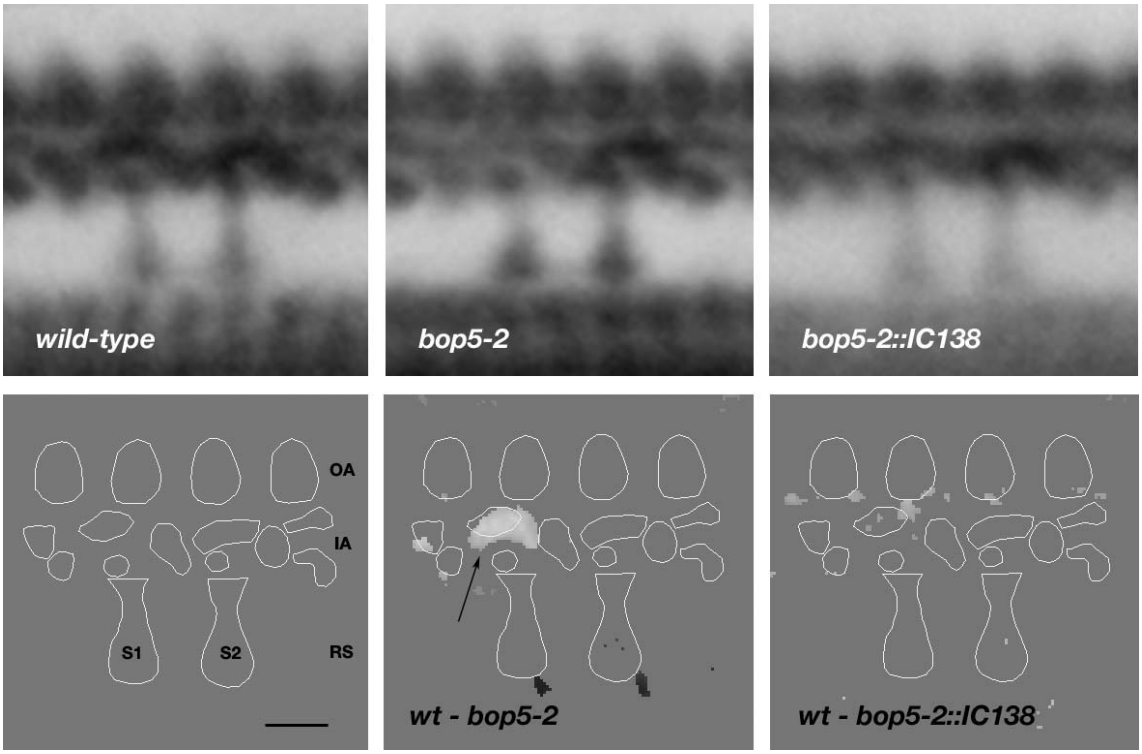

Figure 2.4. Microtubule sliding velocity increases upon transformation of *bop5-2* with *IC138,* but not with *TBY-HA* (K. VanderWaal and L. Fox).

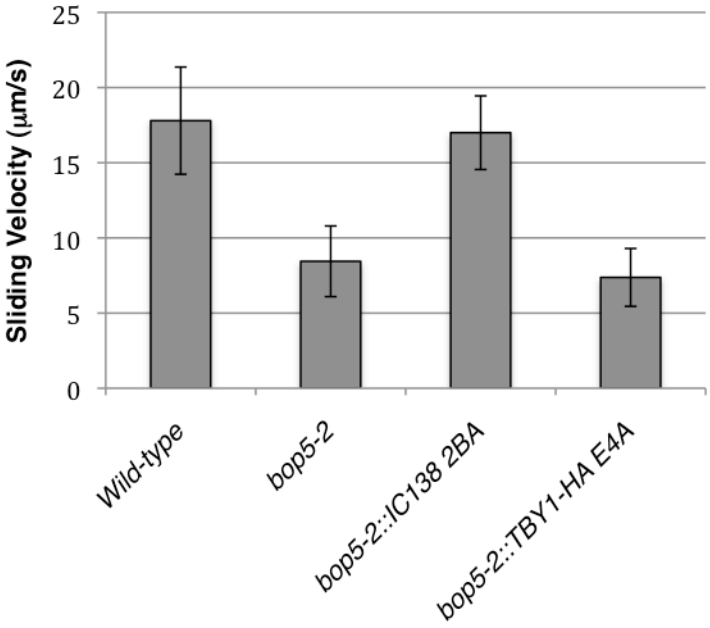

Figure 2.5. The deletion in *bop5-2* covers a >20 kb region that includes several transcripts. (A) Map of region of Chromosome 12/Scaffold 31 from JGI v4.0 that is affected by the *bop5-2* deletion. Putative transcripts that are deleted in *bop5*-2 are shown here. Also shown is an illustration of the sequence homology with the related alga *Volvox carteri.* (B) Table showing details for each transcript. (K. VanderWaal)

(A)

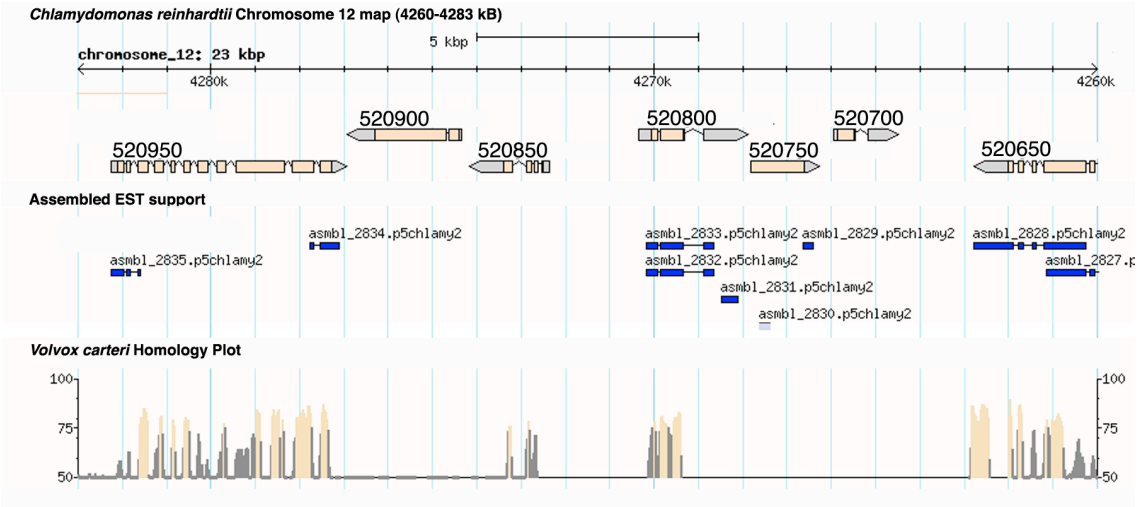

(B)

Locus Name	*Alias*	*Chromosome 12 Location*	*Length (aa)*	*Best non-Algal hit with NCBI BLASTp*
520950	*BOP5*	4276945 - 4282254	1057	XP_003056207.1 flagellar inner arm intermediate chain, 669 aa [*M. pusilla*]; Score = 305 bits (780)
520900		4274349 - 4276930	618	No non-*Chlamydomonas* hits
520850		4272349 - 4274160	141	XP_002279047.1 similar to SOH1 (Mediator of RNA polymerase II transcription subunit) family protein, 198 aa [*V. vinifera*]; Score = 119 bits (299)
520800		4267883 - 4270348	213	XP_625502.1 possible secreted protein with long stretch of threonines, mucin, 905 aa [*C. parvum Iowa II*]; Score = 37.0 bits (84)
520750		4266263 - 4267828	396	No non-algal hits
520700		4264493 - 4265958	124	XP_003102696.1 hypothetical protein, 1083 aa [*C. remanei*]; Score = 42.4 bits (98)
520650	*TBY1*	4259822 - 4262784	451	XP_002508919.1 tubby-like protein, 595 aa [*M. sp. RCC299*]; Score = 306 bits (784)

Figure 2.6. Tubby protein alignment from several species and Northern blots of *TBY* transcripts in *Chlamydomonas.* (A) Clustal-W alignment between *Chlamydomonas reignardtii* TBY1 protein (CrTBY1), *Chlamydomonas reignardtii* TBY2 protein (CrTBY2), and the best BLASTp hits to CrTBY1 from *Mus musculus* (Tubby-like protein 2 or MmTULP2), *Homo sapiens* (Tubby or HsTubby), *C. elegans* (Tub-1 or CeTub-1), and *Oryza sativa* (rice, Tubby-like protein 11 or OsTLP11). The Tubby domain is shaded in grey. (B) Northern blot autoradiograms of total RNA isolated before (0 min.) or after deflagellation (45 min.). RNA (20 μg per lane) was separated on a 1% formaldehyde agarose gel, and hybridized with either a 0.50 kb *TBY1* or 0.65 kb *TBY2* RT-PCR product from the 5' end of the *TBY1* or *TBY2* genes. Blots were also probed with a control probe for the *CRY1* gene, which encodes the S14 ribosomal protein subunit. (K. VanderWaal and D. Tritschler)

A)

```
OsTLP11   ------------------------------------------------------------
CeTub1    ------------------------------------------------------------
HsTubby   MGARTPLPSFWVSFFAETGILFPGGTPWPMGSQHSKQHRKPGPLKRGHRRDRRTTRRKYW 60
MmTULP2   -------------------------------------------MDREGPRGPRSGASQ-- 15
CrTBY1    ------------------------------------------------------------
CrTBY2    ------------------------------------------------------------


OsTLP11   ------------MSFRSVIQEVKGEIGAISRRGFRSRPG------------RVRRVAAAA 36
CeTub1    ---------MTDTNSQWIEMNLQRQRKMLEDKQKQKRHQ-------SAG---SVRTTSTA 41
HsTubby   KEGREIARVLDDEGRNLRQQKLDRQRALLEQKQKKKRQEPLMVQANADGRPRSRRARQSE 120
MmTULP2   ENEQWKKETLEDEFSGVRLQKLEQQRQLFEKKQRRKRQEPLMVQANPDATLRHRRPRRGE 75
CrTBY1    ---------MDSDSDDERAAGYVPVLAASMPRAAAAAAVASPAAKQPSNVLQDGVSLYTN 51
CrTBY2    -----MAKLIKNVGASLRARTHDEDDTMMKQKGATGVFRNLAFADADDNLVSTSARAMAT 55
                                       :

OsTLP11   EEPPDESSAAALVMR---------ESCWTQLPPELLREVLAR------------------ 69
CeTub1    MSMNSMKDYPTFDNS---------LPFSISDNS---SVSVSMNTPLIP------------ 77
HsTubby   EQAPLVESYLSSSGS---------TSYQVQEADSLASVQLGATRPTAPASAKRTKAAATA 171
MmTULP2   ERFQSDSSWGLGVGSPFLQENVPQAHLPSGAHSALVTMSYVADGSGERAPLLSPRGAVYT 135
CrTBY1    ELFTDNNGDVLGEGP--------GLASPSGAAPGSARKGLAAKRQERLQG---------- 93
CrTBY2    SESTKKNNFFGGSQDNIASIDVTPRSRDAGNGASSWAHADLPTSASKRVG---------- 105
                ..

OsTLP11   ------------------------------------------------------------
CeTub1    -----------------TQDPIAQPRMQSMPR-------------------------Q 93
HsTubby   GGQGGAARKEKKGKHKGTSGPAALAEDKSEAQGPVQILT----------------VGQSD 215
MmTULP2   RGNGPAVRHHLCWLPDSSDSDVEEVTMEDIPVISRPPQTNLANLRRGWLASPGPGISQEE 195
CrTBY1    ----------------NAYTPNSLLKNASLRNPGAPASP-----------------GMRD 120
CrTBY2    ----------------STGSASTPVKSATFARTASAQKR-----------------AK 130


OsTLP11   -------------------------VEESEGWWPRRRDVVACAGVCRSWRGIVREIVRTP 104
CeTub1    QPQQVQ-----------------ESLISIGDYPD-NDINAKLSKVNLTSCVVSD--DED 132
HsTubby   HAQDAG-----------------ETAAGGGERPSGQDLRATMQRKGISSSMSFDEDEED 257
```

```
MmTULP2   KEEEVGSTDARVEDKTPSPDPDPDPTVNSDGDHGDLAPCKVEENTAQKNTETASGIGDED 255
CrTBY1    SPSSFR-----------------PSTLSQTGTATTVETTLVSPNRNSNNQGIAGGVGMVH 163
CrTBY2    NATAIQ-----------------EISAFEHEHAVMDEMSGSEDGERPAGLVSGGSAIGA 172


OsTLP11   EASGN------------------------------------------------LTFPISLKQP 119
CeTub1    EDKRSYADSPWNTDV------------VADRIPSE----VLPD--YNFIKNNLAKFVEDP 174
HsTubby   EEENSSSSSQLNSNTRPSSATSRKSVREAASAPSP----TAPEQPVDVEVQDLEEFALRP 313
MmTULP2   REKGEVTESTETNYAPVASKVLQGDDGDASNHNAWNMTCPQPRIPGPRLGEDMEAYVLLP 315
CrTBY1    GLRASYDPNEGQEEP------------VPSTRYVAPAAVPVARAVPQLDLSDMPAFLQQP 211
CrTBY2    TTSTTVIAVRSVARGP---------SITQQVSTSGSVRAWEEEVKRLIASGRHEDAVRWV 223


OsTLP11   GPRDAPMKCFIVRNRTTQTYYLYIGLTDALTDDGK------FLLAARKCRRTTCTEYLIS 173
CeTub1    AVEHCLYKCSITRQKSGVDKGMFPTYFLHLEEFDTDKRQKIFLLAARKRKKSTTANYLLS 234
HsTubby   APQGITIKCRITRDKKGMDRGMYPTYFLHLDREDG---KKVFLLAGRKRKKSKTSNYLIS 370
MmTULP2   APRDHMVQCRIVRNKHGMDKGMFPSYYLYLEAEDG---VAHFLLAGRKRKRSKTSNYLIS 372
CrTBY1    GPKNGPVQCVIVRDRG--SAKMYPRYSLFLEEGRR------FLLSARKRKKQTTSNYIIS 263
CrTBY2    APSDGIIRCTVRRVKN--FLGHTLAYQLFLDSGDT------FVLAARKRKKSKASNFVLS 275
          .      :* : * :              *           *:*:.** :: . :::::*


OsTLP11   LDMNDISKRTDSYVGKLRSNFLGTKFTIYDAHPPYAGDVISKGQSARVIGSNHLSPRIPA 233
CeTub1    TDPTNLSREGEGYCAKVRSNALGTQFTVYDSGQNPKKTTN----HAAIRQE--------- 281
HsTubby   VDPTDLSRGGDSYIGKLRSNLMGTKFTVYDNGVNPQKASSSTLESGTLRQE--------- 421
MmTULP2   LDPKDMSRNGSNFVGKVRSNVLGTKFTIFDNGVNPERSYWVP-DSARIREE--------- 422
CrTBY1    MDYEDLSRESGSFFGKVRANFVGTEFTVYDRGVKAGKKDAQG---DGQREE--------- 311
CrTBY2    TSQEDLGKDSDHCIAKLRANFVGTEYGLVSRTGGHISGSMDIDGGAQSGGK--LAPPAEP 333
           .  ::.:      .*:*:* :**:: : .                    .


OsTLP11   GNYPVSHISYELNVLGSRG-PRRMHCAMDSIPVSAIEQGGTAPTQTEFPLSYHESFTSIP 292
CeTub1    ----LAAVIYETNVLGFKG-PRKMTIVMPGIEPPTENR----------------PAVRCP 320
HsTubby   ----LAAVCYETNVLGFKG-PRKMSVIVPGMNMVHE----------------------RVS 455
MmTULP2   ----LGVVCYETNVLGFRG-PRKMTVILPGMDSRKQ----------------------RMK 456
CrTBY1    ----LGAVTYQYNVLGTRG-PRKMMAAIPGVDGSGR----------------------RM 344
CrTBY2    FSREEIAVHYKQTALTAKGGPRTMLVATPLPEVSWAPS-----------------AADGS 376
                 : *: ..*  :* ** *


OsTLP11   FFKSKSVRANNSTASLLTQNGSKLVLKNKSPRWHEHLQCWCLNFHGRVTVASVKNFQLVA 352
CeTub1    VRPIQDKHTLLERYRLND-LDSLKILSNKSPQWNDETQSYVLNFHGRVTQASVKNFQIIH 379
HsTubby   IRPRNEHETLLARWQNKN-TESIIELQNKTPVWNDDTQSYVLNFHGRVTQASVKNFQIIH 514
MmTULP2   VQPQNDQDSILSRVQKGA-GHGLLLLQNKAPSWSDESGAYVLNFHGRVTRASVKNFQIVH 515
CrTBY1    FNPSGDADTILERLKHRKGLEELVVMGNKPPRWNDELNAYCLNFNGRVTEASVKNFQLVS 404
CrTBY2    DSLANCLEAARRRELSPRMERQLCMLATRPPEWDPSLKAYTLDFHGRIRASSVKNFQLVH 436
                 :                : .:.* *     .: *:*:**:  :******::


OsTLP11   SDESNPTNQEHDDVILQFGKVGK--DMFTMDYRYPISAFQAFAICLSSFDTKIACE- 406
CeTub1    QSS-------PEYIVMQFGRISD--DEFTMDFRYPLSAVQAFGIAMTSFHGKLACE- 426
HsTubby   GND-------PDYIVMQFGRVAE--DVFTMDYNYPLCALQAFAIALSSFDSKLACE- 561
MmTULP2   PDE-------PDHLVLQFGRVAP--NIFTMDFRYPLCPLQAFAICLSSFDGKLACE- 562
CrTBY1    DDN-------HNHVILQFGKVGK--DTFTMDYQWPISAFQAFAICMSSFDNKLACE- 451
CrTBY2    WDHN--TDRKGSDLVLQFGKIDENTDDFALDFTYPLSLQKAFAIALASTDTKLCYAL 491
           .         . :::***::    : *::*: :*:.  :**.*.::* . *:.
```

B)

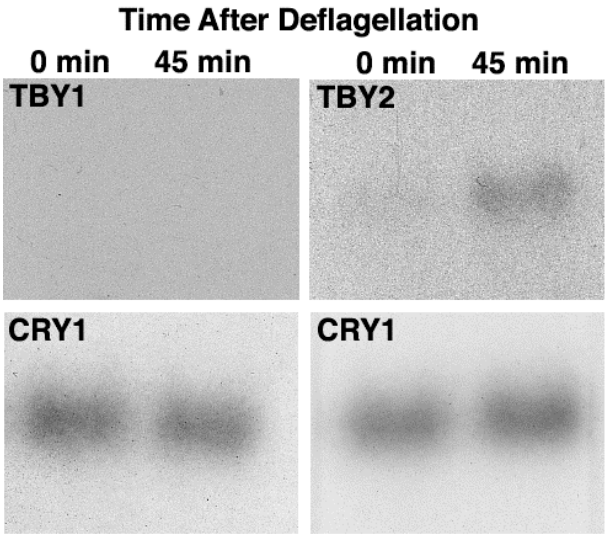
Time After Deflagellation
0 min
45 min
0 min
45 min
TBY1
TBY2
CRY1
CRY1

Table 2.2. Tubby genes with localization analysis and mutant phenotype data in several organisms.

Species	*Gene*	*Expression*	*Mutant Phenotypes*	*Relevant Work*
Mus musculus	*Tubby (TUB), Tubby-like protein 1, 2, and 3 (TULP1-3)*	Brain, eye, testes, other	Sterility, retinal degeneration, neurosensory defects, obesity, embryonic lethal	North *et al.,* 1996; Carrol *et al.,* 2004
Homo sapiens	*Tubby (TUB)/ Tubby-like protein 1, 2, and 3 (TULP1-3)*	Brain, gonads, eye, other	Retinal degeneration, risk factor for obesity	Carrol *et al.,* 2004; Shiri-Sverdlov *et al.,* 2006
Caenorhabditis elegans	*Tub-1*	Ciliated neurons	Chemosensation defects, fat storage defects	Mak *et al.,* 2005; Mukhopadhyay *et al.,* 2007
Arabidopsis thaliana	*Tubby-like protein 1-11 (TLP1-11)*	All tissues	TLP9 mutants are abscisic acid insensitve	Lai *et al.,* 2004; Yang *et al.,* 2008
Chlamydomonas reinhardtii	*Tubby 1 (TBY1), Tubby 2 (TBY2)*	Basal body region, unknown	N/A	Stolc *et al.,* 2005; This study.

Figure 2.7. *bop5-2* is null for TBY1. Western blot showing expression of the TBY1, TBY1-HA, and TBY1-GFP polypeptides in wild-type (*cc125)*, *bop5-2*, and *bop5-2::TBY1-GFP (3F12), bop5-2::TBY1-HA (E4A)*, *cc1691::TBY1-HA (B12),* and *cc1691::TBY1-GFP (3D4).* Also probed with OEE3 as a loading control. Note that the last three lanes are from a different blot than the first three lanes. The second blot shows wild-type, the TBY1-HA expressing strains and *bop5-2* probed with at antibody to HA to confirm HA expression (K. VanderWaal and J. Reck).

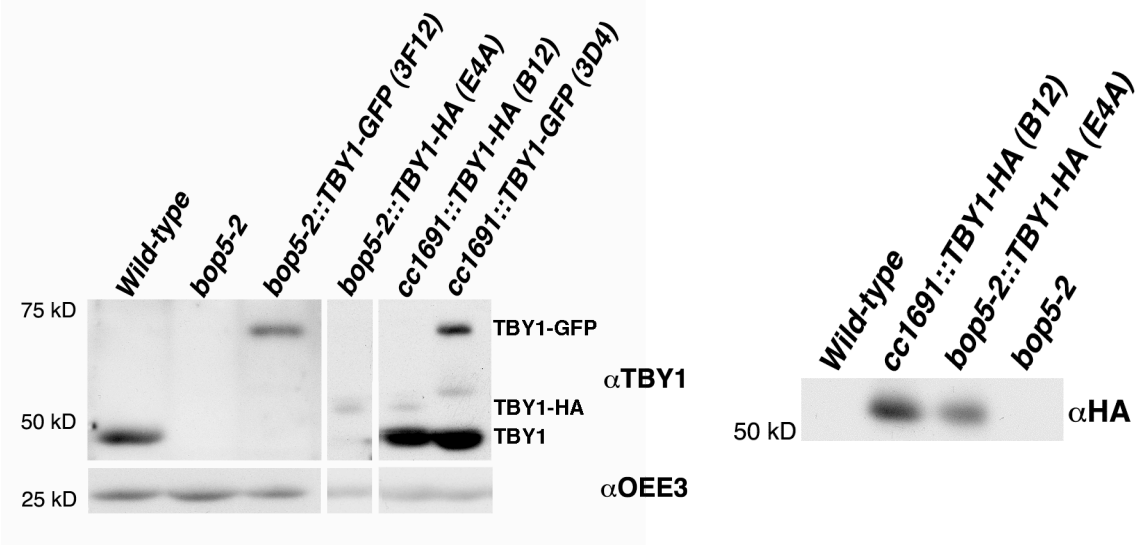

Table 2.3. Transformation of *bop5-2* and *cc1691* with both IC138 and TBY1 constructs. Strains were co-transformed with pSI103, which has a gene for paromomycin resistance, and plated on TAP plus paromycin. Colonies that grew on these plates were picked and screened by phase contrast microscopy for improved motility and/or by Western blot for restored protein. ND = not determined (K. VanderWaal)

Host strain	*Construct(s) Transformed*	*Transform-ations attempted (N)*	*Colonies screened (n)*	*Colonies with wild-type motility (n)*	*Colonies expressing transformed construct*
TBY1 Rescues:					
cc1691	*TBY1-HA*	1	105	105	7
cc1691	*TBY1-GFP*	1	83	83	1
bop5-2 6D	*TBY1-HA*	1	85	0	4
bop5-2	*TBY1-GFP*	2	308	0	2
bop5-2 6D	*TBY1-GFP*	1	26	0	0
bop5-2	*TBY1*	1	168	0	0
Double Rescues:					
bop5-2	*IC138, TBY1*	2	544	0	ND
bop5-2 6D	*IC138, TBY1-HA*	1	94	0	ND
bop5-2::IC138	*TBY1-HA*	3	970	0	ND
bop5-2::IC138	*TBY1*	1	404	0	ND
bop5-2::IC138	*TBY1-GFP*	3	624	0	ND
bop5-2::TBY1-GFP	*IC138*	3	112	0	ND

Figure 2.8. Cell fractionation of strains expressing *TBY1-GFP* or *PF2-GFP*. Whole cells expressing either *TBY1-GFP* or *PF2-GFP* were fractionated by pH shock and differential centrifugation into cell bodies, isolated flagella, and isolated axonemes. Samples of each fraction were loaded stoichiometrically onto a polyacrylamide gel, blotted, and probed with antibodies to GFP, OEE3, and IC69. The fractionation of PF2-GFP illustrates the pattern seen for a typical axonemal protein. The IC69 antibody labels an outer arm dynein intermediate chain and illustrates the enrichment of this protein in the flagellar and axonemal fractions. The OEE3 antibody labels a cell body protein and indicates the extent of cell body contamination in the flagellar and axonemal samples. The GFP signal for TBY1-GFP is a 60 min, exposure while PF2-GFP is a 30 min. exposure. (K. VanderWaal)

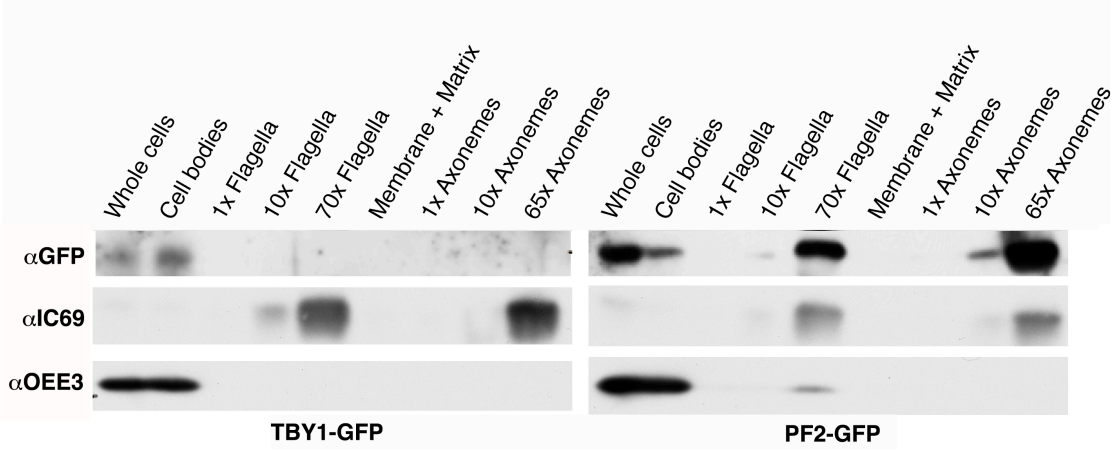

Figure 2.9. The TBY1 protein is localized in the anterior region of the cell near the basal bodies. (A) Maximum intensity Z-projections of TBY1-GFP and PF2-GFP signals in live, *bop5-2::TBY1-GFP (2F4)* and *pf2::PF2-GFP* cells, along with the corresponding DIC images. (B) DIC and immunofluorescence images of fixed wild-type (*cc125*) cells probed with the anti-TBY1 antibody, *cc1691::TBY1-GFP (3D4)* probed with anti-GFP antibody, and *cc1691::TBY1-HA (B12)* probed with anti-HA antibody. (C) DIC and fluorescence images of live TBY1-GFP cells at different stages of the cell cycle showing the location of the TBY1-GFP signal. Note abundant autofluorescence in the cell bodies of most cells compared to the brighter TBY1 signal. (K. VanderWaal).

A) TBY1-GFP and PF2-GFP signal in live, *bop5-2::TBY1-GFP (2F4)* and *pf2::PF2-GFP* cells

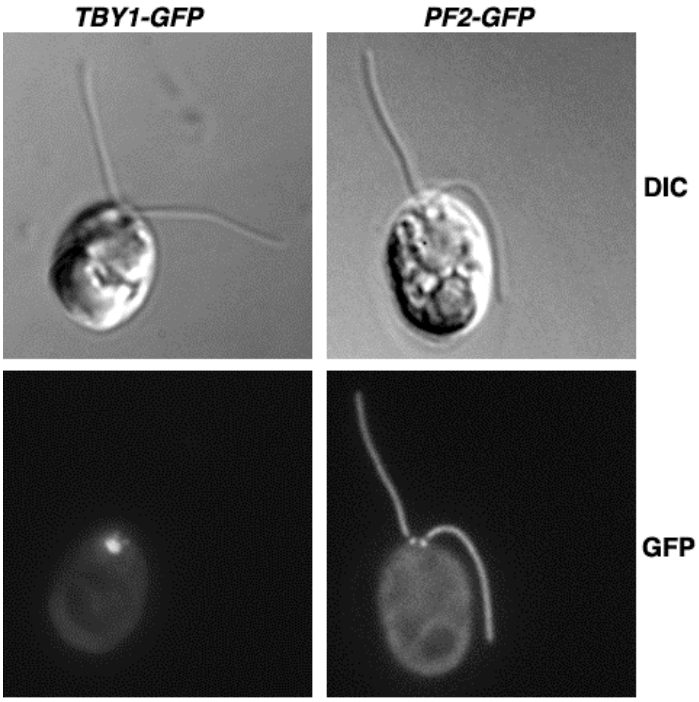

B) TBY1 signal in fixed, wild-type cells

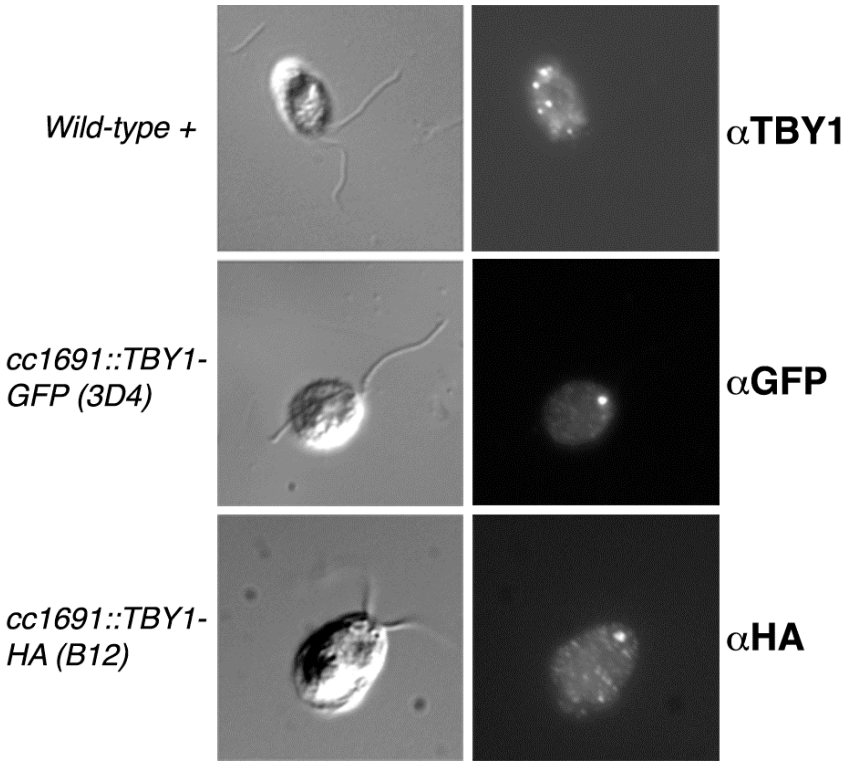

C) TBY1-GFP in different cell cycle stages in live, *bop5-2::TBY1-GFP (3F12)* cells

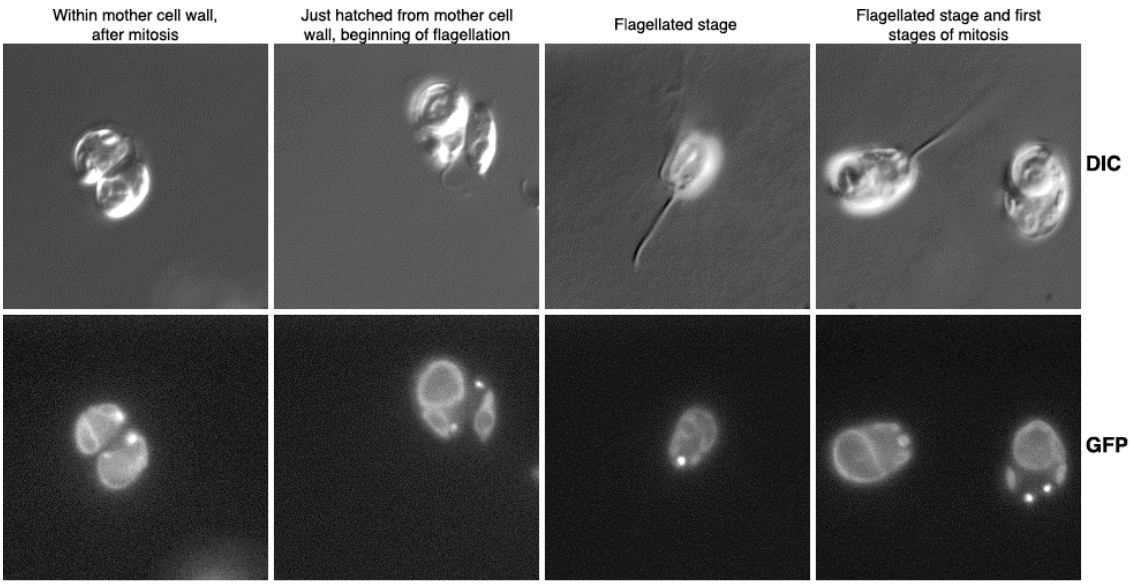

Figure 2.10. TBY1-GFP is observed in a ring shaped structure at the anterior end of the cell. (A) Images of the ring structure in *bop5-2::TBY1-GFP 3F12* cells. Images were taken of live cells; GFP signal at the anterior end of the cell corresponds to TBY1-GFP. (B) Illustration based on Merchant *et al.* (2007) showing various structures at the anterior of the cell. At the base of the two flagella are the two basal bodies connected by the distal and proximal striated fibers. The red line at the proximal end of the basal bodies illustrates where ε-tubulin is located (Dutcher *et al.,* 2002). Below the basal bodies is one of the two contractile vacuoles; the other one would be located directly underneath the one shown. The nucleus is shown below the contractile vacuole. (K. VanderWaal)

A)

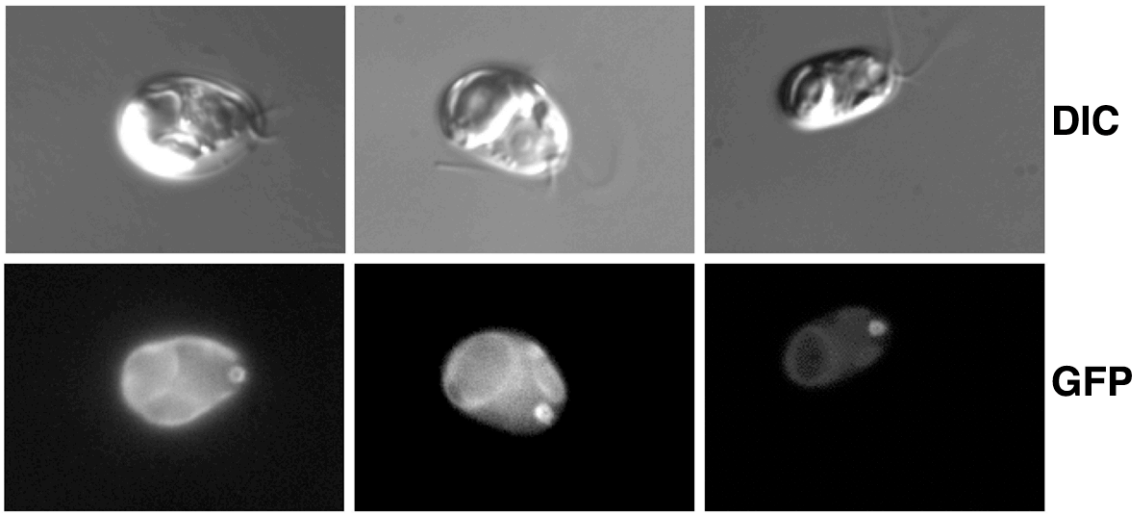

B)

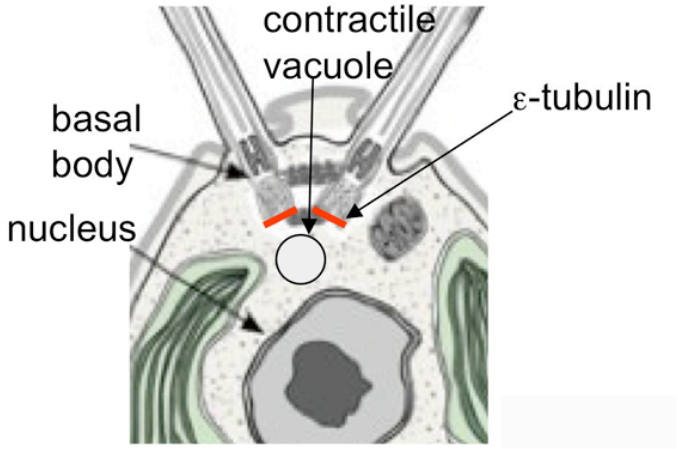

Figure 2.11. Images showing the distribution of TBY1-GFP and TBY1 relative to various cell organelles. (A) Images of live cells demonstrate that the TBY1 ring is located between the two contractile vacuoles. (B-D) Images of *bop5-2::TBY1-GFP (3F12)* fixed cells by immunofluorescence. (B) Localization of ε-tubulin (anti-ε-tubulin) and TBY1-GFP (anti-GFP) shows that the GFP signal is posterior to ε-tubulin signal. (C) Staining of the nucleus with DAPI shows that the anti-GFP signal is located anterior to the nucleus. (D) Staining of the nucleus with DAPI, the nuclear flagellar apparatus with anti-centrin antibody, and TBY1-GFP with anti-GFP antibody shows that the GFP signal is located within the centrin basket. (E) Localization of TBY1-GFP (3F12) and PF2-GFP in isolated, unfixed nucleo-flagellar apparatuses (NFAPs). (K. VanderWaal)

A) *bop5-2::TBY1-GFP (3F12)* in relation to vacuoles

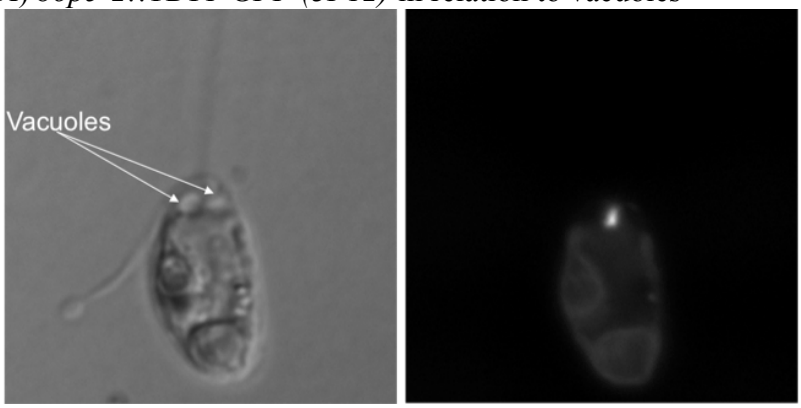

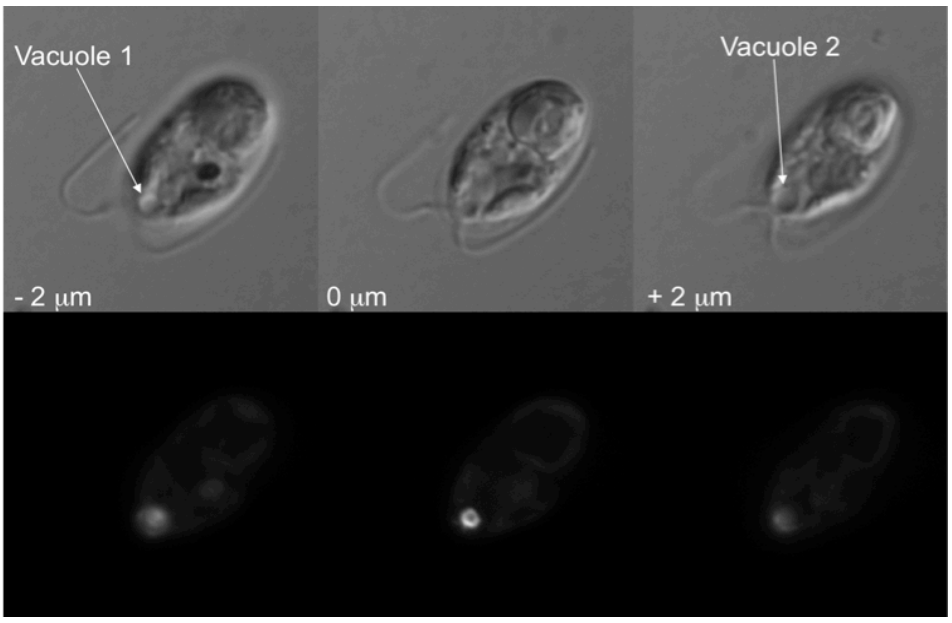

B) *bop5-2::TBY1-GFP (3F12)* in relation to ε-tubulin (labels posterior of basal bodies).

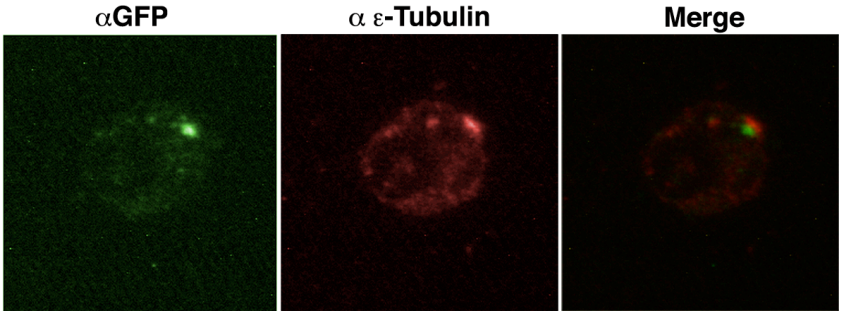

C) *bop5-2::TBY1-GFP (3F12)* in relation to DAPI (labels nucleus).

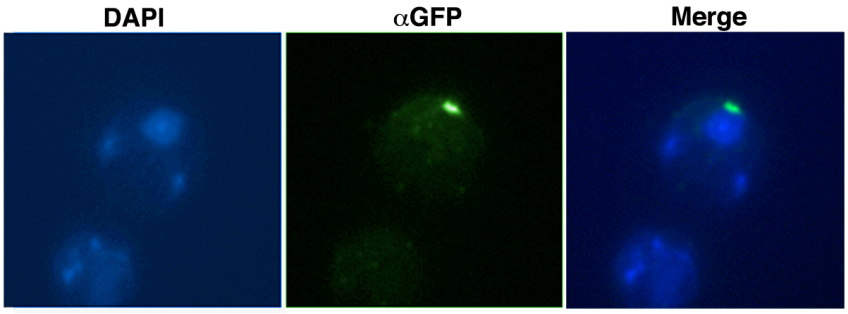

D) *bop5-2::TBY1-GFP (3F12)* in relation to centrin.

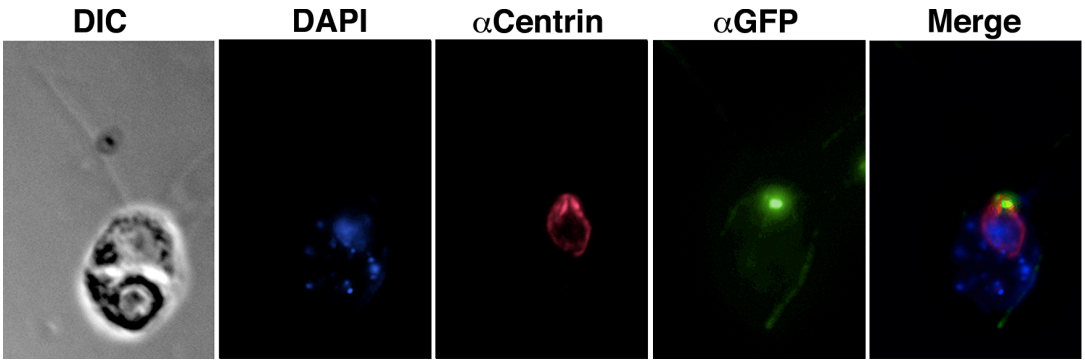

E) TBY1-GFP (3F12) and PF2-GFP in unfixed nucleo-flagellar apparatuses.

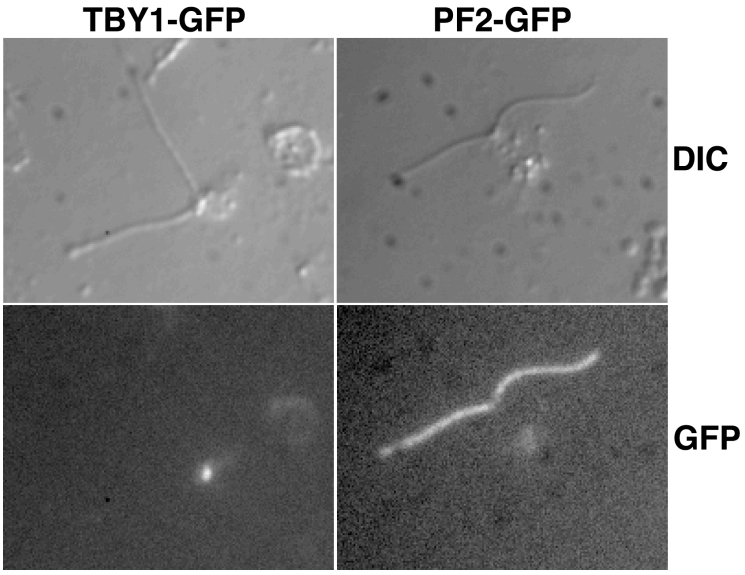

Figure 2.12. Changes in motility after transformation of *bop5-2* with IC138, *TBY1-HA* or *TBY1-GFP*. (A) Motility counts of various strains showing the percentage of cells swimming forwards, backwards, or spinning (n > 150 cells). (B) Motility counts excluding spinning cells in wild-type, *bop5-2 6D, bop5-2::TBY1-HA* and *bop5-2::TBY1-GFP strains* showing the percentage of cells swimming forwards versus backwards (n > 800 cells). (C) Images of cell tracks taken with 0.5 sec exposures of wild-type, *bop5-2 6D, bop5-2::TBY1-HA* and *bop5-2::TBY1-GFP* strains demonstrating the overall progression of individual cells within the population. (K. VanderWaal)

A)

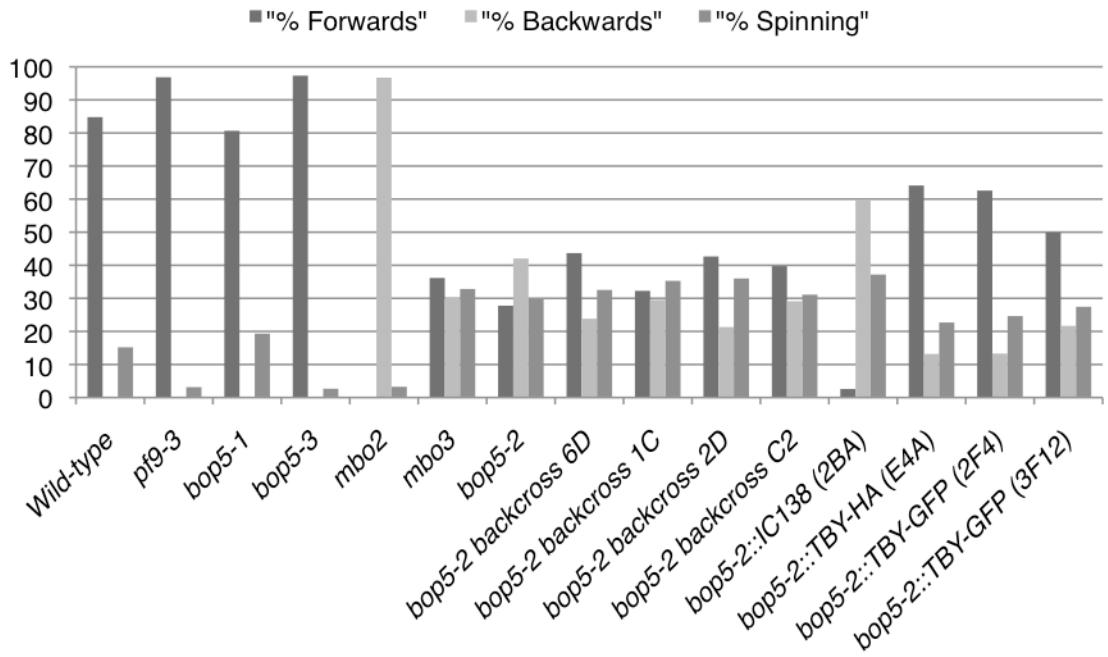

B)

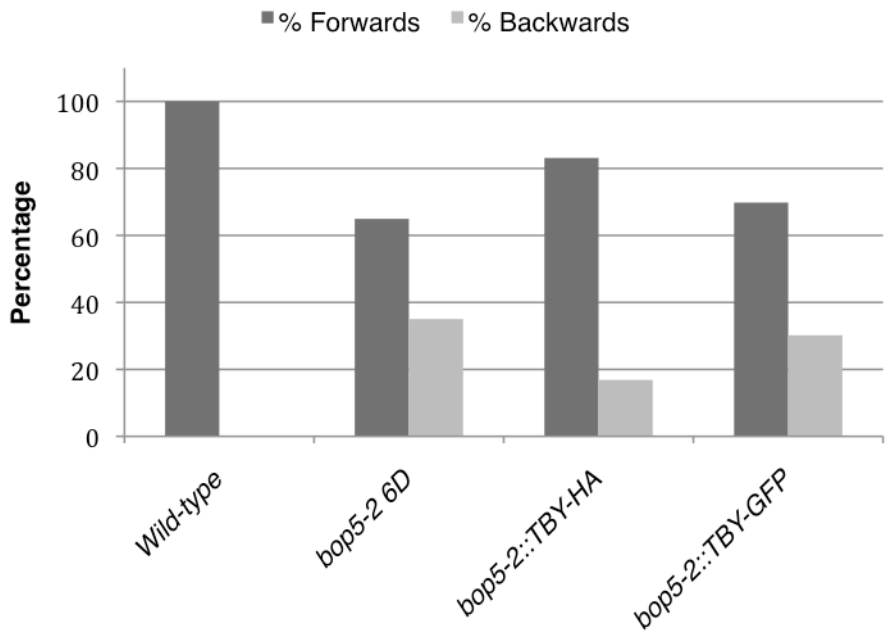
% Forwards
% Backwards
Percentage
100
80
60
40
20
0
Wild-type
bop5-2 6D
bop5-2::TBY-HA
bop5-2::TBY-GFP

C)

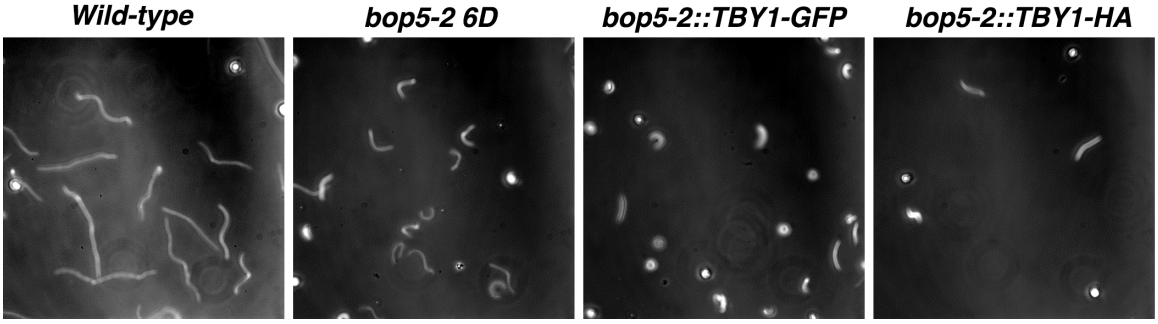
Wild-type
bop5-2 6D
bop5-2::TBY1-GFP
bop5-2::TBY1-HA

Figure 2.13. *bop5-2* strains fail to assemble MBO2 into the axoneme. Western blots of whole cell extracts (top) and isolated whole axonemes (bottom) from *bop5-2* and *mbo* related strains probed with antibodies to MBO2, IC69 (loading control), and OEE3 (cell body protein control). (K. VanderWaal)

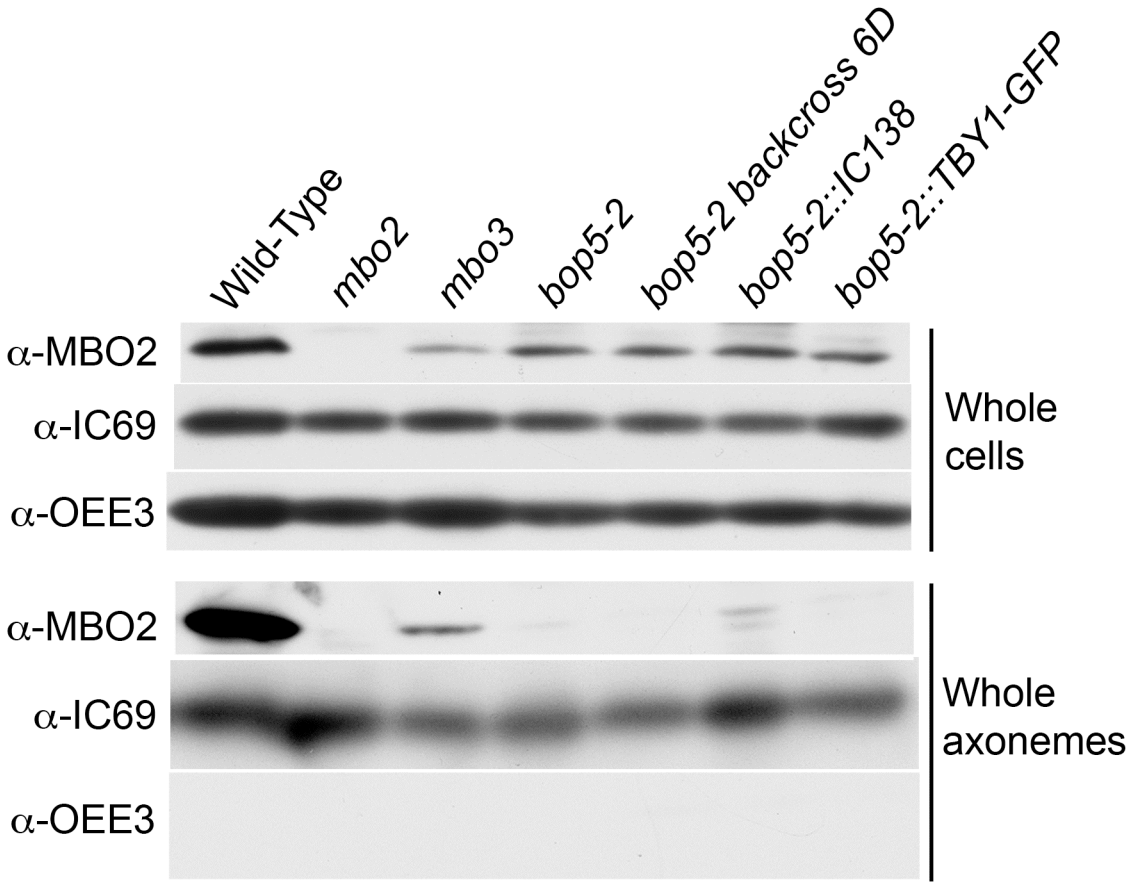

Figure 2.14. Electron micrographs showing cross-sections of *bop5-2* flagella. Doublets 1, 5, and 6 are labeled in each image. Beak structures are evident in doublet #1, but they are missing in both doublets #5 and 6. (E. O'Toole)

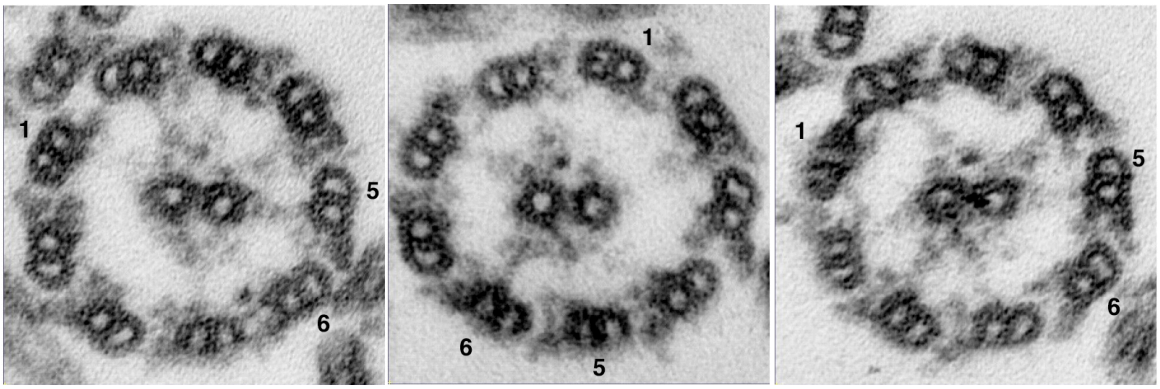

Table 2.4. Phenotypes of diploid strains containing *mbo3* and either *bop5-2* or *bop5-2::IC138* mutations. Mating type minus is dominant to mating type plus, so all diploid cells should only mate with a mating type plus strain, but also contain copies of both mating type alleles as detected by PCR. ND = Not Determined (K. VanderWaal)

Strain Name	*Mating type by mating type test*	*PCR band for mating type +/ -*	*Swimming phenotype*
mbo3	minus	No / Yes	Mix of backwards, spinning and slow forwards
bop5-2	plus	Yes / No	Mix of backwards, spinning and slow forwards
bop5-2::IC138	plus	Yes / No	Mix of backwards, spinning and slow forwards
mbo3 bop5-2 #2	minus	Yes / Yes	Fast forwards (not wild-type)
mbo3 bop5-2 #3	minus	Yes / Yes	Slow forwards
mbo3 bop5-2 #4	minus	Yes / Yes	Medium forwards
mbo3 bop5-2 #5	minus	Yes / Yes	Fast forwards (not wild-type)
mbo3 bop5-2::IC138 #1	minus	Yes / Yes	Slow forwards
mbo3 bop5-2: IC138 #3	minus	Yes / Yes	Slow forwards
mbo3 bop5-2::IC138 #6	minus	Yes / Yes	Slow forwards
mbo3 bop5-2::IC138 #9	ND	Yes / Yes	Slow forwards

Figure 2.15. BAC clones containing putative flagellar genes located near the *bop5-2* deletion. (A) Map of chromosome 12/scaffold 31 showing the BAC clones and flagellar related genes centered ~600 kB around *bop5-2* deletion (bases 550,136 – 1,300,015). Putative flagellar genes are shown in green with an arrowhead depicting the direction of transcription. Individual BACs are shown in pink and appear below the scaffold base numbers. (B) Table describing the putative flagellar genes and BACs shown in part A. (C) Table summarizing the transformations results for each BAC clone with respect to the number of transformation attempts and the number of colonies screened for rescue of the backwards swimming phenotype. (K. VanderWaal)

A)

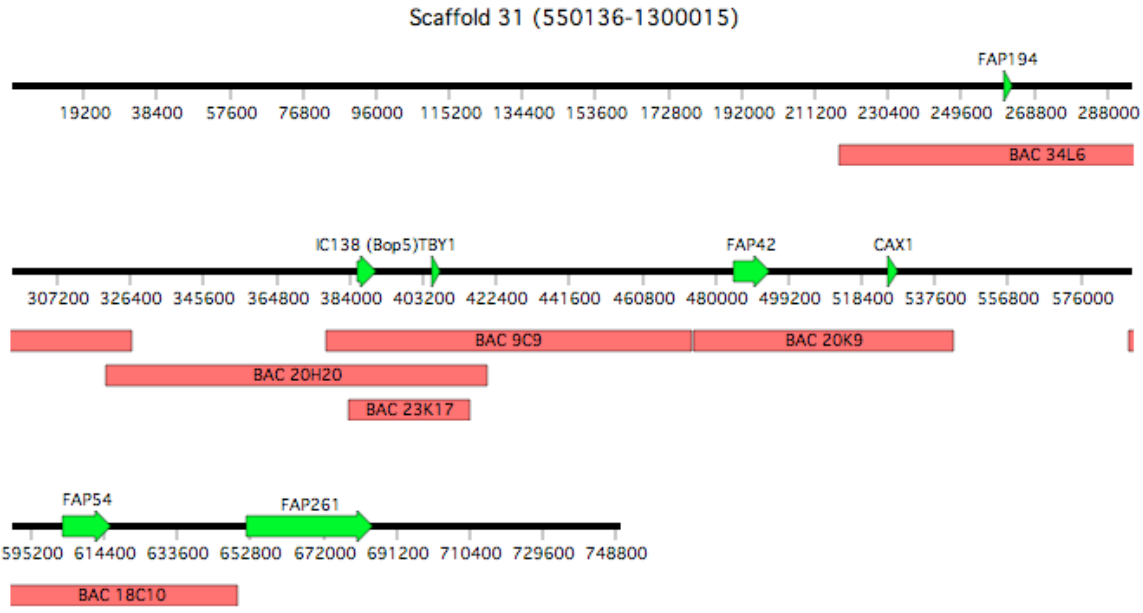

B)

Gene	*BAC covering gene*	*Found in flagellar proteome (Pazour, et al., 2005)*	*Possible Functions*
FAP194	34L6	Yes	Similar to axoneme central pair apparatus protein found in Rat
BOP5	20H20, 9C9, 23K17	Yes	Encodes IC138
TBY1	20H20, 9C9, 23K17	No	Encodes TBY1
FAP42	20K9	Yes	Similar to adenylate/guanylate kinases
CAX1	20K9	No	Putative $Ca^{2+/}H^{+}$ antiporter, related to fungi and plant $Ca^{2+/}H^{+}$ antiporters
FAP54	20K9	Yes	Also identified in the flagellar basal body proteome
FAP261	None	Yes	No close matches

C)

Strain transformed	*BAC transformed*	*Number of transformations*	*Number of colonies screened*
bop5-2	23K17	3	501
bop5-2	9C9	1	60
bop5-2	20H20	1	76
bop5-2	18C10	1	63
bop5-2	20K9	1	107
bop5-2	34L6	1	48

CHAPTER 3

bop5 mutations reveal new roles for the IC138 phosphoprotein in the regulation of flagellar motility and asymmetric waveforms

Modified from
VanderWaal, K.E., Yamamoto, R., Wakabayashi, K., Fox, L., Kamiya, R., Dutcher, S.K., Bayly, P.V., Sale, W.S. and Porter, M.E. (2009). *bop5* mutations reveal new roles for the IC138 phosphoprotein in the regulation of flagellar motility and asymmetric waveforms. *Molecular Biology of the Cell,* epub ahead of print.*

*Modifications are minor and include no semi-colons in the double mutants, a few slight changes to sentence structure and formatting.

Abbreviations:

BOP, bypass of paralysis
FAP, flagellar associated protein
HC, heavy chain
IC, intermediate chain
IDA, inner dynein arm
LC, light chain
MBO, move backwards only
MIA, modifier of inner arms
PF, paralyzed flagella

Footnote: Using the new nomenclature for dynein genes in *Chlamydomonas* (Hom *et al*., submitted), the IC138 subunit of the I1 inner arm dynein is encoded by the *DIC4* gene (previously known as the *BOP5* gene), and mutations in *DIC4* are designated *bop5* alleles.

3.1. INTRODUCTION

The axonemal dyneins are microtubule motors necessary for production of the elegant and sophisticated movement of cilia and flagella. Axonemal dyneins consist of two main classes: two or three-headed outer arm dyneins, which are responsible for generation of power and flagellar beat frequency (Brokaw and Kamiya, 1987), and multiple inner arm dyneins, which control the size and shape of the flagella bends (Porter and Sale, 2000; Smith and Yang, 2004; King and Kamiya, 2009). The inner dynein arms consist of more than seven different subspecies that are localized to specific regions within each 96 nm repeat (Mastronarde *et al*., 1992; Porter *et al*., 1996; Porter and Sale, 2000; Nicastro *et al*., 2006; Wirschell *et al*., 2007; Bui *et al*., 2008; Brokaw and Kamiya, 1987; Brokaw, 1994; Kamiya,. 2002; Yagi *et al*. 2009) Each inner arm dynein likely plays a unique role in the formation of the flagellar bend (Kamiya, 2002; Brokaw, 1994; 2009), but the specific function of each isoform is still unclear.

To begin to understand each inner arm dynein's role in motility, we have focused on one subspecies, known as I1 or *f* dynein (reviewed in Porter and Sale, 2000; Kamiya, 2002; Wirschell *et al*., 2007). I1 dynein is the most highly conserved and widely distributed inner arm dynein (Wickstead and Gull, 2007). The I1 complex is the only two-headed inner arm dynein, and it assembles as a tri-lobed structure near the base of radial spoke 1 (Figure 3.1). The two heads contain the motor domains of the two DHCs, 1α and 1β, and the base consists of the DHC tail domains, intermediate chains (IC97, IC138, and IC140), light chains (LC7a, LC7b, LC8, TcTex1, and Tctex2b) and FAP120. (Goodenough and Heuser, 1985a,b; Piperno *et al*., 1990; Smith and Sale, 1991, 1992; Porter *et al*., 1992; Myster *et al*., 1997, 1999; Harrison *et al*., 1998; Perrone *et al*., 1998, 2000; Yang and Sale, 1998; DiBella *et al*., 2004a,b; Hendrickson *et al*., 2004; Wirschell *et al*., 2009, Bower *et al.,* 2009; Ikeda *et al.,* 2009). A collection of mutations in the genes encoding different I1 subunits, which result in the assembly of partial I1 dynein complexes in the axoneme, has been useful in determining the locations of and interactions between different subunits of the complex. Likewise, these mutant strains have given us insights into the function of each subunit.

The first I1 mutant to be extensively studied was *pf9-3,* which affects the *DHC1* gene and is null for the 1α DHC subunit (Myster *et al*., 1997). Loss of the 1α DHC prevents the I1 complex from being assembled in the axoneme (Myster *et al*., 1997). Most mutations in the 1β DHC subunit (*ida2)* and IC140 (*ida7*) also block assembly of the I1 dynein (Yagi *et al*., 2009; Perrone *et al*., 1998, 2000). These mutant strains exhibit slow forward swimming velocities, reduced microtubule sliding, an inability to phototax, and abnormal flagellar waveforms (Perrone *et al*., 2000). Notably, transformation of the mutants with gene fragments sometimes results in the partial assembly of I1 dynein in the axoneme. For example, transformation with constructs encoding the N-terminal portions of the DHCs resulted in strains (*pf9::DHC1* and *ida2::DHC10*) that assemble all I1 subunits except the 1α or 1β motor domain and display increased swim speeds and phototaxis ability (Myster *et al*., 1999; Perrone *et al*., 2000). More recent studies have revealed the distinct functional capability of each motor domain in I1 dynein complex (Toba *et al*., 2011).

Another subunit thought to play a key role in the function of I1 dynein and control of flagellar bending is IC138. For example, *in vitro* studies revealed that changes in phosphorylation of IC138 correlates with changes in microtubule sliding velocities (Habermacher and Sale, 1997). In addition, analyses of the *mia* mutants, which cannot phototax and swim slowly, showed hyper-phosphorylation of IC138 in the axoneme (King and Dutcher 1997). These results suggested that IC138 is a regulatory phosphoprotein important for control of motility. The first *IC138* mutation, *bop5-1*, was isolated as a suppressor that could restore partial motility to the paralyzed flagellar mutant *pf10* (Dutcher et al., 1988). The *DIC4/BOP5* gene encodes IC138[1], and the *bop5-1* mutation produces a truncated protein whose activity supports the idea that IC138 is a key regulatory subunit (Hendrickson *et al*., 2004). When the full-length, wild-type *DIC4* gene is transformed into *bop5-1,* the motility and protein defects are rescued (Hendrickson *et al*., 2004). However, because *bop5-1* is not a true null, further analysis of IC138 function was limited.

The first IC138 null to be characterized in detail was the *bop5-2* strain (Bower *et al*., 2009). Analysis of *bop5-2* showed that IC138 is required for the assembly of four

subunits at the base of the I1 dynein: IC138, LC7b, IC97 and FAP120, which is named the IC138 sub-complex (Figure 3.1, and Bower *et al*., 2009). This study also showed that regulation of microtubule sliding velocities by the central pair/radial spoke phosphorylation pathway depends on the presence of the IC138 sub-complex (Bower *et al*., 2009; Wirschell *et al*., 2009). Similar to *bop5-1,* microtubule sliding defects in *bop5-2* and *bop5-2 pf17* were restored upon transformation with the wild-type *IC138* gene and reassembly of the IC138 sub-complex. However, because *bop5-2* has additional mutations, it was not possible to discern how the loss of IC138 affects flagellar motility and cell behavior (Bower *et al*., 2009).

In this study, we used the entire complement of *bop5* mutants affecting IC138: *bop5-1* through *bop5-6* (Hendrickson *et al*., 2004; Bower *et al*., 2009; Ikeda *et al*., 2009), to determine the specific roles of IC138 in regulating flagellar motility. Based on earlier studies of I1 dynein mutants, we postulated that assembly of IC138 would be required to control swimming speed, flagellar waveform, and phototaxis. We determined that while the I1 dynein is necessary for normal phototaxis, the IC138 sub-complex is not. In contrast, the loss of any subunit of the I1 complex is sufficient to impair cell reversal during the photoshock response. Also, we characterized the flagellar waveform of the *bop5-3* mutant and compared it to those previously described for wild-type and *ida3* (missing the entire I1) strains (Bayly *et al*., 2010) to determine how waveform might be affected by loss of the IC138 sub-complex. We observed that the *bop5-3* waveform is intermediate between wild-type and *ida3*. Mutations in I1 do not affect the maximum and minimum curvature of the waveform, but they do affect the sliding velocity and shear amplitude of the wave patterns during forward swimming. Thus, we propose that the IC138 IC/LC sub-complex is critical for control of microtubule sliding and flagellar waveform, but it is not required for phototaxis. Given the high degree of I1 dynein subunit conservation, these observations have important implications for the mechanisms by which IC/LC sub-complexes regulate dynein motor activity in many species.

3.2. MATERIALS AND METHODS

Strains, Culture Conditions, and Genetic Analyses

All strains discussed in this study are shown in Table 3.1. Strains were grown on Tris acetate phosphate (TAP) medium (Harris, 1989). For most assays, a pea-sized amount of cells was resuspended in minimal media lacking nitrogen (Harris, 1989) and rocked overnight under constant light to encourage maximum flagellar assembly and motility. Photobehaviors, especially phototaxis, were more robust in gametic versus vegetative cells. For flagellar waveform analysis, cells were cultured overnight in R media (Harris, 1989).

Rescued *bop5-3* strains were generated by co-transformation of *bop5-3* with the pSI103 plasmid containing the *aphVIII* gene (Sizova *et al*., 2001) and the pHX plasmid containing the gene that encodes IC138 (Hendrickson *et al*., 2004). Transformants that grew on TAP plus 10 μg/ml paromomycin were screened for rescue of the motility and protein defects. To generate double mutants, nonparental ditype tetrads were dissected and analyzed by light microscopy, PCR, and/or Western blots to identify the appropriate double mutant combination.

Polymerase Chain Reaction (PCR) Analyses

PCR and sequencing of the *IC138* gene in each mutant was performed using primers designed in the MacVector program (MacVector, Cary, NC) to the *IC138* genomic sequence (GenBank accession AY743342). The PCR products were sequenced directly (Genewiz, Inc.), and specific mutations or deletions were identified in *bop5-3, bop5-4, bop5-5,* and *bop5-6*.

Isolation of Axonemes, SDS-Polyacrylamide Gel Electrophoresis (PAGE) and Western Blot Analysis

To isolate axonemes, cells were subjected to pH shock, and then isolated flagella were demembranated by 0.1% NP-40 treatment as described previously (Witman, 1986). The resulting axonemes were resuspended in HMEEN (10 mM HEPES, pH 7.4, 5 mM

$MgSO_4$, 1 mM EGTA, 0.1 mM EDTA, 30 mM NaCl) with 0.1 μg / ml protease inhibitors (pepstatin, leupeptin, aprotinin) and 1 mM dithiothreitol (Bower *et al*., 2009).

Axoneme samples were run on 5-15% polyacrylamide gradient gels and transferred to Immobilon P (Millipore, Billerica, MA) as described previously (Bower *et al*., 2009). Antibodies were used as follows: IC138, 1:10,000 (Hendrickson *et al*., 2004); IC97, 1:10,000 (Wirschell *et al*., 2009); IC140, 1:10,000 (Yang and Sale, 1998); FAP120, 1:10,000 (Ikeda *et al*., 2009); IC69, 1:50,000 (Sigma-Aldrich). Signal was detected with alkaline-phosphatase conjugated secondary antibodies and the Tropix detection system (Bower *et al*., 2009).

Analysis of Swimming Speed and Motility Assays

To measure forward swimming velocity, gametic cells were viewed on an Axioscope (Carl Zeiss, Thornwood, NY) with 20x phase contrast optics and a halogen light source. Short (30 sec – 1 min) movies were recorded with a Rolera-MGi EM-CCD camera (Q-Imaging, Tucson, AZ), and velocities were calculated using MetaMorph software version 7.6.5.0 (Molecular Devices, Sunnyvale, CA), as described previously (Bower *et al*., 2009). All data are expressed as mean plus/minus standard deviations. F-tests and T-tests were used to determine the significance of differences between means. To assay motility in a population of cells, long (1 sec.) exposures were taken with the Rolera-MGi EM-CCD camera. Final images are cropped regions of the field of view that show several motile cells.

Microtubule Sliding Assays

Microtubule sliding velocity was determined using the methods developed by Okagaki and Kamiya (1986) with minor modifications (Howard *et al.,* 1994; Habermacher and Sale, 1996, 1997; Hendrickson *et al.,* 2004; Toba *et al*., 2011). Flagella were resuspended in buffer lacking protease inhibitors, demembranated with 0.5% Nonidet-P-40, and placed in perfusion chambers. Sliding was started by adding buffer with 1 mM ATP and 3 μg/ml subtilisin A type VIII protease (Sigma-Aldrich). Recordings of sliding were made on an Axiovert 35 microscope (Carl Zeiss, Thornwood,

NY) with dark field optics and a Silicon intensified camera (VE-1000; Dage-MTI, Michigan City, IN). The analog videos were digitized and velocity was determined manually on the flat computer screen by measuring displacement of microtubules calibrated with a stage micrometer. All data are expressed as mean plus/minus standard deviations, and F-tests and T-tests were used to determine the significance of differences between means.

Flagellar Waveform Analysis of forward swimming cells

Analysis of the flagellar waveform during forward swimming was done using *bop5-3; uni1* double mutant cells grown overnight in minimal media. The acquisition and analysis of flagella waveforms was conducted as described in Bayly *et al.* (2010). Briefly, 600 frame videos (350 frames per second, 2.88 ms shutter speed) were taken on a Zeiss Universal Microscope (Carl Zeiss, Thornwood, NY) at 100x phase contrast with a Dragonfly Express IEEE-1394b Digital Camera System and FlyCapture software (Point Grey Research, Scottsdale, AZ) and saved as avi files. Videos were analyzed using custom Matlab programs (The Mathworks, Natick, MA), which include correction of rigid-body motion, identification of flagellar point clouds, sorting the point clouds, fitting curves to the data, and characterization and statistical analysis of the final waveforms (Bayly *et al.,* 2010). To determine if a waveform parameter is dependent on flagellar length, SAS 9.2 software (SAS Institute, Inc., Cary, NC) was used to create a general linear model of the data with the strain as a class variable.

High speed movies of biflagellate cells were taken on an Axioscope (Carl Zeiss, Thornwood, NY) with 63x DIC optics and a halogen light source. Movies were recorded with a 1024 PCI high-speed camera (Motion Engineering Company, Inc., Indianapolis, IN) at 500 frames per second. To facilitate viewing the movies, ImageJ (NIH, Bathesda, MD) was used to compile every fourth frame into a QuickTime movie with a playback speed of 15-30 frames per second, depending on the strain. Movies of wild-type, *bop5-3* and *pf9-3* are shown in supplemental materials (Movies S1, S2, and S3).

Photoaccumulation, Phototaxis and Photoshock Assays

For photoaccumulation assays, gametic cells at a concentration of 2.5 x 10^6 cells/ml were transferred to 35 mm petri dishes, and dark adapted for 10 min. Cells were then exposed to a fluorescent light source located 30 cm away (2 W/m^2) for 10 min. Cell densities on both sides of the dish were determined at various time points and recorded by digital photography to determine relative photoaccumulation ability. Each strain was independently assayed at least three times or tested separately for phototaxis to confirm the results. For phototaxis, cells were dark adapted in red light before illumination by uni-directional blue-green light. The cell behavior was recorded and the angle between the light direction and the swimming direction of each cell was measured and pooled into 30˚ bins, as described previously (Okita *et al*., 2005). Where applicable, the direction of the movement relative to the light source is noted: positive if towards the light source, and negative if away from the light source.

To assay for the photoshock response, we noted if forward swimming cells exhibited any change in behavior upon brief exposure to bright light. Cell movement was recorded using phase contrast microscopy at 20x and a red filter. The cells were then briefly exposed to bright light using a GFP excitation filter on the epi-illuminescence port (λ = 450-500 nm). The position of each cell (n>30) before and after light exposure was traced and scored as no change, paused, changed in forward direction only, or reversed.

3.3. RESULTS

Molecular characterization of the mutations in bop5-3, bop5-4, bop5-5, and bop5-6

To determine the nature of the *bop5* mutations that lead to decreased *IC138* expression in the collection first described in Ikeda, *et al* (2009), the entire *IC138* gene in each strain was recovered by PCR and sequenced directly (Figure 3.2). In *bop5-3,* we were unable to amplify a small region at the 5' end of the gene, and no other mutations were found in the rest of the gene. This led to the conclusion that *bop5-3* has a deletion that removes most of the 5'UTR and the first four exons, but does not extend into the adjacent gene in the 5' direction. The deleted region is between 1500-2000 bp (data not shown). *bop5-4* contains a G to T mutation towards the end of the fourth exon that results in a premature stop codon (TAG) instead of a glutamic acid residue (GAG) (Figure 3.2). Another premature stop is created in *bop5-5,* from deletion of a single G that results in a frame-shift mutation and a stop codon at the end of the second exon (Figure 3.2). The last *bop5* allele, *bop5-6,* contains a single G to A mutation in the third intron (Figure 3.2). This mutation does not directly alter the predicted wild-type splice site, but sequence analysis of RT-PCR products indicates that this mutation results in multiple alternatively spliced transcripts (data not shown). Most of these transcripts contain premature stop codons and would likely not produce a functional protein. A small amount of normally spliced message is also present in *bop5-6,* which results in the expression of an IC138 polypeptide at lower levels than in wild-type (Ikeda *et al*., 2009 and Figure 3.3).

The various *bop5* mutations affect expression of *IC138* and assembly of several other I1 subunits into the axoneme. Figure 3.3 shows an immunoblot that summarizes these results. As previously described (Hendrickson *et al*., 2004; Bower *et al*., 2009, Ikeda *et al*., 2009), *bop5-1* assembles a truncated IC138 and no FAP120 into the axoneme. Assembly of IC97 is not significantly affected. Similar to *bop5-2,* the *bop5-3, bop5-4,* and *bop5-5* strains lack IC138, and do not assemble IC97 or FAP120 into the axoneme. *bop5-6* shows a reduction of IC138, IC97 and FAP120 expression in the axoneme. IC140 serves as a loading control, as it is an I1 component whose assembly is

not affected by *bop5* mutations (Bower *et al*., 2009, Ikeda *et al*., 2009). *bop5-3* transformed with a wild-type copy of the *IC138* gene shows restoration of all I1 subunits missing in the *bop5-3* mutant. Because *bop5* mutants still assemble the two I1 dynein HCs, IC140, and other LCs (Bower et al., 2009; Ikeda et al., 2009), these mutants provide a unique opportunity to study the role of IC/LC sub-complexes in the regulation of dynein motor activity.

Forward swim speeds and microtubule sliding velocities are defective in bop5 mutants

Many I1 mutants, such as *pf9, ida7,* and *ida2*, show defects in swimming, where the cells swim slowly, but smoothly, in a forward direction, which has led to the hypothesis that slow, smooth swimming is a hallmark of strains with defects in the I1 dynein complex (Myster *et al*., 1997; Perrone *et al*., 1998; 2000). Consistent with this hypothesis, the *bop5* strains, which are not complicated by second mutations, also display a slow, smooth swimming phenotype (Figure 3.4A). The *pf9-3* mutant swims most slowly (48.3 +/- 10.8 μm/s), whereas *bop5-1, bop5-3, bop5-4* and *bop5-6* all swim between 70 and 90 μm/s (73.8 +/- 12.7, 90.2 +/- 14.9, 77.1 +/- 11.2 μm/s, 78.5+/1 11.2 μm/s, respectively). Neither *bop5-2* nor *bop5-5* was analyzed in greater detail as they both contain additional mutations that affect motility (Bower *et al*., 2009 and unpublished results). Transformation of *bop5-3* with the wild-type *IC138* gene restores forward swim speeds to near wild-type velocities (see Figure 3.4A).

We also investigated the phenotype of a *bop5-3; pf10* double mutant, as the original *bop5-1* mutant, which encodes a truncated IC138 polypeptide, was initially isolated as a suppressor of *pf10* (Dutcher *et al*., 1998). Interestingly, the *bop5-3; pf10* double mutant, which lacks the IC138 sub-complex, also suppresses the *pf10* phenotype, as seen by tracking the forward motility of several cells in long exposure movies. Motility in the double mutants is not restored to wild-type levels, but the double mutant cells progress forwards more rapidly than *pf10* cells, which circle in place (Figure 3.4B).

Previous studies on I1 function showed that mutations in I1 subunits cause microtubule sliding defects (DiBella *et al.,* 2004, Hendrickson *et al.,* 2004, Wirschell *et al.,* 2009, Bower *et al.,* 2009; Toba *et al*., 2011). Specifically, both *bop5-1* and *bop5-2*

have reduced microtubule sliding velocities (Hendrickson *et al.,* 2004; Bower *et al.,* 2009). As expected, *bop5-3, bop5-4* and *bop5-6* also show decreases in microtubule sliding velocity, to about 75% of the wild-type rate and similar to that of the I1 mutant *ida2-6* (Figure 3.4C). Microtubule sliding velocities are restored to near wild-type rates in the *bop5-3* IC138 rescued strains (Figure 3.4C).

Analysis of bop5-3 waveforms identifies defects in shear amplitude, sliding velocities, and bend propagation

Because *bop5-1* results in the assembly of a truncated IC138, and *bop5-2* has other mutations that affect motility (Hendrickson *et al*., 2004; Bower *et al*., 2009), the *in vivo* motility phenotypes of an *IC138* null mutant have never been analyzed in significant detail. To investigate the *IC138* null phenotypes, we first looked at flagellar waveform of forward swimming cells. Because *bop5* mutants swim slowly but do not show a significant reduction in beat frequency (Table 3.2 and data not shown), and the *ida3* mutant, which lacks the entire I1 complex, has an altered waveform (Bayly *et al*., 2010), we hypothesized that *bop5-3* would also show changes in waveform. To better illustrate the parameters assayed, two individual waveform tracings from wild-type and *ida3* are highlighted (Figure 3.5A). The principal bend is the bend with higher curvature, meaning the radius of a circle approximating the curve is smaller, and the reverse bend is the one with lower curvature. Although the waveform tracings from wild-type and *ida3* have similar maximum and minimum curvatures, the two waveforms look different because the regions of high curvature are of different sizes. If the curvature was imposed by two circles, as shown in Figure 3.5A, the *ida3* flagellum would be wrapped around a shorter arc of each circle than the wild-type flagellum (Figure 3.5A). In other words, the bends (the regions of roughly constant, higher curvature) occur over smaller sections in *ida3* flagella compared to wild-type (Figure 3.5A). When the bends are shorter, the result is a narrower ("stunted") waveform, as in *ida3* compared to wild-type. Reducing the length of the bends reduces shear amplitude and shortens the stroke. This idea is also illustrated in the plots of the shear angle of each waveform, in which the regions of constant slope correspond to portions of the flagella with constant curvature. In the shear angle plots of

wild-type flagella, relatively long sections have either a constant negative or constant positive slope. These regions of constant-slope are shorter in shear angle plots for *ida3* flagella, so the curves have lower amplitude, and the distribution of shear angles is narrower in *bop5-3* flagella (Figure 3.5A).

The differences between *bop5-3, ida3,* and wild-type are evident in the traces of the overall waveform beat pattern (Figure 3.5B), where *bop5-3* waveforms are narrower than wild-type, but not as severely affected as *ida3*. These differences can also be seen in the supplemental movies (Suppl. movies S1-S3). To characterize the waveforms quantitatively, shear angle curves were plotted (Figure 3.5C), and various parameters of the curves were calculated, as described in Bayly *et al*. (2010). Qualitatively, wild-type exhibits larger oscillations in shear angle than *bop5-3,* and the *bop5-3* shear angle curves have larger oscillations than those of *ida3* (Figure 3.5C); the *bop5-3* and *ida3* graphs of shear angle distribution are narrower than wild-type. These oscillations in shear angle are represented quantitatively by the RMS (root-mean-square) shear amplitude. Wild-type values are higher than *bop5-3,* and *bop5-3* values are higher than *ida3* (0.68 +/- 0.05 rad, 0.58 +/- 0.05 rad, 0.52+/- 0.04 rad, respectively, $p < 0.05$, Table 3.2).

The sliding velocities in the principal and reverse bends (average minimum, or R, sliding velocity and average maximum, or P, sliding velocity) in *bop5-3* and *ida3* also differ significantly from their values in wild-type. These parameters describe the average minimum (or maximum) inter-doublet sliding velocity at each point over the middle 80% of the flagellar length. The minimal sliding velocity at a given point occurs as the reverse bend propagates past that point; the maximum sliding velocity at a point occurs as the principal bend propagates. Both the *bop5-3* and *ida3* display reduced sliding velocities in the reverse bend relative to wild-type, but the values for *bop5-3* and *ida3* are not significantly different from each other. The sliding velocity of the principal bend in *bop5-3* is significantly lower than in wild-type, but significantly higher than in *ida3* (Table 3.2). These reductions in the calculated microtubule sliding velocities are similar to the reductions measured in the *in vitro* sliding assays (Figure 3.4C).

The final parameter that exhibits differences between *bop5-3* and wild-type is the propagation speed of the reverse bend (Table 3.2). As this value is also dependent on

flagellar length, we compensated for minor variations in length by analyzing the ratio of the reverse propagation speed to the principal propagation speed. The values of this ratio in *bop5-3* and *ida3* are 15-20% lower than those of wild-type. These lower values result primarily from the lower propagation speed of the reverse bend, suggesting that the effective stroke is affected most strongly. Speed of bend propagation is closely related to (though not completely determined by) the speed of microtubule sliding, which is significantly less during the effective strokes of *bop5-3* and *ida3* (see previous paragraph and Discussion).

I1 dynein mutants exhibit defects in photoshock behavior

To further characterize the effect of the missing IC138 sub-complex, we compared the photoshock response in the I1 mutant strains to that of wild-type and other mutants (Table 3.3). Wild-type cells normally swim forwards using an asymmetric ciliary-type waveform, but abruptly halt upon sudden exposure to bright light and convert their waveforms to a more symmetric flagellar-type beat in response to elevated intracellular calcium. This results in a brief period (~0.5 sec) of backwards movement (photoshock), but then, as intracellular calcium levels drop, the cells switch back to the more asymmetric ciliary waveform and resume normal forwards motility (Witman, 1993, see Table 3.3, Figure 3.6). In contrast, mutant cells with defects in the flagellar membrane voltage activated calcium channel (*ppr2*) or mutant cells with defects in outer doublet beak structures (*mbo2*) do not alter their motility in response to sudden bright light (Matsuda *et al*., 1998; Fujiu *et al*., 2008; Segal *et al*., 1984; see Table 3.3).

All of the I1 mutants displayed an altered photoshock response, where the cells paused upon bright light exposure (suggesting that they detected the light stimulus), but the cells did not appear to swim backwards any significant distance (Figure 3.6 and Table 3.3). The *mia1* and *mia2* mutants, which exhibit altered IC138 phosphorylation (King and Dutcher, 1997) also did not appear to reverse during the photoshock response. Interestingly, backwards movement during photoshock can be observed in *bop5-3, bop5-1, pf9-3,* and *ida2-7* strains that have been rescued by transformation with genes encoding IC138, 1α HC, or 1β HC respectively (Table 3.3).

One possible interpretation is that cells with an altered I1 complex might not be capable of converting their waveforms to the more symmetric flagellar-type beat. However, previous analysis of an I1 mutant has shown that waveform conversions are possible (Brokaw and Kamiya, 1987). In addition, we constructed double mutants containing both *bop5-3* and *mbo2* mutations, and we observed vigorous backwards swimming when the double mutant cells were viewed with conventional light microscopy (Table 3.1). These results strongly suggest that cells lacking the IC138 sub-complex can alter their waveforms, but may not generate enough power to swim backwards efficiently during photoshock (see Discussion).

I1 null mutants, but not bop5 mutants, have impaired phototaxis

Because I1 mutants such as *pf9/ida1*, *ida2, ida3,* and *mia1* and *mia2* exhibit phototaxis defects (King and Dutcher, 1997; Okita *et al*., 2005), we assayed phototactic ability in the *bop5* mutants using both photo-accumulation and quantitative phototaxis assays (Table 3.4, Figure 3.7). As the phototaxis measurements showed similar results to the photo-accumulation assays (Table 3.4), phototaxis diagrams are only illustrated for a subset of the strains (Figure 3.7B). Wild-type mating-type plus (CC-125) and mating-type minus (CC-124) cells showed positive and negative taxis, as reported previously (Pazour *et al*., 1995; Okita *et al*., 2005). The phototactic sign (positive or negative) depends on the genetic background (*AGG1* or *agg1*) of each strain (Smyth and Ebersold, 1985; Iomini *et al*., 2006). As expected, the I1 DHC mutants (*pf9-3* and *ida2-7*) did not show significant phototaxis in either direction (Myster *et al*., 1999; Perrone *et al*., 2000). However, the DHC rescued strains (*pf9-3::DHC1* and *ida2-7::DHC10*) were able to phototax, although the strain with the full-length 1β DHC (*pf9-3::DHC1*) displayed more robust photo-accumulation than the strain with the full-length 1α DHC (*ida2-7::DHC10*) (Table 3.4).

The *mia1* and *mia2* mutants, which contain the entire I1 complex but exhibit hyper-phosphorylation of IC138, are not able to phototax, (King and Dutcher 1997; Okita *et al*., 2005). Surprisingly, all of the *bop5* mutant strains were able to phototax, in either the positive or negative direction, as well as wild-type (Figure 3.7, Table 3.4). Because

bop5 strains can phototax, but are missing the IC138 sub-complex, and *mia* strains cannot phototax, even though they have the entire I1 complement of proteins, we hypothesized that the hyper-phosphorylation of IC138 in *mia1* and *mia2* might cause the phototaxis defect in these strains (see Discussion). To test this hypothesis, we constructed double mutant strains containing *bop5-1, bop5-3* or *bop5-4* with either *mia1* or *mia2,* to see if loss of the IC138 sub-complex might suppress the *mia* phototaxis defects. Interestingly, the *bop5 mia* double mutants were not able to phototax, and their forward swimming velocities were very similar to those displayed by the single *mia* mutants (Table 3.4, Figure 3.7, data not shown).

3.4. DISCUSSION

The IC138 sub-complex is necessary for normal flagellar motility

Although the IC138 sub-complex is not required for the stability, targeting and/or docking of I1 dynein in the axoneme (Bower *et al*., 2009), the IC138 sub-complex is essential for control of the size and shape of the flagellar waveform during forward swimming. All four *bop5* mutant strains (*bop5-1, bop5-3, bop5-4, bop5-6)* show similar motility defects. This suggests not only that the IC138 sub-complex is necessary for normal flagellar motility, but that either a reduction in IC138 sub-complex subunits (*bop5-6*) or a truncated IC138 and missing LC7b (*bop5-1*) can also cause abnormal motility (Hendrickson *et al*., 2004; Bower *et al*., 2009). All four mutants swim at ~2/3 the velocity of wild-type strains (Figure 3.4A). The reduction in swimming velocity is caused by altered and inefficient flagellar waveforms, not reduced beat frequency, similar to other I1 mutants (Brokaw and Kamiya, 1987; Perrone *et al*., 2000; Myster *et al*., 1997, 1999; Bayly *et al*., 2010). The reduced swim speeds are further correlated with reduced microtubule sliding velocities in *bop5* axonemes (Figure 3.4C). In addition, the *bop5* mutations partially suppress the motility defects seen in the *pf10* mutant (Figure 3.4B). These observations suggest that the IC138 sub-complex and the protein product encoded by the *PF10* gene interact directly or indirectly to regulate motility. Further insight into this interaction will require identification and localization of the *PF10* gene product.

Loss of the IC138 sub-complex changes the shape and amplitude of the flagellar waveform

Comparisons of waveform parameters between wild-type, *bop5-3,* and *ida3* mutants have provided new insights into the role of both the I1 dynein and the IC138 sub-complex in controlling motility. First, the overall distances between principle and reverse curvature extremes are approximately equal in all three strains (Table 3.2, Figure 3.5B). Strains lacking the IC138 sub-complex or the entire I1 dynein are still able to generate bends with curvatures similar to wild-type. This suggests that the net forces bending the flagella are similar to those in wild-type; i.e., that the loss of the I1 dynein or IC138 sub-

complex does not dramatically affect the total dynein force summed over the length of the flagellum.

In contrast, the calculated microtubule sliding velocities in mutants lacking I1 or the IC138 sub-complex significantly differ from the sliding velocities in wild-type flagella (Table 3.2). Moreover, calculated sliding velocity and shear amplitude are affected more severely in *ida3* than in *bop5-3* flagella, suggesting that the I1 dynein contributes to control of microtubule sliding and shear, even in the absence of the IC138 sub-complex (Table 3.2). Consistent with the calculated reduction in waveform sliding velocity, direct measurement in isolated axonemes also reveals reductions in the microtubule sliding velocity when the IC138 sub-complex fails to assemble (Figure 3.4C). This reduction in sliding velocity suggests that even if the total force summed along the length of the flagellum is similar to the corresponding cumulative force in wild-type, the local force generated by dyneins at any one point on the flagellum is reduced in I1 mutants.

If dynein force generation is reduced at any one point, but similar overall, we wondered how dynein force generation is being altered in the I1 mutants. The spatial distribution of dynein activity must be different; this affects the overall shape of the mutant waveforms, as seen by the reduction in shear amplitude (Table 3.2). It is clear that *ida3* and *bop5-3* flagella exhibit shorter regions of constant curvature than wild-type. Once again, the effect is most severe in *ida3,* and intermediate in *bop5-3*. This may mean that fewer dynein cross-bridges are active per unit length of the flagellum than in wild-type, or alternatively, that the mechanisms that coordinate the selective activation and inactivation of different dyneins during bending are disrupted in the I1 mutants. The latter is consistent with the notion that I1 dynein plays a role in the local inhibition of sliding driven by other dyneins (Porter et al., 1992; Smith, 2002; Kotani *et al*., 2007; Toba *et al*. 2011). Moreover, multiple connections between I1 dynein and other inner and outer arm dyneins have recently been observed by cryoelectron tomography of isolated axonemes (Nicastro et al., 2006; Bui et al., 2008; Heuser et al., 2009).

Another parameter that differs significantly between wild-type and the I1 mutants is the ratio of propagation speeds. This ratio represents the speed of the reverse bend

compared to the speed of the principal bend and reveals whether the dyneins in one type of bend are activated/inactivated differently than in another type of bend. The ratio of propagation speed is reduced more severely in *ida3* flagella than *bop5-3* flagella, but both ratios are lower than the ratio for wild-type flagella. The reduction is caused by the reduced speed of the reverse bend (see Table 3.2). One possible explanation is that dyneins are not being properly inactivated during the effective stroke. The lack of inactivation may limit curve progression, which could slow down the overall speed of the bend. Both the reduction of shear amplitude and reverse bend propagation speed in *bop5* mutants leads to the hypothesis that dyneins are not being properly activated and inactivated temporally and spatially along the flagella, which is consistent with the model that the IC138 sub-complex is important in regulating shape of the flagellar bend (Bower *et al*., 2009; Hendrickson *et al*., 2004). The defects in waveform also explain the slow swimming phenotype seen in both *bop5* and other I1 mutants.

The IC138 sub-complex is necessary for an efficient photophobic response

All I1 mutants showed a similar defect in the photoshock response: they paused, but did not reverse (Figure 3.6, Table 3.3). This includes the *mia* mutants, which have altered phosphorylated IC138 levels, and *bop5-1,* which is only missing part of IC138, LC7b, and FAP120 (Table 3.3). The defects in the photoshock response are partially restored in the rescued strains. Interestingly, in mutant cells missing the 1α motor domain, the photoshock response is more effectively restored compared to mutants lacking only the 1β motor domain (Table 3.3). These results suggest that the 1β motor domain is more important in regulating the photoshock response. This hypothesis is in line with recent work that suggests that the 1β HC is a more effective motor that the 1α HC (Toba *et al*., 2011).

The basis of the "no reversal" phenotype is not well understood, but it is consistent with the phenotype seen in other dynein mutants (Kamiya and Okamoto, 1985; King and Kamiya, 2009). One hypothesis is the cells may not be able to generate a backwards, more symmetric, flagellar-type waveform without assembly of I1 dynein. However, *bop5-3 mbo2* mutant cells swim backwards efficiently (Table 3.3), and

waveform conversion has been detected in the I1 mutant, *ida98*, now known as *ida1-1* (Brokaw and Kamiya, 1987), and so this seems very unlikely. It is more probable that although *bop5* cells can switch their waveforms, these waveforms do not generate enough power to result in the net backwards movement of the cell body during the brief time period (~0.5 sec) of the photoshock response. Whether waveform conversion in wild-type cells is modulated by phosphorylation of the IC138 subcomplex would however be an interesting avenue for future study.

The IC138 sub-complex is not required for phototaxis

Phototaxis is a very sensitive measure of the coordination and precise control of bending for each flagellum in *Chlamydomonas* (Witman 1993). Moreover, I1 mutant cells also display defects in phototaxis when measured using simple photo-accumulation assays (King and Dutcher, 1997) or more quantitative phototaxis measurements (Okita *et al*., 2005). We have confirmed these observations using the I1 DHC mutants (Table 3.4; Myster *et al*., 1999; Perrone *et al*., 2000). Secondly, assembly of only one of the two motor head domains is sufficient to restore phototaxis ability, as the loss of either the 1α or 1β motor domain does not impair phototaxis (Table 3.4; Myster *et al*., 1999; Perrone *et al*., 2000). Cells missing the 1α motor domain show better phototaxis than cells lacking the 1β motor domain (see Table 3.4). These results correlate with recent observations showing that the 1β dynein has higher motor activity than the 1α dynein (Toba *et al*., 2011). Although the I1 motor domain mutants and outer arm mutants (*pf28)* can each undergo phototaxis, double mutant cells missing both the outer arms and an I1 motor domain cannot (Table 3.4). This suggests a functional interaction between the motor domains in I1 dynein and the outer dynein arms.

Because nearly all of the *bop5* mutant strains can phototax, we conclude that the IC138 sub-complex is not absolutely required for phototaxis (Table 3.4). These observations suggest that the remaining subunits of the I1 complex must play an essential role in phototaxis, even in the absence of the IC138 sub-complex. However, the *bop5; mia* double mutant strains are all defective in phototaxis (Table 3.4, Figure 3.7). This is a significant observation, because it has been assumed that phototaxis defects in the *mia*

mutants were primarily the result of hyper-phosphorylation of IC138, leading to inhibition of I1 dynein. Because the rest of the I1 dynein is present, but the IC138 sub-complex is missing in the double mutants, we postulate that defects in other, unknown axonemal proteins may be the real cause of the phototaxis defects observed in the *mia* mutants.

The C-terminal region of IC138 plays a critical role in I1 dynein function

The motility defects of the *bop5-1* (truncated IC138) mutant are very similar to those of the *bop5* null strains. The forward swimming velocities of *bop5-1, bop5-3, bop5-4* and *bop5-6* are ~80 μm/sec, which suggests that their waveform parameters may be very similar (Figure 3.4A). The *bop5-1* strain also displays a similar defect in the photoshock response (Table 3.3). These results indicate that the C-terminal region of IC138, which binds LC7b and possibly FAP120, plays a critical role in I1 dynein function (Hendrickson *et al*., 2004; Ikeda *et al*., 2009).

Our study of the *bop5* mutant alleles provides new insights into the function of the IC138 sub-complex. Loss of the IC138 sub-complex has several effects *in vivo*: reduced swimming velocities, altered waveforms, and inefficient reversal responses during photoshock. Microtubule sliding velocities are reduced both *in vivo* and during sliding disintegration *in vitro*. The net result is that the amplitude of the flagellar waveform is reduced: *bop5* cells are less efficient at moving forwards during normal motility and less effective at moving backwards during photoshock. However, contrary to expectation, loss of the IC138 sub-complex does not result in phototaxis defects. More work is needed to determine exactly how the I1 dynein contributes to control of phototaxis without the IC138 sub-complex. Nonetheless, evidence presented here demonstrates that the IC138 sub-complex plays an important role in controlling both the shape of the flagellar waveform and the response of the cell to environmental stimuli. Given the high degree of conservation of I1 dynein subunits (Wickstead and Gull, 2007), the IC138 sub-complex is likely to play a critical role in regulating flagellar motility in many species. In addition, the *bop5* mutants demonstrate that an IC/LC complex can modulate dynein motor activity independent of any effects on complex stability and/or cargo binding.

3.5. TABLES AND FIGURES

Table 3.1. Strains used in this study.

Strain (CC #)	*Motility*	*Axonemal Phenotype*	*Original Study*
Control strains			
Wild-type *mt+ (CC-125)*	Fast forwards	Wild-type	
Wild-type *mt– (CC-124)*	Fast forwards	Wild-type	
ppr2	Slow forwards, no photoshock response	Defective CAV2 channel	Fujiu *et al*., 2009
mia1 (CC-4265)	Slow forwards, phototaxis defect	hyperphosphorylation of IC138, missing Mia1p	King and Dutcher, 1997
mia2 (CC-4266)	Slow forwards, phototaxis defect	Hyperphosphorylation of IC138, missing Mia2p	King and Dutcher, 1997
mbo2 (CC-3664)	Backwards swimming	Missing beak proteins, MBO2	Segal *et al*., 1984 Tam and Lefebvre, 2002
pf10 (CC-3666)	Spins in circles	unknown	Dutcher *et al*., 1988
uni1-2 (CC-2507)	Spins in circles	Uni-flagellate	Huang *et al*., 1982
I1 DHC mutants			
pf9-3 (CC-3913)	Slow forwards	Missing I1 dynein	Myster *et al*, 1997
pf9-3::DHC1-G41a (CC-3920)	Faster forwards	Missing 1α HC motor domain	Myster *et al*. 1999
pf28 pf9-2::DHC1 G4 (CC-3917)	Slow forwards	Missing outer arms, 1α HC motor domain	Myster *et al*., 1999
pf28 pf9-2 E8 (CC-3903)	Spins in circles	Missing outer arms, I1 dynein, full-length flagella	Porter *et al*., 1992
ida2-7 (CC-3923)	Slow forwards	Missing I1 dynein	Perrone *et al*., 2000
ida2-7::DHC10	Faster forwards	Missing 1β HC motor domain	Perrone *et al*., 2000
pf28 ida2-7::DHC10 (CC-4079)	Slow forwards	Missing outer arms, 1β motor domain	Perrone *et al*., 2000
IC138 mutants			
bop5-1 (CC-4080)	Slow forwards	Truncated IC138, missing LC7b, FAP120	Dutcher *et al*., 1988 Hendrickson *et al*., 2004; Ikeda *et al*., 2009

bop5-2 (CC-4284)	Mixed motility	Missing IC138 sub-complex, MBO2	Bower *et al*., 2009
bop5-3	Slow forwards	Missing IC138 sub-complex	Ikeda *et al*., 2009
bop5-4	Slow forwards	Missing IC138 sub-complex	Ikeda *et al*., 2009
bop5-5	Slow forwards	Missing IC138 sub-complex	Ikeda *et al*., 2009
bop5-6	Slow forwards	Reduced IC138 sub-complex	Ikeda *et al*., 2009
bop5-1::IC138 (CC-4081)	Fast forwards	Wild-type	Hendrickson *et al*., 2004
bop5-2::IC138 (CC-4285)	Mostly backwards	Missing MBO2	Bower *et al*., 2009
bop5-3::IC138 2D1	Fast forwards	Wild-type	This study
bop5-3::IC138 2E1	Fast forwards	Wild-type	This study

Double mutants			
pf10 bop5-3	Slow forwards	Missing IC138 sub-complex	This study
mbo2 bop5-3	Slow backwards	Missing IC138 sub-complex, MBO2p	This study
uni1-2 bop5-3	Uniflagellate, spin	Missing IC138 sub-complex	This study
mia1 bop5-1	Slow forwards	Missing IC138 sub-complex, Mia1p	This study
mia2 bop5-3	Slow forwards	Missing IC138 sub-complex, Mia2p	This study
mia1 bop5-4	Slow forwards	Missing IC138 sub-complex, Mia1p	This study

Figure 3.1. Diagrammatic representation of I1 dynein sub-structure in the axoneme. This diagram illustrates the structure of the I1 dynein and the proposed interactions between I1 subunits based on published previously work (Myster *et al*., 1998; Perrone *et al*., 2000; Porter and Sale, 2000, Ikeda *et al*., 2009, Wirschell *et al*., 2009, modified from Bower *et al*., 2009). (K. VanderWaal)

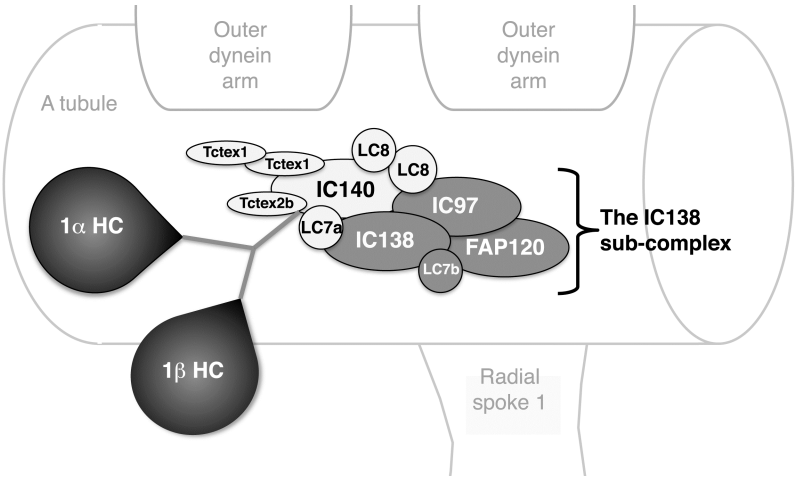

Figure 3.2. Schematic of the *bop5* mutations. The molecular defects in each *bop5* mutant are shown in this intron-exon diagram of the *IC138* gene. *Bop5-1* and *bop5-2* were characterized in Hendrickson *et al*., 2004 and Bower *et al*., 2009. *Bop5-3, 4, 5, 6* mutations were identified by PCR and sequencing of the *IC138* gene. *Bop5-3* has a deletion affecting the 5' end of the gene; *bop5-4* and *bop5-5* have mutations that result in premature stops; and *bop5-6* has a mutation in an intron that results in alternative splicing. (K. VanderWaal)

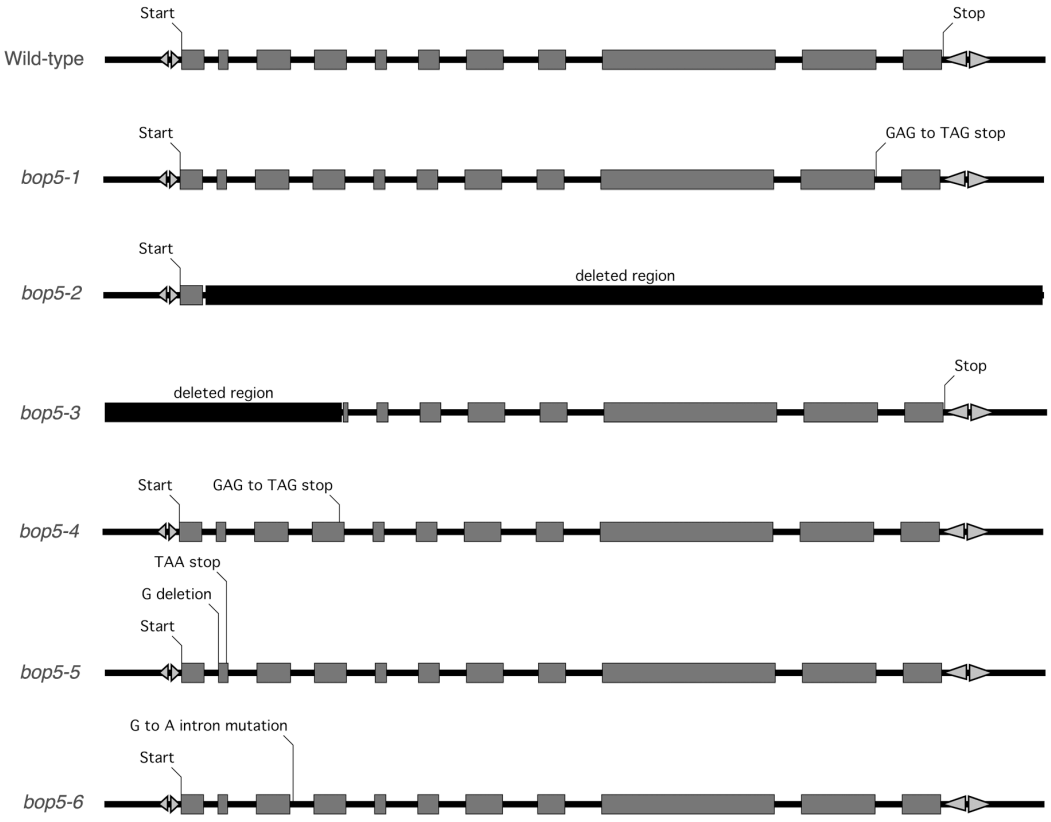

Figure 3.3. Assembly of I1 dynein subunits in *bop5* mutant axonemes. Western blots of isolated axonemes were probed with antibodies to I1 dynein subunits. IC140 serves as a loading control, as it is not affected in any *bop5* mutant. IC138 is shifted in *bop5-1* and missing in *bop5-2* through *bop5-5*. FAP120 is missing in all *bop5* strains. IC138, IC97, and FAP120 are reduced in *bop5-6*. Note the reassembly of all I1 subunits in *bop5-3* strains that had been transformed with a wild-type copy of the *IC138* gene (2D1 and 2E1). (K. VanderWaal)

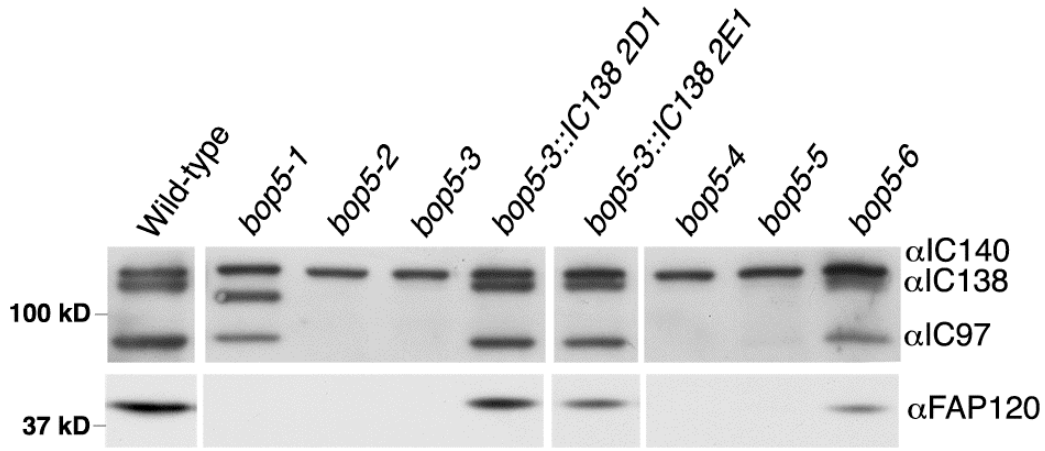

Figure 3.4. Forward swimming behavior and microtubule sliding in *bop5* mutants. (A) Graph showing the average forward swimming velocities for wild-type, *pf9-3, bop5-1, bop5-3, bop5-4, bop5-6,* and the *bop5-3* rescued strains. Approximately 190-552 cells were measured for each strain. The swimming velocities of the IC138 rescued strains are significantly faster than the *bop5* mutants ($p < 0.005$), not significantly different from one another ($p = 0.832$), and only slightly slower than wild-type ($p < 0.005$). (B) Long exposure (1 sec) images showing the forward progression of wild-type*, bop5-3, pf10,* and *bop5-3 pf10* cells. (C) Isolated axonemes from wild-type and mutant strains were treated with protease and ATP, and the velocities of microtubule sliding were measuring during axoneme disintegration *in vitro* ($n > 16$ axonemes per strain). The sliding velocities of the *bop5* strains are not significantly different from another or *ida2-6*, with the exception that *bop5-4* is slightly faster than *bop5-1* ($p < 0.005$). The sliding velocities of the IC138 rescued strains are significantly faster than all of the *bop5* mutants, including *bop5-3* ($p < 0.005$), but not significantly different from one another or wild-type. (K. VanderWaal, L. Fox).

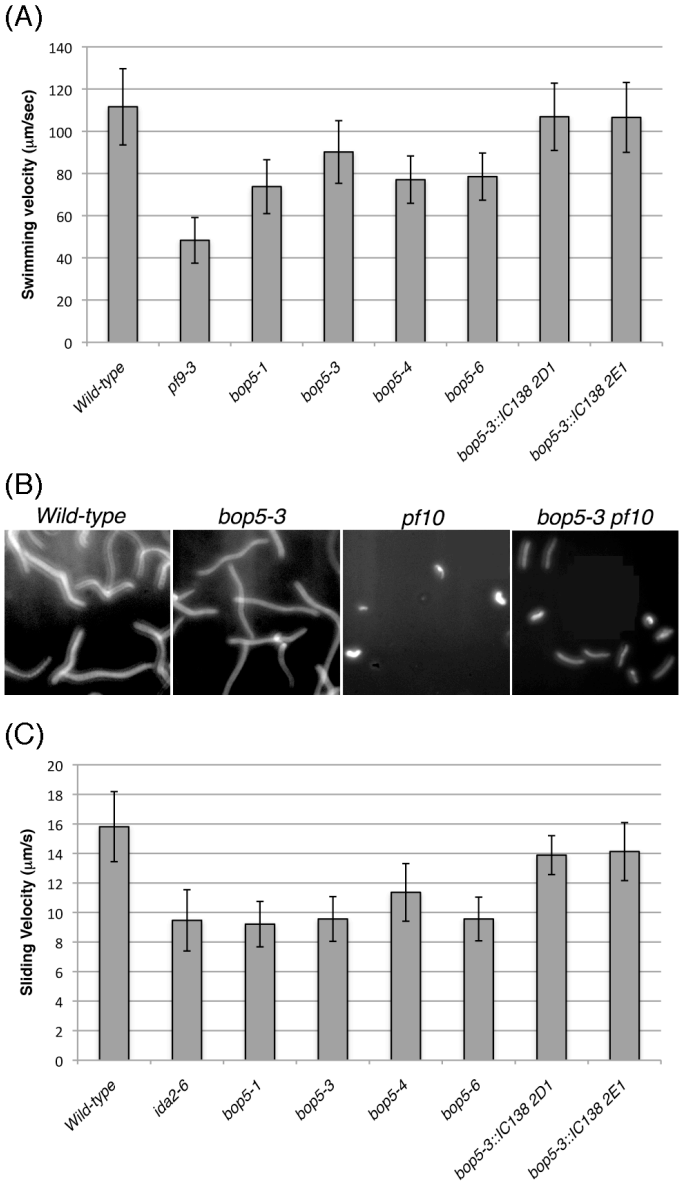

Figure 3.5. Asymmetric waveforms of I1 mutant strains during forward swimming. (A) Illustration of flagellar waveforms (left) and shear angle curves (right) plotted vs. normalized distance along the flagellum (*s/L*). The effects of bend curvature and bend arc length on the amplitude of flagellar waveform are illustrated on the left. Either reduced curvature (larger radius of curvature) or shorter curved regions (less wrapping) will lead to narrower waveforms. The effective stroke is dominated by the reverse bend, and the recovery stroke is dominated by the principal bend. (B) Flagellar waveforms of 5 representative cells of wild-type, *bop5-3,* and *ida3,* showing every 1/12th cycle. (C) Spatial distribution of shear angle of the same 5 representative cells of wild-type, *bop5-3* and *ida3,* showing every 1/12th of a cycle. Data on *wild-type* and *ida3* reprinted with modification from Bayly *et al*., 2010. (K. VanderWaal, P. Bayly)

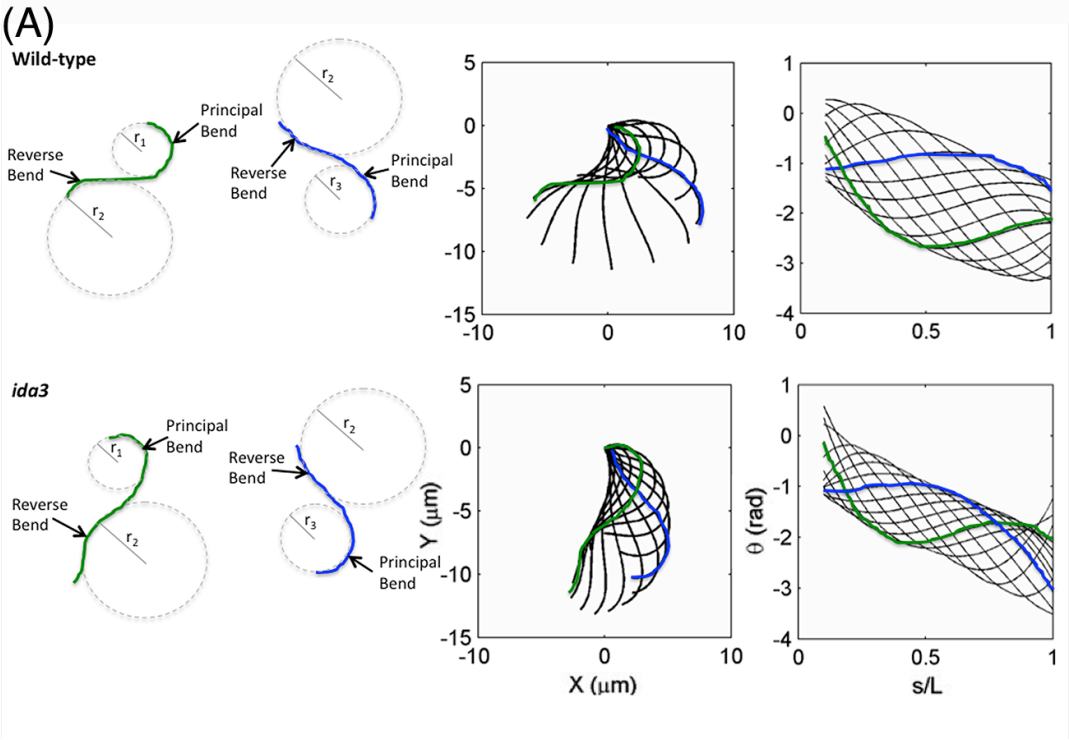

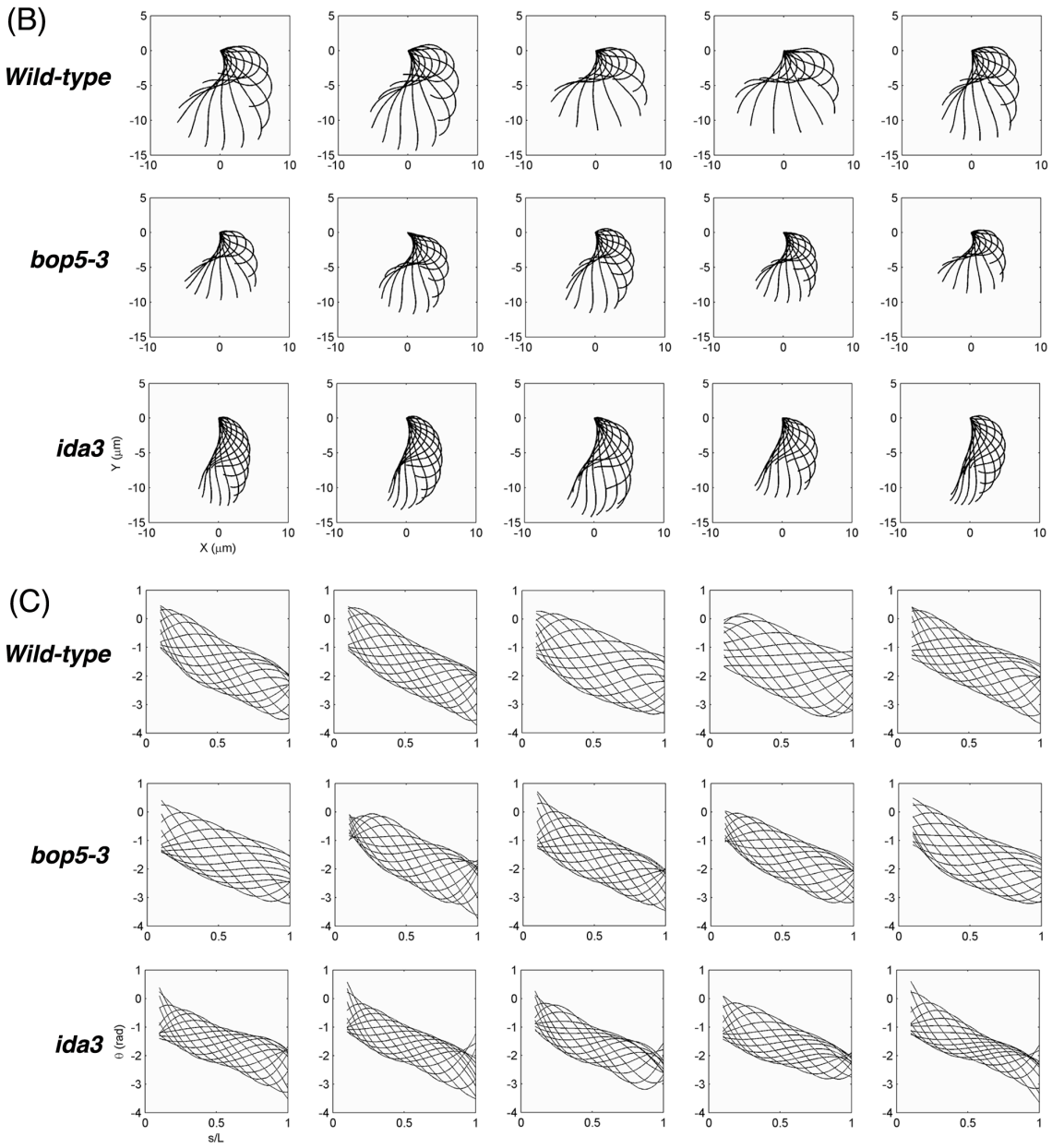
(B)
Wild-type
bop5-3
ida3
Y (μm)
X (μm)
(C)
Wild-type
bop5-3
ida3
θ (rad)
s/L

Table 3.2. Flagellar waveform parameters. (K. VanderWaal, P. Bayly)

	Wild-type	***bop5-3***	***ida3***
Flagellar Beat Frequency (Hz)	69.45 +/- 8.41	69.59 +/- 10.35	64.29 +/- 7.26
Body revolutions per second*+	4.52 +/- 0.95	3.55 +/- 0.91	2.24 +/- 0.40
Length (μm)*+	12.79 +/- 1.15	10.34 +/- 2.14	13.87 +/- 1.17
Avg. RMS shear amplitude (rad)*+	0.68 +/- 0.05	0.58 +/- 0.05	0.52 +/- 0.04
Avg. min. (R) sliding velocity-physical (rad/s)*	-404.1 +/- 50.06	-340.2 +/- 51.09	-313.3 +/- 35.73
Avg. max. (P) sliding velocity-physical (rad/s)*+	543.6 +/- 54.77	488.7 +/- 38.23	430.8 +/- 42.04
Ratio of propagation speeds (Reverse/Principal)*+	1.03 +/- 0.10	0.87 +/- 0.16	0.76 +/- 0.10
Avg. distance between principal and reverse curvature extremes+	0.75 +/- 0.09	0.78 +/- 0.04	0.72 +/- 0.08

Parameters for which values for *bop5-3* and *ida3* were significantly different from wild-type are marked with an asterisk. Parameters for which values for *bop5-3* and *ida3* were significantly different from each other are marked with a plus sign ($p < 0.05$). The average minimum and maximum sliding velocities are spatial averages of the minimum (maximum) sliding velocity at each point on the flagellum, averaged over the middle 80% of its length. The minimum sliding velocity occurs in the reverse (R) bend and characterizes the effective stroke; the maximum sliding velocity occurs in the principal (P) bend and describes the recovery stroke.

Figure 3.6. Photoshock behavior in I1 mutant strains. The movement of wild-type, *ppr2,* and *bop5-3* cells were recorded before, during, and after exposure to a bright light stimulus. Six frames from each movie are shown here, illustrating the movement of an individual cell for ~0.90 seconds. Forward motion is towards the top of the figure, and reverse motion is towards the bottom. Upon sudden exposure to bright light, the wild-type cell stops forwards motion, moves backwards briefly, and then resumes forward motion. The *ppr2* cell moves forward at a constant rate throughout the assay. The *bop5-3* cell stops briefly, but does not reverse before recovering and swimming forwards again. (K. VanderWaal)

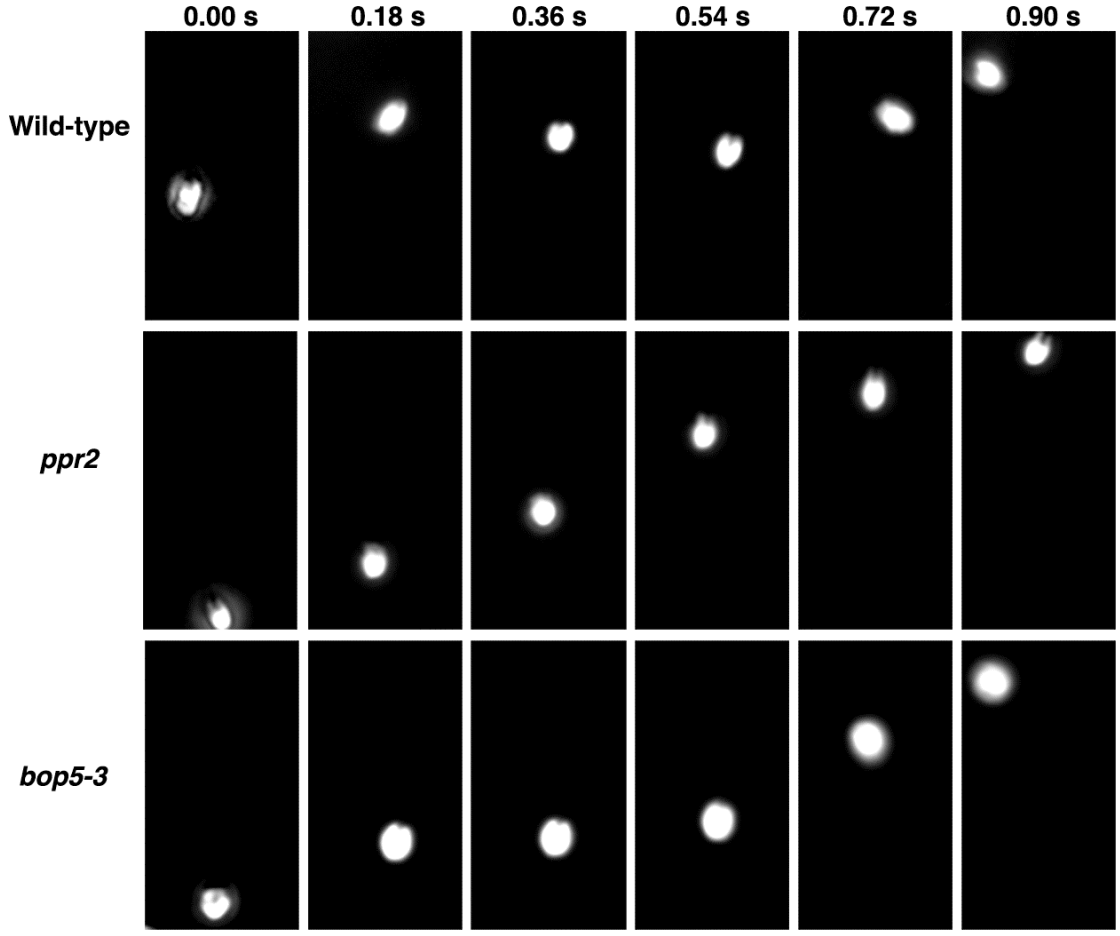

Figure 3.7. Phototaxis behavior in wild-type and I1 mutant strains. (A) Photographs of selected strains showing their photo-accumulation behavior in a petri dish after 10 min in front of a light box. The light box is located at the right of the page. (B) Polar histograms showing the swimming direction of individual cells ~5 seconds after the phototactic light source was turned on at 0 degrees (right side). (Wild-type + is CC-125, *137c mating type plus,* and wild-type – is CC-124, *137c mating type minus*) (R. Yamamoto, K. Wakabayashi, K. VanderWaal)

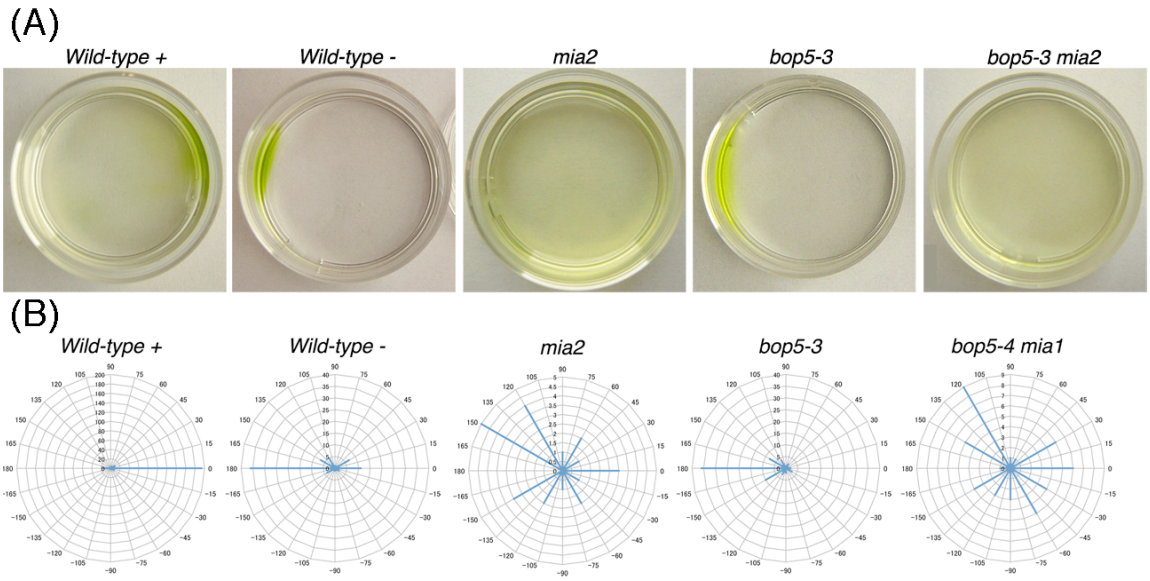

Table 3.3: Photoshock responses in wild-type and mutant strains. (K. VanderWaal)

Strain	*Reversal*	*Pause/direction change*	*No change*	*Number of cells scored*
Wild-type +	**92%**	8%	0%	50
Wild-type -	**90%**	10%	0%	30
mia1-1	0%	**100%**	0%	30
mia2-1	0%	**100%**	0%	30
mbo2	0%	5%	**95%**	20
ppr2	0%	12%	**88%**	25
pf9-3	0%	**79%**	21%	53
pf9-3::DHC1	**90%**	10%	0%	30
pf28 pf9-2::DHC1	0%	45%	55%	78
pf28 pf9-2 E8	0%	52%	48%	66
ida2-7	0%	**81%**	19%	67
ida2-7::DHC10	**16%**	66%	18%	85
pf28 ida2-7::DHC10	0%	57%	43%	23
bop5-1	0%	**80%**	20%	50
bop5-1::IC138	**70%**	27%	3%	30
bop5-3	0%	**100%**	0%	54
bop5-3::IC138 2D1	**63%**	37%	0%	30
bop5-3::IC138 2E1	**67%**	33%	0%	30
bop5-3 mbo2 5e	0%	0%	**100%**	30
bop5-3 mbo2 7b	0%	0%	**100%**	20
bop5-4	0%	**97%**	3%	30
bop5-5	0%	**68%**	32%	30
bop5-6	0%	**97%**	3%	30

Actively moving cells were exposed to a brief flash of bright light and then scored for reversal, pausing and/or change in forward direction, or no change in direction of movement.

Table 3.4: Phototaxis response in wild-type and mutant strains. (R. Yamamoto, K. Wakabayashi, K. VanderWaal)

Strain	*Photoaccumulation*	*Phototaxis*	*Direction*
Wild-type *mt+*	Yes	Yes	Positive
Wild-type *mt-*	Yes	Yes	Negative
mia1	No	No	NA
mia2	No	No	NA
ppr2	Yes	NT	Positive
pf9-3	No	NT	NA
pf9-3::DHC1-G41a	Yes	NT	Negative
pf28 pf9-2::DHC1 G4	No	NT	NA
pf28 pf9-2 E8	No	NT	NA
ida2-7	No	NT	NA
ida2-7::DHC10	Yes, weak	NT	Positive
pf28 ida2-7::DHC10	No	NT	NA
bop5-1	Yes	Yes	Positive
bop5-1::IC138	Yes	NT	Positive
bop5-3	Yes	Yes	Negative
bop5-3::IC138 2D1	Yes	Yes	Negative
bop5-3::IC138 2E1	Yes	Yes	Negative
bop5-4	Yes	Yes	Positive
bop5-6	Yes	Yes	Variable
mia1 bop5-1	No	NT	NA
mia2 bop5-3	No	No	NA
mia1 bop5-4	No	No	NA

NT=not tested in this study. NA=not applicable.

SUPPLEMENTAL MATERIALS

Table 3.S1. Statistical analysis of forward swimming velocities. (K. VanderWaal)

	wild-type	*pf9-3*	*bop5-1*	*bop5-3*	*bop5-4*	*bop5-6*	*bop5-3 ::IC138 2D1*	*bop5-3 ::IC138 2E1*
wt	NA	<0.005	<0.005	<0.005	<0.005	<0.005	<0.005	<0.005
pf9-3		NA	<0.005	<0.005	<0.005	<0.005	<0.005	<0.005
bop5-1			NA	<0.005	<0.005	<0.005	<0.005	<0.005
bop5-3				NA	<0.005	<0.005	<0.005	<0.005
bop5-4					NA	<0.005	<0.005	<0.005
bop5-6						NA	<0.005	<0.005
Bop5-3 ::IC138 2D1							NA	**0.832**

The swimming velocities of all strains shown in Figure 3.4A were compared using F-tests and T-tests, and the P values are shown here. The samples were scored as significantly different at P values less than 0.005. Because of the large sample sizes (N=190 to 552), small but significant differences were noted between all strains with respect to swimming velocities. The IC138 rescued strains are significantly faster than the *bop5-3* mutant (and other *bop5* mutants), not significantly different from one another, and slightly but significantly slower than wild-type.

Table 3.S2. Statistical analysis of *in vitro* microtubule sliding velocities. (K. VanderWaal)

	wild-type	*ida2-6*	*bop5-1*	*bop5-3*	*bop5-4*	*bop5-6*	*bop5-3 ::IC138 2D1*	*bop5-3 ::IC138 2E1*
wt	*NA*	<0.005	<0.005	<0.005	<0.005	<0.005	**0.007**	**0.036**
ida2-6		NA	**0.263**	**0.581**	**0.142**	**0.600**	<0.005	<0.005
bop5-1			NA	**0.513**	<0.005	**0.515**	<0.005	<0.005
bop5-3				NA	**0.013**	**0.991**	<0.005	<0.005
bop5-4					NA	**0.012**	<0.005	<0.005
bop5-6						**NA**	<0.005	<0.005

The *in vitro* microtubule sliding velocities of all strains shown in Figure 3.4C were compared using T-tests and the P values are shown here. Samples were scored as significantly different at P values less than 0.005. All of the mutants are significantly slower than wild-type. The differences in sliding velocities between the mutant strains are not statistically significant, except for the difference between *bop5-4* and *bop5-1*. The sliding velocities of the IC138 rescued strains are significantly faster than *bop5-3*.

Table 3.S3. Additional waveform parameters. (K. VanderWaal, P. Bayly)

	Sig. influenced by flagellar length?	**Wild-type**	***bop5-3***	***ida3***
Avg. propagation speed of R bend (μm/s)*	Yes, still sig.	1449.7 +/- 240.2	1074.8 +/- 198.5	1140.2 +/- 111.0
Avg. propagation speed of P bend (μm/s)	Yes	1411.7 +/- 191.8	1240.4 +/- 268.8	1506.0 +/- 191.6
Avg. min. (R) curvature-physical (rad/μm)+	Yes	-0.55 +/- 0.08	-0.60 +/- 0.04	-0.50 +/- 0.06
Avg. max. (P) curvature-physical (rad/μm)+	No	0.20 +/- 0.04	0.18 +/- 0.03	0.22 +/- 0.03
Initial delay between P and R bends (cyc)+	N/A	0.44 +/- 0.02	0.40 +/- 0.07	0.32 +/- 0.04

Parameters where values for *bop5-3* and *ida3* were significantly different from wild-type are marked with an asterisk. Parameters where values for *bop5-3* and *ida3* were significantly different from each other are marked with a plus sign ($p < 0.05$).

CHAPTER 4

Characterization of *D1bLIC* mutants and knockdowns as well as other IFT mutants suggests defects in ciliary signaling

Abbreviations:

IFT, intraflagellar transport
FAP, flagellar associated protein
HC, heavy chain
IC, intermediate chain
LIC, light intermediate chain
LC, light chain
MBO, move backwards only
PF, paralyzed flagella

4.1. INTRODUCTION

Assembly and maintenance of eukaryotic cilia and flagella requires the conserved, bidirectional movement of protein complexes along the length of the axoneme known as intraflagellar transport (IFT) (Rosenbaum and Witman, 2002; Scholey, 2003). The IFT process was first observed in *Chlamydomonas reinhardtii* by differential interference (DIC) microscopy (Kozminski *et al.,* 1993). The IFT particles are moved from the cell body to the tip of the flagellum (anterograde transport) by heterotrimeric kinesin-2 (Kozminski *et al.*, 1995; Piperno and Mead, 1997; Cole *et al.*, 1998; Table 4.2) and then back to the cell body by cytoplasmic dynein 1b (Pazour *et al.*, 1999; Porter *et al.*, 1999; Signor *et al.*, 1999; Wicks *et al.*, 2000; Table 4.2). Biochemical isolation of IFT complexes from *Chlamydomonas* demonstrated they contain at least 16 – 23 additional

proteins that are organized into two sub-complexes, A and B (Piperno and Mead, 1997; Cole *et al.*, 1998; Piperno *et al.,* 1998; Cole, 2003; Follit *et al.,* 2009; Table 4.2). Most of these IFT proteins have homologues in ciliated organisms (reviewed in Ishikawa and Marshall, 2011; Table 4.2).

It is thought that IFT transports flagellar components from the basal body region to their assembly sites in the flagella and removes turnover products (Qin *et al.,* 2004). *Chlamydomonas* strains with mutations in genes encoding IFT motor subunits or IFT accessory proteins typically have shortened or no flagella (Porter *et al.,* 1999; Pazour *et al.*, 2000; Brazelton *et al.*, 2001; Hou *et al.,* 2004). IFT is also important for cilia-specific functions, such as mating and flagella length control in *Chlamydomonas* (Pan and Snell, 2002; Marshall and Rosenbaum, 2001), and the function of sensory cilia in *C. elegans* and *D. melanogaster* (Collet *et al.*, 1998; Cole *et al.*, 1998; Cole, 2003; Han *et al.*, 2003; Haycraft *et al.*, 2003; Sarpal *et al.*, 2003). In addition, IFT transports specific receptors and signaling proteins into and out of the cilium (Christensen et al., 2007; Pan et al., 2005). For example, in mice, proteins involved in both Wnt and Sonic Hedgehog signaling are localized to the cilia, and defects in IFT are linked to defects in these signaling pathways (Huangfu *et al.*, 2003; Ocbina *et al.,* 2011; reviewed in Berbari *et al.,* 2009).

The motor that facilitates retrograde IFT is cytoplasmic dynein 1b (Pazour et al., 1999; Porter et al., 1999; Signor et al., 1999), and like other dyneins, it is a minus-end directed microtubule motor composed of several proteins including heavy chains (HCs), light chains (LCs), intermediate chains (ICs) and light intermediate chains (LICs) (reviewed in King, 2002; Ishikawa and Marshall, 2011). To date, four components of the retrograde dynein complex have been identified: heavy chain DHC1b, light chain LC8, light intermediate chain LIC and intermediate chain FAP133 (Porter *et al.,* 1999; Pazour *et al.,* 1999; Pazour *et al.,* 1998; Perrone *et al.,* 2003; Rompolas *et al.,* 2007; Table 4.2). In *Chlamydomonas,* null mutations (*stf1-1, stf1-2)* in the *DHC16* gene encoding the DHC1b protein result in stumpy flagella that accumulate IFT particles, suggesting a retrograde IFT defect (Pazour *et al.,* 1999; Porter *et al.,* 1999). The function of DHC1b in retrograde IFT is conserved in other organisms, such as *C. elegans* (Signor et al., 1999;

Schafer *et al.,* 2003) and vertebrates (Mikami *et al.,* 2002; Rana *et al.,* 2004). In addition, the null mutations (*fla14*) in the *Chlamydomonas LC8* gene also result in cells with stumpy flagella and defects in retrograde IFT (Pazour et al., 1998). More recent work has indicated that LC8 interacts with a dynein IC known as FAP133 (Rompolas *et al.,* 2007).

The LIC subunit of the retrograde dynein complex was first identified in mammals and then further characterized in *Chlamydomonas* and *C. elegans* (Grissom et al., 2002; Mikami et al., 2002; Hou et al., 2004; Perrone et al., 2003; Schafer et al., 2003; Table 4.2; Figure 4.1). In mammalian cells, LIC is highly expressed in ciliated tissues and interacts with DHC1b (Grissom *et al.,* 2002; Mikami et al., 2002; Figure 4.1). Mutations in the *C. elegans LIC* gene *XBX-1* and in the *Chlamydomonas d1blic* gene result in shortened cilia or flagella that accumulate IFT particles, similar to the results seen with *stf1* and *fla14* (Shafer *et al.,* 2003; Hou *et al.,* 2004). The *Chlamydomonas* LIC subunit interacts directly with DHC1b (Perrone *et al.,* 2003). FAP133 also appears to be a member of this complex as it is a conserved, WD-repeat protein with similarities to other dynein ICs that associates with DHC1b, LIC, and LC8 under certain conditions (Rompolas, *et al.,* 2007; Table 4.2; Figure 4.2).

To better understand the function of retrograde IFT in flagellar assembly, motility, and signaling, we have analyzed null mutations that disrupt components of the IFT machinery as well as temperature sensitive, flagellar assembly mutations known as *fla*. The *fla* strains assemble nearly full-length flagella at 21˚C, but resorb their flagella within a few hours after a shift to 32˚C (Huang et al. 1977; Adams et al. 1982). However, more subtle defects in the velocity and frequency of IFT and various cell behaviors can be assessed at the permissive temperature (Piperno et al. 1998; Iomini et al. 2001). The *fla* mutants can be categorized into at least two groups that affect different phases of IFT. The first group is characterized by decreases in either the velocity or frequency of anterograde IFT particles and the accumulation of IFT complex proteins at the basal body region (Table 4.2). Mutations in the subunits of the Kinesin-2 anterograde IFT motor fall into this group and include *fla1*, *fla3*, *fla8* and *fla10* (Walther et al. 1994; Miller et al. 2005; Mueller *et al.,* 2005; Pedersen *et al.,* 2006). These include mutants in the first two phases of IFT: phase I, where retrograde particles return from the flagella and are

modified into anterograde particles near the basal body, and phase II, where anterograde particles move from the base to the tip of the flagella (Iomini *et al.,* 2001). The second group shows the opposite phenotype: decreases in the velocity or frequency of retrograde IFT particles and the accumulation of IFT complex proteins in the flagella. Recent studies have identified the mutant gene products in several of these strains: the *fla11* strain is defective in IFT172, a complex B protein (Pedersen *et al.,* 2005), *fla15* is defective in the complex A subunit IFT144, and *fla16* and *fla17* are defective in the complex A subunit IFT139 (Cole *et al.,* 1998; Iomini *et al.,* 2001; Iomini *et al.,* 2009; Table 4.2). However, the gene products of the retrograde mutants *fla2* and *fla24* are unknown. These mutants affect phase III, where anterograde particles are modified into retrograde particles at the flagellar tip, and phase IV, where retrograde particles move from the flagellar tip back to the cell body (Iomini *et al.,* 2001).

In this study, we have further characterized the function of various components of the retrograde IFT complex. Specifically, we have quantified the defects in retrograde IFT observed in a series of *d1blic* mutants, and we have further shown that the *d1blic* flagellar assembly defect can be rescued by transformation with a LIC-GFP transgene. We demonstrate that many of the LIC mutant phenotypes are expressed in a dose-dependent manner. Finally, we have analyzed the expression and distribution of several IFT components in different *fla* mutants, and we have attempted to correlate these patterns with defects in IFT parameters and other behavioral phenotypes. We provide new evidence that defects in IFT motors can alter photoshock and phototaxis behaviors in different strains.

4.2. MATERIALS AND METHODS

Strains and Culture Conditions

All strains discussed in this study (see Table 4.1) were grown on Tris acetate phosphate (TAP) medium (Harris, 1989). Unless indicated differently, a pea-sized amount of cells was resuspended in minimal media lacking nitrogen (Harris, 1989) and rocked overnight under constant light to stimulate maximal flagellar assembly and motility. Photobehaviors, especially phototaxis, are typically more robust in gametic versus vegetative cells (Matsuda *et al.,* 1998).

Generation of RNAi strains, and LIC-GFP and FAP133-GFP expressing strains

To knockdown expression of the LIC, a 9 kb *Sac*1 genomic subclone of the *DLI1* gene (Perrone et al., 2003) was cut with *Asc*1 (in the last exon of *DLI1*) and *BamH*1 (in the multiple cloning site) to release the 3' end of the gene. A *DLI1* cDNA clone was also cut with the same enzymes and ligated into the genomic clone in the opposite orientation.

To generate a *LIC-GFP* construct, a *Chlamydomonas GFP* sequence (BioCat gmbH) was amplified using primers 5'-GGCGCGCCCCGGCGCGCCGATGG-3' and 5'-CCCGCGCCTTACTTGTACAGCTCGTC-3', ligated into pGEM, released with *Asc*I, and religated into the *Asc*I site near the 3' end of the genomic subclone (Perrone *et al*., 2003). To make a *FAP133-GFP* construct, the *DIC5* gene was subcloned from BAC 40p18 (10.5 kb *ApaI/BamHI* fragment) into pBlueScript (Stratagene). The stop codon was mutated to a *BstEII* site by site-directed mutagenesis using the following primers: 5'-CGGCAACTTCACGCGGTtaccTGGCAGTGCCGGCAG-3' and 5'-CTGCCGGCACT GCCAggtaACCGCGTGAAGTTGCCG-3' (mutated bases to form *BstEII* site are in lower case). The *GFP* tag was amplified with primers 5'-GGTTACCTATGGCCAAGG GCGAGGAGC-3' and 5'-GGTAACCTTACTTGTACAGCTCGTCCATGCC-3'and ligated into the *BstEI1* site of the *DIC5* subclone.

Strains expressing different constructs were generated by co-transformation with the pSI103 plasmid containing the *aphVIII* gene (Sizova et al., 2001) and selection on TAP (Tris Acetate Phosphate) medium plus 10 μg/ml paromomycin. Positive

transformants were screened for reductions in LIC or the presence of GFP by Western blots.

Preparation of antibodies against the FAP133 protein

To make antibody specific to the FAP133 protein, FAP133 fusion proteins were made by PCR using the primers 5'-GGATCCATGCAAGAGGTCCCGCC-3' and 5'-GAATTCGGTGGCGTTGAGGTCCTGG-3', ligation into pGEM, digestion with BamH1 and EcoRI, and re-ligation into pET30A (Novagen) and pGEX-2T (GE Healthcare Life Sciences). Expression was induced in BL21(DE3) pLysS cells (Promega) by growth in LB + 0.1mM IPTG at 20˚C overnight. The soluble FAP133-6xHIS fusion protein was purified using a nickel column (Novagen) and used as an antigen for polycolonal antibody production in rabbits (Spring Valley Laboratories).

The soluble, FAP133-GST fusion protein was purified by cross-linking to a glutathione agarose column (Novagen). Purified fusion protein was rocked with 5 ml of glutathione agarose in 50 ml of 50 mM HEPES pH 8.5 for 2h at 4˚C. The matrix was then washed 3 x 50ml with 200 mM HEPES pH 8.5, and then the cross-linker DMP (Sigma) was added to a final concentration of 20mM and rocked for 1hr at 20˚C. The column was then washed twice with 50ml 200 mM ethanolamine (Sigma) and three times with 50ml Tris buffered saline (TBS). The FAP133 polyclonal antibody was affinity purified on the FAP133-GST column as described in Perrone et al., 2003.

Isolation and extraction of Flagella and Axonemes, Immunoprecipitation and Western Blot Analysis

To isolate flagella, cells were subjected to pH shock, and then isolated flagella were separated from the cell bodies as described previously (Witman, 1986). The resulting flagella were resuspended in HMEEN (10 mM HEPES, pH 7.4, 5 mM $MgSO_4$, 1 mM EGTA, 0.1 mM EDTA, 30 mM NaCl) with 0.1 μg / ml protease inhibitors (pepstatin, leupeptin, aprotinin) and 1 mM dithiothreitol (Bower et al., 2009) before subsequent extraction and sucrose density centrifugation of the dynein extracts (Porter *et al.,* 1992, Perrone *et al.,*2000, Perrone et al., 2003). Immunoprecipitation of the dynein

extracts was done using protein A-Sepharose beads and affinity-purified antibodies to LIC and DHC1b (Perrone et al., 2000, 2003). Samples were run on 5-15% polyacrylamide gradient gels, transferred to Immobilon P (Millipore, Billerica, MA), and probed as described previously (Bower et al., 2009). Primary antibodies for western blotting included: anti-LIC at 1:20,000 and anti-DHC1b at 1:1000 (Perrone *et al.*, 2003); anti-FAP133 at 1:20,000 (Rompolas *et al.,* 2007); anti-IFT139 at 1:500, anti-IFT81 at 1:3000, anti-IFT172 at 1:3000, and anti-FLA10 at 1:5000 (Cole et al., 1998); anti-KAP at 1:1000 (Mueller *et al.,* 2005); anti-1β DHC at 1:1000 (Perrone *et al.,* 2000); anti-Agg3 at 1:2000 (Iomini *et al.,* 2006); anti-IC69 at 1:20,000 (Sigma Aldrich); anti-tubulin at 1:2000 (Sigma T-5168); and anti-LC8 at 1:50 (R4058, King and Patel-King, 1995; King *et al.*, 1996).

Immnofluorescence Light Microscopy, Flagella Length Analysis and Intraflagellar Transport Analysis

Chlamydomonas cells were fixed for immunofluorescence microscopy using the cold methanol procedure of Sanders and Salisbury (1995). Fixed cells were labeled with primary antibodies against the LIC at 1:1000 (Perrone et al., 2003), FAP133 at 1:200 (this study), IFT139 at 1:100 (Cole et al., 1998), and IFT172 at 1:100 (Cole et al., 1998)) and the appropriate Alexafluor-488 labeled, secondary antibodies (Molecular Probes, Eugene, OR). Slides were washed in three changes of PBS and then mounted in Prolong antifade medium (Molecular Probes). Images were obtained with an Axioscope (Carl Zeiss, Thornwood, NY) and a CoolSnap ES CCD camera (Photometrics, Tuscon, AZ), and processed using Metamorph version 7.6.5.0 (Molecular Devices, Sunnyvale, CA).

To measure flagellar length, strains were grown at room temperature in liquid TAP medium with aeration for 2-4 days. Samples were removed, fixed with 1% gluteraldehyde, and imaged using 40x phase contrast microscopy as described above. The flagellar lengths were measured using Metamorph version 7.6.5.0 (Molecular Devices, Sunnyvale, CA) as described in Mueller, et al. (2005). For the regeneration experiments, the cells were grown in TAP media. Then, flagella were removed by pH

shock, and samples were taken and fixed at selected time points during flagellar regeneration.

For analysis of IFT using DIC microscopy, strains were immobilized in agarose to limit flagellar motility and imaged using a 100x,1.3NA Plan Neofuor lens, a 4x TV tube, and a C2400 Newvicon camera (Hamamatsu, Bridgewater, NJ) as described by Mueller et al., 2005. Kymographs were created in Metamorph software (Molecular Devices, Sunnyvale, CA) and rotated so the proximal part of the flagella is in the bottom left corner. Velocities and particle frequencies were measured from the kymographs (Mueller et al., 2005).

For IFT analysis using both epifluorescence and DIC microscopy, several variations were used. First, the cells were not mounted in agarose because of background fluorescence, and second images were collected using a Rolera-MGi EM-CCD camera (Q-Imaging, Tucson, AZ) and a 1.3x TV tube. For TIRF imaging, cells were mounted as they were for epifluorescence imaging. Flagella that had adhered to the coverslip were imaged for TIRF on either a Zeiss or Nikon TIRF microscope (for details, see Engel *et al.,* 2009).

Photoaccumulation and Photoshock Assays

For photoaccumulation assays, gametic cells at a concentration of 2.5 x 10^6 cells/ml were transferred to 35 mm petri dishes, and dark adapted for 10 min. Cells were then exposed to a fluorescent light source located 30 cm away (2 W/m^2) for 10 min. Cell densities on both sides of the dish were determined at various time points and recorded by digital photography to determine relative photoaccumulation ability. Each strain was independently assayed at least three times. Where applicable, the direction of the movement relative to the light source, positive or negative, is noted.

To assay for the photoshock response, cell movement was recorded using phase contrast microscopy at 20x and a red filter. The cells were then briefly exposed to bright light using a GFP excitation filter on the epi-illuminescence port (λ = 450-500 nm). The position of each cell (n>30) before and after light exposure was traced and scored as no change, paused, changed in forward direction only, or reversed.

4.3. RESULTS

Chlamydomonas DLI1 and DIC5 genes have homologues in other species

Chlamydomonas reinhardtii dynein genes are highly conserved, including the *DLI1* gene encoding LIC and the *DIC5* gene encoding FAP133. The LIC is closely related to the human cytoplasmic dynein light intermediate chain (Dc2LIC1) with 22.45% sequence identity and 33.8% similarity (Figure 4.1A, Perrone *et al.,* 2003; Hou *et al.,* 2004). FAP133 is most similar to a poorly characterized human gene encoding the WD-repeat 34 protein, with 27.30% sequence identity and 33.22% similarity (Figure 4.2A, Rompolas *et al.,* 2007). Both proteins are also conserved in several other organisms that assemble cilia and flagella. When searching with the BLASTp algorithm, the best hits for the LIC are the D1bLIC protein from *Vista volvox* (alga), a hypothetical protein from *Strongylocentrotus purpuratus* (sea urchin), the human D2LIC1, mouse D2LIC1, and related proteins from *Trypanosoma cruzi, Caenorhabditis elegans* and *Drosophila melanogaster* (Figure 4.1B). The best hits for FAP133 are less well-characterized proteins. The *Volvox, Strongylocentrotus,* and *Trypanosoma* FAP133 homologues are hypothetical proteins, and there are no clear homologues in either *Caenorhabditis elegans* or *Drosophila melanogaster* (Figure 4.2B). However, closely related WD-repeat protein homologues to FAP133 are found in both humans and mice (Figure 4.2B).

LIC and FAP133 co-fractionate with DHC1b and directly interact with one another

Previous work has suggested that LIC and FAP133 are both components of the retrograde IFT motor complex (Perrone *et al.* 2003, Hou et al., and Rompolas *et al.* 2007). To confirm and extend these studies we analyzed dynein extracts from E8 mutant flagella by sucrose density gradient centrifugation and immunoprecipitation. The E8 mutant lacks the both outer arm dynein and the I1 inner arm dynein complexes, but assembles flagella of wild-type length (Porter et al., 1992). Dynein complexes often share LC subunits, such as LC8 (Pazour *et al.,* 1998). Using a strain that lacks the outer arm and I1 dyneins simplifies the polypeptide composition of the dynein extracts. As

shown in Figure 4.3A, significant quantities of the LIC, FAP133 and DHC1b proteins were released into the membrane plus matrix fraction when flagella were treated with non-ionic detergents; the rest were released after extraction with ATP (Figure 4.3A, and Perrone *et al.,* 2003, Rompolas *et al.,* 2007). This is in contrast to other axonemal dynein subunits like the 1β HC of the I1 dynein, which is released only in high salt, or the FLA10 subunit of the IFT kinesin, which is primarily extracted with ATP. Instead, the extraction of DHC1b/FAP133/LIC is more similar to IFT complex proteins IFT81 and IFT139, which also extract in the membrane plus matrix fraction. (Figure 4.3A, Perrone *et al.,* 2003, Rompolas *et al.,* 2007).

To better understand the relationship between these subunits, we also analyzed both membrane plus matrix and ATP extracts by sucrose density gradient centrifugation. As shown in Figure 4.3B, FAP133, LIC and DHC1b co-sediment in fractions 6 – 16 when the membrane plus matrix extracts are fractionated on 5-20% sucrose gradients (Figure 4.3B). However, both Rompolas *et al.,* (2006) and we observed that the sedimentation pattern is different with more stringent extraction conditions (Figure 4.3C). We found that when ATP extracts were run on sucrose gradients, LIC and DHC1b still co-sediment at a peak around 19S but FAP133 sediments with a peak of around 10S (Figure 4.3C). This is similar to the results of Rompolas *et al.,* (2006), in which DHC1b sedimented at ~19S and FAP133 sedimented at ~10S when extracts were run on sucrose gradients after a freeze thaw cycle. Sucrose density centrifugation of extracts from mammalian cells indicates that DHC2 and D2LIC of the retrograde IFT complex usually sediment at ~15S, but thus far the behavior of the FAP133 homologue, WDR34, has not been examined (Vaisberg *et al.*, 1996; Criswell and Asai, 1998; Grissom *et al.*, 2002; Figure 4.3B).

To demonstrate that LIC, FAP133, and DHC1b are specifically associated with one another, we performed immunoprecipitations with dynein extracts using the LIC antibody to pull down the LIC and associated proteins and analyzed the resulting supernatants and pellets by Western blots. As shown in Figure 4.3D, all of the proteins assayed are clearly present in the ATP extracts. After immunoprecipitation with a control antibody to another dynein subunit (an I1 inner arm DHC), only the IgG band is visible in

the pellet. However, after immunoprecipitations with the LIC antibody, additional bands are seen in the pellet fraction for the LIC, DHC1b, and FAP133 proteins (Figure 4.3D). An interaction between LIC and DHC1b was previously shown in Perrone *et al.* (2003), but here we show that the FAP133 subunit is also present in the complex (Figure 4.3C). Other proteins involved in IFT that do not directly interact with the LIC, such as LC8, IFT139 and KAP, do not co-immunoprecipitate with the LIC antibody (Figure 4.3D).

LIC is reduced or missing in LIC RNAi and d1blic strains and restored after transformation with LIC-GFP

To understand how the LIC subunit might contribute to the function of the retrograde IFT motor, we screened several collections of motility mutants obtained by insertional mutagenesis to see if we could identify an LIC mutant. No LIC mutant was identified in our initial screens (Perrone et al., 2003), and so we turned to RNA interference (Rohr *et al.,* 2004) to reduce LIC expression. Using a genomic sub-clone that contains a cDNA fragment ligated in the opposite orientation, we transformed a strain with wild-type motility and screened transformants for reduced expression of the LIC protein by Western blotting. A significant and reproducible decrease in LIC expression was observed in 7 transformants out of 300 colonies screened (Figure 4.4A). Two of the more severe knockdowns were kept for further analysis (see Figure 4.4C): *RNAi-A*, where expression in whole cells is reduced to <10% of wild-type levels, and *RNAi-B,* where LIC expression is ~20% of wild-type levels. The RNAi-B strain assembles full-length flagella with apparent wild-type motility, whereas the RNAi-A strain assembles short but motile flagella (Figure 4.8A, Table 4.5, Table 4.6).

To directly observe the behavior of the LIC subunit in living cells, we constructed a LIC-GFP fusion protein and introduced this construct into both the *d1blic* null mutant described in Hou *et al.* (2004) and the *E8* strain*,* which lacks the I1 and outer arm dyneins (Porter et al., 1992) (Figure 4.4B). *d1blic* lacks any LIC expression in whole cells (Figure 4.4C). The original mutant strain (T8D9) was isolated following insertional mutagenesis and screening for flagellar assembly defects by Tran Bui and Carolyn Silflow (University of Minnesota) and then further characterized as a potential retrograde

IFT mutant by electron microscopy (William Dentler, University of Kansas). The original T8D9 mutant obtained from the Dentler laboratory assembles short flagella, but it is also paralyzed (Hou *et al.,* 2004; our unpublished results). Because the LIC RNAi strains are motile, we analyzed both the RNAi strains and the null mutant to determine how the LIC might contribute to flagellar assembly and flagellar motility.

Transformation of the *d1blic* mutant did not restore wild-type motility, but careful screening of the transformants did identify GFP positive strains that assemble full-length flagella. These results suggest that the LIC-GFP construct rescues the flagellar assembly defects associated with the *LIC* mutation, but also suggests that there may be additional mutations that affect motility in the original *d1blic* mutant strain. These observations confirm that we can rescue the assembly defects seen in *d1blic,* as well as view the LIC-GFP protein movement *in vivo* (see below). Western blots of cell extracts prepared from the *d1blic::LIC-GFP* strain indicated that the LIC-GFP protein migrates at a higher molecular weight, consistent with the presence of the GFP tag, and that it is expressed at close to wild-type levels (Figure 4.4C). To confirm the GFP-tagged protein acts similarly to endogenous LIC, we also analyzed extracts from *E8::LIC-GFP* cells on sucrose density gradients and determined that the LIC-GFP protein co-sediments with the endogenous LIC and DHC1b, suggesting it is also part of the retrograde IFT complex containing DHC1b, LIC and FAP133 (Figure 4.4C).

Expression of LIC, FAP133, and IFT particle components in d1blic

To determine how the reduction and/or loss of the LIC might affect the stability of the retrograde IFT motor, we analyzed the expression and localization of other dynein subunits by Western blotting and immunofluorescence. As shown in Perrone *et al.,* (2003), LIC is concentrated in wild-type cells at the base of the flagella and in the basal body region, but also detected as punctate spots along the length of the flagella (Figure 4.5B). As expected, there is no concentration of LIC staining to the basal body region in the *d1blic* mutant (Hou et al., 2004), but LIC staining is restored in the LIC-GFP rescued strain (Figure 4.5B). In whole cell blots, FAP133 appears to be expressed at close to wild-type levels in the *d1blic* mutant (Figure 4.5A). However, despite normal overall

levels of FAP133, the localization of FAP133 to the basal body region is lost in the *d1blic* mutant. The localization of FAP133 to the basal body region is restored in the LIC-GFP rescued strain (Figure 4.5B).

We also analyzed the localization of the IFT particle proteins in the LIC null strain. Previous studies have indicated that a subset of flagellar mutants accumulate IFT particles in their shortened flagella due to inefficient retrograde IFT (Pazour *et al.*, 1998, 1999; Porter *et al.*, 1999, Iomini *et al.,* 2001; Pederson *et al.,* 2005). We therefore stained both wild-type and mutant strains with antibodies against IFT subunits and looked for the accumulation of IFT139, a subunit of IFT complex A, and IFT172, a subunit of complex B. Consistent with previous results (Hou *et al.* 2004), we observed an increase in the concentration of IFT172 in the flagellar stumps of the *d1blic* mutant (Figure 4.5B). We also observed an increased accumulation of IFT139 in the *d1blic* mutant (Figure 4.5B). However, following transformation with the LIC-GFP, both IFT subunits became re-distributed to the basal body region in the rescued cells (Figure 4.5B).

Expression of IFT and flagellar proteins in LIC RNAi *strains*

To determine if similar defects in protein expression and localization are observed in the *LIC RNAi* strains as in the LIC null strain, we performed another series of Western blot and immunofluorescence experiments. First, as in *d1blic,* the *RNAi* strains expressed reduced amounts of the LIC in whole cell extracts (Figure 4.6A, 4.6B). This reduction is more dramatic in *RNAi-A* than in *RNAi-B* (Figure 4.6A, 4.6B). In addition, as in *d1blic,* FAP133 bands in whole cell extracts of *RNAi* strains are nearly as strong as the wild-type FAP133 band (Figure 4.6A). We also looked at expression levels of DHC1b in whole cells, as Hou *et al.* (2004) observed decreased expression of DHC1b in the *d1blic* mutant. As expected, DHC1b bands are less intense in the *LIC RNAi* strains than in wild-type (Figure 4.6B).

Because the *LIC RNAi* strains assemble longer flagella than the *d1blic* mutant, we were also able to assess protein levels in isolated flagella by Western blot. First, the blots were probed with an antibody to IC69 as a loading control. Because all three strains are loaded evenly (Figure 4.6C), we examined levels of other flagellar proteins in

comparison to wild-type. It is possible to detect a decrease in LIC levels in isolated flagella of *LIC RNAi-A* and *B* (Figure 4.6C). Because cDhc1b and FAP133 co-immunoprecipitate with the LIC, we also analyzed the levels of these subunits in the isolated flagella. Even though FAP133 is expressed at near wild-type levels in whole cell extracts, we observed a reduction of FAP133 in the isolated flagella from the *LIC RNAi-B* and *LIC RNAi-A* strains (Figure 4.6C). Similar results were observed with cDhc1b (data not shown). Given the apparent accumulation of IFT particle proteins in the stumpy flagella of the LIC null strain by immunofluorescence, we also analyzed isolated flagella from the *LIC RNAi* strains to see if we could detect any changes in IFT particle proteins. Here, it is evident that both IFT81 and IFT172 complex B proteins are increased in *RNAi-A* relative to *RNAi-B,* and increased in *RNAi-B* as compared to wild-type (Figure 4.6C). Preliminary results suggest that IFT139, a complex A protein, is also increased in *LIC RNAi* strains (data not shown).

The decrease in LIC expression in whole cells and flagella can also be observed by immunofluorescence staining. Some LIC staining is observed in the flagella and basal body region of the *LIC RNAi-B* cells, but significantly less than in wild-type cells, and very little LIC signal is detected in the *LIC RNAi-A* cells (Figure 4.6D). Because FAP133 levels are reduced in whole flagella, but not in whole cells, we also analyzed the localization of FAP133 in fixed cells. Similar to the results observed with *d1blic* null mutant, we observed that FAP133 is not concentrated in the basal body region of flagella in either *LIC RNAi* strain (Figure 4.6D), despite its presence on blots of whole cells and isolated flagella (Figure 4.6C). We also analyzed the localization of IFT139 and IFT172 in the *LIC RNAi* strains as compared to the *d1blic* mutant, where IFT139 and IFT172 accumulate in the flagellar stumps. Both proteins localize near the basal bodies and in puncta along the length of the flagella in wild-type cells (Figure 4.6D). A similar pattern is seen in the *LIC RNAi* strains, but we also observed an increase in the concentration of IFT139 (complex A) and IFT172 (complex B) staining at the flagellar tips (Figure 4.6D).

Expression of IFT and flagellar proteins in other IFT mutant strains

Previous studies have indicated that IFT mutant strains show significant differences with respect to the accumulation of various IFT protein components in their flagella (Iomini *et al.,* 2001; Perrone *et al*., 2003; Hou *et al*., 2004; Pederson *et al*., 2005; Rompolas *et al.,* 2007). To confirm and extend these studies, we probed Western blots and performed immunofluorescence experiments on IFT mutant strains that disrupt other components of the retrograde motor complex. Both *fla14,* the LC8 mutant, and *stf1,* a DHC1b mutant, are caused by null mutations in retrograde IFT subunits and have extremely short flagella (Pazour *et al.,* 1998; Porter *et al.,* 1999). Both Perrone *et al.* (2003) and Rompolas *et al.* (2007) analyzed the levels of LIC and FAP133 in whole cells from *stf1* and *fla14,* and found that FAP133 is expressed at close to wild-type levels in both mutants, whereas the LIC is only reduced in *stf1*. We confirmed these results as shown on the Western blots in Figure 4.7A; *stf1* has reduced amounts of LIC but wild-type levels of FAP133, and neither LIC nor FAP133 are affected in *fla14* or the rescue *fla14::LC8*.

Because *stf1* and *fla14* have short, stumpy flagella, we were unable to purify flagella free of cell body contamination and accurately quantitate protein expression in isolated flagella. We therefore assessed the localization of LIC and FAP133 in these strains by immunofluorescence. As shown in Figure 4.7C, both the LIC and FAP133 are concentrated in the basal body region of *fla14,* but they are not observed in the short flagellar stumps, consistent with previous reports (Perrone *et al*., 2003; Rompolas *et al*. 2007). These observations indicate that LC8 is not required for the stability of either the LIC or FAP133, nor is LC8 required for their targeting to the basal body region, but it may be required for their efficient entry into the flagella. In contrast, in *stf1,* we did not see any concentration of either LIC or FAP133 staining in the basal body region (Figure 4.7C). These results suggest that the cDHC1b subunit is essential for both LIC and FAP133 targeting to the basal body region.

fla16 is a retrograde IFT mutant that accumulates IFT complex B subunits along its length and at the flagellar tips (Piperno et al., 1998; Iomini et al., 2001). Recent studies have demonstrated the *fla16* phenotype is the result of a mutation in the complex A subunit IFT139 (Iomini et al., 2009). To assess the location of the retrograde IFT

motor in this strain, we analyzed the distribution of motor subunits by immunofluorescence (Figure 4.7C). Both the LIC and FAP133 are concentrated in the basal body region of the *fla16* mutant, similar to wild-type, but are also found in bright spots at the tip of the *fla16* flagella. These observations are consistent with earlier studies using the cDHC1b and complex B antibodies (Perrone et al., 2003), and indicate that the subunits of the retrograde motor complex co-localize with the disrupted IFT particles in the *fla16* flagella.

At least four genes have been implicated in flagellar length control, and mutations in these genes result in cells with abnormally long (*lf*) or unequal length (*ulf*) flagella (Tam *et al.,* 2003; Nguyen *et al.,* 2004; Tam *et al,* 2007; reviewed in Wemmer *et al.,* 2007). Both the frequency and velocity of IFT are similar to wild-type in the *lf* mutant flagella (Dentler, 2005). However, these mutants also accumulate IFT components in small blebs along the length or at the tip of their two flagella (Dentler, 2005), including the cDHC1b and LIC subunits of the retrograde motor (Perrone et al., 2003). As shown in Figure 4.7C, we have found that FAP133 also localizes in the flagellar blebs of the *lf* mutants.

fla2 and *fla24* are two temperature sensitive flagellar assembly mutants that have previously been characterized as defective in retrograde IFT, but the mutant gene products have not been identified (Iomini *et al.,* 2001). To determine if defects in either the LIC or FAP133 genes might be responsible for the mutant phenotypes, we analyzed the expression of the LIC and FAP133 in each strain. Western blots of flagella isolated at the permissive temperature indicate that the FAP133 is present at reduced amounts in *fla2* mutant flagella while LIC is approximately equal relative to wild-type flagella (Figure 4.7B). In *fla24,* LIC is present at increased amounts and FAP133 is approximately equal relative to wild-type flagella (Figure 4.7B). Antibody staining of fixed cells at the permissive temperature indicated that the LIC is concentrated in the basal body region and present in flagella, similar to wild-type. However, the intensity of flagellar staining may be reduced in *fla24*. Further work is needed to more accurately quantitate these images and to assess the distribution of FAP133. Additional studies at the restrictive

temperature may reveal more significant differences in the expression and distribution of the retrograde motor subunits.

Previous work has shown that the IFT particle subunits accumulate in the flagella of both *fla2* and *fla24*, especially at the restrictive temperature (Cole *et al.,* 1998; Iomini *et al.,* 2001, see also Figure 4.7B). To investigate whether we see similar effects on the accumulation of IFT particle proteins, we assessed expression of IFT81 and IFT172, two complex B proteins. We observed increases in IFT172 and IFT81 expression in *fla24* flagella, but we did not detect obvious changes in either protein in *fla2* flagella at the permissive temperature (Figure 4.7B). Preliminary results also show increases of IFT139, as complex A protein, in *fla24* flagella, but not in *fla2* flagella (data not shown).

Knockdown or knockout of the LIC is associated with defects in flagellar assembly

Mutations in both LC8 (*fla14*) and cDHC1b (*stf1*) result in mutant strains with very short flagella. To determine if reduction of the LIC is also associated defects in flagellar assembly and maintenance, we analyzed the flagellar length distributions in wild-type, *LIC RNAi-A, LIC-RNAi-B, d1blic,* and *d1blic::LIC-GFP* strains (Figure 4.8). We observed that the average flagellar length decreases as the concentration of the LIC in the cell is reduced. The average length of wild-type flagella is 11.6 +/- 1.6 μm, as compared to 9.3 +/- 1.4 μm for the *LIC RNAi-B* strain, 4.3 +/- 1.3 μm for the *LIC RNAi-A* strain, and 2.6 +/- 2.2 μm for the *d1bic* null mutant (Figure 4.8A). The average flagellar length is increased to 9.2 +/- 1.5 μm in the LIC-GFP rescue (Figure 4.8A). We also analyzed the rate of flagellar regeneration after flagellar excision by pH shock. As shown in the experiment in Figure 4.8B, wild-type cells regenerated full-length flagella in approximately 120 minutes. However, *LIC RNAi-A* cells required more than 175 minutes to regenerate approximately half-length flagella (Figure 4.8B). The large variation in flagellar lengths of the LIC null strain and slow regeneration is consistent with results observed following knockdown of the retrograde motor in *Tetrahymena* cells. When the IFT dynein was disabled in *Tetrahymena,* cilia were slow to regenerate, were generally shorter, and displayed highly variable ciliary length distributions (Asai *et al.,* 2009).

IFT processes are affected in LIC knockdowns and null strain

Although previous studies demonstrated the accumulation of IFT particle proteins in the *d1blic* strain (Hou *et al.,* 2004), neither anterograde nor retrograde IFT was analyzed directly. We therefore used DIC microscopy to analyze both the frequency and velocity of IFT particle movement in the LIC mutant and rescued strains. As shown in Table 4.3 and Figure 4.9, anterograde IFT particles move at ~2.1 +- 0.3 μm/sec and retrograde IFT particles move at ~3.4 +/- 0.7 μm/sec in wild-type cells. The average frequency of particles is ~5.6 +/- 1.0 particles/sec, with an anterograde to retrograde frequency ratio of ~0.5 +/- 0.1. The velocity and/or frequency of anterograde IFT is reduced in the kinesin-2 mutants *fla10 (pf15 fla10), fla8* and *fla3,* but retrograde IFT is relatively wild-type (Iomini *et al.,* 2001; Mueller *et al.,* 2005; Table 4.3, Figure 4.9B). In contrast, mutants that affect retrograde IFT processes such as *fla2* and *fla24* have reduced retrograde velocity, reduced overall frequency, and fewer retrograde particles (Iomini *et al.,* 2001; Table 4.3, Figure 4.9B). As the values that we measured for IFT in *fla2* and *fla24* differed slightly from those published in Iomini *et al.* (2001), we have included both rates published in Iomini *et al.* (2001) and our measurements in the graph shown in Figure 4.9B. The reason for the discrepancy is unknown.

To evaluate the contribution of the LIC to the function of the retrograde IFT motor, we analyzed both anterograde and retrograde IFT in the *d1blic* and the *LIC RNAi* strains. As shown in Table 4.3, both the velocity and frequency of anterograde IFT are similar to wild-type in the *d1blic, RNAi-A* and *RNAi-B* strains. However, both velocity and frequency of retrograde IFT are reduced in the LIC mutants (Table 4.3, Figure 4.9). Moreover, the defects in IFT are correlated with the amount of reduction of the LIC (Table 4.3). Knockdown of the LIC to ~20% of wild-type levels in RNAi-B reduces retrograde velocity by 30% and retrograde frequency by 50%. The velocity and frequency decreases are even more significant in the *d1blic* and *RNAi*-A strains (60% reduction in velocity and 85% reduction in frequency), but interestingly, retrograde IFT does persist even in the complete absence of the LIC in the *d1blic* null mutant (Table 4.3). Transformation with the LIC-GFP transgene increases both the frequency and velocity of retrograde IFT (see Table 4.3, Figure 4.9), but IFT is not completely restored

to wild-type levels. Less than wild-type rates could be due to the presence of the GFP tag in the LIC protein or reduced expression of the transgene as compared to expression of the wild-type gene. To determine if the GFP tag causes a reduction, we also transformed *LIC-GFP* into the *E8* strain, which does not have an LIC defect, and assessed IFT rates (Figure 4.9C). In this experiment, we analyzed cultures from both strains on the same day and measured IFT by DIC microscopy. We observed that the rates of IFT in the *E8::LIC-GFP* strain were significantly faster in both the retrograde and anterograde directions than the rates observed for the *d1blic::LIC-GFP* strain ($p < 0.005$, Figure 4.9C). These observations suggest that the slower rates observed in *d1blic::LIC-GFP* strain are due to reduced expression and not because the GFP tag altered dynein activity.

TIRF-microscopy and epi-fluorescence microscopy of GFP tagged KAP and LIC

To verify that the anterograde and retrograde motor proteins are moving at the same rates as the IFT particles observed by DIC microscopy, we also analyzed the movement of GFP tagged subunits by epifluorescence and TIRF microscopy. In previous work, we identified the *fla3* mutation as a defect in the KAP subunit of the Kinesin-2 anterograde motor (Mueller *et al.,* 2005). We observed by DIC microscopy that both the frequency and velocity of anterograde IFT were reduced in *fla3,* and that transformation with a *KAP-GFP* transgene fully rescued the IFT defects (Mueller *et al.,* 2005; Table 4.3). We were also able to detect movement of the KAP-GFP subunit by both epi-fluorescence and confocal microscopy. However, we were unable to obtain more quantitative measurements of particle velocity and frequency because of technical limitations with the various cameras used to collect the fluorescence images and the rapid photobleaching of the fluorescence signal. Since that time, we obtained a faster, more sensitive camera (see Materials and Methods), and so we have now compared the rates of the GFP-tagged subunits to the rates of the IFT particle observed by DIC. Because of the optical requirements for each type of assay, we were not able to collect DIC and fluorescence images from the same cells, but we did collect DIC and fluorescence images using cells from the same cultures.

When we compared IFT parameters obtained by DIC microscopy with those obtained by epifluorescence, the velocity of KAP-GFP subunit appeared to be slightly but significantly slower than the velocity of the IFT particles measured by DIC (Table 4.4, Figure 4.10C). This effect was especially obvious on the anterograde rates. Because observation of the GFP tagged subunits by epifluorescence microscopy required illumination of the cells with a high intensity light source, we hypothesized that the observed differences in rate might be the result of a phototoxic effect. To address this, we used DIC microscopy and a halogen light source to obtain images of IFT, and then we exposed the same cell to the high intensity light source used for epifluorescence imaging. We saw an immediate effect on the anterograde velocity: with halogen illumination alone, the velocity of anterograde IFT was ~1.9 +/- 0.2 μm/sec, but after illumination with halogen plus the high intensity light source, the velocity of anterograde IFT in the same cell was ~1.5 +/- 0.2 μm/sec (Figure 4.10A). This difference is significant ($p < 0.005$). Retrograde rates increased slightly with UV illumination, from ~2.7 +/- 0.5 μm/sec to ~2.8 +/- 0.6 μm/sec, but this difference is not significant ($p = 0.685$; Figure 4.10A).

As an alternative to continuous illumination of the whole cell with a high intensity light source and epifluorescence imaging, we hypothesized that illuminating the cells with a monochromatic laser and imaging the flagellum by TIRF microscopy might be a better strategy for analyzing IFT. In addition to using a monochromatic light source, TIRF microscopy only illuminates the thickness of the effervescent wave, which allows us to limit excitation to the flagella and exclude excitation of the cell body. This approach both prevents auto-fluorescence of the cell body from contaminating the fluorescence signal from the flagella, and it also protects against photo-damage of GFP-tagged subunits in the cell body that could lead to a rate reduction (For review of using TIRF to visualize IFT in *Chlamydomonas*, see Engel *et al.,* 2009). As shown in Table 4.4, when we analyzed anterograde IFT of the KAP-GFP strain by TIRF microscopy, the KAP-GFP subunit moved at ~2.7 +/- 1.0 μm/sec whereas the IFT particles moved at ~2.4 +/- 0.8 μm/sec, as measured by DIC (Table 4.4, Figure 4.10C). The apparent increase in the rates seen with TIRF microscopy is also observed with measurements of retrograde

IFT, and both increases are statistically significant ($p < 0.005$; Table 4.4, Figure 4.10C). The source of this discrepancy is unknown, but the values that we measured for KAP-GFP are very similar to those published by Engel *et al.* (2009) and Lechtreck *et al.* (2009) (see Table 4.4). Another advantage to TIRF microscopy is the clarity of the kymograph images used to analyze IFT rates (Figure 4.10B).

To verify that the LIC is transported into the flagellum as an anterograde cargo and moves out of the flagella as a subunit of the retrograde motor, we analyzed the velocity of the LIC-GFP by conventional fluorescence and TIRF and compared it the velocities of the IFT particles observed by DIC. As seen above with KAP-GFP, the anterograde velocity of the LIC-GFP measured by epifluorescence was reduced relative to the particle velocities observed by DIC ($p < 0.005$; Table 4.4, Figure 4.10C). In this case, we also observed a reduction in the retrograde velocity of the LIC-GFP ($p < 0.005$; Table 4.4, Figure 4.10B). However, when we compare the anterograde velocities of LIC-GFP (measured by TIRF) to those of the IFT particles (measured by DIC on the same microscope), we observed very similar rates that were not significantly different (~2.4 +/- 0.9 μm/sec and ~2.3 +/- 0.8 μm/sec, respectively) (Table 4.4, Figure 4.10C). We also measured a significant increase in the apparent velocities of retrograde IFT by TIRF versus DIC, (~3.0 +/- 1.3 μm/sec for DIC to ~3.7 +/- 1.5 μm/sec for TIRF, $p < 0.005$; Table 4.4, Figure 4.10C). More assays of the movement of the KAP-GFP and LIC-GFP proteins and the IFT particles need to be done to understand the origin of the apparent increase of velocity using TIRF illumination.

IFT related mutant strains have defects in photoshock and phototaxis

Several proteins involved in ciliary signaling, such as PKD2 in *Chlamydomonas* and smoothened in mammals, appeared to be transported either into or out of the flagellum via IFT (Huang *et al.,* 2007; Corbit *et al.* 2005). Also, several signaling processes in *Chlamydomonas* involve the flagella, including mating, photobehaviors, and mechanical responses (Huang *et al.,* 2007; Iomini *et al.,* 2006; Fujiu *et al.,* 2009; Fujiu *et al.,* 2011). Because many of the proteins involved in photoresponses are found in the membrane or matrix fractions of the *Chlamydomonas* flagella, such as BBS4, a protein

involved in phototaxis and flagellar protein trafficking, CAV2, a flagellar calcium channel needed for photoshock, and AGG2 and AGG3, two proteins involved in phototaxis (Lechtreck *et al.,* 2009; Fujiu *et al.,* 2009; Iomini *et al.,* 2006), we hypothesized that defects in retrograde IFT might be associated with defects in a variety of photobehaviors. To determine if IFT defects correlate with specific changes in photoshock or phototaxis, we assayed several of the IFT mutants with apparent wild-type motility for their ability to both photoshock and phototax (the *d1blic* mutant was not assayed because these cells swim extremely poorly). Wild-type cells normally swim forwards, but abruptly stop and briefly reverse directions in response to bright flashes of light and an increase in intracellular calcium before recovering and swimming forwards again (Witman, 1993). Mutant cells with defects in the flagellar calcium channel (*ppr2)* and cells that swim backwards only (*mbo2*) do not alter their motility in response to bright light (Table 4.5, Chapter 3).

In these initial experiments, we only analyzed photobehaviors at the permissive temperature for the *fla* mutants. Under these conditions, IFT continues but depending on the mutant analyzed, different phases of the IFT cycle are compromised. For example, in *fla10,* a mutant in the anterograde kinesin-2 motor, the velocity of anterograde IFT is reduced, but there are only minimal effects on the frequency of IFT particles at the permissive temperature (Iomini et al., 2001). *fla10* exhibited both photoshock and phototaxis responses, although phototaxis was weaker than in wild-type strains (Tables 4.6, 4.7). In the *fla3* at the permissive temperature, the mutation in the KAP subunit also affects the frequency of anterograde IFT (Mueller et al., 2005). Interestingly, *fla3* displayed an abnormal photoshock response where some cells did not change motion at all and some stopped, but did not reverse (Table 4.5), but its phototaxis response was relatively wild-type (Table 4.6). Rescue of the *fla3* mutant with the KAP-GFP transgene resulted in a more normal photoshock response. These results suggest that different photobehaviors are sensitive to disruption in different phases of the IFT cycle.

To determine if any of the photobehaviors also required functional retrograde IFT, we analyzed the four retrograde mutants with apparent wild-type flagellar motility. The *LIC RNAi-B* strain, which exhibits relatively mild defects in both the velocity and

frequency of retrograde IFT, did not show any apparent defects in either photoshock or phototaxis (Tables 4.6, 4.7). The velocity of retrograde IFT is more severely compromised in the *fla24* strain, but both the photoshock and phototaxis responses in *fla24* were similar to wild-type (Tables 4.6, 4.7). These observations suggest that the velocity of retrograde IFT by itself may not have a significant impact on photobehaviors.

To determine if other factors might affect the photobehaviors, we also analyzed the *LIC-RNAi A* strain, which displays severe defects in both the velocity and frequency of retrograde IFT, and the *fla2* strain, which displays relatively mild defects in our IFT assays (Table 4.3). Both the photoshock and phototaxis responses were disrupted in the *LIC-RNAi-A* strain (Tables 4.6, 4.7). These results suggest that the LIC may play a previously undefined role in the transport of components required for these behaviors. We have attempted to confirm these observations by analysis of the *d1blic* null mutant, but the motility of this strain is so poor that we cannot perform the assays. Interestingly, the *fla2* strain, which exhibits relatively mild defects in both the velocity and frequency of retrograde IFT, was severely compromised with respect to both photoshock and phototaxis responses (Tables 4.6, 4.7). The *FLA2* gene product is unknown, but these observations suggest it may also be an important factor in the transport of signaling molecules.

4.4. DISCUSSION

DLIC and FAP133 are components of the DHC1b complex

To determine if the LIC and FAP133 proteins are subunits of a retrograde IFT motor complex, we first performed a series of sequential extractions of isolated flagella. As reported previously, FAP133, LIC and DHC1b co-extract primarily in the membrane plus matrix and 1 mM ATP fractions, with some protein still remaining in the high salt extract (Figure 4.3A, Perrone *et al.,* 2003; Hou *et al.,* 2004; Rompolas *et al.,* 2006). This is somewhat similar to the extraction pattern observed for the IFT particle subunits, IFT81 and IFT139, as they also extract in the membrane plus matrix fraction; however, no protein is seen in the high salt extract for the complex proteins (Figure 4.3A, Perrone *et al.,* 2003; Hou *et al.,* 2004; Rompolas *et al.,* 2006). Other proteins, such as FLA10, which corresponds to a kinesin-2 motor subunit, and 1β HC, which corresponds to an I1 inner arm DHC, do not extract in the membrane plus matrix fraction, and signal is not seen until ATP extraction. The co-extraction of the LIC, FAP133, and DHC1b suggested that they act as members of the same complex.

Flagellar IFT proteins can be separated into at least four distinct complexes on sucrose density gradients, including IFT complex A, IFT complex B, kinesin-2, and DHC1b (Cole *et al.,* 1998; Perrone *et al.,* 2003). As reported in Rompolas *et al.* (2006), we found that FAP133 co-sediments with DHC1b and LIC on sucrose gradients under certain conditions, adding support to the proposed interaction between the three proteins. However, FAP133 also dissociates from LIC and DHC1b with more stringent extraction conditions, which suggests that the interaction of FAP133 with LIC and DHC1b is weaker than the interactions between LIC and DHC1b (Rompolas, *et al.,* 2006).

To test for a direct interaction, Rompolas *et al.,* (2006) did immunoprecipitations using an antibody to FAP133. They determined that FAP133 directly interacts with DHC1b, in addition to IFT81, IFT139, FLA10 and LC8. They did not test for a direct interaction between FAP133 and LIC. Therefore, we performed immunoprecipitations using the LIC antibody and pulled down FAP133, suggesting LIC and FAP133 directly interact, as well as DHC1b. Taken together, FAP133, LIC and DHC1b likely act together

as a retrograde IFT complex because they co-sediment (to an extent) on sucrose gradients and because they co–immunoprecipitate in reciprocal IPs. FAP133 also interacts directly with LC8 and IFT139, while LIC does not (Rompolas *et al.,* 2006; Figure 4.3C). These results suggest that FAP133 may connect LIC and DHC1b to the rest of the IFT machinery.

LIC reductions coincide with abnormal expression of FAP133 and DHC1b

Previous studies based on work in the *d1blic* and *stf1* mutant strains have suggested that loss of the LIC prevents the localization of FAP133 to the basal body region (Rompolas *et al.,* 2007). We have observed that when the LIC protein is reduced or missing (as in the *d1blic* and *LIC RNAi* strains), the levels of FAP133 in whole cells remain near wild-type (Figure 4.5A, 4.6A). However, the wild-type pattern of peri-basal body and flagellar localization of FAP133 was not seen in any of these strains (Figure 4.5B, 4.6C, 4.6D). We additionally showed that both LIC and FAP133 localization to the peri-basal body region and flagella is restored when *d1blic* is transformed with LIC-GFP construct (Figure 4.6B). As shown in both Perrone *et al.* (2003) and Rompolas *et al.* (2007), we also find that *stf1,* the DHC1b null strain, has reduced amounts of LIC but normal amounts of FAP133 in whole cells. In addition, neither the LIC nor FAP133 were localized to the peri-basal body region (Figure 4.7A, 4.7C). Finally, we confirmed that the expression of both the LIC and FAP133 and their localization to the basal body region are normal in the LC8 null strain, *fla14* (Perrone *et al.,* 2003; Rompolas *et al.,* 2007; Figure 4.7A, 4.7C). Based on the above data, we conclude that a reduction of LIC in whole cells coincides with lack of FAP133 localization to the basal body region.

Reduction or loss of the LIC also affects expression of cDHC1b in whole cells (Figure 4.6B), similar to that observed in Hou *et al.* (2004). In addition, the amount of DHC1b expression correlates with the amount of reduction of LIC. *LIC RNAi-A* has less LIC and DHC1b expression than *RNAi-B* (Figure 4.6B). Reduced FAP133 expression is only seen in whole flagella and not in whole cells (Figure 4.6A, 4.6C). Therefore, we conclude that the greater the reduction of LIC expression, the more DHC1b is reduced in whole cells, and the more FAP133 is reduced in flagella.

fla24 and *fla2* strains express relatively normal levels of LIC, but *fla2* showed reduced expression of FAP133 in whole flagella (Figure 4.7B), suggesting that expression of FAP133 can be reduced without changing expression of the LIC. The localization of FAP133 in both *fla2* and *fla24* cells still needs to be evaluated by immunofluorescence. In addition, further study of both mutants at the restrictive temperature could be informative.

Different IFT mutants accumulate specific IFT complexes

Hou *et al.* (2004) first observed accumulation of IFT172, a protein in IFT complex B, in the flagellar stumps of *d1blic* and concluded there must be a defect in retrograde IFT. We also observed an increase of IFT172 in *d1blic* flagellar stumps (Figure 4.5B). Because *d1blic* does not assemble full-length flagella, we wondered if we would see a similar increase of IFT172 in the longer flagella of the *LIC RNAi* strains. Indeed, we observed an accumulation of IFT172 near the flagellar tips of both *RNAi* strains, which we confirmed by Western blot (Figure 4.6B, 4.6C). Moreover, more IFT particle proteins accumulate in *RNAi-A* than *RNAi-B* flagella (Figure 4.6B). To extend the results described in Hou *et al.* (2004), we also probed flagella from the LIC mutant and knockdown strains with antibodies to IFT81 (from complex B) and IFT139 (from complex A). We observed similar increases in accumulation for these proteins in *d1blic, LIC RNAi-A,* and *LIC RNAi-B* (Figure 4.5B, 4.6B, 4.6C). Together, these results suggest that both IFT complexes accumulate in strains with reduced expression of LIC and that the more LIC is reduced, the greater the accumulation.

Our observations are consistent with previous work that suggests that IFT particle proteins accumulate in retrograde IFT mutants (Cole *et al.,* 1998; Iomini *et al.,* 2001). Published work on *fla2* suggests that IFT particles accumulate slightly at room temperature, but the effect is much more pronounced at the restrictive temperature (Cole *et al.,* 1998). These results may explain why we did not see an obvious increase in IFT complex proteins in *fla2,* as we performed our experiments at room temperature (Figure 4.7B). Also, Iomini *et al.* (2001) reported that *fla24* accumulates complex B, but not complex A in flagella. This is consistent with our results, where we observed increases

in both IFT81 and IFT172 (complex B) in *fla24* (Figure 4.7B). To further confirm published results, and to see if the *LIC RNAi* strains are consistent with trends in other retrograde mutants, we should also assess accumulation of complex A subunits, as well as assess expression of all proteins at the restrictive temperature of 32˚C to determine if these conditions enhance the mutant phenotypes.

Reductions in LIC cause flagellar assembly defects in a dose specific manner

Hou *et al.* (2004) showed that the *d1blic* has very short flagella. We have confirmed that the short flagella phenotype of *d1blic* can be rescued by transformation with the *LIC-GFP* transgene (Figure 4.8A). The *d1blic::LIC-GFP* cells still do not have wild-type length flagella, but at least some of the flagellar assembly defects caused by loss of the LIC are restored. This phenotype is consistent with previous work, because both *stf1* (DHC1b null) and *fla14* (LC8 null) also affect subunits of the retrograde IFT complex and have defects in flagellar assembly and length (Porter *et al.,* 1999; Pazour *et al.,* 1998; Figure 4.7C). We also determined that the length of the flagella depends on the amount of LIC present. *LIC RNAi-B,* with only a slight knockdown, has slightly shorter flagella, while *LIC RNAi-A,* with much less LIC, has even shorter flagella (Figure 4.8A). Moreover, it takes *LIC RNAi-A* cells longer to assemble the short flagella than wild-type cells to assemble normal length flagella (Figure 4.8B). The hypothesis that decreases in retrograde IFT subunits affect flagellar length in a dose specific manner could be further tested by developing RNAi strains that knockdown either the cDhc1b or FAP133 subunits. However, our results are consistent with observations by Asai *et al.,* (2009), in which knockdown of dynein-2 in *Tetrahymena* resulted in slow cilia growth, fewer cells with cilia and generally shorter flagella.

Reductions in LIC cause IFT defects in a dose specific manner

Hou *et al.* (2004) did not analyze IFT parameters in the *d1blic* mutant, and so we analyzed IFT directly by DIC microscopy. Not surprisingly, we observed that the *d1blic* has IFT defects, with reduced retrograde velocity, reduced particle frequency, and fewer retrograde particles (Table 4.3, Figure 4.9). To confirm these defects were specific to the

loss of LIC, we also assessed IFT parameters in the rescued strain, *d1blic::LIC-GFP*. Here, we observed increases in the retrograde velocity, frequency and frequency ratio back towards wild-type levels (Table 4.3, Figure 4.9). However, like the flagella length experiments, the recovery was not completely wild-type (Table 4.3, Figure 4.9). Incomplete rescue could be due to reduced expression of LIC-GFP protein by the transgene relative to the wild-type protein (Figure 4.5A, Figure 4.9C). In any case, we conclude that the IFT defects in *d1blic* are caused by loss of LIC.

The effects on IFT are more severe as expression of the LIC decreases. *LIC RNAi-B* has reduced retrograde velocity, frequency, and frequency ratios compared to wild-type, but increased as compared to *RNAi-A* (Table 4.3, Figure 4.9). Notably, the decreases in retrograde IFT in the *RNAi-A* strain were similar to those measured in the *d1blic* null mutant (Table 4.3, Figure 4.9), even though the average flagellar length was slightly longer. Interestingly, decreases in velocity seen in either *LIC RNAi-A* or *d1blic* are not quite as severe as those seen in two other retrograde IFT mutants, *pf15 fla2* and *pf15 fla24* (Table 4.3, Figure 4.9). This may suggest that the yet-unidentified polypeptides affected in *fla2* and *fla24* have a more drastic effect on the retrograde IFT complex.

IFT particle movement versus GFP tagged IFT subunit movement

When we first observed movement of the GFP tagged subunit KAP (Mueller *et al.,* 2005), we were unable to obtain quantitative data on IFT parameters due to technical limitations of our imaging system. Since then, we and other groups have begun to assess the movement of GFP tagged molecules using cameras with greater sensitivity and time resolution. Interestingly, we first noticed that the KAP-GFP (and LIC-GFP) proteins observed by conventional fluorescence microscopy appeared to move ~30% slower than the IFT particle observed by DIC (Table 4.4, Figure 4.10C). We further determined that the high intensity light source used to illuminate cells during conventional fluorescence microscopy was responsible for the decreased rates of IFT (Figure 4.10A).

To adjust for this limitation, we have recently used TIRF microscopy in combination with DIC microscopy. Both Engel *et al.* (2009) ad Lechtreck *et al.* (2009)

used TIRF methods to investigate the movement of KAP-GFP, but these groups did not determine whether the IFT particle viewed by DIC moves at the same rate as the GFP tagged KAP. Our recent measurements suggest that the GFP-tagged proteins (KAP-GFP and LIC-GFP) move significantly faster when observed by TIRF microscopy than the IFT particles from cells in the same culture ($p < 0.005$, Table 4.4, Figure 4.10C). This increase in speed is more apparent in the retrograde direction (Table 4.4, Figure 4.10C). Lechtreck *et al.* (2009) also observed an apparent increase in rate between the IFT particle and KAP-GFP (Table 4.4); however, they did not address this anomaly in their discussion of the data. Additional work is needed to determine the source of this discrepancy.

Several hypotheses can be made that could explain this phenomenon. First, it is possible that LIC-GFP and KAP-GFP actually move faster than the IFT particle, but this seems unlikely as other evidence has suggested that there is only one IFT motor for each direction in *Chlamydomonas*. It is also possible that halogen light used for DIC microscopy also has a phototoxic effect on the cells, and that illuminating the cells with a monochromatic laser in TIRF provides the most accurate estimates of the IFT rates. Finally, it is possible that not enough IFT particles have been analyzed in direct comparison to the GFP tagged proteins, as the number of flagella analyzed thus far for IFT particle movement is much less than the number of flagella analyzed for GFP-tagged protein movement. This question can be addressed by 1) analyzing more flagella by DIC microscopy on the TIRF microscope; and 2) by analyzing an individual cell for both IFT particle and GFP tagged protein movement. In this case, we can directly compare both types of movement. Efforts are currently underway to increase our sample sizes as well as establish conditions for imaging the same cell with both DIC and TIRF optics.

We have also determined clearly that the KAP-GFP protein undergoes retrograde transport (Table 4.4, Figure 4.10C). This is in contrast to Engel *et al.,* (2009), who published that KAP-GFP does not undergo retrograde IFT movement. Furthermore, they hypothesized that KAP-GFP must diffuse slowly back to the cell body from the flagella tip (Engel *et al.,* 2009). Our work, plus the KAP-GFP retrograde rates published in Lechtreck *et al.* (2009) refute this hypothesis.

Disruptions of IFT cause photobehavior defects

Several studies have found that defects in proteins that are transported by IFT are correlated with defects in photobehaviors. First, CAV2, a calcium channel involved in the photoshock response, appears to be transported by IFT. In the *ppr2* mutant null for CAV2, cells are unable to exhibit a photoshock response (Fujiu *et al.,* 2009). Similarly, BBS4, a signaling protein with putative roles in protein trafficking to the flagella, is transported by IFT. *bbs4* mutant cells null for BBS4 are unable to phototax normally (Lechtreck *et al.,* 2009). From these studies, we hypothesized that disrupting the IFT machinery might prevent signaling proteins such as CAV2 and BBS4 from getting into or out of the flagella and result in defects in photobehaviors. Our hypothesis was correct in that some IFT mutants (*fla3, LIC RNAi-A,* and *fla2*) displayed abnormal photobehaviors, but other IFT mutants exhibited normal photobehaviors (*fla10, LIC RNAi-B* and *fla24;* Table 4.5, Table 4.6). At this point, we cannot make simple generalizations about which class of mutants will or will not exhibit normal photobehaviors. For example, some anterograde mutants like *fla10* can undergo both photoshock and phototaxis responses while *fla3* does not. This is also the case for retrograde mutants, as both the *LIC RNAi-A* and *fla2* display defects in photobehavior whereas *LIC RNAi-B* and *fla24* do not (Table 4.5, 4.6).

To determine what characteristics of an IFT mutant might be correlated with defects in phototaxis and photoshock, we also analyzed the expression of various IFT proteins in isolated flagella. First, we analyzed whether changes in the levels of complex A or B proteins might be correlated with changes in behavior. Complex A and B are increased in both *LIC RNAi* strains and *fla24,* but not *fla2,* whereas photobehaviors are affected only in *LIC RNAi-A* and *fla2* (Figure 4.6C, 4.7B; Table 4.5, 4.6). Thus, changes in complex A or B do not appear to be correlated with photobehavior. Reduction of the LIC might cause behavior defects, as *LIC RNAi-A* has lower LIC and abnormal photobehaviors as compared to *LIC RNAi-B*. However, *fla2* has wild-type LIC levels and abnormal photobehaviors (Figure 4.6C, 4.7B; Table 4.5, 4.6). Therefore, the level of LIC expression does not always correlate with photobehavior defects. The only case where

protein expression might be correlated with photobehavior defects is FAP133. Here, strains with reduced levels of FAP133 in the flagella (*fla2, LIC RNAi-A*) were unable to photoshock and phototax, while *fla24* and *LIC RNAi-B* have normal FAP133 expression and normal photobehaviors (Figure 4.6C, 4.7B, Table 4.5, 4.6). Additional studies of the *fla* mutants at the restrictive temperature as well as FAP133 mutants generated by RNAi may provide additional insights into the relationship between retrograde transport and photobehavior.

It is also possible that subtle changes in the levels of IFT motor and particle proteins cannot be used to predict which signaling proteins might be transported into and out of flagella. Rather, the expression of other proteins involved in sorting signaling proteins might be more relevant in predicting photobehavior phenotypes. To investigate this hypothesis, we will probe whole flagella with antibodies to other signaling proteins, such as CAV2, BBS4, AGG2, and AGG3. To start, we probed whole flagella with an antibody to AGG3, a protein involved in phototaxis (Smyth and Ebersold, 1985; Iomini *et al*., 2006). We saw a reduction of AGG3 protein in all IFT mutant flagella (Figure 4.7B, Table 4.5, 4.6). However, it is unclear if this reduction is due to inefficient transport of Agg3 into the flagella or results from the different genetic backgrounds of the strains. To determine which explanation is more plausible, we will probe CC-125 and CC-124, two wild-type strains with opposite phototaxis signs, for Agg3 expression. If we see low expression of Agg3 in CC-124 (negative phototaxis), we can assume that Agg3 expression depends on the genetic background, not IFT. Next, we will use antibodies to CAV2 and BBS4 to determine if changes in levels of these proteins correlates with photobehavior changes.

In summary, we have evaluated the role of the LIC in flagellar assembly, retrograde IFT, and the response of the cell to various light induced stimuli. We have demonstrated that the levels of LIC expression are closely correlated with defects in these pathways. In addition, we have shown that a LIC-GFP transgene will rescue both flagellar assembly and IFT defects in a null mutant. Additional work is needed to obtain convincing data that the GFP-tagged subunits of both the anterograde and retrograde motors move at rates comparable to that of the IFT particle visible by DIC microscopy.

We have identified several experimental parameters that have affected the quality of the data that we obtained. We will continue to develop strategies that will permit us to make more accurate measurements of these parameters. We have also evaluated several other IFT mutants to determine which strains are associated with defects in photobehavior, but we have not yet been able to determine what characteristic of the strains causes the abnormal phenotypes. Additional work is needed to more rigorously define the protein composition of the isolated in flagella in those strains with clearly defined defects in photobehaviors.

4.5. TABLES AND FIGURES

Table 4.1. Summary table of IFT mutant strains.

	Axonemal Phenotype	*IFT Direction Affected*	*Original Study*
Control Strains			
Wild-type +(CC-125)	Wild-type	None	
Wild-type – (CC-124)	Wild-type	None	
ppr2	Defective CAV2 channel	None	Fujiu *et al.,* 2009
mia2 (CC-4266)	Increased P-IC138	None	King and Dutcher, 1997
Anterograde Motor Mutants			
fla10 (CC-1919)	Kinesin ts mutant	Anterograde	Huang *et al.,* 1977; Adams *et al.,* 1982
fla3 1b (CC-4283)	KAP ts mutant	Anterograde	Mueller *et al.,* 2005
fla3 1B::KAP-GFP (CC-4296)	KAP-GFP rescue	None	Mueller *et al.,* 2005
Retrograde Motor Mutants			
stf1 (CC-3915)	DHC1b null		Porter *et al.,* 1999
d1blic (T8D9)	LIC null	Retrograde	Hou *et al.,* 2004
d1blic::LIC-GFP	LIC-GFP rescue	None	This study
LIC RNAi – B (4A2)	LIC knockdown (20%)	Retrograde	This study
LIC RNAi – A (4Ell)	LIC knockdown (<10%)	Retrograde	This study
fla14 (CC-3937)	LC8 mutant	Retrograde	Pazour *et al.,* 1998
fla14::LC8 (CC-3939)	LC8 rescue	None	Pazour *et al.,* 1998
Retrograde IFT Mutants			
fla2 (CC-1390)	Unknown	Retrograde	Huang *et al.,* 1977; Adams *et al.,* 1982
fla15 (CC-3861)	IFT144 ts mutant	Retrograde	Piperno *et al.,* 1998; Iomini *et al.,* 2009
fla16 (CC-3862)	Unknown	Retrograde	Piperno *et al.,* 1998
fla17 (CC-3863)	IFT139 ts mutant	Retrograde	Piperno *et al.,* 1998; Iomini *et al.,* 2009
fla24 (CC-3866)	Unknown	Retrograde	Huang *et al.,* 1977; Adams *et al.,* 1982
Length Control Mutants			
lf3 (CC-2289)	LF3p mutant	None, but IFT particles accumulate	Barsel *et al.,* 1988; Tam, *et al.,* 2003

Table 4.2. Proteins in the *Chlamydomonas reinhardtii* IFT machinery, their associated mutants, and homologues in *C. elegans* and humans, if known.

C. reinhardtii IFT protein, mutant if known	*C. elegans* Protein homologue	*H. sapiens* Protein homologue
Heterotrimeric Kinesin-2		
FLA10, *fla10*	KLP-20	KIF3A
FLA8, *fla8*	KLP-11	KIF3B
KAP, *fla3*	KAP-1	KAP3
Cytoplasmic dynein 2		
DHC1b, *stf1*	CHE-3	DYNCH1
LIC, *d1blic*	D2LIC, XBX-1	DYNC2LI1
FAP133	DYCI-1	WDR34
LC8, *fla14*	DLC-1	DYNLL1
IFT Complex A		
IFT144, *fla15*	DYF-2	WDR19
IFT140	CHE-11	IFT140
IFT139, *fla17*	ZK328.7	THM1
IFT122	DAF-10	IFT122
IFT121	IFTA-1	WDR35
IFT43	-	IFT43
IFT Complex B		
IFT172, *fla11*	OSM-1	IFT172
IFT88, *ift88*	OSM-5	IFT88
IFT81	IFT-81	IFT81
IFT80	CHE-2	IFT80
IFT74/72	IFT-74	IFT74/72
IFT70	DYF-1	TTC30
IFT57	CHE-13	IFT57
IFT54/FAP116	DYF-11	IFT54/MIPT3
IFT52, *bld1*	OSM-6	IFT52/NGDS
IFT46, *ift46-1*	DYF-6	IFT46/C11orf60
IFT27	-	IFT27/RABL4
IFT25/FAP232	-	IFT25/HSPB11
IFT22/FAP9	IFTA-2	RABL5
IFT20	Y110A7A.20	IFT20

Figure 4.1. Cr LIC has human homologues. (A) Clustal-W alignment between *Chlamydomonas reinhardtii* dynein light intermediate chain (LIC) vs. *Homo sapiens* dynein (cytoplasmic 2) light intermediate chain 1 (Dc2LIC1). (B) Table showing BLAST results for the *Chlamydomonas* LIC protein. (K. VanderWaal)

A)

B)

Organism	*Protein name of best hit*	*Accession number*	*BLAST score*	*E-value*
Volvox carteri	Cytoplasmic dynein 1b light intermediate chain, D1bLIC	XP_002952157	595	5e-168
Strongylocentrotus purpuratus	Hypothetical protein	XP_794270	137	4e-30
Homo sapiens	Cytoplasmic dynein 2 light intermediate chain isoform 1	NP_057092	134	3e-29
Mus musculus	cytoplasmic dynein 2 light intermediate chain 1	Q8K0T2	133	6e-29
Trypanosoma cruzi	dynein light intermediate chain	XP_812285	112	1e-22
Caenorhabditis elegans	X-Box promoter element regulated family member (xbx-1)	NP_506683	94	4e-17
Drosophila melanogaster	IP11519p	AAY54788	63	7e-08

Figure 4.2. Cr FAP133 has human homologues. (A) Clustal-W alignment between *Chlamydomonas reinhardtii* FAP133 vs. *Homo sapiens* WD34. (B) Table showing BLAST results for the *Chlamydomonas* FAP133 protein. (K. VanderWaal)

A)

```
FAP133          MQEVPPDFEDVHIAEAR---------------VDVPSTWR DQIVNTNAVATETHPLKCA 44
WDR34           -SAGVAALATVGVASGPGPGRPGPLQDETLGVASVPSQWRAVQGIRGETKSCQTASIATA 59
                 .   . :  * :*..                 ..*** **  * :. :: : :* .:  *

FAP133          EVETQTGSKDNQGTQTDDAGGGRPPSPSKVQASGVADFMAKVEGMVAGELVKATEEHEVL 104
WDR34           SASAQARNHVDAQVQTEAPVPVSVQPPSQYDIPRLAAFLRRVEAMVIRELNKNWQSHAFD 119
                ...:*: .: :  .**: .      .**: : . :* *: :**.**  ** *  :.* .

FAP133          EPFTRAADDEQEPATCIHYLSPFQQDAAANQDLNATSTQLNKHKLVVTGVSWSSTGQTIA 164
WDR34           G--FEVNWTEQQMVSCLYTLGYPPAQAQG---------------LHVTSISWNSTGSVVA 162
                    ..   **: .:*:: *.    :* .               * **.:**.***..:*

FAP133          ASFGRYDVVGWCTYPGMLCTWNLGREEVNATRPDTRIDTDTCLMSCAFHPAHPALIAGGT 224
WDR34           CAYGRLDHGDWSTLKSFVCAWNLDRRDLRPQQPSAVVEVPSAVLCLAFHPTQPSHVAGGL 222
                .::** *  .*.*  .::*:***.*.::.. :*.: ::. :.::. ******:*: :***

FAP133          FNGELYVWDLSLEGDSQRGRSDVLLDVRHMEPIIAITWQYNMTDAAKYGTKDKSYRLVTL 284
WDR34           YSGEVLVWDLSRLEDPLLWR-TGLTDDTHTDPVSQVVWLP-------EPGHSHRFQVLSV 274
                :.**: *****   *.   *   * *  * :*:  :.*           :.: ::::::

FAP133          GADGKVLTWLWHKLDAPVYGYQLMFPQPGVDRKFVWGGACMGFQREPRGTSTAARDKETG 344
WDR34           ATDGKVLLWQGIGVGQLQLTEGFALVMQQLPR-------STKLKKHPRGETEVG--ATAV 325
                .:***** *    :.       : :    : *       .  :::.*** : ..    :

FAP133          LHGGDAAGTFLVGTEGGKIFKCYNDANDVNTKEFSRAVGAGERVELRTPVREGGYQPHAG 404
WDR34           AFSSFDPRLFILGTESGFPLKCSLAAGEAALTRMP------SSVPLRAPAQFT-FSPHGG 378
                 ...  .  *::***.*  :**   *.:.  ..:.      . * **:*.:   :.**.*

FAP133          AVFGLDCSPFQRELFLTGSTDGSVRMYSSLRMQPLLHLEPTSSYLFVVQWSPFRPLVFAA 464
WDR34           PIYSVSCSPFHRNLFLSAGTDGHVHLYSMLQAPPLTSLQLSLKYLFAVRWSPVRPLVFAA 438
                .::.:.****:*:***:..*** *::** *:  **  *: : .***.*:***.*******

FAP133          AAGDGCVYLFDLARQQEVVRPVLTLDANGMRKPVYSLAFNPRKPDMLATGDPTG-IQIWR 523
WDR34           ASGKGDVQLFDLQKSS--QKPTVLIKQTQDESPVYCLEFNSQQTQLLAAGDAQGTVKVWQ 496
                *:*.* * **** :..   :*.: :. .  ..***.* **.::.::**:**. * :::*:
```

B)

Organism	*Protein name of best hit*	*Accession number*	*BLAST score*	*E-value*
Volvox carteri	Hypothetical protein	XP_002956238	587	2e-165
Strongylocentrotus purpuratus	Hypothetical protein	XP_788363.2	281	2e-73
Mus musculus	WD repeat-containing protein 34	NP_001008498.2	238	2e-60
Homo sapiens	WD repeat domain 34	AAH11874	233	6e-59
Trypanosoma cruzi	Hypothetical protein, conserved	EAN85940.1	134	3e-38
Caenorhabditis elegans	none			
Drosophila melanogaster	none			

Figure 4.3. The LIC and IC are subunits of the DHC1b complex.

A) Western blots of extractions of the E8 strain. WF = whole flagella, M+M = membrane plus matrix, WA = whole axonemes, 1mM, 5mM, and 10mM = MgATP concentrations in ATP extractions, HSE = high salt extraction with 0.6M NaCl, OD = axonemal proteins remaining after extraction including outer doublets. Extracts are probed with antibodies to DHC1b, FAP133, LIC, LC8, IFT81, IFT139, FLA10 and 1β HC. LIC, FAP133, and DHC1b extract similarly; IFT81 and IFT139 extract similarly; and FLA10 and 1β HC extract similarly (R. Bower and C. Perrone, Perrone *et al.,* 2003).

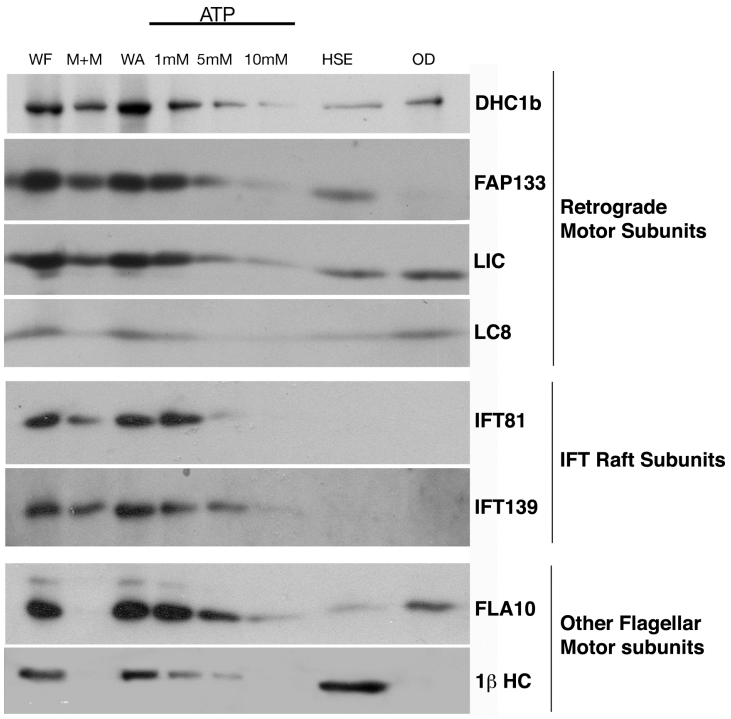

B) Membrane plus matrix extracts from (A) are loaded on sucrose density gradients and centrifuged. Western blots of the resulting fractions are probed with antibodies to LIC, DHC1b and FAP133 and demonstrate co-sedimentation of FAP133, LIC and DHC1b (R. Bower and C. Perrone, Perrone *et al*., 2003).

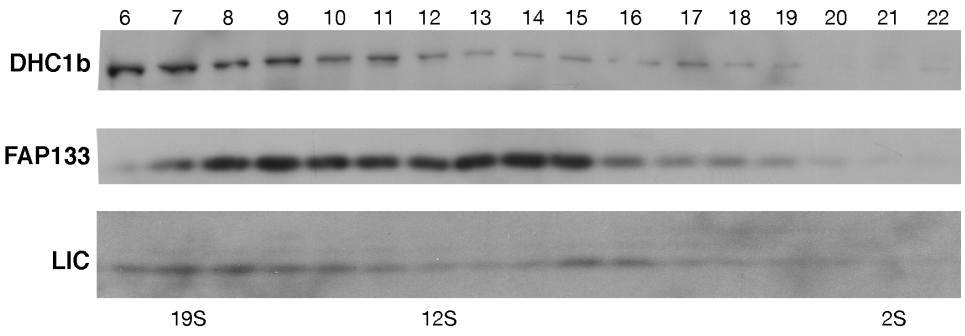

C) 1mM ATP extracts from (A) are loaded on sucrose density gradients and centrifuged. Western blots of the resulting fractions are probed with antibodies to LIC, DHC1b and FAP133 and demonstrate co-sedimentation of LIC and DHC1b, with FAP133 dissociation (R. Bower and C. Perrone, Perrone *et al*., 2003).

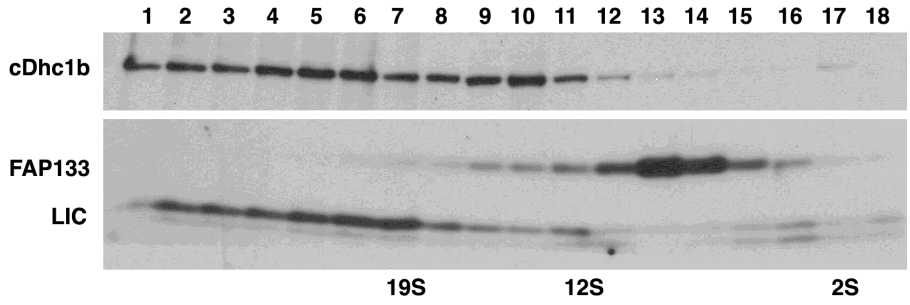

D) ATP extracts from (A) are used for immunoprecipitations. The first column shows the ATP extract, the second is a control IP and the third, an IP using the LIC antibody. All are probed with DHC1b, LIC, FAP133, LC8, IFT139 and KAP antibodies. Bands for all proteins are visible in the ATP extract; the IgG band is the only band visible in the control IP; the LIC IP pulls down LIC along with DHC1b and FAP133 (R. Bower, Perrone *et al*., 2003).

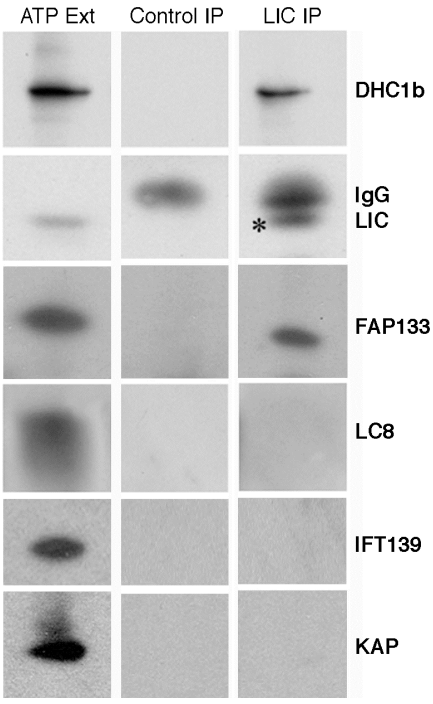

Figure 4.4. Knockdown of LIC expression and rescue by transformation with LIC-GFP. (A) Schematic diagram of the genomic and cDNA construct used to knockdown expression of the LIC (D. Tritschler). (B) Schematic diagram of a GFP-tagged LIC gene construct used to for transformation and rescue of the LIC mutant (D. Tritschler). (C) Western blot of whole cell extracts from wild-type, *LIC RNAi*, *d1blic,* and *d1blic::LIC-GFP* strains probed with antibodies against the LIC and tubulin as a loading control (D. Tritchler and R. Bower). (D) Western blot of fractions obtained by sucrose density gradient centrifugation of a membrane plus matrix extract of E8 flagella. The LIC-GFP co-sediments with the endogenous LIC and DHC1b subunits in the bottom half of the gradient. (D. Tritchler and R. Bower).

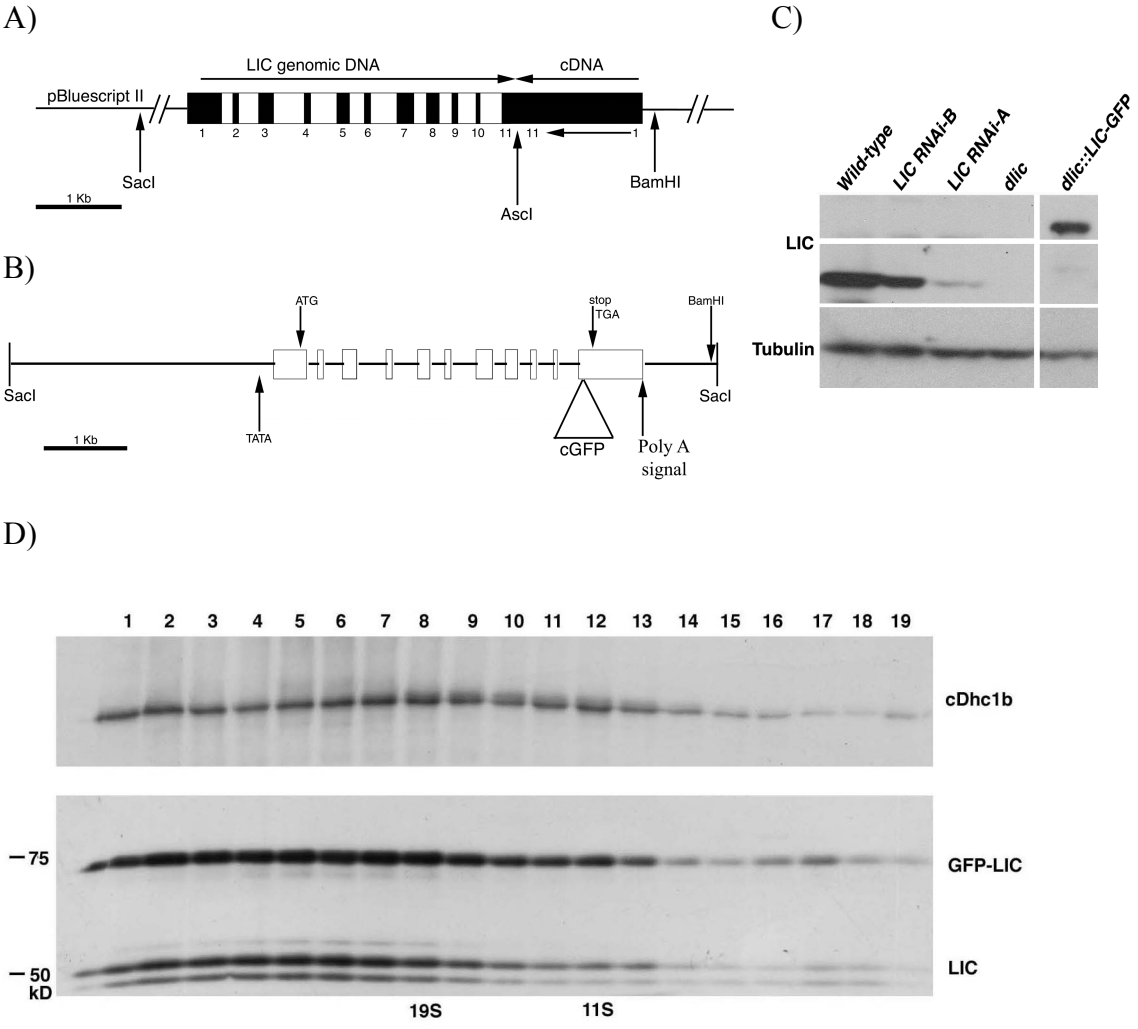

Figure 4.5. Expression of LIC, FAP133, IFT139 and IFT172 in the wild-type, *d1blic,* and *d1blic::LIC-GFP* strains. (A) Immunoblots of whole cell extracts probed with antibodies to LIC, FAP133 and tubulin (loading control). (B) DIC and epifluorescence images of fixed cells probed with LIC, FAP133, IFT139 (complex A) and IFT72 (Complex B) antibodies. (C. Perrone, D. Tritschler and R. Bower)

A) Whole cell blots.

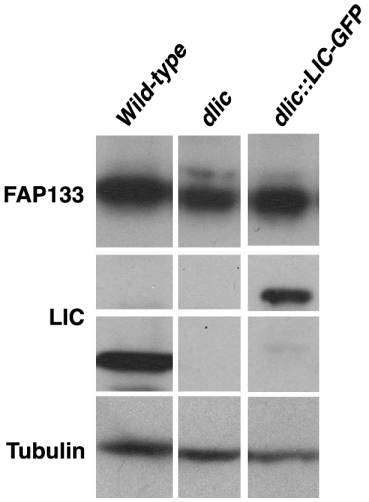

B) Immunofluorescence

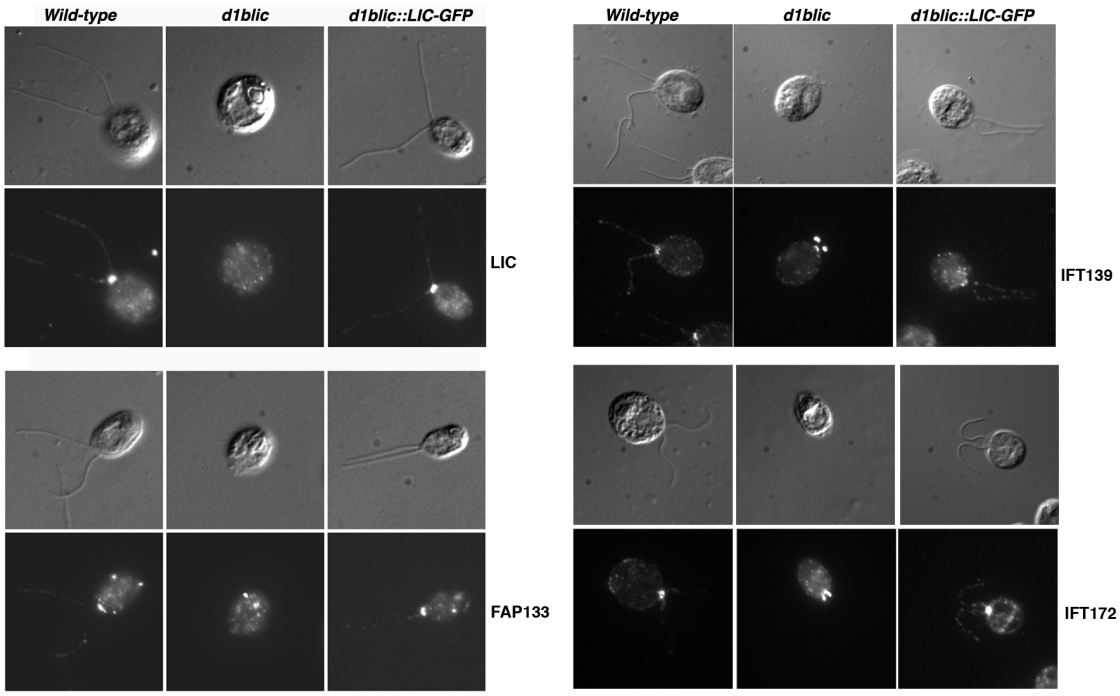

Figure 4.6. Expression of LIC, FAP133, DHC1b, IFT139 and IFT172 in wild-type, *LIC RNAi-A* and *LIC RNAi-B* strains. (A) Immunoblots of whole cell extracts were probed with antibodies against the LIC, FAP133 and tubulin (loading control). FAP133 levels are approximately the same in all three strains while LIC levels are reduced in the *LIC RNAi* strains (D. Tritchler, R. Bower). (B) Immunoblots of whole cell extracts probed with antibodies against DHC1b, LIC, and tubulin. Again, LIC levels are reduced in the *LIC RNAi* strains as well as DHC1b levels (D. Tritchler, R. Bower). (C) Immunoblots of isolated flagella probed with antibodies against the LIC, FAP133, IFT81, IFT172, Agg3 and IC69 (loading control). LIC and FAP133 gradually reduce in the *RNAi* strains, while IFT81 and IFT172 appear to accumulate. IC69 levels are slightly higher in both *LIC RNAi* strains than in wild-type (K. VanderWaal, J. Reck).

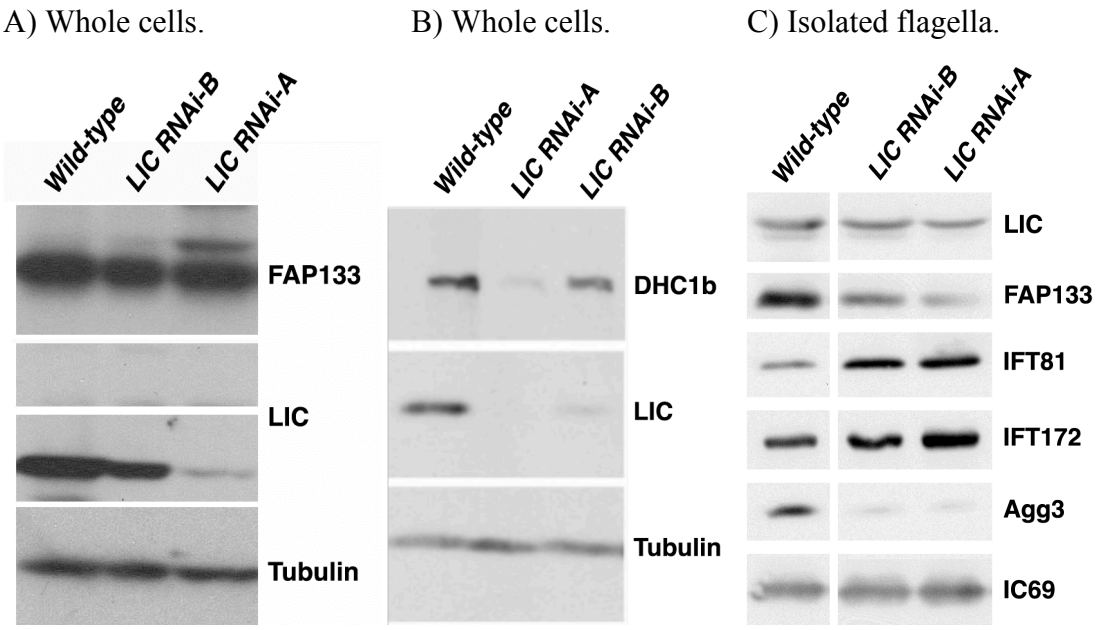

D) DIC and epifluorescence images of fixed wild-type and *LIC RNAi* cells probed with antibodies against the LIC, FAP133, IFT139, and IFT72 (C. Perrone).

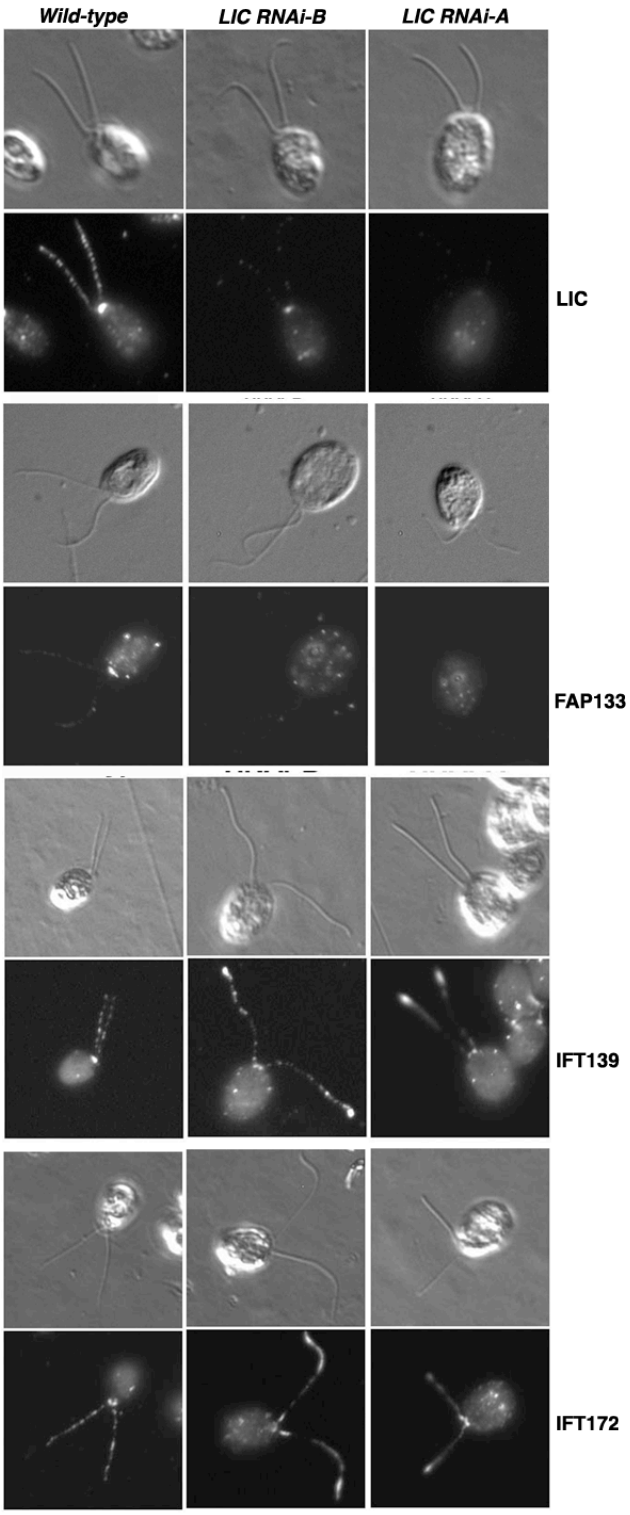

Figure 4.7. Expression and distribution of FAP133, LIC, IFT139 and IFT172 in IFT mutant strains. (A) Immunoblots of whole cell extracts from wild-type, *stf1, fla14,* and *fla14::LC8* were probed with antibodies against the LIC, FAP133 and tubulin. LIC and FAP133 levels are approximately wild-type in the *fla14* strains, but slightly reduced in *stf1* (D. Tritschler, R. Bower). (B) Immunoblots of whole flagellar extracts from wild-type and two retrograde mutants *fla2* and *fla24* probed with antibodies against LIC, FAP133, IFT81, IFT172, Agg3, and IC69. *Fla2* has reduced amounts of FAP133 and Agg3. *fla24* has increased amounts of LIC, IFT81, IFT172 and Agg3. (K. VanderWaal, J. Reck).

A) Whole cells.

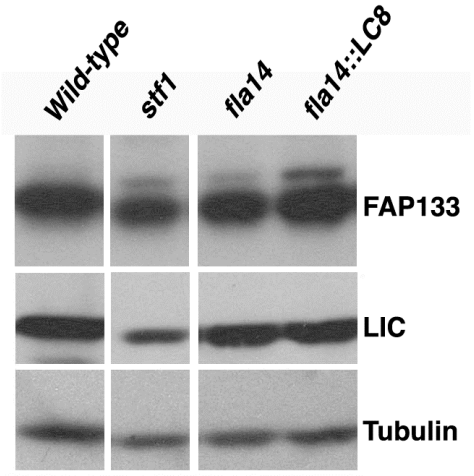

B) Whole flagella.

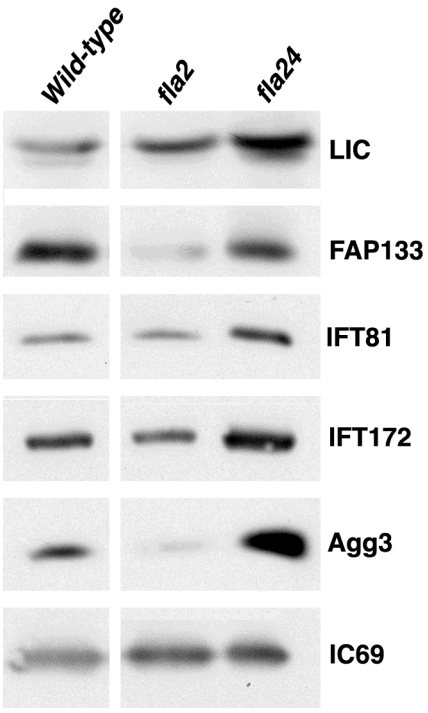

C) DIC and epifluorescence images of fixed wild-type *fla14, sft1, fla16* and *lf3* labeled with LIC and FAP133 antibodies. (K. VanderWaal)

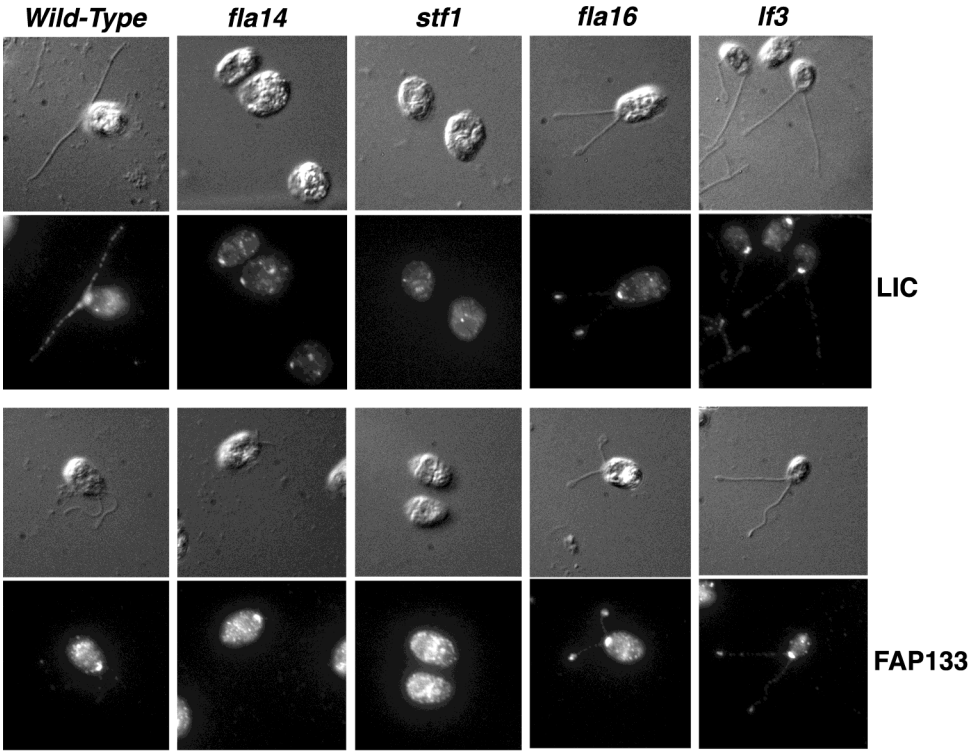

D) DIC and epifluorescence images of fixed wild-type, *fla2* and *fla24* probed with LIC antibody. (C. Perrone, K. VanderWaal)

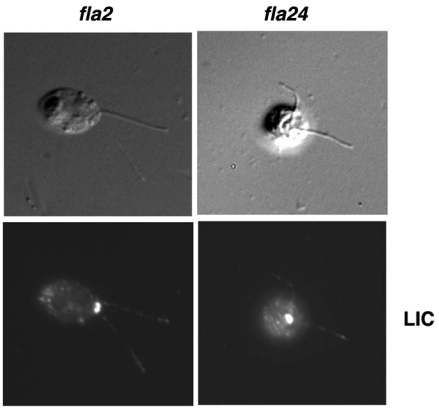

Figure 4.8. LIC RNAi knockdown strains and LIC null strains have flagellar assembly defects. **(**A) *dlic* and *LIC RNAi* strains have shorter flagella than wild-type. Length is restored to near *RNAi-B* levels in *dlic::LIC-GFP* (n = 70 flagella per strain) (D. Tritschler). (B) Flagellar regeneration after excision by pH shock. Growth is slower in the RNAi-A strain (n = 50 flagella per time point per strain) (D. Tritschler).

A)

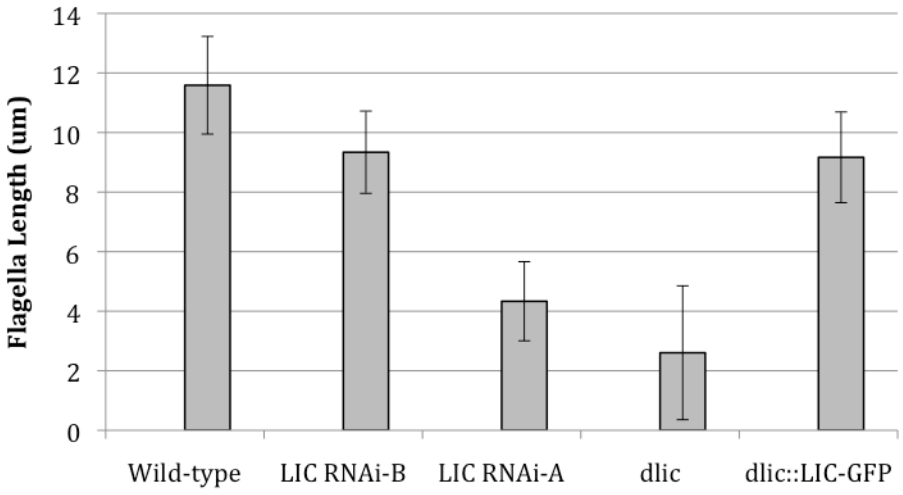

B)

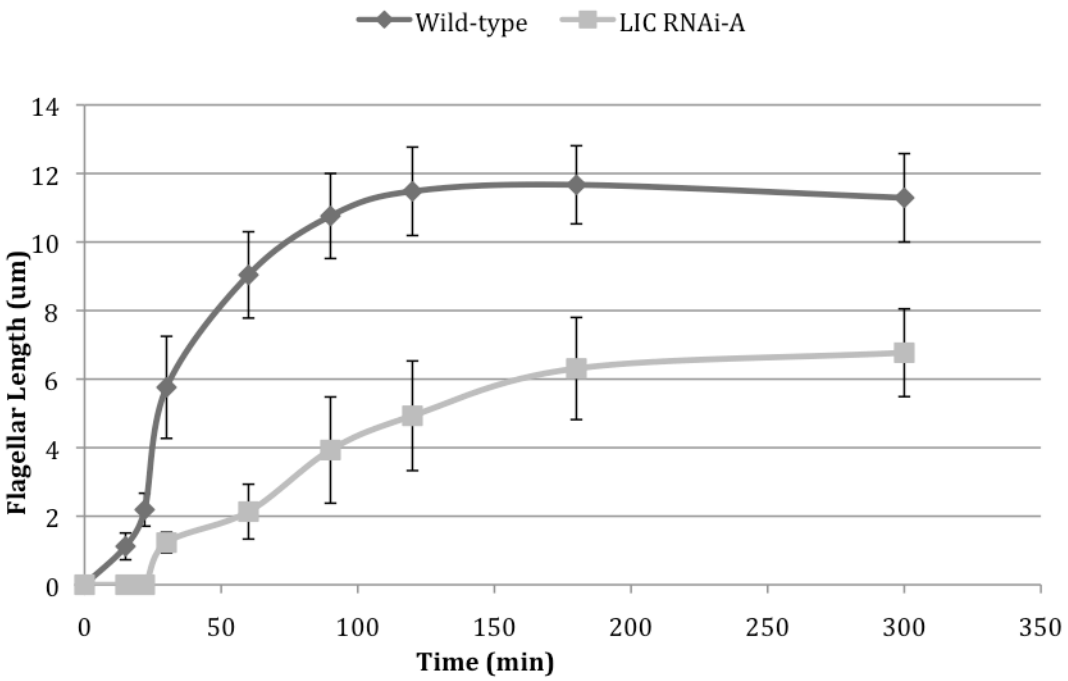

Table 4.3. IFT rates of IFT mutant strains and rescues via DIC microscopy. (C. Perrone, K. VanderWaal)

Strain	*Flagella/ Particles analyzed (N / n)*	*Ant. Velocity (μm/s)*	*Ret. Velocity (μm/s)*	*Frequency (p/s)*	*Ant. Frequency (p/s)*	*Ret. Frequency (p/s)*	*Ant./Ret. Frequency ratio*
Control Strains							
Wild-type	22 / 440	2.1 (0.3)	3.4 (0.7)	5.6 (1.0)	2.0 (0.4)	3.6 (0.7)	0.5 (0.1)
Anterograde Motor Mutants							
*pf15 fla10**	13 / NR	1.4 (0.2)	3.5 (0.4)	3.0 (0.8)	NR	NR	0.6 (0.1)
fla31b	22 / 376	1.6 (0.3)	2.8 (0.5)	2.3 (0.6)	0.5 (0.2)	1.9 (0.5)	0.2 (0.1)
fla3 1b:: KAP-GFP	13 / 360	2.2 (0.3)	3.4 (0.7)	4.2 (0.8)	1.5 (0.4)	2.8 (0.6)	0.6 (0.1)
Retrograde Motor Mutants							
d1blic	24 / 420	2.1 (0.3)	1.5 (0.5)	2.1 (0.7)	1.4 (0.4)	0.5 (0.5)	2.7 (2.0)
d1blic:: LIC-GFP	19 / 380	1.8 (0.3)	2.8 (0.5)	4.9 (0.8)	1.8 (0.4)	3.1 (0.4)	0.6 (0.1)
LIC RNAi-A	49 / 978	1.7 (0.3)	1.4 (0.6)	1.5 (0.6)	1.0 (0.4)	0.5 (0.3)	2.4 (1.5)
LIC RNAi-B	12 / 240	2.1 (0.3)	2.3 (0.7)	3.4 (1.0)	1.6 (0.3)	1.9 (0.8)	1.1 (0.9)
Retrograde IFT Mutants							
*pf15 fla2**	13 / NR	1.6 (0.2)	1.3 (0.3)	1.5 (0.5)	NR	NR	2.5 (0.6)
fla2	6 / 120	1.6 (0.3)	2.1 (0.4)	3.2 (0.8)	1.1 (0.3)	2.1 (0.6)	0.6 (0.1)
*pf15 fla24**	16 / NR	1.6 (0.2)	0.9 (0.2)	1.4 (0.3)	NR	NR	2.3 (0.7)
fla24	6 / 120	1.8 (0.2)	1.1 (0.2)	2.2 (0.9)	1.2 (0.5)	1.0 (0.4)	1.3 (0.2)

*Rates from Iomini et al., 2001.
NR = Not reported
Ant. = Anterograde
Ret. = Retrograde

Figure 4.9. Kymographs showing patterns of IFT in *LIC* mutant and rescued strains and graphs representing IFT rates. (A) Representative kymographs showing IFT in an individual flagellum acquired by DIC microscopy of wild-type, *LIC RNAi-B, LIC RNAi-A, d1blic,* and *d1blic::LIC-GFP*. (B) Graphs showing retrograde IFT rates obtained by DIC microscopy. Starred strains represent rates published in Iomini *et al.* (2001). (C. Perrone, K. VanderWaal)

A)

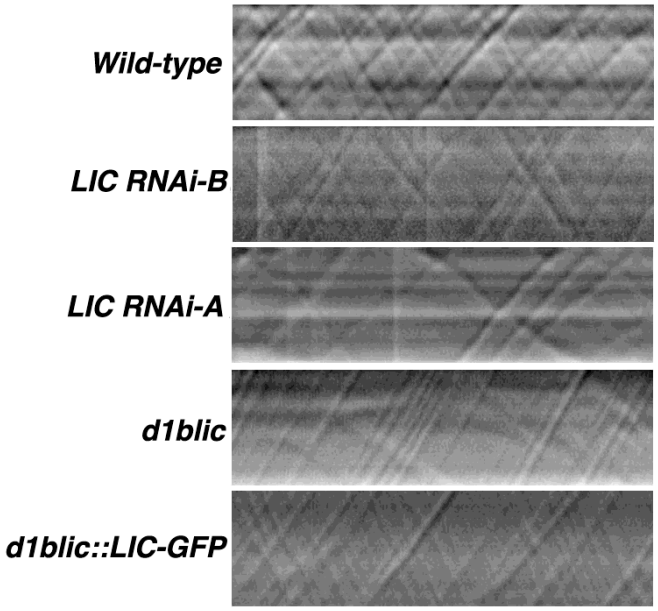

B)

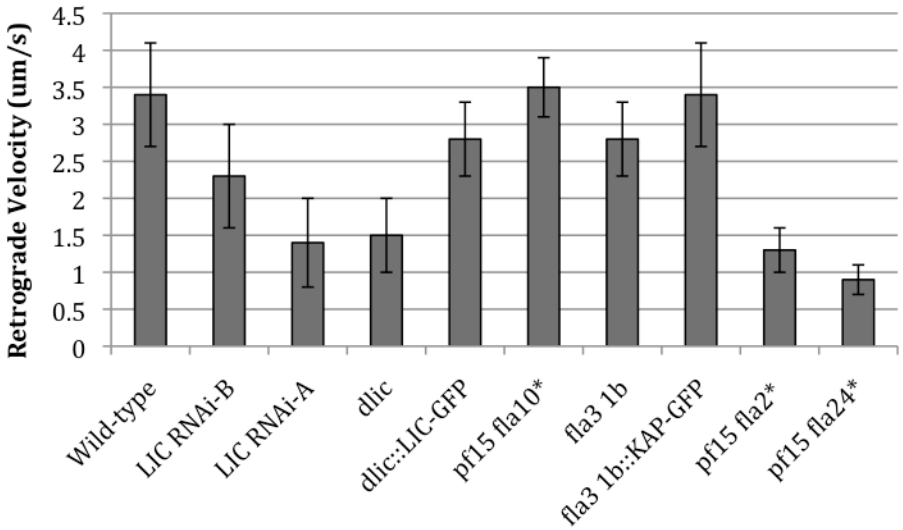

C) Graph and corresponding table of *E8::LIC-GFP* and *d1blic::LIC-GFP* IFT rates acquired by DIC microscopy from the same date. *E8::LIC-GFP* rates are significantly faster than *d1blic::LIC-GFP* ($p < 0.005$). (C. Perrone, K. VanderWaal)

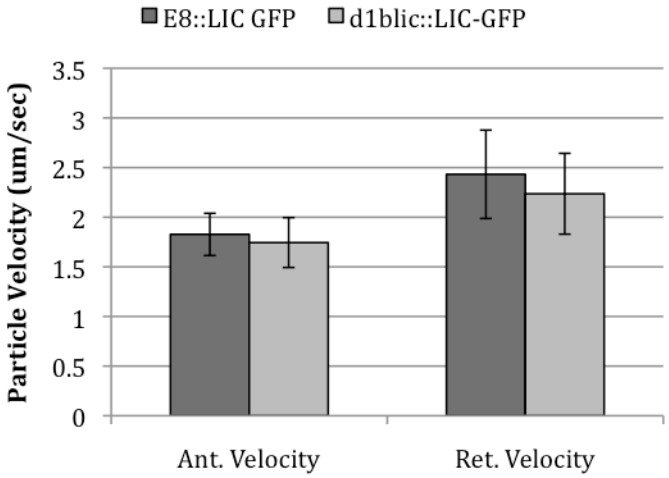

Strain	*Flagella / Particles analyzed (N / n)*	*Ant. Velocity (μm/s)*	*Ret. Velocity (μm/s)*
E8::LIC-GFP	17 / 170	1.8 (0.2)	2.4 (0.4)
d1blic::LIC-GFP	17 / 170	1.7 (0.3)	2.2 (0.4)

Table 4.4. IFT rates of strains expressing LIC-GFP and KAP-GFP by conventional fluorescence and TIRF with corresponding DIC rates. KAP-GFP and LIC-GFP protein velocities are measured using epifluorescence and TIRF microscopy; IFT particle velocities are measured with DIC microscopy. Within each grouping of our data (not from Engel *et al.* 2009 or Lechtreck *et al.,* 2009), numbers that are significantly different from one another are in bold ($p < 0.005$). (K. VanderWaal)

Strain and Rate Type	*Anterograde flagella/particles analyzed (N/n)*	*Anterograde Velocity (μm/s)*	*Retrograde flagella/particles analyzed (N/n)*	*Retrograde Velocity (μm/s)*
fla3 1b::KAP-GFP				
DIC & Epifluor. assays				
IFT particle	56 / 477	**1.9 (0.4)**	56 / 419	2.5 (0.8)
KAP-GFP	36 / 267	**1.5 (0.4)**	36 / 236	2.4 (0.7)
DIC & TIRF assays				
IFT particle	18 / 209	**2.4 (0.8)**	15 / 82	**3.4 (1.4)**
KAP-GFP	31 / 526	**2.7 (1.0)**	31 / 249	**4.3 (2.1)**
KAP-GFP+	NR	1.5 – 2.3	NR	NR
IFT particle#	39 / NR	~1.8	17 / NR	~2.8
KAP-GFP#	57 / NR	~2.1	26 / NR	~4.1
d1blic::LIC-GFP				
DIC and Epifluor. assays				
IFT particle	78 / 1143	**1.8 (0.4)**	78 / 1042	**2.4 (0.7)**
LIC-GFP	71 / 569	**1.2 (0.4)**	71 / 496	**1.9 (0.6)**
DIC and TIRF assays				
IFT particle	17 / 189	2.3 (0.8)	15 / 60	**3.0 (1.3)**
LIC-GFP	37 / 844	2.4 (0.9)	37 / 493	**3.7 (1.5)**

+Rates from Engel et al., 2009
#Rates from Lecktreck et al., 2009
NR = Not Reported

Figure 4.10. Patterns of IFT in *LIC* mutant and rescued strains. (A) IFT rates of one *d1blic::LIC-GFP* flagella acquired by DIC microscopy using halogen light illumination or halogen plus UV illumination. Anterograde rates are significantly slower with UV light ($P < 0.005$) but retrograde rates are not affected ($p = .685$). (B) Representative kymographs acquired by epi- and TIR- fluorescence microscopy of *LIC-GFP* expressing cells. Much better clarity is seen with TIRF. Horizontal bar represents 1 sec, vertical bar represents 3 μm. (K. VanderWaal)

A)

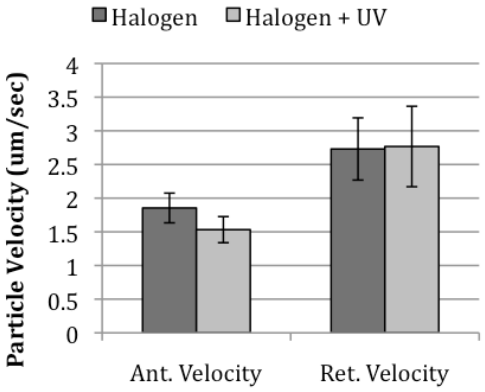

Illumination	*Particles analyzed (n)*	*Ant. Velocity (μm/s)*	*Ret. Velocity (μm/s)*
Halogen	55	1.9 (0.2)	2.7 (0.5)
Halogen + UV	90	1.5 (0.2)	2.8 (0.6)

B)

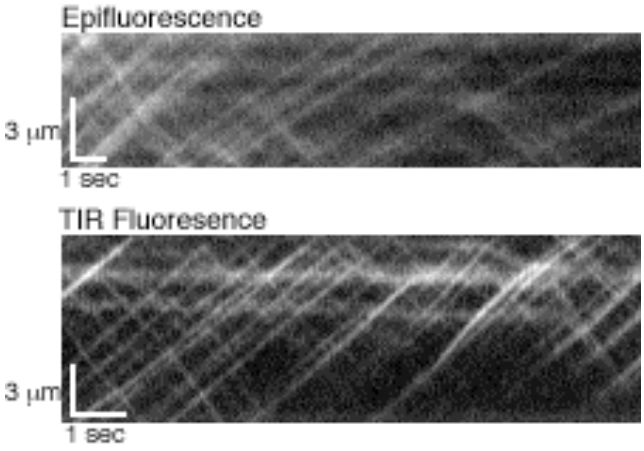

C) Graphs showing IFT rates obtained by fluorescence or TIRF microscopy (See Table 4.4). (K. VanderWaal)

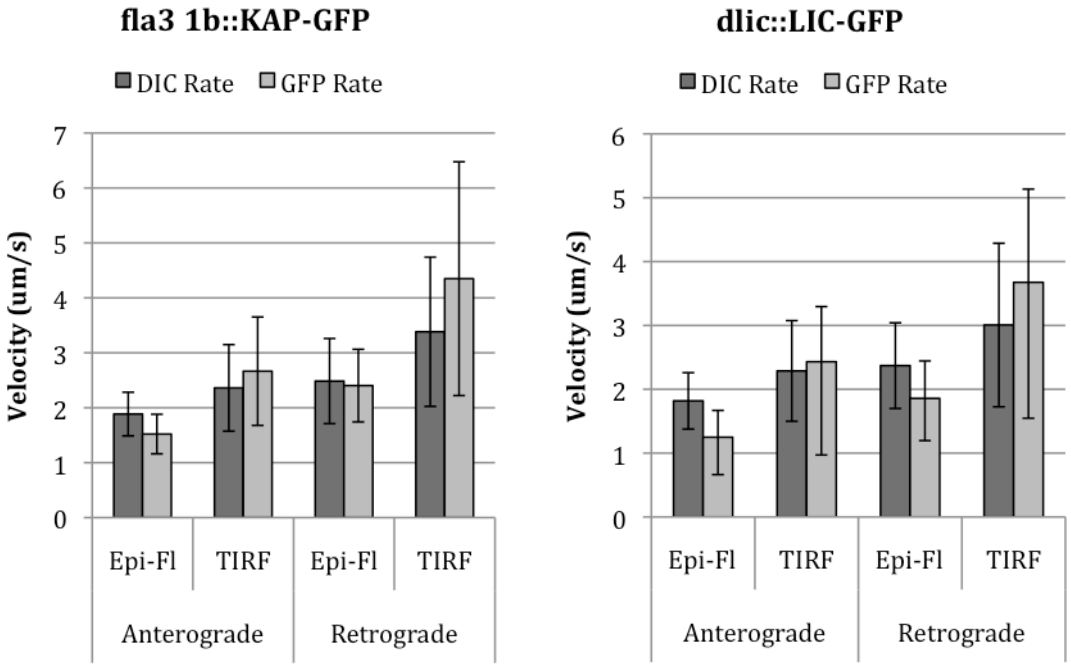

Table 4.5. Photoshock responses in wild-type and mutant strains. (See Figure 3.6 on photoshock for example photographs of photoshock behavior) (K. VanderWaal, J. Reck)

Strain	*Reversal*	*Pause/direction change*	*No change*	*Number of cells scored*
Control strains				
Wild-type +	**92%**	8%	0%	50
Wild-type -	**90%**	10%	0%	30
mia1-1	0%	**100%**	0%	30
ppr2	0%	12%	**88%**	25
Anterograde Motor Mutants				
fla10	**78%**	22%	0%	68
fla3 1b	23%	**46%**	31%	96
fla3 1b::KAP-GFP	**56%**	23%	21%	106
Retrograde Motor Mutants				
LIC RNAi-A	1%	21%	**78%**	90
LIC RNAi-B	**65%**	26%	9%	102
Retrograde IFT Mutants				
fla2	3%	28%	**69%**	60
fla24	**86%**	14%	0%	56

Actively moving cells were exposed to a brief flash of bright light and then scored for reversal, pausing and/or change in forward direction, or no change in direction of movement.

Table 4.6. Phototaxis response in wild-type and mutant strains. (See Figure 3.7 on phototaxis for example photographs of photoaccumulation behavior.) (K. VanderWaal, J. Reck)

Strain	*Photoaccumulation*	*Direction*
Control strains		
Wild-type +	Yes	Positive
Wild-type -	Yes	Negative
mia2	No	NA
ppr2	Yes	Positive
Anterograde Motor Mutants		
fla10	Yes, weak	Positive
fla3 1b	Yes	Negative
fla3 1B::KAP-GFP	Yes	Negative
Retrograde Motor Mutants		
LIC RNAi-A	No	NA
LIC RNAi-B	Yes	Negative
Retrograde IFT Mutants		
fla2	No	NA
fla24	Yes	Negative

NA=not applicable.

COMPLETE BIBLIOGRAPHY

Adams, G.M., Huang, B., Luck, D.J. (1982). Temperature-sensitive, assembly-defective flagella mutants of *Chlamydomonas reinhardtii.* Genetics. *100,* 579-86.

Asai, D.J., Rajagopalan, V., Wilkes, D.E. (2009). Dynein-2 and ciliogenesis in *Tetrahymena*. Cell Motil Cytoskeleton. *66,* 673-7.

Badano, J.L, Mitsuma, N., Beales, P.L., and Katsanis, N. (2006). The ciliopathies: An emerging class of human genetic disorders. Ann Rev Genomics and Human Genetics. *7*, 125-148.

Barsel, S.E., Wexler, D.E., Lefebvre, P.A. (1988). Genetic analysis of long-flagella mutants of *Chlamydomonas reinhardtii*. Genetics. *118, 637-48.*

Bayly, P., Lewis, B. L., Kemp, P. L., Pless, R. B., and Dutcher, S.K. (2010). Efficient spatiotemporal analysis of the flagellar waveform of *Chlamydomonas reinhardtii*. Cytoskeleton. *67,* 56-69.

Berbari, N.F., O'Connor, A.K., Haycraft, C.J., Yoder, B.K. (2009). The primary cilium as a complex signaling center. Curr Biol. *19,* R526-35.

Beisson, J., and Wright, M. (2003). Basal body/centriole assembly and continuity. Curr Opin Cell Biol. *15,* 96-104.

Bloodgood, R.A., (1981). Flagella-dependent gliding motility in *Chlamydomonas*. Protoplasma. *106*,183-192.

Bloodgood, R.A., Woodward, M.P., Salomonsky, N.L. (1986). Redistribution and shedding of flagellar membrane glycoproteins visualized using an anti-carbohydrate monoclonal antibody and concanavalin A. J Cell Biol. *102,* 1797-812.

Bower, R., VanderWaal, K.E., O'Toole, E., Fox, L., Perrone, C.A., Mueller, J., Wirschell, M., Kamiya, R., Sale, W.S., and Porter, M.E. (2009). IC138 defines a subdomain at the base of the I1 dynein that regulates microtubule sliding and flagellar motility. Mol Biol Cell. *20,* 3055-3063.

Bowers, A. K., Keller, J. A., and Dutcher, S. K. (2003). Molecular markers for rapidly identifying candidate genes in *Chlamydomonas reinhardtii*. *ERY1* and *ERY2* encode chloroplast ribosomal proteins. Genetics *164*, 1345–1353.

Brazelton, W., Amundsen, C., Silflow, C., Lefebvre, P. (2001). The *bld1* mutation identifies the *Chlamydomonas osm-6* homolog as a gene required for flagellar assembly. Curr Biol. *11,* 1591-4.

Brokaw, C., and Kamiya, R. (1987). Bending Patterns of *Chlamydomonas* flagella: IV. Mutants with defects in inner and outer dynein arms indicate differences in dynein arm function. Cell Motil Cytoskeleton. *8,* 68-75.

Brokaw, C.J. (1994). Control of flagellar bending: a new agenda based on dynein diversity. Cell Motil Cytoskeleton. *23,* 199-204.

Brokaw, C. (2009). Simulation of the cyclic dynein-driven sliding, splitting and reassociation in an outer doublet pair. Biophys J. *97,* 2939-2947.

Bui, K.H., Sakakibara, H., Movassagh, T., Oiwa, K., and Ishikawa, T. (2008). Molecular architecture of inner dynein arms *in situ* in *Chlamydomonas reinhardtii* flagella. J Cell Biol. *183,* 923-932.

Carroll, K., Gomez, C., Shapiro, L. (2004). Tubby proteins: the plot thickens. Nat Rev Mol Cell Biol. *5,* 55-63.

Christensen, S.T., Pedersen, L.B., Schneider, L., Satir, P. (2007). Sensory cilia and integration of signal transduction in human health and disease. Traffic. *8.* 97-109.

Cole, D., Diener, D., Himelblau, A., Beech, P., Fuster, J., Rosenbaum, J. (1998). Chlamydomonas kinesin-II-dependent intraflagellar transport (IFT): IFT particles contain proteins required for ciliary assembly in *Caenorhabditis elegans* sensory neurons. J Cell Biol. *141,* 993-1008.

Cole, D. (2003). The intraflagellar transport machinery of *Chlamydomonas reinhardtii.* Traffic. *4,* 435-42.

Collet, J., Spike, C., Lundquist, E., Shaw, J., Herman, R. (1998). Analysis of *osm-6*, a gene that affects sensory cilium structure and sensory neuron function in *Caenorhabditis elegans.* Genetics. *148,* 187-200.

Corbit, K.C., Aanstad, P., Singla, V., Norman, A.R., Stainier, D.Y.R., Jeremy F Reiter, J.F. (2005). Vertebrate Smoothened functions at the primary cilium. Nature. *437,* 1018-21.

Coss, R.A. (1974). Mitosis in Chlamydomonas reinhardtii basal bodies and the mitotic apparatus. J Cell Biol. *63,* 325-9.

Criswell, P.S., and Asai, D.J. (1998). Evidence for four cytoplasmic dynein heavy chain isoforms in rat testis. Mol Biol Cell. *9,* 237-47.

Dawe, H.R., Farr, H., Gull, K. (2007). Centriole/basal body morphogenesis and migration during ciliogenesis in animal cells. J Cell Sci. *120,* 7-15.

Deffert, C., Niel, F., Mochel, F., Barrey, C., Romana, C., Souied, E., Stoetzel, C., Goossens, M., Dolfus, H., Verloes, A., Girodon, E., Gerald-Blanluet, M. (2007). Recurrent insertional polydactyly and situs inversus in a Bardet-Biedl syndrome family. Am J Med Genet A. *143*, 208-213.

Dentler, W.L. (2005). Intraflagellar transport (IFT) during assembly and disassembly of *Chlamydomonas* flagella. J. Cell Biol. *170*, 649-659.

Dentler, W. (2005). Intraflagellar transport (IFT) during assembly and disassembly of *Chlamydomonas* flagella. J Cell Biol. *170,* 649-59.

Dentler, W., VanderWaal., K., Porter, M.E. (2009). Recording and analyzing IFT in *Chlamydomonas* flagella. Methods Cell Biol. *93,* 145-55.

DiBella, L., Smith, E., Patel-King, R., Wakabayashi, K., and King, S. (2004). A novel Tctex2-related light chain is required for stability of inner dynein arm I1 and motor function in the *Chlamydomonas* flagellum. J Biol Chem. *279,* 21666-21676.

DiBella, L., Sakato, M., Patel-King, R., Pazour, G., and King, S. (2004). The LC7 light chains of *Chlamydomonas* flagellar dyneins interact with components required for both motor assembly and regulation. Mol Biol Cell. *15,* 4633-46.

Diener, D.R., Curry, A.M., Johnson, K.A., Williams, B.D., Lefebvre, P.A., Kindle, K.L., Rosenbaum, J.L. (1990) Rescue of a paralyzed-flagella mutant of *Chlamydomonas* by transformation. Proc Natl Acad Sci USA. *87,* 5739-43.

Dutcher, S. K. (1995). Mating and tetrad analysis in *Chlamydomonas reinhardtii*. Methods Cell Biol. *47*, 531–540.

Dutcher, S.K., W. Gibbons and W.B. Inwood. (1998). A genetic analysis of suppressors of the *pf10* mutation in *Chlamydomonas reinhardtii*. Genetics. *120,* 965-976.

Dutcher, S., Morrissette, N., Preble, A., Rackley, C., Stanga, J. (2002). Epsilon-tubulin is an essential component of the centriole. Mol Biol Cell. *13,* 3859-69.

Engel, B.D., Lechtreck, K., Sakai, T., Ikebe, M., Witman, G.B., Marshall, W.F. (2009). Total internal reflection fluorescence (TIRF) microscopy of *Chlamydomonas* flagella. Methods Cell Biol. *93,* 157-77.

Fliegauf, M., Benzing, T., Omran, H. (2007). When cilia go bad: cilia defects and ciliopathies. Nat Rev Mol Cell Biol. *8,* 880-93.

Follit, J.A., Tuft, R.A., Fogarty, K.E., and Pazour, G.J. (2006). The intraflagellar transport protein IFT20 is associated with the Golgi complex and is required for cilia assembly. Mol Biol Cell. *17*, 3781–3792.

Follit, J.A., Xu, F., Keady, B.T., Pazour, G.J. (2009). Characterization of mouse IFT complex B. Cell Motil Cyto. *66,* 457-68.

Fujiu, K., Nakayama, Y., Yanagisawa, A., Sokabe, M., and Yoshimura, K. (2009). *Chlamydomonas* CAV2 encodes a voltage-dependent calcium channel required for the flagellar waveform conversion. Curr Biol. *19,* 133-139.

Fujiu, K., Nakayama, Y., Iida, H., Sokabe, M., Yoshimura, K. (2011). Mechanoreception in motile flagella of *Chlamydomonas*. Nat Cell Biol. *13,* 630-2.

Gaillard, A.R., Fox, L.A., Rhea, J.M., Craige, B., Sale, W.S. (2006). Disruption of the A-kinase anchoring domain in flagellar radial spoke protein 3 results in unregulated axonemal cAMP-dependent protein kinase activity and abnormal flagellar motility. Mol Biol Cell. *17,* 2626-35.

Gilbert, S. (2000). The early development of vertebrates: Fish, birds, and mammals. *Developmental biology 6th edition.* Sinauer Associates, Inc.

Gonzalez-Ballester, D., Caser, D., Cokus, S., Pellegrini, M., Merchant, S., Grossman, A. (2010). RNA-seq analysis of sulfur-deprived *Chlamydomonas* cells reveals aspects of acclimation critical for cell survival. Plant Cell. *22,* 2058-84.

Goodenough, U.W., and Heuser, J.E. (1985). Outer and inner dynein arms of cilia and flagella. Cell. *41,* 341-342.

Goodenough, U.W., and Heuser, J.E. (1985). Substructure of inner dynein arms, radial spokes, and the central pair/projection complex of cilia and flagella. J Cell Biol. *100,* 2008-2016.

Grissom, P., Vaisberg, E., McIntosh, J. (2002). Identification of a novel light intermediate chain (D2LIC) for mammalian cytoplasmic dynein 2. Mol Biol Cell. *13,* 817-29.

Habermacher, G., and Sale, W. (1996). Regulation of flagellar dynein by an axonemal type-1 phosphatase in *Chlamydomonas*. J Cell Biol. *109,* 1899-1907.

Habermacher, G., and Sale, W. (1997). Regulation of flagellar dynein by phosphorylation of a 138-kD inner arm dynein intermediate chain. J Cell Biol. *136,* 167-176.

Hagstrom, S.A., North, M.A., Nishina, P.L., Berson, E.L., Dryja, P. (1998). Recessive mutations in the gene encoding the *tubby-like protein TULP1* in patients with retinitis pigmentosa. Nat Genet. *18,* 174-6.

Hagstrom, S.A., Adamian, M., Scimeca, M., Pawlyk, B.S., Yue, G., Li, T. (2001). A role for the Tubby-like protein 1 in rhodopsin transport. Invest Ophthalmol Vis Sci. *42,* 1955-62.

Han, Y., Kwok, B., Kernan, M. (2003). Intraflagellar transport is required in *Drosophila* to differentiate sensory cilia but not sperm. Curr Biol. *13,* 1679-86.

Harris, E.H. (1989). The *Chlamydomonas* Sourcebook: A Comprehensive Guide to Biology and Laboratory Use, San Diego: Academic Press.

Harris, E.H. (2001) *Chlamydomonas* as a model organism. Ann. Rev. Plant Physiol. Plant Mol. Biol. *52*, 363-406.

Harrison, A., Olds-Clarke, P., and King, S. (1998). Identification of the t complex-encoded cytoplasmic dynein light chain tctex1 in inner arm I1 supports the involvement of flagellar dyneins in meiotic drive. J Cell Biol. *140,* 1137-1147.

Haycraft, C.J., Schafer, J.C., Zhang, O., Taulman, P.D., Yoder, B.K. (2003). Identification of CHE-13, a novel intraflagellar transport protein required for cilia formation. Exp Cell Res. *284,* 251-63.

Hendrickson, T.W., Perrone, C.A., Griffin, P., Wuichet, K., Mueller, J., Yang, P., Porter, M.E., and Sale, W.S. (2004). IC138 is a WD-repeat Dynein Intermediate Chain Required for Light Chain Assembly and Regulation of Flagellar Bending. Mol Biol Cell. *15*, 5431-5442.

Heuser, T., Raytchev, M. Krell, J., Porter, M.E., and D. Nicastro (2009). The dynein regulatory complex is the nexin link and a major regulatory node in cilia and flagella. J. Cell Biol. *187*, 921-933.

Hom, E.F.Y., Witman, G.B., Harris, E.H., Dutcher, S.K., Kamiya, R.**,** Mitchell, D.R., Pazour, G.J., Porter, M.E., Sale, W.S., Wirschell, M., Yagi, T.**,** and King, S.M. (2011). A systematic dynein gene nomenclature for *Chlamydomonas*. Submitted.

Hou, Y., Pazour, G., Witman, G. (2004). A Dynein Light Intermediate Chain, D1bLIC, Is Required for Retrograde Intraflagellar Transport. Mol Biol Cell. *15,* 4382-94.

Huang, B., M Rifkin, M., Luck, D. (1977). Temperature-sensitive mutations affecting flagellar assembly and function in *Chlamydomonas reinhardtii.* J Cell Biol. *72,* 67-85.

Huang, K., Diener, D.R., Mitchell, A., Pazour, G.J., Witman, G.B., Rosenbaum, J.L. (2007). Function and dynamics of PKD2 in *Chlamydomonas reinhardtii* flagella. J Cell Biol. *179,* 501-14.

Huangfu, D., Liu, A., Rakeman, A., Murcia, N., Niswander, L., Anderson, K. (2003). Hedgehog signalling in the mouse requires intraflagellar transport proteins. Nature. *426,* 83-7.

Howard, D.R., Habermacher, G., Glass, D.B., Smith, E.F., and Sale, W.S. (1994). Regulation of *Chlamydomonas* flagellar dynein by an axonemal protein kinase. J Cell Biol. *127,* 1683-1692.

Ikeda, S., He, W., Ikeda, A., Naggert, J.K., North, M.A., Nishina, P.M. (1999). Cell-specific expression of *tubb*y gene family members (*tub, Tulp1,2, and 3*) in the retina. Invest Ophthalmol Vis Sci. *40,* 2706-12.

Ikeda, A., Ikeda, S., Gridley, T., Nishina, P.M., Naggert, J.K. (2001). Neural tube defects and neuroepithelial cell death in *Tulp3* knockout mice. Hum Mol Genet. *10,* 1325-34.

Ikeda, K., Yamamoto, R., Wirschell, M., Yagi, T., Bower, R., Porter, M.E., Sale, W.S., and Kamiya, R. (2009). A novel ankyrin-repeat protein interacts with the regulatory proteins of inner arm dynein f (I1) of *Chlamydomonas reinhardtii*. Cell Motil Cytoskeleton. *66*, 448-456.

Iomini, C., Babaev-Khaimovm V., Sassaroli, M., and Piperno, G. (2001). Protein particles in *Chlamydomonas* flagella undergo a transport cycle consisting of four phases. J. Cell Biol. *153*, 13-24.

Iomini, C., Li, L., Mo, W., Dutcher, S.K., and Piperno, G. (2006). Two flagellar genes, *AGG2* and *AGG3*, mediate orientation to light in *Chlamydomonas*. Curr Biol. *16,* 1147-1153.

Iomini, C., Li, L., Esparza, J.M., Dutcher, S.K. (2009). Retrograde intraflagellar transport mutants identify complex A proteins with multiple genetic interactions in *Chlamydomonas reinhardtii.* Genetics. *183,* 885-96.

Ishikawa, H., and Marshall, W.F. (2011). Ciliogenesis: building the cell's antenna. Nat Rev Mol Cell Biol. *12,* 222-34.

Kamiya, R. and Okamoto. M. (1985). A mutant of *Chlamydomonas reinhardtii* that lacks the flagellar outer arm but can swim. J. Cell Sci. *74*, 181-191.

Kamiya, R. (2002). Functional diversity of axonemal dyneins as studied in *Chlamydomonas* mutants. Int Rev Cytol. *219,* 115-155.

Kathir, P., LaVoie, M., Brazelton, W., Haas, N., Lefebvre, P., Silflow, C. (2003). Molecular map of the *Chlamydomonas reinhardtii* nuclear genome. Eukaryot Cell. *2,* 362-79.

Keller, L.R. (1995). Enrichment of mRNA encoding flagellar proteins. Methods Cell Biol. *47,* 551-57.

Kikushima, K. and Kamiya, R. (2008). Clockwise translocation of microtubules by flagellar inner-arm dyneins *in vitro.* Biophys J. *94,* 4014-9.

Kindle, K.L., Schnell, R.A., Fernandez, E., Lefebvre, P.A. (1989). Stable nuclear transformation of *Chlamydomonas* using the *Chlamydomonas* gene for nitrate reductase. J Cell Biol. *109,* 2589-2601.

Kindle, K.L. (1990). High-frequency nuclear transformation of *Chlamydomonas reinhardtii.* Proc Natl Acad Sci USA. *87,* 1228-1232.

King, S., and Patel-King, R. (1995). Identification of a Ca(2+)-binding light chain within *Chlamydomonas* outer arm dynein. J Cell Sci. *108,* 3757-64.

King, S.M., Barbarese, E., Dillman, J.F., Patel-King, R.S., Carson, J.H., Pfister, K.K. (1996). Brain cytoplasmic and flagellar outer arm dyneins share a highly conserved Mr 8,000 light chain. J Biol Chem. *271,* 19358-66.

King, S., and Dutcher, S.K. (1997). Phosphoregulation of an inner dynein arm complex in *Chlamydomonas reinhardtii* is altered in phototactic mutant strains. J Cell Biol. *136,* 177-191.

King, S.M. (2002). Dyneins motor on in plants. Traffic. *3,* 930-1.

King, S.M, and Kamiya, R. (2009). Axonemal Dyneins: Assembly, Structure, and Force Generation. *In* The *Chlamydomonas* Sourcebook, 2nd Edition, Volume 3, pp 131-208. edited by G.B. Witman, Academic Press, San Diego, CA

Kotani, N., Sakakibara, H., Burgess, S.A., Kojima, H., and Oiwa, K. (2007). Mechanical properties of inner-arm dynein-f (dynein I1) studied with *in vitro* motility assays. Biophys J. *93,* 886-94.

Kozminski, K.G., Johnson, K.A., Forscher, P. and Rosenbaum, J.L. (1993). A motility in the eukaryotic flagellum unrelated to flagellar beating. Proc. Natl. Acad. Sci. U.S.A. *90*, 5519-5523.

Kozminski, K.G., Beech, P.L., and Rosenbaum, J.L. (1995). The *Chlamydomonas* kinesin-like protein FPA10 is involved in motility associated with the flagellar membrane. J. Cell Biol. *131*, 1517-1527.

Kozminski, K.G. (1995). High-Resolution Imaging of Flagella. Meth. In Cell Biol. *47*, 263-271.

Kou, Y., Qiu, D., Wang, L., Li, X., Wang, S. (2009). Molecular analysis of the rice *tubby-like protein* gene family and their response to bacterial infection. Plant Cell Rep. *28,* 113-21.

Lai, C., Lee, C., Chen, P., Wu, S., Yang, C., Shaw, J. (2004). Molecular analysis of the *Arabidopsis TUBBY-like protein* gene family. Plant Physiol. *134,* 1586-97.

Lechtreck, K., Johnson, E.C., Sakai, T., Cochran, D., Ballif, B.A., Rush, J., Pazour, G.J., Ikebe, M., Witman, G.B. (2009). The *Chlamydomonas* reinhardtii BBSome is an IFT cargo required for export of specific signaling proteins from flagella. J Cell Biol. *187,* 1117-32.

Lefebvre, P.A., and Rosenbaum, J.L. (1986). Regulation of the synthesis and assembly of ciliary and flagellar proteins during regeneration. Annu Rev Cell Biol. *2,* 517-46.

Li, J., Gerdes, J., Haycraft, C., Fan, Y., Teslovich, T., May-Simera, H., Li, H., Blacque, O., Li, L., Leitch, C., Lewis, R., Green, J., Parfrey, P., Leroux, M., Davidson, W., Beales, P., Guay-Woodford, L., Yoder, B., Stormo, G., Katsanis, N., Dutcher, S. (2004). Comparative genomics identifies a flagellar and basal body proteome that includes the *BBS5* human disease gene. Cell. *117,* 541-52.

Lim, Y.S., Chua, C.E. L., Tang, B.L. (2011). Rabs and other small GTPases in ciliary transport. Biol Cell. *103,* 209-21.

Mak, H.Y., Nelson, L.S., Basson, M., Johnson, C.D., Ruvkun, G. (2006). Polygenic control of Caenorhabditis elegans fat storage. Nat Genet. *38,* 363-8.

Marshall, W., and Rosenbaum, J. (2001). Intraflagellar transport balances continuous turnover of outer doublet microtubules: implications for flagellar length control. J Cell Biol. *155,* 405-14.

Marshall, W.F. (2008). The cell biological basis of ciliary disease. J. Cell Biol. *180*, 17-21.

Matsuda, A., Yoshimura, K., Sineshchekov, O.A., Hirono, M., and Kamiya, R. (1998). Isolation and characterization of *Chlamydomonas* mutants that display phototaxis but not photophobic response. Cell Motil Cytoskeleton. *41,* 353-362.

Mastronarde, D., O'Toole, E., McDonald, K., McIntosh, J., and Porter, M. (1992). Arrangement of inner dynein arms in wild-type and mutant flagella of *Chlamydomonas*. J Cell Biol. *118,* 1145-1162.

Mayfield, S.P., Bennoun, P., Rochaix, J.D. (1987). Expression of the nuclear encoded OEE1 protein is required for oxygen evolution and stability of photosystem II particles in *Chlamydomonas reinhardtii.* EMBO. *6,* 313-8.

Merchant, S. S., Prochnik, S. E., Vallon, O., Harris, E. H., Karpowicz, S. J., Witman, G. B., Terry, A., Salamov, A., Fritz-Laylin, L. K., Marechal-Drouard, L., Marshall, W. F., Qu, L. H., et al. (2007). The *Chlamydomonas* genome reveals the evolution of key animal and plant functions. Science. *318*, 245–250.

Mikami, A., Tynan, S., Hama, T., Luby-Phelps K., Saito, T., Crandall, J., Besharse, J., Vallee, R. (2002). Molecular structure of cytoplasmic dynein 2 and its distribution in neuronal and ciliated cells. J Cell Sci. *115,* 4801-8.

Miller, M.S., Esparza, J.M., Lippa, A.M., Lux, F.G., Cole, D.G., Dutcher, S.K. (2005). Mutant kinesin-2 motor subunits increase chromosome loss. Mol Biol Cell. *16,* 3810-20.

Mitchell, D.R., and Kang, Y. (1991). Identification of *oda6* as a *Chlamydomonas* dynein mutant by rescue with the wild-type gene. J Cell Biol. *113,* 835-42.

Mitchell, D.R. (2000). *Chlamydomonas* flagella. J Phycol. *36*, 261–273.

Molnar, A., Bassett, A., Thuenemann, E., Schwach, F., Karkare, S., Ossowski, S., Weigel, D., Baulcombe, D. (2009). Highly specific gene silencing by artificial microRNAs in the unicellular alga *Chlamydomonas reinhardtii.* Plant J. *58,* 165-74.

Mueller, J., Perrone, C.A., Bower, R., Cole, D.G., Porter, M.E. (2005). The *FLA3* KAP subunit is required for localization of kinesin-2 to the site of flagellar assembly and processive anterograde intraflagellar transport. Mol Biol Cell. *16,* 1341-54.

Mukhopadhyay, A., Deplancke, B., Walhout, A.J.M., Tissenbaum, H.A. (2005). *C. elegans* tubby regulates life span and fat storage by two independent mechanisms. Cell Metab. *2,* 35-42.

Mukhopadhyay, A., Pan, X., Lambright, D.G., Tissenbaum, H.A. (2007). An endocytic pathway as a target of tubby for regulation of fat storage. EMBO Rep. *8,* 931-8.

Mukhopadhyay, S., Wen, X., Chih, B., Nelson, C.D., Lane, W.S., Scales, S.J., Jackson, P.K. (2010). TULP3 bridges the IFT-A complex and membrane phosphoinositides to promote trafficking of G protein-coupled receptors into primary cilia. Genes Dev. *24,* 2180-93.

Mukhopadhyay, S., and Jackson, P. (2011). The tubby family proteins. Genome Biology. *12,* 225.

Myster, S., J.A. Knott, E. O'Toole, and M.E. Porter. (1997). The *Chlamydomonas Dhc1* gene encodes a dynein heavy chain subunit required for assembly of the I1 inner arm complex. Mol. Biol. Cell. *8,* 607-620.

Myster, S.H., Knott, J.A., Wysocki, K.M., O-Toole, E., and Porter, M.E. (1999). Domains in the 1-alpha dynein heavy chain required for inner arm assembly and flagellar motility in *Chlamydomonas*. J Cell Biol. *146,* 801-818.

Nachury, M.V., Loktev, A.V., Zhang, O., Westlake, C.J., Peränen, J., Merdes, A., Slusarski, D.C., Scheller, R.H., Bazan, J.F., Sheffield, V.C., Jackson, P.K. (2007). A core complex of BBS proteins cooperates with the GTPase Rab8 to promote ciliary membrane biogenesis. Cell. *129,* 1201-13.

Nakamura, S.,Tabino, H., and Kojima, M.K. (1987). Effect of lithium on flagellar length in *Chlamydomonas reinhardtii*. Cell Struct. Funct. *12,* 369-374.

Nelson, J.A., Savereide, P.B., Lefebvre, P.A. (1994). The CRY1 gene in *Chlamydomonas reinhardtii:* structure and use as a dominant selectable marker for nuclear transformation. Mol Biol Cell. *14,* 4011-9.

Nguyen, R., Tam, L., Lefebvre, P. (2004). The *LF1* Gene of *Chlamydomonas reinhardtii* Encodes a Novel Protein Required for Flagellar Length Control. Genetics. *169,* 1415-1424.

Nicastro, D., Schwartz, C.,Pierson, J., Gaudette, R., Porter, M.E., and McIntosh, J.R. (2006). The molecular architecture of axonemes revealed by cryoelectron tomography. Science. *313,* 944-948.

Nishina, P.M., North, M.A., Ikeda, A., Yan, Y., Naggert, J.K. (1998). Molecular characterization of a novel tubby gene family member, *TULP3*, in mouse and humans. Genomics. *54,* 215-20.

Nonaka, S., Tanaka, Y., Okada, Y., Takeda, S., Harada, A., Kanai, Y., Kido, M., Hirokawa, N. (1998). Randomization of left-right asymmetry due to loss of nodal cilia generating leftward flow of extraembryonic fluid in mice lacking KIF3B motor protein. Cell. *95*, 829-37.

North, M.A., Naggert, J.K., Yan, Y., Noben-Trauth, K., Nishina, P.M. (1997). Molecular characterization of TUB, TULP1, and TULP2, members of the novel tubby gene family and their possible relation to ocular diseases. Proc Natl Acad Sci USA. *94*, 3128-33.

Ocbina, P.J.R., Eggenschwiler, J.T., Moskowitz, I., Anderson, K.V. (2011). Complex interactions between genes controlling trafficking in primary cilia. Nat Genet. *43,* 547-54.

Ohlemiller, K.K., Hughes, R.M., Mosinger-Ogilvie, J., Speck, J.D., Grosof, D.H., Silverman, M.S. (1995). Cochlear and retinal degeneration in the *tubby* mouse. Neuroreport. *6,* 845-9.

Okagaki, T., and Kamiya, R. (1986). Microtubule sliding in mutant *Chlamydomonas* axonemes devoid of outer or inner dynein arms. J Cell Biol. *103,* 1895-1902.

Okita, N., Isogai, N., Hirono, M., Kamiya, R., and Yoshimura, K. (2005). Phototactic activity in *Chlamydomonas* 'non-phototactic' mutants deficient in Ca2+-dependent control of flagellar dominance or in inner-arm dynein. J Cell Sci. *118*, 529-537.

O'Toole, E., Mastronarde, D., McIntosh, J.R., Porter, M.E. (1995) Computer-assisted analysis of flagellar structure. Methods Cell Biol. *47,* 183-91.

Pan, J. and Snell, W. (2002). Kinesin-II is required for flagellar sensory transduction during fertilization in *Chlamydomonas.* Mol Biol Cell. *13,* 1417-26.

Pan, J., Wang, Q., Snell, W.J. (2005). Cilium-generated signaling and cilia-related disorders. Lab Invest. *85,* 452-63.

Pazour, G.J., Sineshchekov, O.A., and Witman, G.B. (1995). Mutational analysis of the phototransdution pathway in *Chlamydomonas reinhardtii.* J Cell Biol. *131,* 427-40.

Pazour, G., Wilkerson, C., Witman, G. (1998). A dynein light chain is essential for the retrograde particle movement of intraflagellar transport (IFT). J Cell Biol. *141,* 979-92.

Pazour, G., Dickert, B., Witman, G. (1999). The DHC1b (DHC2) isoform of cytoplasmic dynein is required for flagellar assembly. J Cell Biol. *144,* 473-81.

Pazour, G., Dickert, B., Vucica, Y., Seeley, E., Rosenbaum, J., Witman, G., Cole, D. (2000). *Chlamydomonas IFT88* and its mouse homologue, polycystic kidney disease gene *tg737*, are required for assembly of cilia and flagella. J Cell Biol. *151,* 709-18.

Pazour, G., and Witman, G. (2003). The vertebrate primary cilium is a sensory organelle. Curr Opin Cell Biol. *15,* 105-10.

Pazour, G.J., Agrin, N., Leszyk, J., Witman, G.B. (2005). Proteomic analysis of a eukaryotic cilium. J Cell Biol. *170,* 101-113.

Pedersen, L.B., Miller, M.S., Geimer, S., Leitch, J.M., Rosenbaum, J.L., Cole, D.G. (2005). *Chlamydomonas IFT172* is encoded by *FLA11*, interacts with CrEB1, and regulates IFT at the flagellar tip. Curr Biol. *15,* 262-6.

Pedersen, L.B., Geimer, S., Rosenbaum, J.L. (2006). Dissecting the molecular mechanisms of intraflagellar transport in *Chlamydomonas.* Curr Biol. *16,* 450-9.

Periz, G., Dharia, D., Miller, S.H., and Keller, L.R. (2007). Flagellar elongation and gene expression in *Chlamydomonas reinhardtii*. Eukaryotic Cell. *6*, 1411-1420.

Perrone, C.A., Yang, P., O'Toole, E., Sale, W.S., and Porter, M.E. (1998). The *Chlamydomonas IDA7* locus encodes a 140-kDa dynein intermediate chain required to assemble the I1 inner arm complex. Mol Biol Cell. *9,* 3351-3365.

Perrone, C.A., Myster, S., Bower, R., O'Toole, E., and Porter, M.E. (2000). Insights into the structural organization of the I1 inner arm dynein from a domain analysis of the 1β dynein heavy chain. Mol Biol Cell. *11,* 2297-2313.

Perrone, C., Tritschler, D., Taulman, P., Bower, R., Yoder, B., Porter, M. (2003). A novel dynein light intermediate chain colocalizes with the retrograde motor for intraflagellar transport at sites of axoneme assembly in *Chlamydomonas* and Mammalian cells. Mol Biol Cell. *14,* 2041-56.

Piasecki, B.P., LaVoie, M., Tam, L., Lefebvre, P.A., Silflow, C.D. (2008). The Uni2 phosphoprotein is a cell cycle regulated component of the basal body maturation pathway in *Chlamydomonas reinhardtii.* Mol Biol Cell. *19,* 262-73.

Piperno, G., Ramanis, Z., Smith, E.F., and Sale, W.S. (1990). Three distinct inner dynein arms in *Chlamydomonas* flagella: molecular composition and location in the axoneme. J Cell Biol. *110,* 379-89.

Piperno, G., and Ramanis, Z. (1991). The proximal portion of *Chlamydomonas* flagella contains a distinct set of inner dynein arms. J Cell Biol. *112,* 701-9.

Piperno, G., and Mead, K. (1997). Transport of a novel complex in the cytoplasmic matrix of *Chlamydomonas* flagella. Proc Natl Acad Sci USA. *94,* 4457-62.

Piperno, G., Siuda, E., Henderson, S., Segil, M., Vaananen, H., and Sassaroli, M. (1998). Distinct mutants of retrograde intraflagellar transport (IFT) share similar morphological and molecular defects. J. Cell Biol. *143*, 1591-1601.

Porter, M.E., Power, J., and Dutcher, S.K. (1992). Extragenic suppressors of paralyzed flagellar mutations in *Chlamydomonas reinhardtii* identify loci that alter the inner dynein arms. J Cell Biol. *188,* 1163-76.

Porter, M.E., Knott, J.A., Myster, S.H., Farlow, S.J. (1996). The dynein gene family in *Chlamydomonas reinhardtii*. Genetics. *144,* 569-85.

Porter, M.E., Bower, R., Knott, J.A., Byrd, P., Dentler, W. (1999). Cytoplasmic dynein heavy chain 1b is required for flagellar assembly in *Chlamydomonas*. Mol Biol Cell. *10,* 693-712.

Porter, M.E., and Sale, W.S. (2000). The 9 + 2 axoneme anchors multiple inner arm dyneins and a network of kinases and phosphatases that control motility. J Cell Biol. *151,* 37-42.

Qin, H., Diener, D.R., Geimer, S., Cole, D.G., Rosenbaum, J.L. (2004). Intraflagellar transport (IFT) cargo: IFT transports flagellar precursors to the tip and turnover products to the cell body. J Cell Biol. *164,* 255-66.

Qin, H., Burnette, D.T., Bae, Y., Forscher, P., Barr, M.M., Rosenbaum, J.L. (2005). Intraflagellar transport is required for the vectorial movement of TRPV channels in the ciliary membrane. Curr Biol. *15,* 1695-9.

Qin, H., Wang, Z., Diener, D., and Rosenbaum, J. (2007). Intraflagellar transport protein 27 is a small G protein involved in cell-cycle control. Curr. Biol. *17*, 193-202.

Rana, A., Barbera, J., Rodriguez, T., Lynch, D., Hirst, E., Smith, J., Beddington, R. (2004). Targeted deletion of the novel cytoplasmic dynein mD2LIC disrupts the embryonic organizer, formation of the body axes and specification of ventral cell fates. Development. *131,* 4999-5007.

Ranum, L.P.W., Thompson, M.D., Schloss, J.A., Lefebvre, P.A., Silflow, C. (1988). Mapping flagellar genes in *Chlamydomonas* using restriction fragment length polymorphisms. Genetics. *120,* 109-122.

Rohr, J., Sarkar, N., Balenger, S., Jeong, B., Cerutti, H. (2004). Tandem inverted repeat system for selection of effective transgenic RNAi strains in *Chlamydomonas*. Plant J. *40,* 611-21.

Rompolas, P., Pedersen, L.B., Patel-King, R.S., King, S.M. (2007). *Chlamydomonas* FAP133 is a dynein intermediate chain associated with the retrograde intraflagellar transport motor. J Cell Sci. *120,* 3653-65.

Ronshaugen, M., McGinnis, N., Inglis, D., Chou, D., Zhao, J., McGinnis, W. (2002). Structure and expression patterns of *Drosophila* TULP and TUSP, members of the *tubby*-like gene family. Mech Dev. *117,* 209-15.

Rosenbaum, J., and Witman, G. (2002). Intraflagellar transport. Nat Rev Mol Cell Biol. *3,* 813-25.

Ruiz, F.A., Marchesini, N., Seufferheld, M., Govindjee, R Docampo. (2001). The polyphosphate bodies of *Chlamydomonas reinhardtii* possess a proton-pumping pyrophosphatase and are similar to acidocalcisomes. J Biol Chem. *276,* 46196-203.

Rupp, G., O'Toole, E., Porter, M.E. (2001). The *Chlamydomonas PF6* locus encodes a large alanine/proline-rich polypeptide that is required for assembly of a central pair projection and regulates flagellar motility. Mol Biol Cell. *12,* 739-51.

Rupp, G., and Porter, M.E. (2003). A subunit of the dynein regulatory complex in *Chlamydomonas* is a homologue of a growth arrest-specific gene product. J Cell Biol. *162,* 47-57.

Salisbury, J.L., Baron, A.T., Sanders, M.A. (1988). The centrin-based cytoskeleton of Chlamydomonas reinhardtii: distribution in interphase and mitotic cells. J Cell Biol. *107,* 635-41.

Sanders, M.A., and Salisbury, S.L. (1994). Centrin plays an essential role in microtubule severing during flagellar excision in *Chlamydomonas reinhardtii.* J Cell Biol. *124,* 795-805.

Santagata, S., Boggon, T.J., Baird, C.L., Gomez, C.A., Zhao, J., Shan, W.S., Myszka, D.G., Shapiro, L. (2001). G-protein signaling through tubby proteins. Science. *292,* 2041-50.

Sarpal, R., Todi, S., Sivan-Loukianova, E., Shirolikar, S., Subramanian, N., Raff, E., Erickson, J., Ray, K., Eberl, D. (2003). *Drosophila* KAP interacts with the kinesin II motor subunit KLP64D to assemble chordotonal sensory cilia, but not sperm tails. Curr Biol. *13,* 1687-96.

Schafer, J., Haycraft, C., Thomas, J., Yoder B., Swoboda, P. (2003). XBX-1 encodes a dynein light intermediate chain required for retrograde intraflagellar transport and cilia assembly in *Caenorhabditis elegans.* Mol Biol Cell. *14,* 2057-70.

Scholey, J. (2003). Intraflagellar transport. Annu Rev Cell Dev Biol. *19,* 423-43.

Segal, R.A., Huang, B., Ramanis, Z., Luck, D.J. (1984). Mutant strains of *Chlamydomonas reinhardtii* that move backwards only. J Cell Biol. *98,* 2026-2034.

Shiri-Sverdlov, R., Custers, A., van Vliet-Ostaptchouk, J.V., van Gorp, P.J., Lindsey, P.J., van Tilburg, J.H.O., Zhernakova, S., Feskens, E.J.M., van der A, D.L., Dollé, M.E.T., van Haeften, T.W., Koeleman, B.P.C., Hofker, M.H., Wijmenga, C. (2006). Identification of TUB as a novel candidate gene influencing body weight in humans. Diabetes. *55,* 385-9.

Silflow, C.D., Kathir, P., Lefebvre, P.A. (1995). Molecular mapping of genes for flagellar proteins in *Chlamydomonas.* Methods Cell Biol. *47,* 525-30.

Silflow, C.D., and Lefebvre, P.A. (2001). Assembly and motility of eukaryotic cilia and flagella. Lessons from *Chlamydomonas reinhardtii.* Plant Physiol. *127,* 1500-7.

Signor, D., Wedaman, K., Orozco, J., Dwyer, N., Bargmann, C., Rose, L., Scholey, J. (1999). Role of a class DHC1b dynein in retrograde transport of IFT motors and IFT raft particles along cilia, but not dendrites, in chemosensory neurons of living *Caenorhabditis elegans*. J Cell Biol. *147,* 519-30.

Sizova, I., Fuhrmann, M., Hegemann, P. (2001). A *Streptomyces rimosus aphVIII* gene coding for a new type of phosphotransferase provides stable antibiotic resistance to *Chlamydomonas reinhardtii*. Gene. *277,* 221-229.

Smith, E., Sale, W. (1991). Microtubule binding and translocation by inner dynein arm subtype I1. Cell Motil Cytoskeleton. *18,* 258-268.

Smith, E., Sale, W. (1992). Regulation of dynein-driven microtubule sliding by the radial spokes in flagella. Science. *257,* 1557-1559.

Smith, E., and Yang, P. (2004). The radial spokes and central apparatus: mechano-chemical transducers that regulate flagellar motility. Cell Motil Cytoskeleton. *57,* 8-17.

Snow, J.J., Ou, G., Gunnarson, A.L., Regina, M., Walker, S., Zhou, H.M., Brust-Mascher, I., and Scholey, J.M. (2004). Two anterograde intraflagellar transport motors cooperate to build sensory cilia on *C. elegans* neurons. Nature Cell Biol. *6*, 1109-1113.

Stolc, V., Samanta, M.P., Tongprasit, W., Marshall, W.F. (2005). Genome-wide transcriptional analysis of flagellar regeneration in *Chlamydomonas reinhardtii* identifies orthologs of ciliary disease genes. Proc Natl Acad Sci USA. *102,* 3703-7.

Supp, D.M., Potter, S.S., Brueckner, M. (2000). Molecular motors: the driving force behind mammalian left-right development. Trends Cell Biol. *10*, 41-5.

Taillon, B.E. and Jarvik, J.W. (1995). Release of the cytoskeleton and flagellar apparatus from *Chlamydomonas*. Methods Cell Biol. *47,* 307-13.

Tam, L., and Lefebvre, P. (1993). Cloning of flagellar genes in *Chlamydomonas reinhardtii* by DNA insertional mutagenesis. Genetics. *135,* 375-84.

Tam, L., Lefebvre, P.A. (2002). The *Chlamydomonas MBO2* locus encodes a conserved coiled-coil protein important for flagellar waveform conversion. Cell Motil Cytoskeleton. *51,* 197-212.

Tam, L., Dentler, W., Lefebvre, P. (2003). Defective flagellar assembly and length regulation in LF3 null mutants in *Chlamydomonas.* J Cell Biol. *163, 597-607.*

Tam, L., Wilson, N.F., Lefebvre, P.A. (2007). A CDK-related kinase regulates the length and assembly of flagella in *Chlamydomonas.* J Cell Biol. *176,* 819-29.

Toba, S., Fox. L.A., Sakakibara, H., Porter, M.E., Oiwa, K., Sale, W.S. (2011). Distinct roles of the 1α and 1β heavy chains of the inner arm dynein I1 of *Chlamydomonas* flagella. Mol Biol Cell. *22,* 342-353.

Tobin, J., Beales, P.L. (2009). The nonmotile ciliopathies. Genet Med. *11,* 386-402.

Vaisberg, E.A., Grissom, P.M., McIntosh, J.R. (1996). Mammalian cells express three distinct dynein heavy chains that are localized to different cytoplasmic organelles. J Cell Biol. *133,* 831-42.

Vysotskaia, V.S., Curtis, D.E., Voinov, A.V., Kathir, P., Silflow, C.D., Lefebvre, P.A. (2001). Development and characterization of genome-wide single nucleotide polymorphism markers in the green alga *Chlamydomonas reinhardtii*. Plant Physiol. *127,* 386-9.

Walther, Z., Vashishtha, M., Hall, J. (1994). The *Chlamydomonas FLA10* gene encodes a novel kinesin-homologous protein. J Cell Biol. *126,* 175-88.

Wang, Q., Pan, J., and Snell, W.J. (2006). Intraflagellar transport particles participate directly in cilium-generated signaling in *Chlamydomonas.* Cell. *125,* 549-62.

Wemmer, K., and Marshall, W.F. (2007). Flagellar length control in *Chlamydomonas*--paradigm for organelle size regulation. Int Rev Cytol. *260,* 175-212.

Wicks, S., de Vries, C., van Luenen, H., Plasterk, R. (2000). CHE-3, a cytosolic dynein heavy chain, is required for sensory cilia structure and function in *Caenorhabditis elegans.* Dev Biol. *221,* 295-307.

Wickstead, B. and Gull, K. (2007). Dyneins across eukaryotes: A comparative genomic analysis. Traffic *8*, 1708-1721.

Wilkerson, C., King, S., Witman, G. (1994). Molecular analysis of the gamma heavy chain of *Chlamydomonas* flagellar outer-arm dynein. J Cell Sci. *107,* 497-506.

Wirschell, M., Hendrickson, T., Sale, W.S. (2007). Keeping and eye on I1: I1 dynein as a model for flagellar dynein assembly and regulation. Cell Motil Cytoskeleton. *64,* 569-79.

Wirschell, M., Zhao, F., Yang, C., Yang, P., Diener, D., Gaillard, A., Rosenbaum, J.L., Sale, W.S. (2008). Building a radial spoke: flagellar radial spoke protein 3 (RSP3) is a dimmer. Cell Motil Cytoskeleton. *65,* 238-48.

Wirschell, M., Yang, C., Yang, P., Fox, L., Yanigasawa, H., Kamiya, R., Witman, G.B., Porter, M.E., and Sale, W.S. (2009). IC97 is a novel intermediate chain of I1 dynein that interacts with tubulin and regulates interdoublet sliding. Mol Biol Cell. *20,* 3044-3054.

Witman, G.B., Plummer, J., Sander, G. (1978). *Chlamydomonas* flagellar mutants lacking radial spokes and central tubules. Structure, composition, and function of specific axonemal components. J Cell Biol. *76,* 729-747.

Witman, G.B. (1986). Isolation of *Chlamydomonas* flagella and flagellar axonemes. Methods Enzymol. *134*, 280-290.

Witman, G.B. (1993). *Chlamydomonas* phototaxis. Trends Cell Biol. *3,* 403-408.

Wright, R. L., Salisbury, J., Jarvik, J.W. (1985). A nucleus-basal body connector in *Chlamydomonas reinhardtii* that may function in basal body localization or segregation. J Cell Biol. *101,* 1903-12.

Yagi, T., Uematsu, K., Liu, Z., Kamiya, R. (2009). Identification of dyneins that localize exclusively to the proximal portion of *Chlamydomonas* flagella. J Cell Sci. *122,* 1306-1314.

Yang, P., and Sale, W.S. (1998). The Mw 140,000 Intermediate Chain of *Chlamydomonas* Flagellar Inner Arm Dynein Is a WD-Repeat Protein Implicated in Dynein Arm Anchoring. Mol Biol Cell. *9*, 3335-3349.

Yang, P., and Sale, S., (2000). Casein kinase I is anchored on axonemal doublet microtubules and regulates flagellar dynein phosphorylation and activity. J Biol Chem. *275,* 18905-12.

Yang, Z., Zhou, Y., Wang, X., Gu, S., Yu, J., Liang, G., Yan, C., Xu, C. (2008). Genomewide comparative phylogenetic and molecular evolutionary analysis of tubby-like protein family in *Arabidopsis,* rice and poplar. Genomics. *92,* 246-53.

Yoshimura, S., Egerer, J., Fuchs, E., Haas, A.K. and Barr, F.A. (2007). Functional dissection of Rab GTPases involved in primary cilium formation. J Cell Biol. *178*, 363–369.

Zamora, I., Feldman, J.L., Marshall, W.F. (2004). PCR-based assay for mating type and diploidy in *Chlamydomonas.* Biotechniques. *37,* 534-536.

APPENDIX 1

Recording and Analyzing IFT in *Chlamydomonas* flagella

Modified from
Dentler, W., VanderWaal., K., Porter, M.E. (2009). Recording and analyzing IFT in *Chlamydomonas* flagella. *Methods in Cell Biology, 93,* 143-153.*

*Slight modifications to format and headings.

A1.I. INTRODUCTION

Intraflagellar transport (IFT) first was observed using a specialized DIC microscope and recording system (Kozminski et al, 1993; Kozminski, 1995). The elegant movies of particle movement within flagella and use of the *ts*-mutant *fla10* to identify the anterograde motor for IFT (Kozminski et al 1995) led to a new area in studies of cilia and flagella and the discovery of ciliary defects associated with a number of human diseases, or ciliopathies (Badano et al, 2006, Marshall, 2008).

Analysis of the rapid bidirectional movement of IFT particles in 0.2μm diameter flagella was made possible by the development of kymograms that displayed particle positions along the flagellum as a function of time (Piperno et al, 1998; Iomini et al, 2001). Although these techniques were major advances in the field, they required equipment and computer programs that were not generally available, so their application was limited. Recent improvements in microscope optics, recording equipment, and computer programs have made it possible for most investigators to visualize IFT at modest cost (Dentler, 2005, Mueller et al, 2005). These techniques permit the analysis of anterograde and retrograde IFT as well as the movement of particles along flagellar surfaces using high-resolution differential interference microscopy (DIC) (Figure A1.1). With the development of GFP-tagged IFT components (Snow et al, 2004; Mueller et. al, 2005) IFT can be observed using wide-field fluorescence microscopy (Figure A1.2).

The purpose of this chapter is to provide methods that can be used to observe, record, and measure IFT using commercially available equipment. It will be focused on observations of IFT in *Chlamydomonas* flagella, because the long flagella are ideal specimens to observe IFT. IFT can be observed using DIC and, with GFP-tagged IFT components, by fluorescence microscopy. The analytical methods described here also are useful for analyzing fluorescently labeled flagella, regardless of the organism from which images were captured.

A1.2. METHODS

The most important decision is to choose cells with long and relatively immobile flagella. In our hands, *pf18*, a *Chlamydomonas* mutant that lacks central microtubules and has fairly straight and rigid flagella, is the easiest strain with which to observe IFT. The flagella attach to coverslips and IFT can be observed throughout the flagellum from the base, where flagella exit the cell wall, to the distal tips. Other paralyzed flagellar mutants to consider include *pf16*, which has an unstable C1 microtubule, and *pf1*, which lacks spoke heads (Kozminski, 2005). For many experiments, motile cells need to be examined, and so methods to immobilize these cells also are described in this chapter.

A. Slide preparation

Slides and coverslips must be clean for optimal imaging. They can be cleaned by soaking in hot water and detergent followed by extensive washing with deionized water and air or oven drying. Alternatively, they can be cleaned by an overnight soak in 6N HCl followed by extensive washing in deionized water, rinsing in 95% EtOH, and air drying (Kozminski, 1995).

For DIC, thin (#0) coverslips can be used as a slide and coverslip. An aluminum slide is cut from a 1mm thick aluminum sheet and an opening, ~7.5 x 3 cm, is cut out for the coverslip. A clean 24x60 mm No 0 coverslip (Gold Seal #3223) is attached to the bar by double stick tape and two small (~2x20 mm) Parafilm spacers are placed on the large coverslip before mounting cells attached to a smaller coverslip (below) to avoid crushing and deflagellating cells.

DIC and fluorescence microscopy also can be carried out using standard cleaned glass slides and #1 or 1.5 coverslips. If cells are mounted in agar (below), the spacers are not needed.

B. Specimen preparation

Observation of IFT in paralyzed mutants is relatively straightforward and primarily requires patience. Observation of IFT in non-paralyzed cells requires

mechanical or chemical methods to paralyze flagella. In each of these methods, cells are applied to coverslips and allowed to sit for 2-5 minutes. This promotes attachment of flagella to the coverslips, which is essential for observing IFT.

Attachment of flagella to coverslips is facilitated by coating coverslips with .01-1 mg/ml Poly-L-Lysine (Sigma P1274). Higher concentrations of polylysine will induce flagella to curl and to detach from cells (Bloodgood, 1981). Polylysine is applied to clean cover glasses and allowed to sit for 5 minutes to overnight. Then rinse coverslips with water and air dry. Apply cells to the coverslips allow cells to attach, and then invert the coverslips over the larger coverslip or slide with Parafilm spacers. Withdraw as much of the medium as possible using filter paper and seal the slides with VALAP.

Agarose can be used to mechanically immobilize motile cells. Kozminski (1995) formed a small agar chamber beneath the coverslip and placed cells in the chamber. We have had more success using 1-2% low EEO agarose (Fisher BP160) dissolved in culture medium and maintained at ~30˚C. Apply the cells to a coverslip and allow them to attach for 2-5 minutes. Remove most of the media, add 8-10µl of the agarose solution to the cells, invert over a slide and seal with VALAP.

VALAP is made by adding equal weights of Vaseline, lanolin, and paraffin to a beaker and heating to melt the mixture. VALAP can be stored indefinitely at room temperature. For use, melt VALAP and apply to the slide with a glass Pasteur pipette. Flatten the bead of VALAP with a warm spatula to minimize the possibility of contaminating the objective lens.

Motile flagella can be paralyzed by adding 20 mM LiCl to the mounting medium. Although LiCl induces flagellar growth (Periz et al 2007; Nakamura et al, 1987), little growth occurs in the time during which IFT is recorded and 20 mM LiCl does not induce changes in the rate or frequency of anterograde or retrograde IFT (Dentler, 2005). Used cautiously, addition of 10-20 mM LiCl can facilitate recording IFT in motile flagella.

C. Microscopy

1. Differential Interference Contrast

IFT was discovered using differential interference contrast microscopy (DIC) and high resolution objective and condenser lenses. Our best images are obtained using infinity-corrected optics and a Zeiss Axioplan 2ie upright microscope. Most flagella remain attached to the cover glass in the upright microscope but it is possible that an inverted microscope may maintain better attachment of flagella and better imaging.

Full and even illumination of the back focal plane of the condenser lens is essential for high-resolution imaging. With fixed tube length optics, a mercury or xenon lamp and a fiber optic scrambler was essential to obtain sufficient illumination to produce high quality images (Kozminski, 1995; Piperno et al, 1998). In our experience, this intense light damages the cells after even short periods of illumination. Light transmission is greatly improved with newer infinity-corrected optics and we currently use a standard halogen lamp built into the microscope base. Together with a UV and IR absorbing filter and a green interference filter, cells can be observed for at least 3 hours without any visible damage.

High resolution DIC requires objective **and** condenser lenses with numerical apertures of 1.4 or greater. Immersion oil must be used between the slide and condenser lens and between the coverslip and objective lens. The microscope must be properly aligned to produce full Koehler illumination.

To record IFT the long axis of the flagellum should fill the camera field as much as possible. This requires 100x NA1.4 planapochromat (for DIC) or 100x NA 1.3 plan fluar (for fluorescence) objective lenses. The image should be projected on the camera face using a 1.6X Bertrand lens (Optovar), and an 8x eyepiece or a 1.2x TV tube magnifier.

Proper specimen orientation is essential. Normally, flagella are best observed when their long axis is perpendicular to the shear axis. For IFT, flagella must be positioned so that their long axis is parallel to the shear axis. The IFT particles then will move perpendicular to the shear axis and be shadowed. When properly oriented, the flagellum may be nearly invisible when observed through the microscope eyepieces but the increased contrast provided by the video camera and computer will make the flagellum and IFT visible on a monitor. While flagella in the proper orientation to the

shear axis can be found by randomly scanning the slide, it is helpful to have a properly aligned rotating stage, so that the flagellum can be rotated to lie in the proper shear axis. For our Axioplan 2ie microscope, if a cell body is in the center of the field, the flagellum should point to ~10 O'clock for optimal orientation.

Flagella are most easily selected by scanning by eye. To observe flagella, close the condenser aperture diaphragm and scan the field. When the specimen to be recorded is found, open the diaphragm to fill the back focal plane for maximum resolution, and view the flagella on the monitor.

2. Fluorescence Microscopy

IFT also can be observed, in tissues or in protozoan flagella if IFT particles contain fluorescently-tagged molecules (Snow et al, 2004; Mueller et al, 2005). Some microscopy facilities may have better equipment for fluorescence microscopy than they do for DIC, so capturing IFT using fluorescence microscopy should be considered.

The major disadvantages of fluorescence microscopy include the requirement for a fluorescently tagged IFT particle or motor protein subunit and problems associated with photobleaching and phototoxicity. The primary requirements for microscope optics and specimen preparation are the same as described for DIC (above).

To minimize photobleaching, first find and orient flagella with observable IFT using DIC. Then switch to fluorescent illumination and record a series of images. Phototoxicity can be a major problem and high levels of UV light can result in GFP-tagged IFT particles slowing down after approximately 30 seconds. To minimize photobleaching and phototoxic effects, we use an X-cite light (Exfo Photonic Solutions, Ontario, Canada) at an intensity of 75% or less to observe movements of GFP tagged KAP subunits (Mueller et al., 2005). Using these conditions, IFT can be observed and recorded for up to one minute. Others have successfully used laser illumination systems to observe movements of GFP-tagged IFT particles (Qin et al.). Use of monochromatic light sources also may reduce phototoxicity. Preliminary reports on the use of TIRF microscopy to study IFT are promising, but no detailed protocols have yet been published.

Are the same particles observed using DIC and fluorescence microscopy? Comparisons of IFT recorded by fluorescence and DIC microscopy (Figure A1.2) indicate that it is likely that the same anterograde particles are observed by both methods. However, the smaller retrograde IFT particles (Iomini et al, 2001; Dentler, 2005; Mueller et al., 2005) are more difficult to resolve using fluorescence microscopy, so many movies and kymographs must be examined to have a sufficient number of particle tracks to confidently assess the retrograde IFT rates using fluorescence microscopy.

D. Recording IFT

1. Cameras

A variety of cameras are available for microscopy, and each laboratory will likely have their own specific equipment. It is helpful to mount the camera on the microscope so that the camera can be rotated to orient the flagellum vertically on the screen. This reduces the size of the image to be captured, and reduces the memory required for image capture, and allows one to focus on IFT within the flagellum.

Our most reliable camera for DIC observations is a Nuvicon Video Camera (NC-70, DAGE-MTI, Michigan City, IN). The camera is sufficiently sensitive to record IFT using halogen lamps (above) and adjustments are adequate to produce high contrast images. Additional image enhancement can be done by sending the Nuvicon signal through an Avio Image Σ processor, but to our knowledge, this equipment no longer is available. The Nuvicon camera must be used with a frame grabber card such as the Scion FG-7 (www.scioncorp.com), which can be used with Macintosh (OS10) and PC computers and Windows (Microsoft Corp). Digital cameras also can be used. We have had limited experience using an Orca ER (Hamamatsu Photonics) and find that it produces excellent images, depending on the capture software and computer buffering capacity.

For fluorescence microscopy, a highly sensitive digital camera must be used along with the appropriate light source. The camera must be sufficiently sensitive to detect a fluorescent signal in a flagellum and be fast enough to record particles moving at IFT

rates. We have had the best experience with a Rolera MGi EMCCD camera (www.qimaging.com). Standard GFP filter sets should be sufficient to image GFP tagged IFT particles, although a Semrock GFP-3035B filter set (www.Semrock.com) provides significantly brighter GFP images than conventional filters. Be aware that the DIC images taken with digital cameras are not as crisp as those taken with the Nuvicon camera, but this is a trade-off between magnification and light intensity that must be made to collect both DIC and fluorescent images from the same camera.

2. Image-capture

Image capture can be carried out with a variety of cameras and programs. Two methods that we use are described below. We also have successfully used Slidebook software ((http://www.intelligent-imaging.com/home.php) and a Hamamatsu Orca ER (www.hamamatsu.com) camera to capture images, but, for DIC, find the Nuvicon cameras to work slightly better than the digital cameras.

It is helpful, although not essential, to have a second (live) monitor that can be used to view and focus the live image. The signal from the camera passes through the live monitor and then into the frame grabber in the computer, where the image appears on the computer monitor.

a. Scion image (Scion Corporation, Frederick, MD)

The least expensive method, in terms of equipment and software, is to use a Nuvicon video camera, Scion frame grabber, and a Macintosh or PC computer. The computer requirements are modest: most of our images were captured with a Macintosh 7600 computer with 512 MB of RAM and a Scion VG5 frame-grabber. A more modern computer with additional memory and newer frame-grabber board will allow capture of larger image stacks. The Nuvicon camera and controller are relatively inexpensive and the Image J program is free (http://rsbweb.nih.gov/ij/).

The following steps describe the capture process with the Scion VG5 frame grabber and Scion Image (http://www.scioncorp.com/frames/fr_technical_support.htm). For the newer FG7 frame grabber, software for Windows and Macintosh computers can

be downloaded from Scion (http://www.scioncorp.com/frames/fr_technical_support.htm). Install the appropriate plug-ins into Image J before capturing image stacks using Image J.

1. Place the specimen on the microscope stage, focus the specimen, adjust the condenser focus and open the field and condenser diaphragms to achieve Koehler illumination.
2. Select cells with straight flagella attached to the coverslips. If possible, select cells that are oriented parallel to the DIC shear. Most of the time, flagella will need to be oriented by rotating the microscope stage to orient the flagellum parallel to the DIC shear. In a Zeiss Axioplan, orient the flagella to point to ~10 O'clock, or ~315˚.
3. Open Scion Image and select Special>Camera(Live).
4. Optimize image contrast using the camera controller.
5. Adjust image contrast and the DIC slider to obtain the best image on the computer and on the live monitor.
6. Rotate the *camera* to orient the image of the flagellum so the flagellum is vertical on the monitor.
7. Select a rectangular area to select the flagellum.
8. Set up to capture a movie. Stacks>Make Movie (movies are simply stacks of images).
    a. Select the number of frames to be captured. We usually use 600 frames, depending on the amount of memory available. Record the number of frames and the time of recording for measurements.
    b. Select the frame rate – usually 30 frames/second
9. Press "OK". The computer will set up a buffer for the frames and will start to collect the images. Some adjustment for focus may need to be made. This is easily done looking at the "live" monitor but can be done viewing the computer image.
10. When frames are captured, save the movie to a file.

b. Metamorph (Molecular Devices, Downington, PA)

The following steps are for Metamorph Version 7.5.6. Some older versions of Metamorph have a bug in the kymograph program that can lead to errors in the estimation of distance and should be used with caution.

1. Open the program and select Acquire>Acquire>Show Live.
2. Select the Center Quad camera area to increase the camera's frame rate capability.
3. Select and adjust the EM gain in the Special tab in the Acquire window. A good starting range is 5 MHz, at a value around 2000.
4. Select an exposure time so that the camera's frame rate is 10 – 30 frames per second. Do not use binning, or the image quality will be too poor for analysis.
5. Set up to capture a movie. Select Acquire>Stream Acquisition. Then, select the number of frames and hit the acquire button to capture the movie.
6. After the movie is acquired, save the movie.

E. IFT analysis

IFT particles rapidly move up and down the flagellum, so it is essential to visually separate anterograde and retrograde particles by preparing kymographs that reveal the location of each particle relative to the time recorded (Iomini et al, 2001). Anterograde particles, moving from base to tip are readily distinguished from retrograde particles, which move from the tip to the flagellar base. The size of the particles can be estimated from the thickness of the path. Kymographs are easily generated using Image J or Metamorph (version 7.5.6)

1. Kymograph preparation

a. Image J

(1) Individual kymographs

1. Open the captured movies (image stack) with Image J and rotate flagellar image stacks so that the flagella is vertical (Image>Rotate>Arbitrarily).
2. Use the rectangle tool to make a rectangular selection of the flagellum, cropping as close as possible to the flagellum.

3. Adjust contrast (Image>adjust>brightness/contrast). Set the maximum and minimum sliders to include the areas in the histogram. Click “Apply” to apply the contrast change to all frames in the image stack.
4. Reslice the image (Image>Stacks>Reslice). Select “Start At”: Left and click the Rotate 90 Degrees box. Then select “OK”. A “Reslice” image will open. This may be relatively faint, so the image can be greatly improved using “Z-project”.
5. Move the slider on the bottom of the Reslice window to select the frames that best show the IFT tracks.
6. With the Reslice window active, select Image>Stacks>Z project. Ignore the warning window and click OK.
7. Select start and stop slices. This can be ignored, if the flagellum is closely cropped, or the slices can be selected by observing the slices that show the best image as the slider in the Reslice window is moved. Select Average Intensity and click OK.
8. A kymogram showing anterograde and retrograde transport will appear in a new window, AVG_Reslice of (file name).
9. Save the kymogram as a tiff file (File>Save As…)

(2) Kymograph montage

To analyze IFT, collect as many movies as possible. Some will show better IFT than others. To compare all tracks in various experiments, a montage combining all kymograms from an experiment can be prepared using Photoshop (Adobe Corp). Kymograph images are then sharpened and enhanced to visualize the IFT tracks and to allow comparison among different experiments.

1. Open each kymograph, adjust contrast with “levels” (select Auto), and copy the kymograph to a single Photoshop page. When all kymograms are arranged on the page, flatten the image layers (Layer > Flatten) and crop the image.
2. To enhance the images:
    a. Select the entire montage and apply Gaussian Blur (Filter>Blur>Gaussian Blur). Select 0.7 pixels and press OK.

b. Apply Unsharp Mask (Filter>Sharpen>Unsharp Mask). Select 298%, 2.7 pixels, threshold = 1 and press OK. This will provide a good set of kymograms in which IFT tracks are readily visible.

3. Save the final filtered montage as an uncompressed TIFF file for analysis with Image J.

b. Metamorph

1. Open the captured movie with Metamorph.
2. Adjust digital contrast to best see IFT (Display>Adjust Digital Contrast).
3. Set up to make the kymograph (Stack>Kymograph).
4. Draw a straight line using the line tool along the length of the flagellum. Change the line width in the Kymograph window to cover the width of the flagellum.
6. Select which frames to make the Kymograph from. All frames can be used if the "All frames" box is checked.
7. Select Create to make the kymograph.
8. Adjust digital contrast on the kymograph so that the IFT tracks are most clearly seen.
9. Save the kymograph as a tiff file (File>Save).

2. Kymograph analysis

IFT particle rates and frequencies are manually scored by analyzing kymograms with Image J or Metamorph software.

For IFT rates, measure the angle of each anterograde (up and to the right) and each retrograde (down and to the right) track using the Image J angle tool or the Metamorph line tool. Save each measurement. Both Image J and Metamorph measurements can be opened in commonly used spreadsheets. Be certain to record the frame rate of the movie by dividing the total number of images (frames) by the recording time. The rate of movement is a function of the tangent of the measured angle of IFT movement and the measured length of the flagellum. The frequency (number of

anterograde or retrograde tracks/time) is measured by counting the number of tracks and dividing by the time recorded.

Estimation of IFT particle frequencies with the fluorescent images is somewhat more problematic due to potential bleaching of the signal over the time course of image capture. We typically use only the first 30 seconds of a recording to estimate particle frequencies.

A1.3. SUMMARY

Recording and analyzing IFT is relatively simple and can be accomplished using commercially available cameras, computers, and software packages. Here we described two different packages but similar results can be obtained with other software. It is critical to have high-resolution optics, microscopes with high light throughput, and, for DIC, properly aligned the optics and flagellar orientation relative to the DIC shear. Of equal importance is patience. Frequently, one will start recording flagella exhibiting beautiful IFT only to find that the cell becomes camera-shy and glides out of the field of view. With patience and experience, however, IFT recordings are easily made.

A1.4 TABLES AND FIGURES

Figure A1.1. IFT particle movement analyzed using kymographs. (A) A flagellum with IFT particles (arrowheads) is shown to the left of "A" and a kymograph showing the movement of these particles is at the right of the flagellum. Anterograde particles move toward the flagellar tip (black arrows) and smaller retrograde particles move toward the base of the flagellum (white arrows). The white arrowhead points to a larger and slowly moving particle, likely moving along the flagellar surface. (B) Thin section of Chlamydomonas flagella showing IFT particles with higher magnification images shown in (C) and (D). It is not known if these are anterograde or retrograde particles. (W. Dentler)

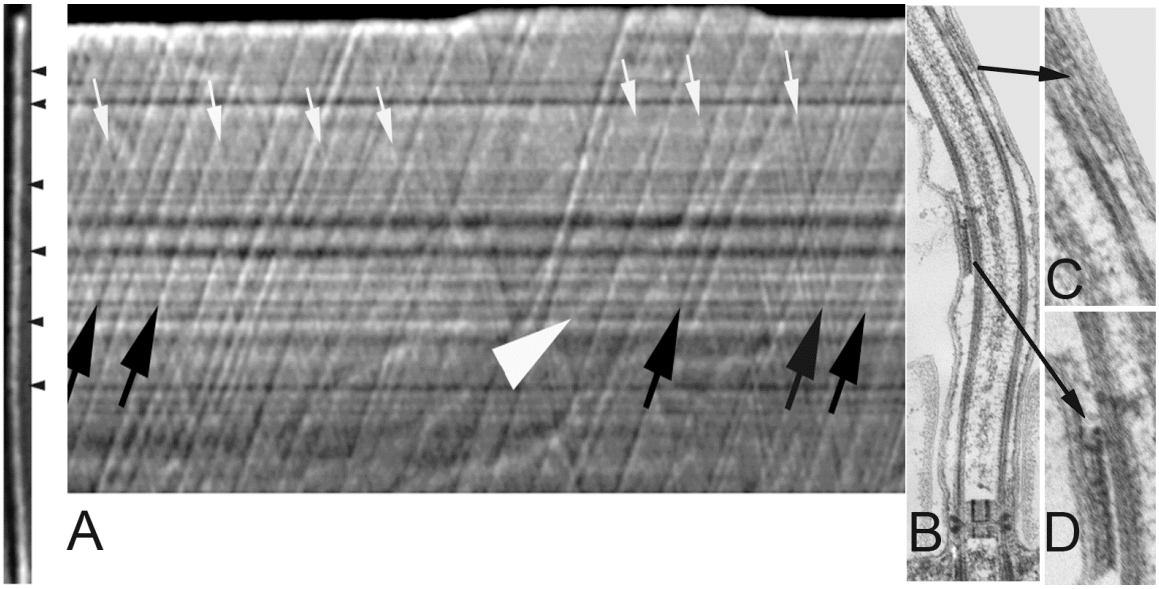

Figure A1.2. Comparison of IFT by DIC and wide-field fluorescence microscopy recorded with a digital camera. The vertical bar is 1 μm and the horizontal bar is 1 s. (K. VanderWaal)